Microwave-assisted synthesis of palladium-based core-shell nanocatalysts and iron phthalocyanines and their applications in direct alkaline alcohol fuel cells

by

Omobosede Oluwatoyin Fashedemi

Dissertation submitted in fulfilment of the requirements for the degree

of

Doctor of Philosophy

In the Faculty of Natural and Agricultural Sciences

University of Pretoria

December 2013

Supervisor: Prof. K. I. Ozoemena

Declaration

I declare that the dissertation, which I hereby submit for the degree of Doctor of Philosophy in the Faculty of Natural and Agricultural Sciences at the University of Pretoria, is my own work and has not previously been submitted by me for a degree at this or any other tertiary institution.

_____

Omobosede Oluwatoyin Fashedemi

U11020751

Dedication

To Our Lady, Sedes Sapientiae, Ancilla Domini.

Acknowledgements

Gratias Tibi Deus, Gratias Tibi!

I wish to say a very big thank you to my supervisor, - Prof Kenneth Ozoemena.

To my Daddie! For all the days and nights you spent at every stage of this study, for your financial and moral support and for all the pieces of advice you showered on me since the onset of the study. You are really a Daddie: a 'Dad-to die-for' anytime! A 'Mega' thank you to my Mummie too, for your prayers, encouragement and care for all of us. To my sisters at Arbor: Agueda, Raquel, Esther, Leslie, Yayoi, Maria Angelica, and Ozo; you all did a good job of being patient with my odd time table during the days of my research. A big thank you also goes to all of my sisters in Lakeview, Atlantika, and Arengo. My siblings: Sis Layo, Pido, Dotun, Tolu, F.F., Man-Niyi, and Shollyboy whose 'night chats' helped my late study hours. You all have been splendid. I thank God for putting you all around me.

I am also grateful to my research group members at the Molecular and Nanomaterials laboratory at department of chemistry, and those of the Carbon materials group in Physics. A big appreciation to my scientific team at ICCOM, Italy, and a special thanks to my 'cappo'- Francesco and Hamish, for your support throughout my stay with you in Florence.

Thanks to the CHRTEM at NNMU, Department of Physics, Western Cape University and EMU at University of Pretoria.

A special thanks to Naomi Steenkamp of the Department of Chemistry.

My 'H- Buddies' are not left out in my appreciation list, Don Alvaro, Boni, Luigi, and 'Lil' WM. You have all been wonderful and truly 'miraculous'.

A special thanks to my University, University of Pretoria, for providing an excellent scientific platform for this study and for her financial support, and to NRF/DST Nanotechnology Flagship Program for doctoral bursary.

Abstract

Palladium-based nano-alloys are well-known for their unique electrocatalytic properties for direct alcohol alkaline fuel cells (DAAFCs). This dissertation describes, for the first time, the synthesis of a novel ternary palladium-based core-shell nanocatalyst containing iron, cobalt and palladium (i.e., FeCo@Fe@Pd) using a microwave-assisted solvothermal technique. This microwave-induced fast and efficient synthesis of sub-10 nm sized palladium-decorated FeCo@Fe core-shell nanoparticles (ca. 3 – 7 nm) from a large-sized FeCo@Fe (0.21 – 1.5 μm) precursor, clearly suggests a 'top-down' nanosizing. I have termed this technique the "*microwave-induced top-down nanostructuring and decoration* (MITNAD)". The nanocatalysts were successfully supported on commercial carbon (C, Vulcan®) and carboxy- and sulphonate-functionalised multi-walled carbon nanotubes (CNT-OH and CNT-SO_3). They were thoroughly characterised using HRTEM, HAADF-STEM, EELS, SAED, FESEM, and EDX. The characterisation clearly proved the elemental composition, nanoparticulate nature, particle size ranges, core-shell nature, and morphology of the nanocatalysts. The nanocatalysts were subjected to electrochemical characterisation to establish their possible application as viable catalysts for DAAFCs. Half-cell anodic oxidation studies were carried out in alkaline medium using both monohydric alcohols (i.e., methanol and ethanol) and polyhydric alcohols (i.e., ethylene glycol and glycerol). Oxygen reduction reaction (ORR) was done in alkaline medium. Electrocatalytic parameters like oxidative onset potential, current response, electron transfer capabilities, Tafel values, ion exchange current densities, catalytic rate constants, and cycling stability as well as alcohol cross-over tests were all determined using various electrochemical techniques. Interestingly, the nanocatalysts exhibited excellent resistance to possible alcohol cross-over during ORR, which gives excellent promise for application in direct alkaline alcohol fuel cells (DAAFC).

In general, the electrochemical performance of the nanocatalysts follows this trend: FeCo@Fe@Pd/CNT-OH >> FeCo@Fe@Pd/CNT-SO_3 ≈ FeCo@Fe@Pd/C. Based on the findings in the half-cell studies, a preliminary screening of the FeCo@Fe@Pd/CNT-OH and FeCo@Fe@Pd/C were carried out in the complete single fuel cell membrane electrode assembly (MEA) test. The catalysts were tested in DAAFCs using the above stated four alcohols. Faradaic and Energy efficiency performances were obtained in the monohydric fuel cells, while the fuel cell exhaust components were analysed in the polyhydric fuel cells to determine their capability for complete oxidation of these fuels. Using NMR, the exhaust products were carefully determined and, surprisingly, the FeCo@Fe@Pd/CNT-OH showed excellent selectivity towards complete oxidation of the polyhydric alcohols.

The second aspect of this research deals with the study of the electrocatalytic properties of a novel N4-macrocyclic complex (i.e., metallophthalocyanine, MPc) catalysts for ORR in alkaline fuel cells. A new hydrophobic form of Fe (II) tetrasulfophthalocyanine was synthesized. As a cathode catalyst for fuel cells, its exceptional resistance to high concentrations of methanol during the cathodic reaction has been quite surprising. It was able to selectively continue the ORR even in the presence of high quantities of alcohol in the electrolyte. This clearly proves that a cheap MPc can serve as an alternative to the costly noble metal catalyst for ORR. Further studies using MEA in real fuel cells will be necessary to ascertain this assumption.

Table of Contents

LIST OF ABBREVIATIONS and SYMBOLS

A	Geometric surface area
AC	Alternating current
AEM-DGFC	Anion-exchange membrane direct glycerol fuel cell
AEMFC	Anion-exchange membrane fuel cell
AFC (s)	Alkaline fuel cell(s)
b	Tafel slope value
bcc	body centred cubic
BP	Black Pearls
CA	Chronamperometry
C_{dl}	Double layer capacitance
CL	Catalyst layer
C_o^0	Concentration of oxidised species
CP	Chronopotentiometry
C_R^0	Concentration of reduced species
C_R^0/C_o^0	Redox couple
CV	Cyclic voltammetry
D	Diffusion coefficient
DAAFC(s)	Direct alkaline alcohol fuel cell(s)
DAFC(s)	Direct alkaline fuel cell(s)
DEFC(s)	Direct ethanol fuel cell(s)
DEGFC(s)	Direct ethylene glycol fuel cell(s)
DGFC(s)	Direct glycerol fuel cell(s)
DMFC(s)	Direct methanol fuel cell(s)
E	Potential

EASA	Electroactive surface area
EDS	Energy dispersive X-Ray spectroscopy
EELS	Electron energy loss spectrum
E_{eq}	Equilibrium potential
EG	Ethylene glycol
EIS	Electrochemical impedance spectroscopy
EOR	Ethanol oxidation reaction
E_{pa}	Anodic peak potential
E_{pc}	Cathodic peak potential
E_{sw}	Square wave pulse amplitude
E_t	Thermo-neutral potential
EtOH	Ethanol
E^{θ}	Standard potential
F	Faraday's constant.
fcc	face centred cubic
FESEM	Field emission scanning electron microscopy
GCE	Glassy carbon electrode
GDL/GL	Gas diffusion layer
GLY	Glycerol
HAADF	High angle annular field imaging
HPLC	High performance liquid chromatography
HRTEM	High resolution transmission electron microscopy
i	Current
i_0	Ion exchange current
I_{buff}	Current in the absence of analyte

I_{cat}	Current in the presence of analyte
i_f	Forward current
i_K	Kinetic current
i_L	Levich current
i_l	Limiting current
i_l^{diff}	Diffusion limiting - current
i_l^{film}	Diffusion limiting - current in the film
i_{max}	Possible maximum current
i_{net}	Net current
I_{pa}	Anodic peak current
I_{pc}	Cathodic peak current
i_r	Reverse current
IR	Infra-red spectroscopy
j	Current density
j_{lim}	Limiting current density
K_{cat}	Catalytic rate constant
K_θ	Standard rate constant / Heterogeneous rate constant
LSV	Linear scan voltammetry
MEA	Membrane electrode assembly
MeOH	Methanol
MOR	Methanol oxidation reaction
MWCNT	Multi walled carbon nanotubes
n	Number of moles of electrons
NMR	Nuclear magnetic resonance
ORR	Oxygen reduction reaction
Pc	Phthalocyanines
PcTc	Tetracarboxylic phthalocyanines

PEMFC	Polymer electrolyte /Proton exchange membrane fuel cell
Q	Columbic charge
R	Ideal gas constant
R_c	Cell resistance.
R_{CT}	Charge transfer resistance
RDE	Rotatory disc electrode
RHE	Reversible hydrogen electrode
R_s	Solution resistance
RSA	Real surface area
SEM	Scanning electron microscopic
SHE	Standard hydrogen electrode
STEM	Scanning transmission electron microscopy
SWV	Square wave voltammetry
t	Time
TAA	Dibenzotetraazaanulenes
tan δ	Loss tangent
TEM	Transmission electron microscopy
TMPP	Tetramethoxyphenyl porphyrins
TPP	Tetraphenyl porphyrins
UPD	Under potential deposition
UV	Ultra - violet spectroscopy
W	Warburg impedance
x	Distance from the electrode surface
XRD	X ray powder diffractogram
Z	Impedance
Z'	Real impedance

Z''	Imaginary impedance

GREEK SYMBOLS

α	Charge/Electron transfer coefficient
γ	Kinematic viscosity
ΔG	Free energy change
ΔG^0	Standard free energy change
ΔH	Enthalpy change
ε′	Dielectric constant
ε″	Dielectric loss
ε_F	Faradaic efficiency
ε_{fc}	Fuel cell (stack) efficiency
ε_H	Hydrocarbon efficiency
ε_r^{cell}	Thermodynamic fuel cell efficiency
ε_v	Electrochemical efficiency
η	Over potential
η_{act}	Activation polarization
η_{con}	Concentration polarization
η_{ohm}	Ohmic polarization
μ_F	Fuel utilization
v	Scan rate
ω	Angular velocity
θ	Degree of electrode surface coverage by oxygen adsorbed species

LIST OF FIGURES

LIST OF SCHEMES

LIST OF TABLES

PART I

Chapter 1

INTRODUCTION AND LITERATURE REVIEW

1.1 Renewable Energy

Energy has been listed as humanity's number one problem for the next 50 years by several agencies. That it surpasses other issues such as water, food, environment, poverty, terrorism, war, disease, education, democracy, and population, underscores the criticality of energy in almost everything that a society does. The United States Department of Energy (USDoE) projects (http://www.eia.doe.gov/oiaf/ieo) that the world's total energy consumption will rise by 54% between 2001 and 2025. This projected increase may be an underestimation due to the rapid economic development in heavily populated countries like India, China, and some countries in Africa. This worldwide competition for energy sources is likely to create tensions among countries unless they can develop new energy sources. It is thus imperative that we must develop alternative energy sources in order to meet our future energy needs. This is because: (i) the fossil fuel reserve will not be sufficient to meet the demand beyond 2050; and (ii) an over-reliance on fossil fuels (many of them are located in politically unstable regions in the Middle East, Central Asia, Africa, and Latin America) has both environmental and political implications[1]. Most of the nations of the world currently rely heavily on coal, oil, and natural gas for energy. These conventional fossil fuels are non-renewable, finite resources that will eventually dwindle, becoming too expensive or too environmentally damaging to retrieve. To achieve a sustainable energy future, fuel diversity must be developed.

Renewable energy technologies are clean sources of energy that have a much lower environmental impact than conventional energy technologies. Renewable energy will not run out while other sources of energy are finite and will someday be depleted. Most renewable energy comes either directly or indirectly from the sun, thus solar energy can be used directly for heating and lighting homes and other buildings, for generating electricity, and for hot water heating, solar cooling, and a variety of commercial and industrial uses.

The sun's heat also drives the *winds*, whose energy is captured with wind turbines. A combination of the winds and the sun's heat causes the evaporation of water; water vapour turns into rain or snow which flows into rivers or streams, its energy can be captured using *hydroelectric power.* Sunlight is also the source of energy for the photosynthetic process in plants. Biomass is the organic matter derived from plants and can be used to produce electricity, transportation fuels, or chemicals. The use of biomass for any of these purposes is called *bioenergy.* Hydrogen on the other hand is an energy carrier (an intermediary or secondary source of energy) and not a primary energy source. As hydrogen can be produced or manufactured through other renewable sources of energy it can be listed among the renewable forms of energy. " if solar energy, in its direct and/or indirect forms (e.g. hydro, wind, etc.), is used to manufacture hydrogen, then both the primary and secondary energy sources are renewable and environmentally compatible, resulting in a clean and permanent energy system"[2]

1.1.1 Hydrogen Energy

Hydrogen is the first element of the Periodic Table consisting of only one proton and one electron. It is the simplest and most abundant element in the universe. Despite its simplicity and abundance, hydrogen does not occur naturally as a gas on the Earth – it is always combined with other elements, and so it can be mined from primary energy sources like water, or non-fossil fuel energy such as solar, wind, and nuclear energy. It is also found in hydrocarbons that make up other common fuels such as gasoline, natural gas, propane, and methanol

Hydrogen can be separated and obtained from these energy sources in different ways; electrolysis is used to separate water into its components of oxygen and hydrogen and hydrogen can be separated from hydrocarbons through reforming process. Currently, most hydrogen is

made this way from natural gas. Once separated from other elements, hydrogen can be burned as a fuel or converted into electricity through fuel cells.

Extended use of hydrogen can lower the emission of greenhouse gases like CO_2 which gives it its unique environmentally benign quality. An engine that burns pure hydrogen produces almost no pollution. NASA (*National Aeronautics and Space Administration)* has used liquid hydrogen since the 1970s to propel the space shuttle and other rockets into orbit. Hydrogen fuel cells power the shuttle's electrical systems, producing a clean by-product - pure water, which the crew drinks[3]. Thus, developing this marvellous clean energy carrier can be a solution to the world's energy appetite.

Hydrogen has been termed the energy of twenty first century and a lot of on-going research and studies are being carried out in hydrogen technology. The properties of hydrogen also make it a unique fuel. It also gives it a number of advantages over conventional fuels. It has been called the optimal replacement for fossil fuels particularly in the transportation sector which represents the majority of petroleum consumption world-wide. I.P. Jain[4] in a brief review on hydrogen gives a concise list of the unique properties which makes hydrogen the 'choice' source of energy in today's world. The reasons are because it / (it is):

- high in energy content
- clean source of energy(without Pollution)
- most abundant element in the universe
- the lightest fuel (It is eight times lighter than methane and fourteen times lighter than air with a density of 0.084 kgm^{-3})
- richest in energy per unit mass (34 $Kcalg^{-1}$).
- can be stored easily
- can be produced by water

- can be directly converted to thermal, mechanical and electrical energy

Veziroglu and Sahin[2] on the other hand listed the advantages of hydrogen over fossil fuels (amidst other 'hydrogen focuses' discussed in their review). These are:

- liquid hydrogen is one of the best transportation fuel when compared to liquid fuels such as gasoline, jet fuels, and alcohols. Gaseous hydrogen is also the best gaseous transportation fuel.
- While hydrogen can be converted to useful energy forms, (thermal, mechanical, and electrical) at the user end through different processes, fossil fuels can only be converted through one process (flame combustion). This makes hydrogen the most versatile fuel.
- Hydrogen also has the highest utilization efficiency when it comes to conversion into useful energy forms. It is 39% more efficient than fossil fuels. It could also be termed the most energy conserving fuel as it saves other primary energy sources.
- When fire hazards and toxicity are taken into account, hydrogen becomes the safest fuel.

In a more recent publication titled "*Hydrogen energy -Abundant, efficient, clean: A debate over the energy-system-of-change*"[5], Winter Carl-Jochen expounds extensively on the importance and use of hydrogen as the future energy source using the phrase "its HY*time*" as his introduction.

1.2 Fuel Cells

A fuel cell is an electrochemical device (a galvanic cell) which directly converts free energy of a chemical reaction (chemical energy) to electrical energy. It converts the chemical energy contained in a fuel electrochemically into electrical energy and other by products like heat and water. The basic structure of a typical fuel cell (Fig 1.1) consists of an electrolyte medium sandwiched between two electrodes. The anode facilitates electrochemical oxidation of fuel, while the cathode promotes electrochemical reduction of oxidant. Ions generated during oxidation or reductions are transported from one electrode to another through the ionically conducting but electronically insulating electrolyte. The electrolyte also serves as a barrier between the fuel and the oxidant. Electrons generated at the anode during oxidation passes through an external circuit / device (hence - generating electricity) on their way to the cathode, where they complete the reduction reaction. The fuel and oxidant do not meet at any point and so no actual burning occurs.

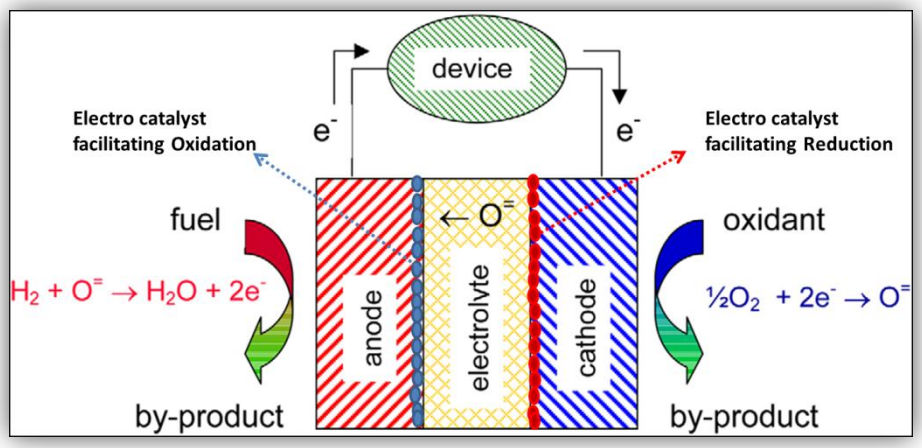

Figure 1.1: A typical fuel cell which consists of an electrolyte medium sandwiched between two electrodes (anode and cathode)[6] (image has been slightly modified by the author for clarity).

1.2.1 History of Fuel Cell Technology

The first scientific research on fuel cell was conducted by a German scientist Christian Fredrich Schonben but the origin of fuel cell dates back to an earlier year. The origin of fuel cell technology is credited to Sir William Robert Grove who introduced the concept of hydrogen fuel cell (1811-1896). Extensive historical details of the evolution of fuel cells can be found in a recent publication titled "Fuel Cells: history and updating. A walk along two centuries" by Andujar and Segura[7]. A brief summary is given in the subsequent paragraphs.

Sir William Grove developed an improved wet-cell battery in 1838 which brought him fame. Using his research and knowledge that electrolysis used electricity to split water into hydrogen and oxygen he concluded that the opposite reaction must be capable of producing electricity. Using this hypothesis, Grove developed a device which would combine hydrogen and oxygen to produce electricity. Thus he developed the world's first gas battery which has become known as the fuel cell.

Ludwig Mond (1839-1909) along with Carl Langer conducted experiments with a hydrogen fuel cell that produced 6 amps per square foot at 0.73 volts. Mond and Langer came across problems using liquid electrolytes. As Mond said *"we have only succeeded by using an electrolyte in a quasi-solid form soaked up by a porous non-conducting material, in a similar way as has been done in the so-called dry piles and batteries"*. Mond used an earthenware plate saturated with dilute sulphuric acid.

Friedrich Wilhelm Ostwald (1853-1932), the founder of the field of physical chemistry, experimentally determined the relationship between the different components of the fuel cell, including the electrodes, electrolyte, oxidizing and reducing agent, anions and cations. Ostwald's work opened doors into the area of fuel cell research by supplying information to future fuel cell researchers.

During the first half of the twentieth century, Emil Baur (1873-1944) conducted extensive research into the area of high temperature fuel cell devices which used molten silver as the electrolyte. He built the first molten carbon fuel cell in 1921.

Francis Thomas Bacon (1904-1992) performed research and significant developments with high pressure fuel cells. In 1939, Bacon was successful in developing a fuel cell that used nickel gauze electrodes and operated at pressures up to 3000 *psi*. Bacon's work continued through World War II as he tried to develop a fuel cell to be used in the Royal Navy submarines. In 1958, his work led to the development of an alkali cell using a stack of 10" diameter electrodes for Britain's National Research Development Corporation. Bacon's developments were successful enough to attract the interest of Pratt & Whitney, and his work was licensed and used in the Apollo spacecraft fuel cells. Similar technology is still being used in space crafts. A pictorial summary of the history of fuel cells down the ages (culled from "*FuelCellToday*") from its origins to its most recent developments is shown in the Fig 1.2 below.

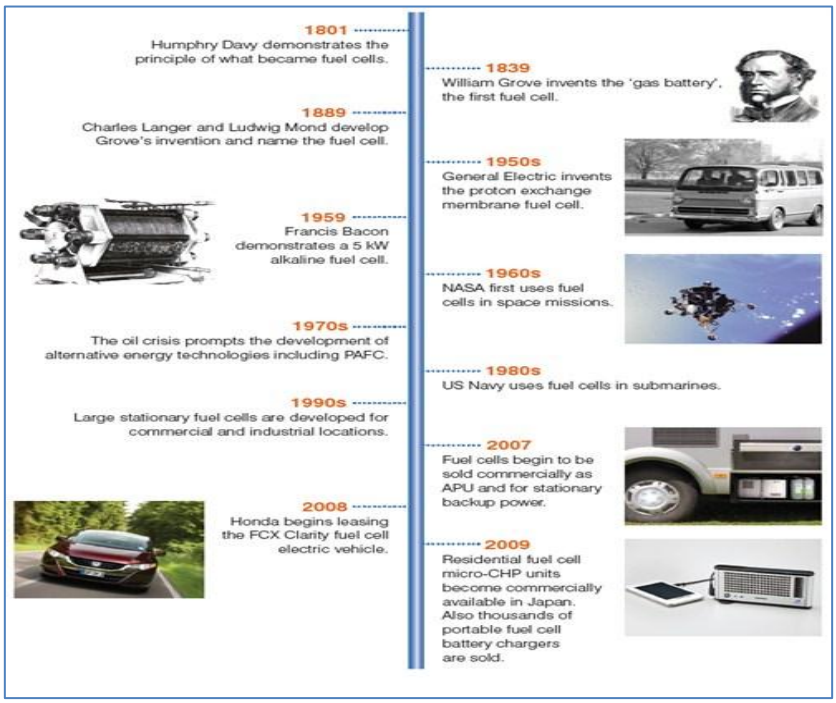

Figure 1.2: History of Fuel cell technology (Source: www.fuelcelltoday.com/history).

1.2.2 Types of Fuel Cells

Fuel cells are named by their electrolytes. The 5 distinct classes of fuel cells that have been developed are:

- alkaline fuel cells
- polymer electrolyte membrane fuel cells
- direct methanol fuel cells
- phosphoric acid fuel cells
- molten carbonate fuel cells
- solid oxide fuel cells

The 'fuel cell wheel' (Fig 1.3) below gives a good summary of these fuel cell and their applications[8]:

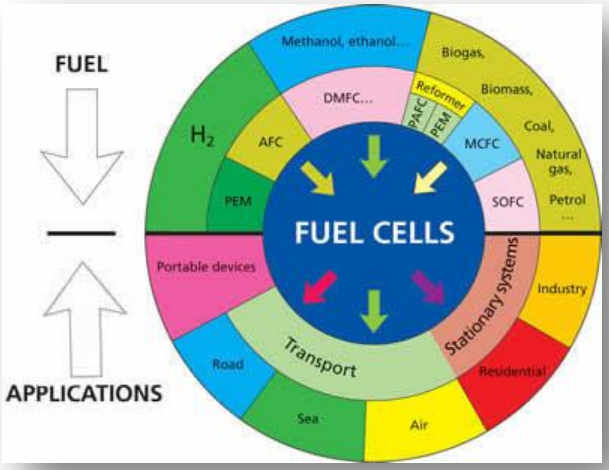

Figure 1.3: Fuel cell wheel showing the 5 classes of fuel cell and their applications (Source: www.google image; retrieved on 16.12.2013).

Some of the main features of the types fuel cells like the electrolyte used, operating temperature, and electrode reactions are further summarised in the Table 1.1 (adapted from www.education.lanl.gov/resources/fuelcells).

Table 1.1: Main features of classes of Fuel Cell Technologies

Fuel Cell	Electrolyte	Operating Temperature (° C)	Electrochemical reactions	Applications	Advantages	Disadvantages
Alkaline (AFC)	Aqueous solution of potassium hydroxide soaked in a matrix	80 – 100	**Anode**: H_2 +2$(OH)^-$-> $2H_2O$ +2e^- **Cathode**: ½ O_2 + H_2O +2e → 2$(OH)^-$ **Cell:** H_2 + ½ O_2→ H_2O	Military space	•Cathode reaction faster in alkaline electrolyte — so high performance	•Expensive removal of CO_2 from fuel and air streams required.
Polymer Electrode Membrane (PEM)	Solid organic polymer poly perfluorosulphonic acid	60 – 100	**Anode**: H_2 -> 2H^+ +2e^- **Cathode**: ½ O_2 + 2H^+ +2e → H_2O **Cell:** H_2 + ½ O_2→ H_2O	Electric utility. Portable power, Transportation	•Solid electrolyte reduces corrosion & management problems •Low temperature • Quick start up	•Low temperature requires expensive Pt catalysts • High sensitivity to fuel impurities
Direct Methanol	Polymer membrane	30-80	**Anode**: CH_3OH + H_2O -> CO_2 + 6H^+ +6e^- **Cathode**: $^3/_2$ O_2 + 6H^+ +6e → $3H_20$ **Cell:** $^3/_2$ O_2+CH_3OH → CO_2 + $2H_2O$	Portable Power	•Liquid fuel, high energy density •Low temperature • Quick start up	•Expensive Pt catalysts needed •Significant fuel cross over
Phosphoric Acid (PAFC)	Liquid phosphoric acid soaked in a matrix	175 – 200	**Anode**: H_2 -> 2H^+ +2e^- **Cathode**: ½ O_2 + 2H^+ +2e → H_2O **Cell:** H_2 + ½ O_2→ H_2O	Electric utility. Portable power, Transportation	•Up to 85 % efficiency in co-generation of electricity and heat •Impure H_2 as fuel	•Pt catalyst • Low current and power • Large size/weight
Molten Carbonate (MCFC)	Liquid solution of lithium sodium or potassium carbonates, soaked in a matrix	600 – 1000	**Anode**: H_2 +CO_3^{2-}---> H_2O +CO_2 +2e^- **Cathode**: ½ O_2 + CO_2+2e^- → CO_3^{2-} **Cell:** H_2 + ½ O_2 CO_2→ H_2O + CO_2	Electric utility	•High temperature advantages	•High temperature enhances corrosion and breakdown of cell components
Solid Oxide (SOFC)	Yttria stabilised zirconia, soaked in a matrix	600 – 1000	**Anode**: H_2 +O^{2-}-> H_2O +2e^- **Cathode**: ½ O_2 + +2e^- → O^{2-} **Cell:** H_2 + ½ O_2→ H_2O	Electric utility	•High temperature advantage. •Solid electrolyte advantages	•High temperature enhances breakdown of cell components

1.2.3 Need for Fuel Cells

Fuel cells are a promising technology. They are being used for a variety of processes already, and have a promising potential for a variety of future applications. The three main markets for fuel cell technology include: stationary power, portable power and transportation. Thus they are used as sources of heat and electricity for buildings, power sources for portable gadgets and as electrical power sources for electric vehicles or Fuel cell vehicles and buses.

Fuel cells are environmentally-friendly, efficient and cleaner. This is because they rely on electrochemistry and not combustion for the production of electrical energy. The main by-products from various fuel cells include: heat, and a minimized release of carbon (IV) oxide which is much smaller than that released by combustion driven sources.

Residential powered stationary fuel cell units have helped in reducing carbon footprint considerably. Some models can serve as a backup power for critical, required loads and may also be used as a supplement to the current power supply especially during extreme climate disasters like the tsunami; hurricanes etc., and in 'off the grid' zones in highly populated regions. In addition, various types of fuel cells can run off biomass, which gives them a great additional advantage in landfill areas which generate anaerobic gases that could also be used in production of electricity.

Fuel cells and batteries are electrochemical devices converting the energy produced by a chemical reaction into usable electric power. However, the fuel cell will produce electricity on demand as long as fuel and oxidant are supplied; never losing its charge unlike the battery which needs to be thrown away once the battery is discharged.

Fuel cells also have a more efficient conversion process; this is because chemical energy is converted directly to electrical energy while operating isothermally without temperature cycling. On the other hand, internal combustion engines, as well as conventional utility power plants, change chemical energy of fuel to thermal energy to generate mechanical and, in the case of a power plant, electrical energy. This makes them less efficient because they include the conversion of thermal to mechanical energy, which is limited by the Carnot Cycle. When used adequately, fuel cell technology proves to be 60 – 90% efficient.

Although, Fuel cells operate best on pure hydrogen, fuels like natural gas, methanol, or even gasoline can be reformed to produce the hydrogen required for fuel cells. Some fuel cells can even be fuelled directly with methanol or other alcohols, without using a reformer. According to Ball and Wietschelb[9], ”a lot of different fuel cell types exist which do not require hydrogen as fuel (as also seen in the previous section). Therefore fuel cells could enter the market independently of hydrogen production or infrastructure build-up. This is especially valid for portable applications and stationary applications. On the other hand stationary (high temperature) fuel cells - for heat distribution and power generation – are not necessarily a market for hydrogen because they can use, e.g. natural gas from the gas mains directly. Conversion of these fuels to hydrogen would only reduce their overall efficiency. However, the situation is different for mobile applications, where the dominant fuel cell type is the Proton Exchange Membrane (PEM) fuel cell, which only functions with pure hydrogen e g. Fuel cell vehicles’’.

1.2.4 Fuel Cell Thermodynamics

To predict how fuel cells interact with the systems where they are applied the influence of some thermodynamic variables e.g. pressure, temperature, gas concentration etc. on fuel cell performance have to be analysed and understood. Understanding the impact of these variables

allows system analysis studies of a specific fuel cell application[10]. In the "Green energy and technology series" Rivera et al[10] outlined the relationships among these thermodynamic variables in fuel cell systems as follows: One of the most simple and common reaction encountered in fuel cells is

$H_2 + ½ O_2 \text{ ----}\rightarrow H_2O$ (1.1)

From a thermodynamic point of view, the maximum work output obtained from the above reaction is related to the free-energy change of the reaction. The reaction is spontaneous and thermodynamically favoured because the free energy of the products is less than that of the reactants. The standard free energy change of the fuel cell reaction is indicated by the equation

$\Delta G = -nFE$ (1.2)

where ΔG is the free energy change, n is the number of moles of electrons involved, E is the reversible potential, and F is Faraday constant. If the reactants and the products are in their standard states, the equation can be represented as

$\Delta G^0 = -nFE^0$ (1.3)

The value of ΔG corresponding to (1.2) is -229 kJmol^{-1}, where $n = 2$, F = 96500 C mol^{-1}, and hence the calculated value of E is 1.229 V. The enthalpy change ΔH for a fuel cell reaction indicates the entire heat released by the reaction at constant pressure. The fuel cell potential in accordance with ΔH is defined as the thermo-neutral potential, E_t,

$\Delta H = -nFE_t$ (1.4)

where E_t has a value of 1.48 V for the reaction represented in equation 1.4. The electrochemical reactions taking place in a fuel cell determine the ideal performance of the cell. These reactions vary according to the types of fuel. The minimum temperature for optimum operating conditions also varies from cell to cell. Thus, the ideal performance of a fuel cell can be represented in different ways. The most commonly used practice is to define it by the Nernst potential represented as the cell voltage[11,10].

1.2.5 Voltage Losses in Fuel Cells

The ideal and actual performance of a fuel cell is quite different, especially when one analyses the potential current response of a fuel cell. Figure 1.3 displays the ideal and actual responses of a typical fuel cell. Electrical energy is obtained from a fuel cell when a current is drawn, but the actual cell potential is lowered from its equilibrium potential because of irreversible losses due to various reasons. Several factors contribute to the irreversible losses in a practical fuel cell. The losses, which are generally called polarization or over potential, originate primarily from activation polarization, ohmic polarization, and gas concentration polarization and are explained below[10,12]. They are shown in Fig 1.4

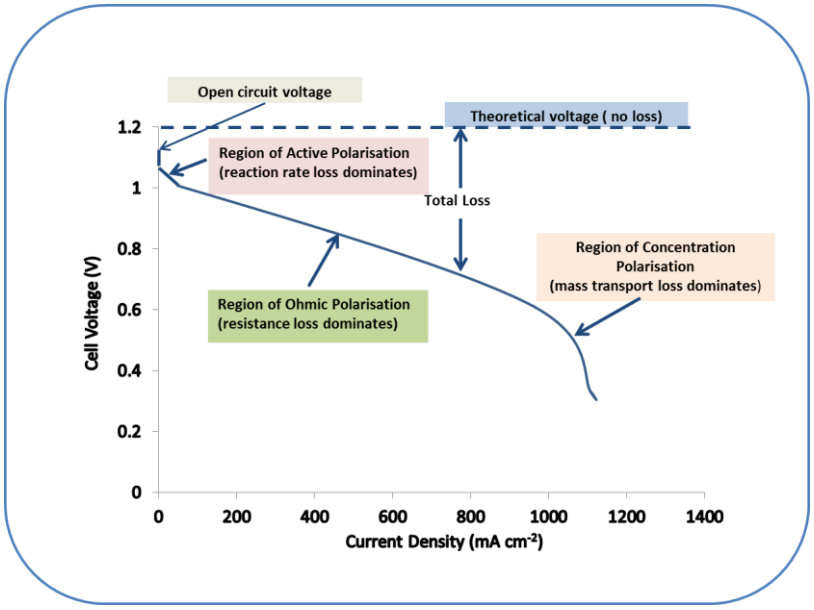

Figure 1.4: Ideal and actual performance of a fuel cell with respect to the potential - current response[10] (slightly modified by author).

1.2.5a Activation Losses

The activation losses arise predominantly due to the kinetics at the electrodes. The effects of these losses are most pronounced in the low current densities region (-1 to 100 $mAcm^{-2}$). In this region, electronic barriers must be overcome before the current and ionic flow begins. The activation loss is directly proportional to the increase in current flow. It can be represented as

$$\eta_{act} = \frac{RT}{\alpha nF} \ln \frac{j}{j_o} \quad (1.5)$$

where η_{act} is the activation polarization, R the universal gas constant, T the temperature, α the charge transfer coefficient, n the number of electrons involved, F the Faraday constant, j the current density, and j_0 the exchange current density. Slow electrochemical reactions give rise to activation potentials both at the cathode and the anode where the species are oxidized or reduced in a fuel cell reaction. It is directly related to the rate at which the fuel or the oxidant is oxidized or reduced.

1.2.5b Ohmic Losses

The ohmic polarization (η_{ohm}) originates from the resistance to the flow of ions in the electrolyte and flow of electrons through the electrodes and the external electrical circuit. The ohmic polarization varies proportionally to the increase in current and increases over the entire range of currents due to the constant nature of fuel cell resistance. It is most pronounced at intermediate current densities (100 - 500 $mAcm^{-2}$), and can be represented as

$$\eta_{ohm} = jR_c \quad (1.6)$$

Where R_c is the cell resistance. The dominant ohmic loss is in the electrolyte, which is reduced by decreasing the electrode separation, enhancing the ionic conductivity of the electrolyte and by modification of the electrolyte properties.

1.2.5c Concentration Losses

The concentration losses occur over the entire range of current density, but these losses become prominent at high limiting current densities (> 500 $mAcm^{-2}$) where it becomes difficult for gas reactant flow (in the case of H_2-utilising fuel cells) or alcohols to reach the fuel cell reaction sites. The concentration polarization can be represented as

$$\eta_{con} = \left(\frac{RT}{nF}\right) \ln\left(1 - \frac{j}{j_l}\right) \quad (1.7)$$

where η_{con} is the concentration polarization, j_l is the limiting current density. As the reactants are consumed at the electrode through the electrochemical reaction, there will be a potential drop due to the drop in the initial concentration of the bulk of the fluid in the surroundings. This leads to the formation of a concentration gradient in the system. Several processes are responsible for the formation of the concentration polarization. These are: (1) slow diffusion of the gas phase in the electrode pores, (2) solution of reactants into the electrolyte, (3) dissolution of products out of the system, and (4) diffusion of reactants and products, from the reaction sites, through the electrolyte. At practical current densities there is slow transport of reactants to the electrochemical reaction site and slow removal of products from the reaction site. This is a major contributor to the concentration polarization.

1.2.6 Fuel Cell Efficiencies

One of the advantages of fuel cells is the high conversion of their fuels; this makes the conversion efficiency of fuels used in fuel cells one of the major topics in fuel cell research. Thus the description of the fuel cell efficiency considers factors that are associated with its practical operations. There are many fuel cell efficiencies depending on the fuel cell type, fuel utilization and the fuel type. The overall fuel cell efficiency for a specified fuel cell stack can be equated as[10,14,14] :

$$\varepsilon_{fc} = \varepsilon_r^{cell} \boldsymbol{\varepsilon_v} \varepsilon_F \varepsilon_H \qquad (1.7)$$

These efficiencies are defined as follows:

ε_r^{cell} = the thermodynamic fuel cell efficiency, defined as the ratio of the Gibbs free enthalpy ΔG and the heating value, which is the enthalpy change of electrochemical reaction ΔH or energy released in burning the fuel

ε_v = electrochemical efficiency, defined as the ratio of the actual cell voltage V to theoretical maximum voltage E;

ε_F = Faradaic efficiency, defined as the ratio of experimental (actual) current I_{exp} to the maximum possible current I_{max}

μ_F = fuel utilization coefficient, defined as the actual fuel reacted to the fuel supplied to the fuel cell on a mass basis; and

ε_H = hydrocarbon efficiency, which is the ratio of the heating value of all fuel components that are converted electrochemically (e.g., H_2) to the heating value of the fuel supplied (e.g., methanol).

The conversion efficiency of the fuel cell system is further reduced by losses in its peripheral components like the parasitic power consumption of auxiliary devices like blowers or pumps. All of these are included in the peripheral efficiency.

The two fuel cell efficiency types that will be discussed later in subsequent chapters are the columbic and energy efficiencies.

1.2.7 Fuel Cell Components

The components of a fuel cell are the anode, anodic catalyst layer, electrolyte, cathodic catalyst layer, cathode, bipolar plates/interconnects and sometimes gaskets for sealing/preventing leakage of gases between anode and cathode[15,16]. The stack of such fuel cells (a repeated stack of such components) is connected in series/parallel connections to yield the desired voltage and current. The anode and cathode consist of porous gas diffusion layers, usually made of highly electron conductivity materials such as porous graphite thin layers. These materials are expected to have (theoretically) zero proton conductivity. The electrolyte is made of such material that it provides high proton conductivity and theoretically zero electron conductivity. The charge carriers (from the anode to the cathode or vice versa) are different depending on the type of the fuel cells. The bipolar plates (also known as *flow field plate*s or *interconnects*) collect the electrical current as well as distribute and separate reactive gases in the fuel cell stack[15,16]. The MEA which is the heart of the fuel is composed of an electrolyte membrane located between an anode and a cathode

catalyst electrode. The anode and cathode catalyst consists of the catalysts layer (CL) and a gas diffusion layer (GL/GDL). By optimising every layer in the MEA, several barriers can be removed such as methanol cross over, electro-catalytic activity, transport and management issues etc. and also conduction distribution can be enhanced. The scheme of a conventional MEA used in this study is shown in Fig 1.5 below:

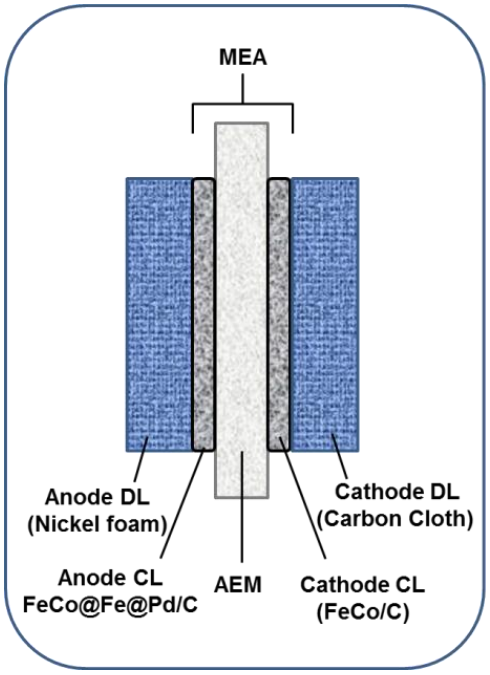

Figure 1.5: Schematic of MEA in the present studies.

Fig 1.6 displays the expounded image of a unit fuel cell comprising the:

1) MEA
2) Gas diffusion layer (GDL) with catalyst layer (CL)
3) Gasket
4) Flow field/Bipolar plates
5) Current collectors
6) Insulator
7) End plates

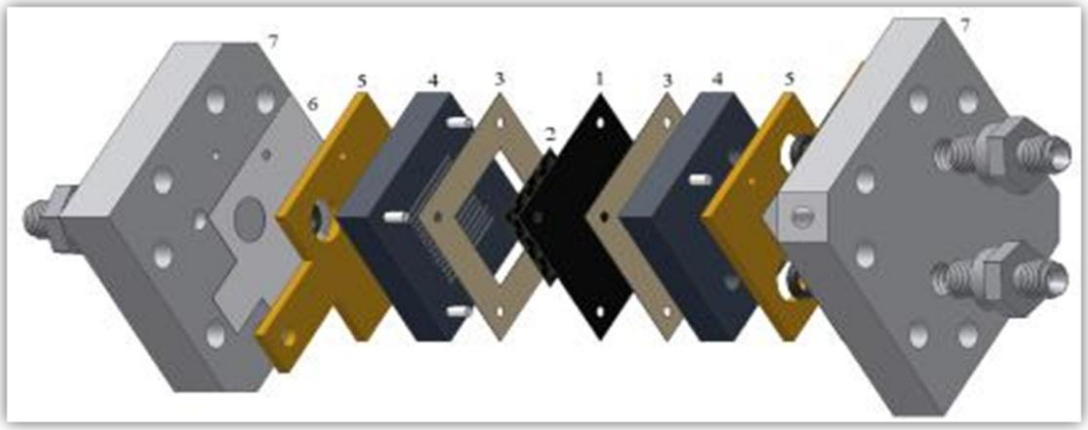

Figure 1.6: An expanded view of a unit fuel cell with all its components[17]

1.3. Direct Alcohol Fuel Cells

Alcohol fuel cells (AFCs) have been widely developed over the years. Extensive research and studies have been carried out on AFCs in the last 20 decades. This section will put together some summaries of research findings on AFCs in recent years.

In a review by Mclean et al[18] on "Recent development in fuel cell technology", the following points were put forward as advantages of AFC over PEMFC (Polymer electrolyte membrane Fuel Cells) : (i) AFCs can theoretically outperform PEMFCs and some of the earliest pressurized AFC systems showed current densities much higher than those achieved today with current PEM technology. (ii) Ambient air operated AFCs produce current densities comparable to ambient air operated PEMFCs. (iii) Cost analysis showed that AFC systems for low power applications including hybrid vehicles are at least competitive with the cost of any equivalent system constructed using PEMFC technology[18]. Blizanac et al [19,20] also highlighted the facile kinetics of ORR in alkaline medium than in acidic. Faster ORR kinetics coupled with the less corrosive nature of the alkaline environment has also facilitated the use of other non-noble metals as catalysts in AFCs. All of these have led to a resurgence of interest in AFCs in recent years[21–23].

The contamination of AFCs due to the presence of CO_2 from air or the oxidation product of the fuel poses an issue for sustained system operation. CO_2 poisons the electrolyte and clogs the electrode with carbonates. This problem has been addressed mainly by the application of alkaline anion exchange membranes (AAEMs)[24–26,27]. In a study on the development of a new alkali polymer for MEAs in AFCS, Varcoe et al highlighted some advantages of AFCs using AAEMs over conventional AFCs, they are: (i) no precipitated carbonate since there is no mobile cation, (ii) no electrolyte weeping, (iii) reduced alcohol crossover, (iv) potentially simplified water management, due to the fact that the water is

produced at the anode and consumed at the cathode, and (v) potentially reduced corrosion.

Direct alcohol fuel cells (DAFCs) operate on liquid fuels e.g. low molecular weight alcohols. Their application as alternative power sources for automobile and portable consumer electronics[28] have been very successful. The liquid fuels have several advantages compared to pure hydrogen, because they can be easily handled, stored and transported. They also have relatively high mass energy density, comparable to that of gasoline. Methanol is a promising fuel for DAFCs[29–32] but other low molecular weight alcohols such as ethanol[33,34] and ethylene glycol[35–37] are also candidates. At present, DAFCs are mostly using acidic proton exchange membrane but a difficulty in kinetics of alcohol oxidation also poses a challenge in the acidic medium. Just as in AFC, operating in a DAFCs in basic medium can improve alcohol oxidation kinetics[38]. In addition, the ionic current in alkali fuel cells is due to the conduction of hydroxide ions and it is the reverse direction to that in proton conducting systems. As such, the direction of the electro-osmotic drag is reversed, reducing the alcohol permeation rate[39]. Several DAFCs which use alkaline anion exchange membrane have already been reported[40–42]. A typical AFC is shown in Fig 1.7 below:

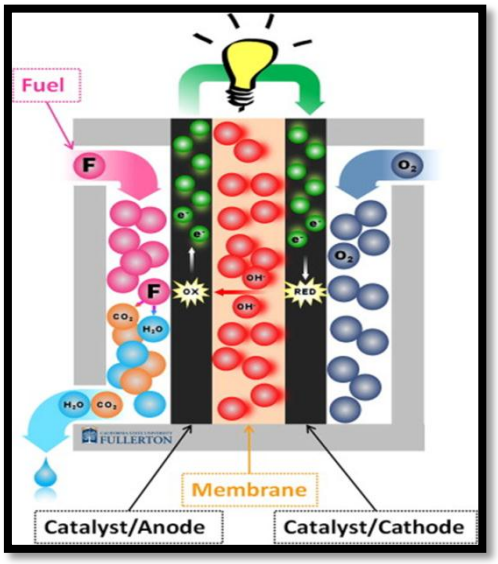

Figure 1.7: A typical alkaline fuel cell (from *Fullerton College*, CA, USA)

The four alcohols chosen in this study for oxidation in alkaline medium using the core shell catalysts – FeCo@Fe@Pd are methanol (MeOH), ethanol (EtOH), ethylene glycol (EG), and glycerol (GLY). Brief summaries of recent researches and study on the each of these fuels in DAAFCs will be given in the subsequent sections. Table 1.2 gives the electro-oxidation reactions of the four alcohols, their oxidation potential vs SHE, and their energy densities.

Table 1.2: Equations of the electrochemical oxidation of MeOH, EtOH, EG and GLY in alkaline medium[43]

Fuel	Anode Reaction	E°/V (SHE)	Energy Density ($WhKg^{-1}$)
Methanol CH_3OH	$CH_3OH + 6OH^- \rightarrow CO_2 + 5H_2O + 6e^-$	−0.81	6100
Ethanol CH_3CH_2OH	$CH_3CH_2OH + 2OH^- \rightarrow CH_3CHO + 2H_2O + 2e^-$ $CH_3CH_2OH + 4OH^- \rightarrow CH_3COOH + 3H_2O + 4e^-$ $CH_3CH_2OH + 12\ OH^- \rightarrow 2CO_2 + 9H_2O + 12e^-$	−0.77	8030
Ethylene glycol $(CH_2OH)_2$	$(CH_2OH)_2 + 14OH^- \rightarrow 2CO_3^{2-} + 10H_2O + 10e^-$ or $(CH_2OH)_2 + 10OH^- \rightarrow (CO_2)_2^{2-} + 8H_2O + 8e^-$	−0.72	5200
Glycerol $HOCH_2CHOHCH_2OH$	$HOCH_2CHOHCH_2OH + 20OH^- \rightarrow 3CO_3^{2-} + 14H_2O + 14e^-$ $HOCH_2CHOHCH_2OH + 12OH^- \rightarrow (COO^- - COH\text{-}COO^-) + 10H_2O + 10e^-$	−0.69	5000

1.3.1 Direct Methanol Fuel Cells

Direct methanol fuel cells (DMFCs) are devices that directly convert the chemical energy of methanol into electrical energy. They have been tagged as promising energy conversion devices[29,30,44–47]. DMFCs operate on a high energy fuel, have a low operating temperature, simple processing, and the possibility of automotive and portable electrical applications like cell phones, laptops etc. Methanol used as fuel in DMFCs is abundant and inexpensive, it can be easily handled, stored and transported thus avoiding problems of storage and transportation[48]. DMFCs also possess fast anodic reaction rates because methanol oxidation

does not break the C–C bond. The DMFC technology is already on the road to commercialisation, the small-scale, portable Toshiba Dynario-cell is available on the market. In addition, Smart Fuel Cells Co. has commercially produced DMFCs from the completely portable 15 W system to the semi-portable 250 W system[49,50]. In a review on anode catalysts for DMFCs, H.Liu et al[51] identified the key challenges of DMFCs as (1) the sluggish kinetics at the anode, and (2) methanol cross-over leading to a decay of the cathode performance. According to the authors, the latter challenge can be overcome by the developing new and better membranes while the former problem will require the development of more active anode catalysts[51]. Other authors[52–54] have suggested the development of nanostructured catalysts with optimised morphology and composition as a possible candidates for better anodic DMFC reaction.

Pt is seen as the choice metal catalysts for DMFCs but its high cost and susceptibility to poisoning by intermediate products of methanol oxidation like CO have led to the search and development of other noble and non-noble metal catalysts. Pd is cheaper than Pt and although it has a lower methanol oxidation activity to that of Pt[55,56]; it displays a relatively high activity in the alkaline media[57,58]. Thus, Pd has come in the fore of the development of Pt-free catalysts. Pd nanocatalysts with different morphologies have been synthesized and studied for their MOR activities. These include Pd hollow nanospheres[47], nano porous Pd[59], Pd nanodots,[60], and Pd nano flowers[61]. Pd nano alloys have also been studied as these alloys have been found to promote the catalytic activity of Pd by a synergistic or electronic effect of the combining cheaper metal. Examples include NiPd-Si/C[62], Pd/MnO_4[63], PdCo/CNT,[64]. These Pd alloys have also been synthesized in form of core shells, such as Pt@Pd/C[50], Pt@Pd /RGO[65], Ni@Pd/C[66], PdCu@PtRu/C[67]. These core shell catalysts were all found to be more catalytically active for methanol oxidation in alkaline medium than their parent noble mono metal catalysts.

1.3.2 Direct Ethanol Fuel Cells

Ethanol (EtOH) is one of the attractive fuels in DAFC applications. It is less toxic than MeOH and has a higher energy density (theoretical energy density of 8 $kWhkg^{-1}$). It is also a bio derived fuel as it can be produced from agricultural bioprocesses[33,58]. Direct ethanol fuel cells (DEFCs) have been shown to operate better in alkaline media than with acid electrolyte[68,69]. Kamarudin et al[34] did a study on DEFCs and highlighted a wide range of DEFCs operating with anion exchange membranes in alkaline media. The same authors also expounded on some challenges faced during DEFC operations. These include: (i) ethanol cross over (though lower than that of methanol); (ii) slow anodic reactions; (iii) heat and water management and (iv) durability and stability due to lack of catalysts to completely break the C-C bonds for an efficient and complete ethanol oxidation. Some of these problems have also been identified by other authors[70,71,72].

Pd has been found to exhibit a high electrocatalytic activity for the oxidation of EtOH in alkaline media compared with other pure metals [58,73]. Pd wires and nanofibres[74,75] have shown good catalytic activities. Some Pd alloys synthesised by adding other metals and metal oxides with Pd have also been investigated. Shen et al used metal oxides like NiO_2 and CeO_2 with Pd to promote EtOH oxidation and Pd gave a better performance than Pt with CeO_2 at equal noble metal loadings[76]. The same authors prepared Pd/C with nano crystalline oxides of CeO_2, CO_3O_4, Mn_3O_4 and NiO and obtained a better EtOH oxidation on Pd-NiO/C modified electrode than in Pt based catalysts[55]. Ternary Pd based alloys have also been investigated for DEFC applications, they include Pd-Ru-Sn/C[77], NiPdPt/CNT[78], AuPtPd nanowires,[79] Ru@Pt/Pd/C[80]. These catalysts have all been found to exhibit better electrocatalytic EtOH oxidation than Pt/C.

1.3.3 Direct Ethylene Glycol Fuel Cells

Among polyhydric fuels, ethylene glycol (EG) has shown a number of favourable characteristics. As outlined by Serov et al[81] in a review on the "Recent Achievements of Direct Ethylene Glycol Fuel Cells" (DEGFC); EG has (i) a relative theoretical capacity of 4.8 (17% higher than that of MeOH -4 $Ahml^{-1}$) and an energy density of 5.9 $KWHL^{-1}$, (ii) a boiling point of 198 ◦C, which makes it safer to work with, and (iii) an already established supply chain as it is widely used in the automobile industry. In addition to all of these, Vizza et al[76] also highlighted the fact that EG is a biofuel as it can be produced by the heterogeneous hydrogenation of cellulose derivatives. The former authors also explained that the main challenge of DEGFCs is in the development of new catalysts for the complete oxidation of EG.

As the mechanism of the electro oxidation of EG by Pd has not been seen to be divergent from that of Pt in alkaline media, quite a number of Pd based catalysts have been studied for their electrocatalytic activity in EG oxidation[58]. Pt, Pd and the alloys of both metals Pt-Pd was investigated by Dalbay and Kadirgan[82] for EG oxidation. The alloys exhibited a better catalytic performance than the pure metals. Ternary alloys have also been studied. Pt-Pd-Bi/C[83] was found to exhibit a higher current response during EG oxidation than Pt-Bi/C. Studies carried out by Vizza et al[84,85] on products of the EG oxidation by Pd based ternary alloys revealed that while Pd/C was more selective catalyst in production of glycolate, mixtures of glycolate, oxalate, and carbonate were obtained on Pd-(Ni-Zn)/C or Pd-(Ni-Zn-P)/C, indicating that the oxidation of EG proceeds via parallel routes on the ternary alloy catalysts.

1.3.4 Direct Glycerol Fuel Cells

Glycerol (GLY) is a non-toxic polyalcohol with a relatively high theoretical energy density of 5.0 $kWhkg^{-1}$. According to Simoes et al[86,87] glycerol is generated during the production of both bioethanol and biodiesel. In the

bioethanol production process, about 4 wt. % of the sugar fermentation leads to the formation of glycerol as by product. However, glycerol is mainly a natural product issued from the methanolysis of vegetable oils, with 10 wt. % of crude glycerol produced by the trans esterification reactions during the production of methyl esters from vegetable oil. Thus, glycerol being a by-product in the production of biodiesel should be well utilized to maximise the profitability of biodiesel production[88]. One of these ways is the selective oxidation of glycerol through fast heterogeneous catalysis in direct glycerol fuel cells (DGFCs).

Mono-metallic catalysts and their multi metallic alloys have been studied in this regard. They include Pd[86,89], Pt[90,91], Au[92,93] PdAu/C[94], and PtPdBi[95] The conditions of these electrocatalytic GLY oxidation reactions have also been investigated as this was found to aid the overall alcohol oxidation process. Gazellot et al[96,97] looked into the optimum pH for GLY oxidation at Pt and Pd modified electrodes. Hutchings[98], Matsouka[24] and Ilie [87] investigated different conditions in the operations of AEM-DGFCs for an optimum GLY oxidation while Bambagioni et al[89] studied Pd/MWCNTs as anode catalysts in an AEM-DGFC. Bianchini and Shen also reported an AEM-DGFC performance using Pd-(Ni-Zn-P)/C anode[58]. Other researchers are looking at studies geared towards the development of catalysts for the full oxidation of glycerol in order to high fuel cell output power density and high Faradic efficiency while also exploring selective glycerol oxidation for the production of valuable chemicals during [99,100].

1.4. Oxygen Reduction Reaction (ORR)

ORR in alkaline medium is a complex process involving four coupled proton and electron transfer steps. Several of these steps involve reaction intermediates leading to a wide choice of reaction pathways. Spendelow and Wieckowski[101] investigated the various pathways of ORR and surmised that it can be divided into three groups: Two of these lead to OH^- as the final product (complete reduction, with transfer of four electrons), and one leads to the production of peroxide (partial reduction, with transfer of two electrons). They further added that the four-electron pathways are often described as the direct pathway and the series pathway, the difference being that the former proceeds directly to OH^-, while the latter produces hydrogen peroxide (existing as HO_2^- in alkaline media) as an intermediate which is subsequently further reduced to OH^-. Table 1.3 compiled by Song et al[102] lists the equations of these ORR reactions in the different media with their corresponding thermodynamic electrode potentials at standard conditions. The authors also explained the significance of each of the various reduction pathways shown in the table: In fuel cell processes, the 4-electron direct pathway is highly preferred. The 2-electron reduction pathway is used in industry for H_2O_2 production. The 1-electron reduction pathway is of importance in the exploration of ORR mechanism[102].

The kinetics of ORR has been found to be more facile in alkaline than in the acidic media. This speculation was supported by the low catalytic activity of catalysts in acidic media due to the presence of so called spectator ions like sulphates and chlorides which block catalytic active sites required for adsorption of oxygen during the ORR process[19,20]. Also due to the milder conditions in the alkaline media, there is improved stability of electrodes and non-noble catalyst metals can be used. These could help in reduction of costs of fuel cells for commercial applications.

Table 1.3: Thermodynamic electrode potentials of electrochemical O_2 reductions[102].

Electrolyte	ORR reactions	Thermodynamic electrode potential at standard conditions (V)
Acidic aqueous solution	$O_2 + 4H^+ + 4e^- \rightarrow H_2O$	1.299
	$O_2 + 2H^+ + 2e^- \rightarrow H_2O_2$	0.70
	$H_2O_2 + 2H^+ + 2e^- \rightarrow 2H_2O$	1.76
Alkaline aqueous solution	$O_2 + H_2O + 4e^- \rightarrow 4OH^-$	0.401
	$O_2 + 2\ H_2O + 2e^- \rightarrow HO_2^- + OH^-$	-0.06
	$HO_2^- + 2H_2O + 2e^- \rightarrow 3OH^-$	0.867
Non–aqueous aprotic solvents	$O_2 + e^- \rightarrow O_2^-$	a
	$O_2^- + e^- \rightarrow O_2^{2-}$	b

Note:a, b: The thermodynamic potentials for the 1-electron reduction reaction to form a superoxide, and its further reduction to O_2^{2-}, are not listed in the table because their values are strongly dependent on the solvent used.

Macrocycles have also been studied as possible cathode materials for ORR. Some of these include transition metal (TM) porphyrins, TM tetraphenylporphyrins (TM TPPs) and TM phthalocyanines (TM Pcs)[103]. Although the TM macrocycles have exhibited promising electrocatalytic ORR activity, they are not very stable. Heat treatments at temperatures of 450–900 °C, were found to result in high ORR activity in alkaline solutions with long-term stability [103]. This observation has been confirmed by other authors[104,105].

1.5 Anode and Cathode Catalyst

A summary of anode and cathode catalysts used in the oxidation of MeOH, EtOH and EG was compiled by Antolini and Gonzalez[37] (Table 1.4).

Table 1.4: Anode and cathode (alcohol-tolerant) catalysts for ADAFCs fuelled with different alcohols[37]

Fuel	Anode catalysts	Cathode catalysts (alcohol tolerant)
Methanol	Pt, Pt-M (M = Ru,Pd,Au), Pt-M_xO_y (M = Ce,Ni,V) Pt-$La_{1-x}Sr_xMO_3$(M = Co,Mn), Ni, Ni-M (M = Ru,Cu), Ni-complex, Pd, PdNi, $AuLa_{1-x}SrxMO_3$(M = Co,Cu), $La_{2-x}Sr_xNiO_4$, Ni-$La_{2-x}Sr_xNiO_4$	Fe-TMPP, Ag, Ag-W_2C, Pd, Pd-Sn
Ethanol	Pd, Pd-M (M = Ru, Au, Sn, Cu), Pd-M_xO_y(M = Ce, Zr, Mg, Co, Mn, Ni, In), Pd-(Ni-Zn), Pd-(Ni-Zn-P), Ru-Ni, Ru-Ni-Co.	Ag-W_2C, Pd, Pt-Ru
Ethylene glycol	Pt, Pt-M (M = Pb,Bi,Tl,Au), Au-M (M = Pb,Bi)	Pt-Pb, $La_{1-x}SrxMnO_3$

In addition to the above list, metal alloys in the form of core shells have also become popular. Yang[106] described core shell or core shell like structures as a convenient way to build multi functionality into the electro catalysts of metal nanoparticles. And according to Zhao et al[30], since the size, shape, composition and phase properties of the core shell structured nanoparticles can be controlled much easier than other nano structured materials, they are the most favourite catalysts for fuel cells. Many authors have further dwelt on the more fundamental studies on the electronic and lattice structures on the surfaces of these core shell nanoparticles as well as their characteristics like lattice shrinking and d-band vacancy as these can be used to further improve their catalytic activity and stability[107–110]. As stated by Qiao and Li[54] the performance and stability of these highly electro active core shell nanocatalysts in MEA for real fuel cell applications need to be further investigated as many of the core shell nanoparticles reported are solution based and are only evaluated on planar supporting electrodes.

1.6. Microwave Irradiation: An Overview

Microwaves are electromagnetic waves at frequencies between 0.3 and 30 GHz situated between radio-waves and infra-red in the electromagnetic spectrum. This corresponds to wavelengths between 1 mm to 1m as can be seen in Figure 1.8. According to a review by Galema[111], by itself the energy of microwave is too low to cleave molecular bonds. In order for microwave to be an effective heat source, the material to which it is being applied must be able to couple with the microwave energy.

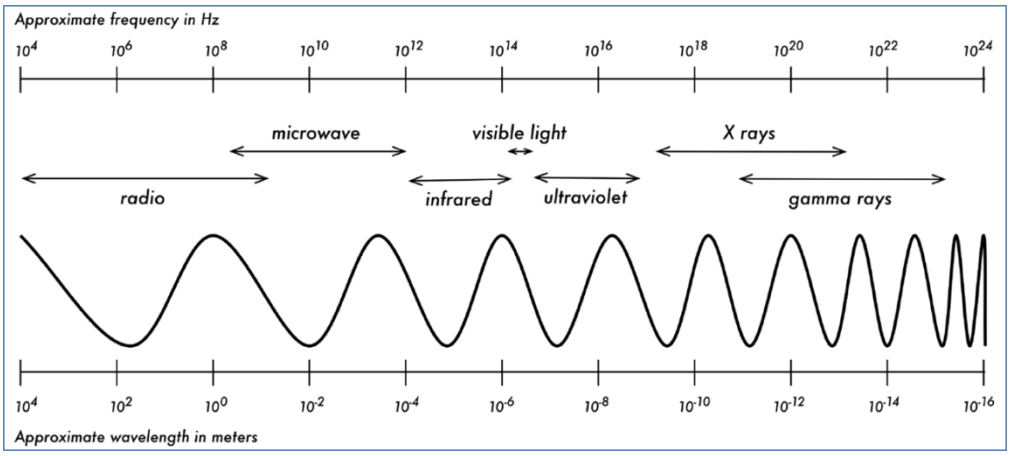

Figure 1.8: Electromagnetic spectrum (Source: www.google image retrieved 16.12.2013)

Heating with microwaves is based on dielectric heating effect. Dielectric heating works by two major mechanisms[111]:

- Dipolar polarization: A substance has to be a dipole in order to gentrate when irradiate with microwaves. The dipoles align themselves to the oscillating field of the microwave (microwave heating is oscillating). This alignment causes rotation which produces friction among the molecules and ultimately results in heat energy.
- Ionic conduction: During ionic conduction, ions dissolved in solution oscillate back and forth under the microwave irradiation and the collisions of the charged particles as a result of these random movements lead to friction and create heat energy.

Thus, a material must possess certain dielectric properties in order to be efficiently heated in the microwave field. This heating characteristic which is the ability of a substance to convert magnetic energy into heat is determined by the loss tangent, tan δ. The loss factor, tan δ is:

$$\tan \delta = \frac{\varepsilon''}{\varepsilon'} \qquad (1.8)$$

where ε'' = dielectric loss (efficiency with which electromagnetic radiation is converted to heat); ε' = dielectric constant (polarization of molecules in the electric field). Substances (especially solvents) are classified into high, (tan δ. >0.5), medium, (tan δ 0.1-0.5) and low microwave absorbing (tan δ < 0.1). Solvents with high tan δ values are required for rapid heating in the microwave field. Ethylene glycol has the highest tan δ of 1.350.[111]

1.6.1. Benefits of Microwave over Conventional Heating in Synthetic Procedures

The conventional heating processes used in the laboratory for synthesis usually go along the following procedures: heat is transferred from the heating source to the surface of the reaction vessel; the heat is then passed on to the contents of the vessel. In contrast during synthesis by microwave irradiation, microwaves pass through the microwave vessels and heat the reaction mixture on a molecular basis- by direct interaction with the molecules (solvents, reagents, catalysts etc.). Due to this direct 'in core' heating, microwave irradiation results in inverted temperature gradients as compared to conventionally heated systems. Conversion of electromagnetic energy to heat energy is highly effective and results in extremely fast heating rates which are not reproducible with conventional heating. Also due to rapid heating to the target temperature, the formation of by products is suppressed. This results in higher product yields[111].

1.7 Synthetic Strategies for Core Shell Nano Catalyst for DAFC

Various synthetic routes have been developed for the fabrication of core shell catalysts as a result of their wide applications in the field of energy, bio medicine (drug encapsulation and delivery, bio imaging), sensing, optics etc. The common synthetic routes for obtaining nanostructured core shell catalysts are by electrochemical and chemical methods.

The electrochemical method occurs through the displacement of under potentially deposition (UPD) a metal, mainly copper which then acts as a sacrificial layer for the electrochemical replacement or deposition of the monolayer coating of a noble metal, thus minimizing the use of noble metals in catalyst synthesis. This method was made popular by Adzic et al and has found good use in the reduction of platinum as cathode catalysts in fuel cell applications especially in PEMFCs[112–114]. The method has also been used in synthesis of double shells over the core layers [115]. Although it only allows for preparation of microgram samples on the RDE or GCE tip, the approach has been modified to scale up to gram-size quantities using an electrochemical cell where the core nanoparticles are dispersed as powder in the electrolyte [116].

A more common and versatile procedure for the synthesis of core shell nano catalysts is via the chemical route. Its greater choice for core shell synthesis is also due to its suitability for large scale and low cost production of core shell catalysts. It can involve the sol-gel, colloidal (solution or organic phase), micro emulsion, and impregnation routes. All of these routes are seed mediated growth routes which involve two or more chemical steps. These steps basically entail:
(i) formation of the core nanoparticles (seeds) through chemical reduction of metallic salts (ii) dispersion of core nanoparticles on substrates and (iii) subsequent deposition of the shell on the core nanoparticles.
The chemical reduction (step (i)) can be carried out by liquid phase reduction using reducing agents (ascorbic acid, oleyl-amine, sodium

borohydride, hydrazine etc.) or gas phase using flowing H_2 or CO as reducing agent under elevated temperatures, the latter leads to the segregation of particular elements to the surfaces of the nanoparticles alloys[117,118]. The steps can also be combined in a one-step or one-pot synthetic route involving a co reduction of the core and shell metal precursors. This involves an immediate simultaneous deposition of the shell following reduction of the core nanoparticles[119–121].

The colloidal route involves the use of an organic agent (mainly surfactants like CTAB, CTAC, PVP, PVA) to protect the metal nanoparticles. This can occur either in the liquid or organic phase. The organic agent also acts as stabilizers to prevent agglomeration of the nanoparticles[50,122,123]. But in order to ensure a good catalytic activity the surfactants have to be removed. This is carried out mostly by a post heating treatment after synthesis.

The micro emulsion route involves mixing the precursor liquid phase in an immiscible liquid (surfactant phase) thus creating an emulsion. The reducing agent can be introduced into the emulsion with the addition of a surfactant to modify the growth of the nanoparticle. Malik et al expounds on this method for the synthesis for core shell nanoparticles in a recent publication[124].

Impregnation method involves depositing the metal (core) catalysts on a support (mostly carbon substrates like Vulcan carbon, SWCNT, MWCNT etc.) by reducing the precursor metal salts on the substrate. The metal (shell) is subsequently reduced on the core nanoparticles by a further reduction of its metallic salts[125]. All three chemical routes have always been known for the synthesis of nanoparticles[126]. Modifications of these methods have led to their being used as synthetic routes of bi and tri metallic and quaternary core shell nano particles.

1.8 Electrochemistry: An overview

This section (1.8) and the two subsequent ones (1.9 and 1.10) give a brief overview of electrochemistry (1.8), and some techniques based on the principle of electrochemistry i.e. voltammetry techniques (1.9) and impedance spectroscopy (1.10). As all these topics have been widely expounded in various texts by renowned authors, the three sections have collated summaries from these editions. The relevant authors have also been duly referenced in each of the ensuing sections.

Electrochemical techniques are inevitable tools in almost every chemical and biochemical research. In addition to their application in fundamental studies of oxidation and reduction processes to unravel reaction mechanisms, these techniques are also used in studying the kinetics and thermodynamics of electron and ion transfer processes[127]. Moreover, electrochemical techniques have also proven to be useful tools for the study of adsorption and crystallization phenomena at electrode surfaces[128].

1.8.1 Classification of Electrochemical Techniques

Electrochemical techniques can either be 'bulk' or 'interfacial' technique. Bulk techniques are based on the phenomena that occur in the bulk solution itself while the interfacial techniques are based on the events occurring at the electrode – solution interface. Interfacial technique is sub-divided into potentiometric and voltammetry methods. Voltammetry technique can be divided into controlled–potential and controlled-current methods. Controlled–potential techniques have more advantages as they exhibit high sensitivity and selectivity. Examples include voltammetry and chronoamperommetry[129].

1.8.2 Faradaic and Non-Faradaic Processes

The objective of a controlled – potential electro analytical experiment is to obtain a current response which is related to the concentration of the

target analyte[127,129,130]. This is accompanied by monitoring the transfer of electron (s) during the redox process of the analyte. The reaction is called the Faradaic process as electrons are transferred across the electrode-solution interface. Non-Faradaic process arises when there is no charge transfer across the electrode-solution interface. When processes such as adsorption and desorption occur, the structure of the electrode-solution interface can change with changing potential or solution. Thus the non-Faradaic process can be governed by 'transient current' when potential, electrode area or solution composition changes.

1.8.3 Galvanic and Electrolytic Cells

Electrochemical cells in which faradaic currents are flowing can be classified as either Galvanic or Electrolytic cells. A galvanic cell is one in which reactions occur spontaneously at the electrodes when they are connected externally by a conductor (Fig 1.9a). They are often employed in converting chemical energies to electrical energy. Galvanic cells of commercial importance include primary/non-rechargeable cells (Leclanche Zn-MnO_2 cell), secondary rechargeable cells and fuel cells. An electrolytic cell is one in which reactions are effected by imposition of an external voltage greater than the open circuit potential (Fig 1.9b) of the cell. These cells are often employed to carry out desired chemical reactions by expending electrical energy .Commercial processes involving electrolytic cells include electro refining, electroplating (Ag or Au)

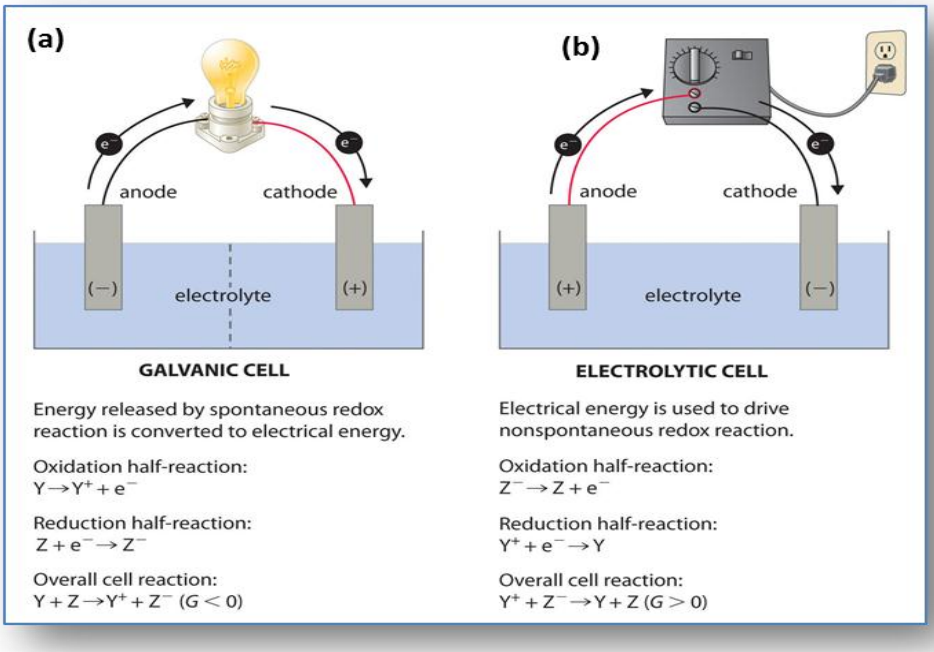

Figure 1.9: Galvanic (a) and Electrolytic (b) electrochemical cells (Source: www.google, image retrieved 16.12.2013)

1.8.4 Mass Transport Processes

In an electrochemical cell, mass transport is a process which governs the net movement of ions, charge or neutral species across the electrode-electrolyte interface. It is considered as mass transfer of an electro active species in an electrolyte near the electrode[129]. The mass transport process can be in form of diffusion, migration, and convection. These processes are summarised in the diagram, Fig 1.10 below.

(i) Diffusion

This is a spontaneous movement under the influence of concentration gradient, from regions of high concentrations to regions of lower concentrations. It is aimed at minimising concentration differences. Thus it is a transport of particles as a result of local difference in the chemical potential[129].

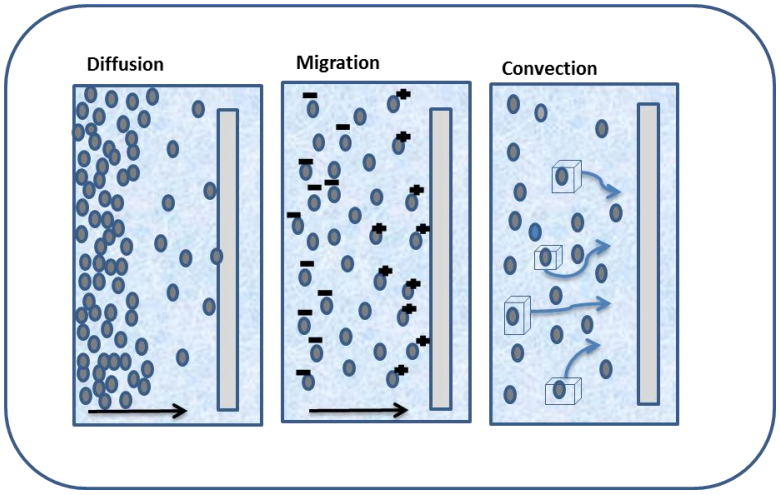

Figure 1.10: The three modes of mass transport

(ii) Migration

This is the movement of charged particles along an electrical field, which is carried through the solution by ions according to their transference number. It is also the type of charge transport related to the movement of ions and the existence of potential gradient between two electrodes in solution. In voltammetry, the use of a supporting electrolyte at concentrations 100 times that of the species being determined eliminates the effect of migration. Thus it can be assumed that the transport of the examined species towards the working electrode is by diffusion only[129].

(iii) Convection

This is transport of ions to the electrode by a gross physical movement; the major driving force for convection is an external mechanical energy associated with stirring or flowing of solution or rotating or vibrating the electrode (i.e. forced convection). Convection can also occur naturally as a result of density gradient. It must be eliminated or controlled accurately to provide controlled transport of the analyte on the electrode. In voltammetry, the effect is eliminated by maintaining the cell under quiet and stable conditions.[129]

1.9 Voltammetric Techniques

1.9.1 Introduction

Among the electrochemical techniques the principal ones are polarographic and voltammetric techniques. Currently, polarographic techniques have almost been completely excluded from research laboratories, and are being replaced by the more sophisticated voltammetric techniques[131]. Their wide application is attributed with the relatively cheap instrumentation, very good sensitivity with wide linear concentration ranges for both inorganic and organic compounds, rapid analysis times (in seconds), and simultaneous determination of several analytes. Voltammetry (abbreviation of volt-amper-metry) is a branch of electrochemistry that was developed by the discovery of polography in 1922 by Jaroslav Heyrovsky (Nobel Prize in 1959). A major breakthrough in voltammetry was made in the early 1960s, when an expanded repertoire of analytical methods were reported, appearing in parallel with the corresponding well-developed theories [127].

The common characteristic of all voltammetric techniques is that they involve the application of a potential (E) to an electrode and the monitoring of the resulting current (i) flowing through the electrochemical cell. In many cases the applied potential is varied or the current is monitored over a period of time (t). Thus, all voltammetric techniques can be described as some function of E, i, and t. They are considered active techniques (as opposed to passive techniques such as potentiometry) because the applied potential forces a change in the concentration of electroactive species at the electrode surface by electrochemically reducing or oxidizing it. The analytical advantages of these various techniques include excellent sensitivity with a very large useful linear concentration range for both inorganic and organic species (10^{-12} to 10^{-1} M), a large number of useful solvents and electrolytes, a wide range of temperatures, rapid analysis times (seconds), simultaneous determination of several analytes, the ability to determine kinetic and mechanistic

parameters, a well-developed theory and thus the ability to reasonably estimate the values of unknown parameters, and the ease with which different potential waveforms can be generated and small currents measured[129]. Analytical chemists routinely use voltammetric techniques for the quantitative determination of a variety of dissolved inorganic and organic substances. The same techniques are widely used by inorganic, physical, and biological chemists for a variety of purposes, including fundamental studies of oxidation and reduction processes in various media, adsorption processes on surfaces, electron transfer and reaction mechanisms, kinetics of electron transfer processes, and transport, speciation, and thermodynamic properties of solvated species. Voltammetric methods are also applied to the determination of compounds of pharmaceutical interest and, when coupled with HPLC, they are effective tools for the analysis of complex mixtures [132]

1.9.2 Basic Electrochemical Principles

Although there are many voltammetric techniques, they are all based on the same electrochemical theory. The effects of the applied potential; and the behaviour of the redox current are described by some electrochemical laws common to all voltammetric techniques[127,130,133]. The applied potential which controls the concentrations of the redox species at the electrode surface (C_o^0 and C_R^0) and the rate of the reaction (k^0) are described by the Nernst or Butler–Volmer equations respectively. In cases where diffusion plays a controlling part, the current resulting from the redox process (known as the faradaic current) is related to the material flux at the electrode–solution interface and is described by Fick's law. The interplay between these processes is responsible for the characteristic features observed in the voltammograms of the various techniques.

Consider the simplest reversible electrochemical reaction

$$\mathbf{O} + n\mathbf{e}^- \longleftrightarrow \mathbf{R} \qquad (1.9)$$

Where **O** refers to the oxidized form of an electro active substance initially present in the electrode cell, while **R** is its reduced form (charges are omitted for the sake of simplicity). At least two well-known laws can be applied for expressing the interdependence between the applied potential and the surface concentrations of **O** and **R**.

For a thermodynamically reversible electrochemical reaction (i.e., a fast reaction where equilibrium is always re-established as changes in electrode potential are made), the potential of the electrode can be used to establish concentrations of **O** and **R** at the surface of the electrode ($C_{\mathbf{O}}^{0}$ and $C_{\mathbf{R}}^{0}$) in compliance to the Nernst equation:

$$E = E^{\theta} + \frac{RT}{nF}\ln\frac{C_{\boldsymbol{R}}^{0}}{C_{\boldsymbol{O}}^{0}} \qquad (1.10)$$

where R is the gas constant (8.3144 $Jmol^{-1}K^{-1}$), T is the absolute temperature (K), n is the number of electrons transferred, F is the Faraday constant (96,485 $Cmol^{-1}$), E^{θ} is the standard/formal potential for the redox couple $C_{\mathbf{R}}^{0}/C_{\mathbf{O}}^{0}$.

For many electrochemical systems, especially for kinetics-controlled equations or experiments in which the current is controlled by rate of electron transfer, it is very useful to use the relationship that links the variables of current, potential and concentration, this is known as the Butler-Volmer equation:

$$j = k^{\theta}\left\{c_{\boldsymbol{O}}^{0}\,\exp[1-\alpha\theta] - c_{\mathbf{R}}^{0}\exp[-\theta\alpha]\right\} \qquad (1.11)$$

$$\theta = nF\left(E - E^{\theta}\right)/RT$$

where j = current density, k^{θ} = standard rate constant/ heterogeneous rate constant, and α = electron transfer coefficient or symmetry factor. This equation allows one to obtain the values of the two analytically important parameters, j and k^{θ}.

Equation (1.11) can be expanded and rewritten as

$$j = j_o \left\{ \exp\left[\frac{(1-\alpha)nF}{RT}.\left(E - E^{\theta}\right)\right] - exp\left[-\frac{\theta nF}{RT}.\left(E - E^{\theta}\right)\right] \right\} \quad (1.12)$$

While the Butler-Volmer equation is valid over the full potential range, simpler approximate solutions can be obtained over more restricted ranges of potential. As overpotentials, either positive or negative, become larger than about 0.05 V, the second or the first term of equation becomes negligible. Thus, for an oxidation or anodic reaction at a high overpotential:

$$j_a = j_o\, exp\left[\frac{(1-\alpha)nF\eta_a}{RT}\right] \quad (1.13)$$

And for a reduction or cathodic reaction at high over potential:

$$j_c = j_o\, exp\left[-\frac{(n\alpha)F\eta_c}{RT}\right] \quad (1.14)$$

$$\eta_c = \frac{RT}{\alpha_c nF} lnj_o - \frac{RT}{\alpha_c nF} lnj_c \quad (1.15)$$

In general either anodic or cathodic equation can be represented as:

$$\boldsymbol{\eta} = \frac{RT}{\alpha nF} lnj_o - \frac{RT}{\alpha nF} lnj \quad \text{or} \quad \eta = \frac{RT}{\alpha nF} \ln(j/j_o) \quad (1.16)$$

$$\ln j = 2.303 \log j$$

$$\eta = \frac{2.303RT}{\alpha nF} \log j_o - \frac{2.303RT}{\alpha nF} \log j \quad (1.17)$$

$$\eta = a + b \log j \quad (1.18)$$

$$b = \frac{2.303RT}{\alpha nF}$$

At 25°C

$$\eta = \frac{0.059}{\alpha n} \log j_o - \frac{0.059}{\alpha n} \log j \quad (1.19)$$

$$a = \frac{0.059}{\alpha n} \log j_o \quad \text{and} \quad b = \frac{0.059}{\alpha n} \quad (1.20)$$

Two key parameters that influence the rate of an electrochemical reaction are the ion exchange current density (j_o) and the Tafel slope (b). j_o is the current flowing equally at the forward and reverse directions, i.e. at equilibrium when the overpotential is equal to zero. In catalytic redox reactions, materials with high j_o values are desirable so that the reaction will proceed at a high voltage efficiency. However, it is desirable to minimise the Tafel slope (b) so as to achieve a high voltage at high operating current densities. The transfer coefficient (α) is the fraction of the overpotential assisting in the reaction, it varies between 0 and 1 but is usually close to 0.5; n is the number of electrons involved in the electron transfer process and it normally has a value of 1. This means that the Tafel slope value should be close to 120 $mVdec^{-1}$ if n has a value of 1, and 59 $mVdec^{-1}$ if n has a value of 2.

Finally, in most cases the current flow also depends on the flux of materials to the electrode surface. When performing electrochemical experiments, applying a potential difference between the working and reference electrodes would alter the surface concentrations of both forms of the redox couple. When new **O** and **R** are created at the surface, the increased concentration provides the force for its diffusion toward the bulk of the solution. Likewise, when **O** or **R** is destroyed, the decreased concentration promotes the diffusion of new materials from the bulk solution to the electrode. The resulting concentration gradient and mass transport is described by the Fick's law which states that the flux of matter (Φ) is directly proportional to the concentration gradient:

$$\Phi = -AD_{\boldsymbol{O}}/(^{\partial c_{\boldsymbol{O}}}/_{\partial x}) \qquad (1.21)$$

where D_o = the diffusion coefficient of **O** and X = the distance from the electrode surface. An analogous equation can be written for **R**. The flux of **O** or **R** at the electrode surface controls the rate of reaction, and thus the faradaic current flowing in the cell. In the bulk solution, concentration gradients are generally small and ionic migration carries most of the

current. For analytical purposes, the main interest is knowing the magnitude of the faradaic current of the voltammogram, which is a quantitative measure of concentration and the kinetics of the redox transformation of given electro active species at the electrode surface. The magnitude of the faradaic current is a function of the analyte concentration, but it is also affected by additional factors, such as the size, shape, and material of the electrode, the solution resistance, the cell volume and the number of electrons transferred[127,130,133].

1.9.3 Electrochemical Cell

Voltammetric experiments are usually carried out in simple electrochemical cells; similar to that shown in Fig 1.11. It consists of a salt dissolved in a solvent (electrolyte), working electrode, reference electrode, and an auxiliary (counter) electrode. The working electrode is an electron conductor at which the reaction or transfer of electrons takes place. It can be of various geometries and materials ranging from small Hg drop to flat Pt discs. Other commonly used electrode materials are gold, platinum and glassy carbon. In all voltammetric experiments, it is necessary to keep one of the electrodes at a constant potential. This electrode, designed to have a constant (reversible) potential, is called a reference electrode. The reference electrode should provide a reversible half-reaction with Nernstian behaviour, be constant over time, and be easy to assemble and maintain. The most commonly used reference electrodes for aqueous solutions are the calomel electrode, with potential determined by the reaction: $Hg_2Cl_{2(s)} + 2e^- = 2Hg_{(l)} + 2Cl^-$ and the silver/silver chloride electrode (Ag/AgCl), with potential determined by the reaction: $AgCl_{(s)} + e^- = Ag_{(s)} + Cl^-$.

The counter electrode is the auxiliary electrode at which a counter reaction to that at the working electrode takes place, for the sake of balancing the total charge in the system. It has a surface area that is much larger than that of the working electrode so as to ensure that the

half-reaction taking place at this electrode can occur fast enough so as not to limit the kinetics of the electrochemical reaction taking place at the working electrode. Most often the counter electrode consists of a thin Pt wire, although Au and sometimes graphite or glassy carbon has also been used.

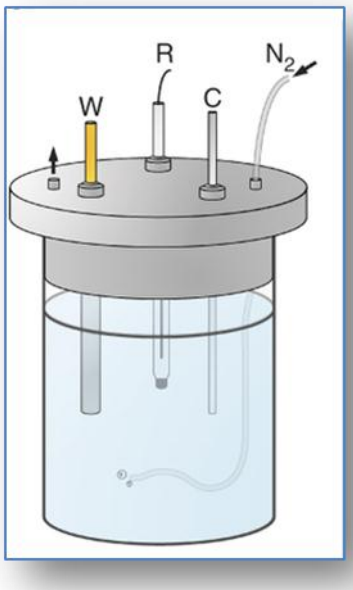

Figure 1.11: An electrochemical cell equipped with a working (W), reference (R) and counter (C) electrodes (Source: www.google image retrieved 16.12.2013)

In the presence of electro active species in the working electrochemical cell, an applied potential will provoke a change in the concentration of the monitored electro active species at the electrode surface by electrochemically reducing or oxidizing them. A change in concentration of any electro active participant at the working electrode surface will cause a mass transport of the analyte towards the electrode, resulting in a flow of current through the electrode which is directly proportional to the concentration of the analyte. This simple dependence between measured current and analyte concentration makes this technique a useful routine test for the quantitative determination of a variety of inorganic and organic compounds.

1.9.4 Instrumentation in Voltammetric Experiments

The modern electro analytical system for voltammetric measurements are usually composed of three modules: a potentiostat, a personal computer, and an electrochemical cell as seen in Fig 1.12. The Potentiostat is considered the 'heart' of electrochemical instrumentation. In voltammetric techniques, the task of the potentiostat is to apply an exact potential and to observe the current changes in the system. The potentiostat package includes electrometer circuits, various converters and amplifiers, as well as microprocessors with internal memory[134].

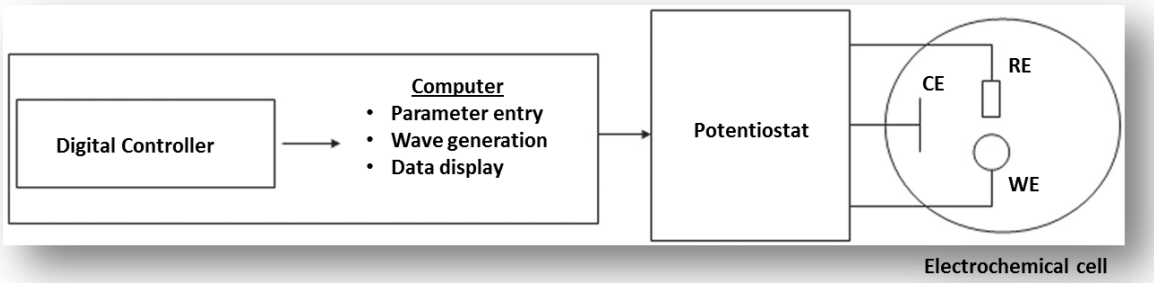

Figure 1.12: A simplified scheme of an electrochemical system designed for voltammetric measurements[134].

1.9.5 Types of Voltammetry

1.9.5.1 Cyclic Voltammetry

Cyclic voltammetry (CV) has become an important and widely used electro analytical technique in many areas of chemistry. Although rarely used for quantitative determinations, it is widely used for the study of redox processes, for understanding reaction intermediates, and for obtaining stability of reaction products. A number of useful thermodynamic information as well as qualitative information on the nature of electron-transfer process can be extracted from CV experiments. These include: (1) formal potential of redox species; (2) reversibility of redox species and its dependency on scan rates; (3)

influence of mass transfer; (4) identifying electro catalytically active species through their turn-over current; (5) distinguishing between the adsorbed and diffusive nature of electrocatalysts[125]. This technique is based on varying the applied potential at a working electrode in both forward and reverse directions (at some scan rate) while monitoring the current. For example, the initial scan could be in the negative direction to the switching potential. At that point the scan would be reversed and run in the positive direction. Depending on the analysis, one full cycle, a partial cycle, or a series of cycles can be performed. The reversible reaction of a molecule containing iron site as a redox-active moiety will be used as an example to explain, (Equation 1.13) the principles of cyclic voltammetry (CV) [127,135]

$$[Fe^{2+}] \longleftrightarrow [Fe^{3+}] + e^{-} \qquad (1.22)$$

Figure 1.13 shows the principles for the generation of a cyclic voltammetric curve.

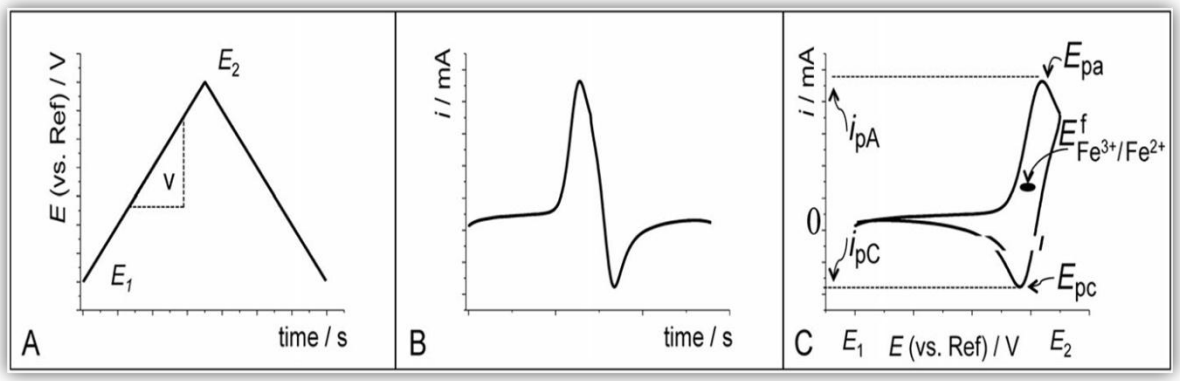

Figure 1.13: Principles for the generation of a cyclic voltammetric curve[135].

A linearly dependent potential (in relation to the reference electrode -RE) is imposed on the working electrode. A CV scan begins at an initial potential (E_1; Fig 1.13A), the scan then proceeds to a final (or reverse) potential (E_2) and then returns to the initial potential. The scan rate (v) is the change of potential as function of time ($v = \frac{dE}{dt}$) and can be deduced from the gradient of the curve (Fig 1.13A). During the scan, the flowing current is recorded (Fig 1.13B), and because potential and current are

both functions of time, they can be easily interrelated thus, the current flow can be plotted as a function of the applied electrode voltage. Fig 1.13C shows the result of a CV experiment (a cyclic voltammetric curve, or voltammogram), of a diffusion controlled process.

The important parameters in a cyclic voltammogram are the cathodic and anodic peak potentials (E_{pc}, E_{pa}), and peak currents (i_{pc}, i_{pa}) of the cathodic and anodic peaks respectively. If the electron transfer process is fast compared with other processes (such as diffusion), the reaction is said to be electrochemically reversible, and the peak separation is

$$\Delta E_p = \left|E_{pa} - E_{pc}\right| = 2.303\ RT/nF \qquad (1.23)$$

Thus, for a reversible redox reaction at 25 °C with *n* electrons, Δ*E*p should be 0.0592/*n* V or about 60 mV for one electron. In practice this value is difficult to attain because of factors such as cell resistance. Irreversibility due to a slow electron transfer rate results in Δ*E*p > 0.0592/*n* V, (> 70 mV for a one-electron transfer reaction). The formal reduction potential (E^o) is a median between the cathodic and the anodic peak potentials for a reversible couple. It provides mainly thermodynamics information and it is given by:

$$E^0 = \frac{E_{pc} + E_{pa}}{2} \qquad (1.24)$$

The magnitudes of the peak currents reveal the kinetics involved in the electrochemical reaction. For a reversible reaction, the concentration is related to peak current by the Randles–Sevčik expression (at 25 °C):

$$i_p = 2.686\ x\ 10^5\ n^{3/2}\ AC_o\ D^{1/2} v^{1/2} \qquad (1.25)$$

where i_p = peak current (A), *A* = geometric area of electrode (cm^2), D = diffusion coefficient ($cm^2 s^{-1}$), C_o = initial concentration of electroactive species in the solution ($molcm^{-3}$), v = scan rate (Vs^{-1}), n = number of electrons transferred.

Cyclic voltammetry is carried out in quiescent solution to ensure diffusion control. The shape of the cyclic voltammogram gives information about

the type of the electrode reaction, the number of electrons involved in the elementary step of electrochemical transformation, as well as about the additional phenomena coupled to the electrochemical reaction of interest, like those for coupled chemical reactions or adsorption and crystallization [127,130,135]

1.9.5.2 Linear Scan Voltammetry

Linear scan voltammetry (LSV) is a voltammetric method where the current at working electrode is measured while the potential between the working electrode and a reference electrode is swept linearly in time (Fig 1.14). Oxidation or reduction species is registered as a peak or trough in the current signal at the potential at which the species begin to be oxidised or reduced[127].

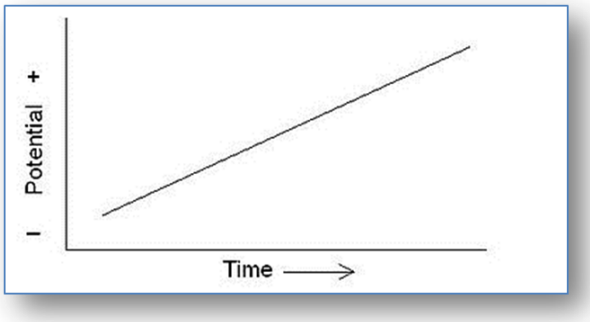

Figure 1.14: Linear Sweep Voltammogram[127]

1.9.5.3 Rotatory Disc Electrode

The Rotatory disc electrode (RDE) is one of the few convective electrode systems for ORR studies. Using the RDE to study ORR electrocatalysts requires understanding of a few basic ideas. For the RDE, the key point is understanding the combined effects of mass transport (*i.e.*, how fast oxygen travels to the disk electrode) and kinetics (*i.e.*, how fast oxygen is reduced once it reaches the electrode)[102].

The RDE consists of a disc embedded in a rod of an insulating material. The electrode is attached to a motor which is directly attached to a flexible shaft and is rotated at an angular velocity of ω. Fig 1.15 shows

the direction of the thin layer of the electrolyte near the surface of the electrode, and how it spins out radially from the center of the disc as it acquires a rotational momentum. The electrolyte at the surface is replenished by the upward flow of the bulk solution as also shown in the diagram

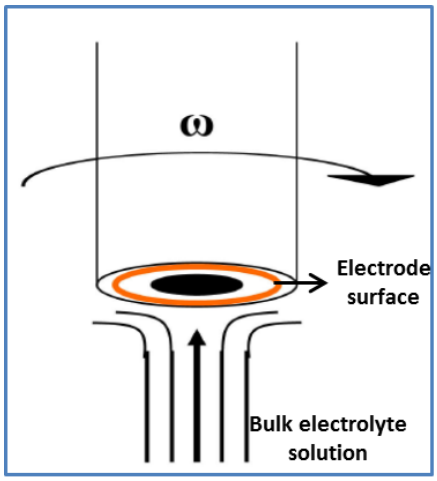

Figure 1. 15: Sketch of a RDE showing the direction of motion of the electrode and the flux of the analyte (Source: www.google, image retrieved 16.12.2013)

RDE Kinetic measurements

A glassy carbon rotating disk electrode coated with a thin layer of an ORR electrocatalyst may be used to reduce dissolved oxygen in an electrolyte solution[127,136,137]. By gradually increasing the rotation rate of the RDE, the rate of mass transport of the dissolved oxygen to the electrode surface increases. Initially, the cathodic (reduction) current at the disk electrode is governed by this mass transport (*i.e.*, the rate at which oxygen arrives at the electrode). As the rotation rate increases, the current increases as the amount of oxygen arriving at the electrode surface increases. Eventually, at a high enough rotation, the rate at which oxygen arrives at the electrode surface approaches the rate at which the electrocatalyst reduces the oxygen. At this point, the current signal measured at the disk electrode begins to be governed (or limited) by the kinetic properties of the catalyst. It is at these higher rotation rates that the measured disk current begins to yield kinetic information. The current response recorded is given by the following equation:

$$\frac{1}{i} = \frac{1}{i_k} + \frac{1}{i_l} \tag{1.26}$$

where i is the observed limiting current, i_k is the kinetic contribution to the current and i_l is the Levich current which governs the mass transport and is expressed as:

$$i_l = 0.21nFAC_o D^{\frac{2}{3}} \upsilon^{-\frac{1}{6}} \omega^{\frac{1}{2}} \tag{1.27}$$

where n is the number of electrons, F is the Faraday constant (96485 $Cmol^{-1}$), A is the active surface area of the electrode, C_o is concentration of O_2 in the electrolyte, D is the diffusion coefficient of O_2 in the electrolyte, v is kinematic viscosity of O_2 and ω angular velocity (in rpm).

i_k is the kinetic contribution and it is expressed as :

$$i_k = nFAC_o k^o \exp\left(\frac{-\alpha nF\left(E - E^o\right)}{RT}\right) = nFAk\ C_o\Gamma \tag{1.28}$$

where k^o is the standard heterogeneous rate constant, k is the heterogeneous rate constant, Γ is the surface coverage by active species and E^o is the formal potential

The combination of these equations (1.27 and 1.28) produces the so called Koutecky-Levich equation

$$\frac{1}{i} = \frac{1}{i_k} + \frac{1}{i_l} = \frac{1}{nFAkC_{O_2}} + \frac{1}{0.21nFAD^{2/3}\gamma^{-\frac{1}{6}}C_{O_2}\omega^{\frac{1}{2}}} \tag{1.29}$$

Hence, for cathodic reactions governed by mixed transport-kinetic control, plots of 1/i vs $\omega^{½}$ for constant values of k, i.e., fixed η, are predicted to generate straight lines having slopes proportional to $1/n$ and intercepts proportional to $1/k$. It is important to note that the slopes of these plots are independent of applied over potential[127,136,137].

However, in real systems, there can be a possibility of the presence of pores or pinholes in the film through which oxygen diffuses to the electrode. This can be due to the presence of polymers, or Nafion thin films, thus a more general analysis which involves separating contribution

of electron transfer from other limiting activity inside the film is needed. The 'two–layer'' (diffusion in both the polymer/ Nafion film used and in the hydrodynamic boundary layer) is used to modify the K-L equation[138,139].

Assuming the reaction in oxygen species is first order and that the electron transfer is the rate determining step, one can express the equation as:

$$\frac{1}{|i|} = \frac{1}{|i_o|\left(\frac{\theta}{\theta_e}\right)\exp\left|\eta/_b\right|} + \frac{1}{i_l^{film-ads}} + \frac{1}{i_l^{diff}} \qquad (1.30)$$

η is the overvoltage expressed as E-E_{eq}, and θ ,θ_e signify the degree of coverage of the electrode surface by oxygen containing adsorbed species at potential E and at the equilibrium potential E_{eq}. As we have assumed the electron transfer step is first order in adsorbed species and that the oxygen evolution (backward reaction) is quite negligible, then one may assume $\theta \approx \theta_e$ at all electrode potentials.

The diffusion limiting current i_l^{diff} of molecular oxygen is controlled by the rotation speed ω, whereas the diffusion limiting current inside the film - i_l^{film} is independent of ω. The diffusion limiting current is given by the Levich law as expressed earlier:

$$i_l = 0.21nFAC_o D^{\frac{2}{3}} \upsilon^{-\frac{1}{6}} \omega^{\frac{1}{2}} \qquad (1.27)$$

$\frac{1}{i_l^{film-ads}}$ is the limiting current density resulting from a mixed control by the diffusion of molecular oxygen inside the film and by adsorption of oxygen at the catalyst surface. The plot of the inverse of the current density is a linear function of $1/\omega$ (K-L) plots. The total number of the exchanged electrons during the oxygen reduction process (n) is realised from the slope of the straight line while the intercept at the origin (ω ->∞) gives the inverse of the kinetic current corrected as a function of the over potential.

$$\frac{1}{|i_k|} = \frac{1}{i_l} + \frac{1}{i_0 \exp \eta/_b} \qquad (1.31)$$

Equation 1.31 shows that at high over potential ($|\eta| \rightarrow \infty$), i_k tends towards i_l; so the limiting current i_l can be obtained by extrapolating equation 1.31 at high over potential, so the whole equation can be re written as:

$$\eta = E - E_{eq} = -b\left(\ln\left|\frac{i_k}{i_l - i_k}\right| + \ln\left|\frac{i_l}{i_o}\right|\right) \tag{1.32}$$

$$\eta = E - E_{eq} = -\frac{1}{\alpha n f}\left(\ln\left|\frac{i_k}{i_l - i_k}\right| + \ln\left|\frac{i_l}{i_o}\right|\right) \tag{1.33}$$

Thus a plot of the over potential η, or the electrode potential E vs ln $|i_k/(i_l - i_k)|$ is a straight line, the slope of which is given by b (tafel slope) and the origin of which gives [-ln (i_l/i_o]. The ion exchange current i_o can be estimated knowing i_l.

1.9.5.4 Chronoamperommetry

Chronoamperommetry (CA) is a pulsed technique in which the current is measured versus time as a response to a (sequence of) potential pulse. The recorded current can be analysed and its nature can be identified from the variations with time. For example: at short times the capacitive current is dominant ($\propto e^{-1/RC}$); with R being the solution resistance and C the capacitance) while at longer time scales, the diffusion limited faradaic current might prevail ($\propto t^{-1/2}$). At the beginning of the experiment the potential of the working electrode is held at E_i (Fig. 1.16a). At t=0 the potential is instantaneously changed to a new value E_1, and corresponding current time response is recorded as shown in Fig. 1.16b.

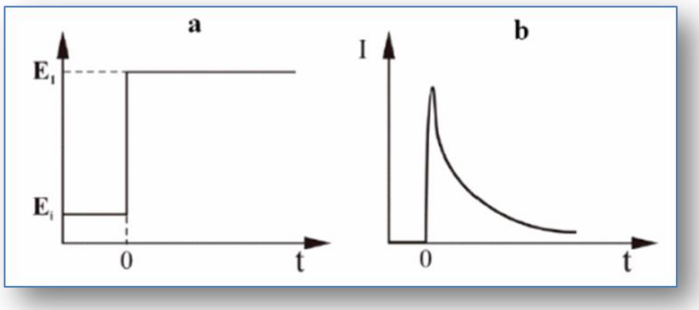

Figure 1.16: a) The potential-time profile applied during CA experiment, E_i is initial value and E_1 is the potential where no reduction of O occurs or some other potential of interest. b) The corresponding response of the current due to changes of the potential[129].

In order to determine the exact form of current-time dependence for a planar electrode the current density, Cottrell equation is used:

$$I = \frac{nFA\,CD^{1/2}}{\pi^{1/2}t^{1/2}} \qquad (1.34)$$

For diffusion controlled process, the current falls as the inverse of the square root of time ($t^{-1/2}$). This feature is frequently used as a test for this type of process and from the slope of I *vs*. $t^{-1/2}$ the diffusion coefficient D can be estimated.

Also using the equation (1.35) one can obtain the catalytic rate constant k *from the plots of* I_{cat}/I_{buff} *vs* $t^{1/2}$

$$\frac{I_{cat}}{I_{buff}} = \pi^{\frac{1}{2}}(kCt)^{1/2} \qquad (1.35)$$

where

I_{cat} and I_{buff} = the currents in the presence and absence of analyte respectively, C = concentration of bulk analyte (molcm^{-3}), t = elapsed time (s), k = catalytic rate constant (M^{-1}s^{-1}). Even though chronoamperommetry is a relatively simple technique, there are a number of difficulties which are related to the interpretation of the current-transient curve. Hence, it is very important to perform a comparative analysis of the chronoamperometric results with those of cyclic voltammetry and other techniques. This type of comparison will also help to understand the studied system more completely and with better precision[129].

1.9.5.5 Chronopotentiometry (CP)

In chronopotentiometry, a current pulse is applied to the working electrode and its resulting potential is measured against a reference electrode as a function of time. The solution is not stirred and a large excess of supporting electrolyte is present in the solution. At the moment when the current is first applied, the measured potential is abruptly changed due to the iR loss, and after that the change becomes a gradual one as it is caused by the concentration gradient developed in the electrolyte as a result of the depletion of reactants (reduced concentration of reactants) at the electrode surface[140].

1.10 Electrochemical Impedance (EIS)

Electrochemical Impedance (EIS) is a powerful method of characterizing many of the electrical properties of materials and their interface with electronically conducting electrodes. It is a technique which is used to characterize electrode processes and complex interfaces. It has been shown to be effective in probing the redox and structural features of surface confined species. Impedance spectroscopy is a very versatile tool widely used in different fields like corrosion, semiconductor electrodes, polymers and coatings, batteries, fuel cells, electrode kinetics and mechanisms, biomedical and biological systems, solid-state systems, etc.

1.10.1 Basics of EIS

In electrochemical impedance spectroscopy (EIS), the system under investigation (typically in the equilibrium state) is excited by a small amplitude AC sinusoidal signal of potential or current in a wide range of frequencies and the response of the current or voltage is measured. Since the amplitude of the excitation signal is small enough for the system to be in the (quasi-)equilibrium state, EIS measurements can be used to effectively evaluate the system properties without significantly disturbing them[127,141]. The usefulness of impedance spectroscopy lies in the ability to distinguish the individual contributions of components under investigation. The modelling procedure of the electrochemical data from EIS uses electrical circuits built from components such as resistors and capacitors to represent the electrochemical behaviour of the coating and the metal substrate. Changes in the values of the individual components indicate their behaviour and performance. Impedance spectroscopy is a non-destructive technique and so can provide time dependent information about on-going processes.

1.10.2 Analysis and Data Presentation in EIS

As written earlier, this method is based on the application of an AC potential ($E(t) = E_o \cos(\omega + t)$) of small amplitude (typically 10 mV). As

a consequence an AC current (I (t) = I_0 cos ($\omega t - \varphi$)) is obtained. From the relation of both signals (Fig 1.17 a) the impedance (Z) is obtained as $Z = E(t)/I(t)$)[141]. The measurements are carried out at different AC frequencies; a typical frequency range is 0.5 Hz to 100 kHz. Impedance methods allow characterizing the double layer interface at the electrodes and the physicochemical processes of widely differing time constants. Electron transfer is sampled at high frequency and mass transfer at low frequency. Impedance results are commonly fitted to equivalent circuits of resistors and capacitors, such as the Randles circuit shown in Fig 1.18c. This is often used to interpret simple electrochemical systems. Nyquist plot shown in Fig 1.17 b provides visual insight into the dynamics at the electrochemical interface. This is a plot of Z_{real} vs Z_{imag}, which normally exhibits a kind of semicircle profile plus a linear region. The points at which the imaginary impedance data cut the real impedance data represent resistance values.

Looking at Fig 1.17 c, R_{ct} is the charge-transfer resistance, which is inversely proportional to the rate of electron transfer and consequently provides us information about the ease of electron transfer at the electrode interface (a rough estimation of R_{ct} is related with the diameter of the semicircle); C_{dl} is the double-layer capacitance and can be obtained from the maximum value of impedance data at the semicircle; R_s is the electrolyte resistance and can be extracted from impedance data at the higher frequencies, while Z_w is the Warburg impedance and is identified with the linear portion of the impedance spectra that appears at the lower frequencies. The Warburg impedance arises from mass-transfer limitations and can be used to measure the effective diffusion coefficients. Another way to represent the impedance results is by using the Bode Plot where the modulus of the impedance (log $|Z|$) and the phase angle (φ) between the AC potential and the AC current is measured as a function of the frequency (log φ). A typical Bode plot is seen in Fig 1.18d. In Bode plots frequency independent data represent the behaviour of the resistive

processes (phase angles close to 0) whereas data dependent on the frequency are more related to capacitive or diffusive processes (phase angles between -90º or -45º). Thus the impedance spectra can give us a broad overview of the different processes taking place at the electrochemical interface (capacitive, resistive, diffusion effects) and which one is more dominant at a specific range of frequencies [141].

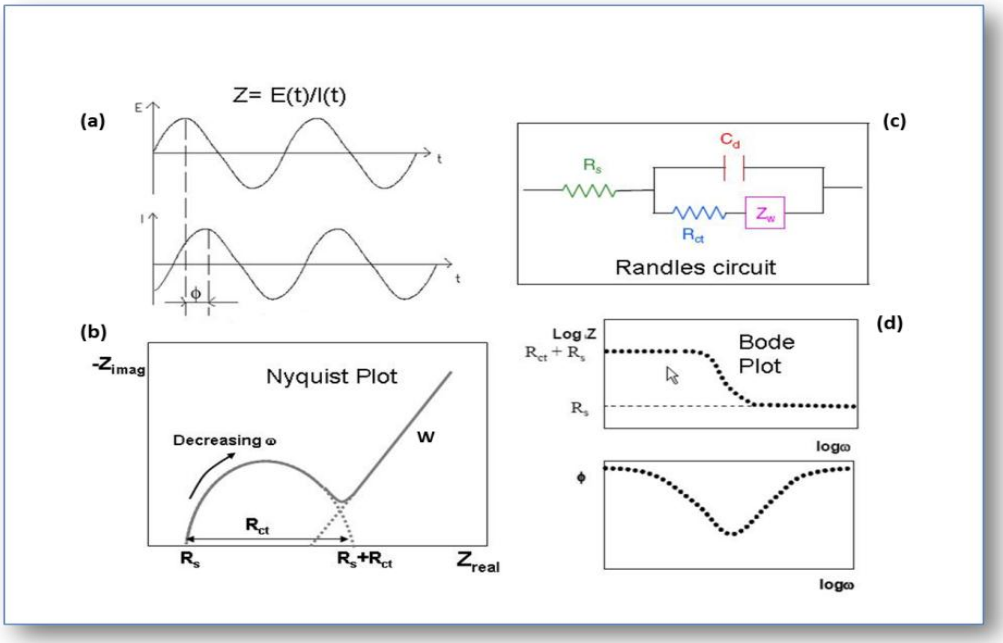

Figure 1.17: Impedance function (a); a typical equivalent circuit at the electrochemical interface - the Randles circuit (c) and the different representations of the impedance data Nyquist (b) and Bode plot (d)[141].

1.11 Microscopic and Spectroscopic Techniques

Microscopic and spectroscopic techniques are widely known in scientific investigations. A summary of some of these techniques highlighting only the areas relevant to this study have been briefly explained in the subsequent sections. All information was obtained from appropriate texts which have been referenced in their proper places in each of the sections.

1.11.1 Scanning Electron Microscopy

The scanning electron microscope (SEM) is a powerful and frequently used instrument, to study, for example, surface topography (morphology and size of the particles making up the object), composition, (the elements and compounds that the object is composed of and their relative amounts), crystallography (how the atoms are arranged in the object).and their properties on a local scale. SEM carries information from a depth in the range of 1 to 2 μm below the surface. Their spatial resolution is better than that of the optical microscope. The SEM has an extremely large depth of focus and is therefore well suited for topographic imaging. Besides surface topographic studies the SEM can also be used for determining the chemical composition of a material, its fluorescent properties, and the formation of magnetic domains. Some constraints are that the samples must be conductive, so non-conductive materials are carbon-coated and, secondly, that materials with atomic number smaller than the carbon are not detected with SEM. [142]

1.11.2 Transmission Electron Microscopy (TEM)

Transmission Electron Microscopy (TEM) is a technique where an electron beam interacts and passes through a specimen. The electrons are emitted by a source and are focused and magnified by a system of magnetic lenses. The images are obtained due to the interactions which take place when the accelerated beam of electrons impinges upon the specimen. The products of these interactions can be used to derive information on the nature of the specimen studied. TEM requires an ultra-high vacuum and a high voltage; it works with an electron column which comprises the

illumination system, the objective lens/stage and the imaging system. The illumination system which takes electrons form the source to the specimen can be operated on two principal modes. The first mode (parallel beam) is used primarily for TEM and the selected area diffraction (SAED) imaging, while the second mode (converging beam) is used mainly for the scanning TEM (STEM) imaging.

Annular dark field imaging is also a method of mapping samples in the STEM. This is known as high- angle annular field imaging (HAADF). Images are formed by collecting scattered electrons with an annular dark microscope. The main beam can also pass to an Electron Energy Loss Spectrum (EELS) detector allowing both types of measurement to be performed simultaneously. Contrast in TEM images can arise due to the differences in the phases of the electron waves scattered through a thin specimen. This phase contrast imaging is capable of resolving sub unit cell detail and it is the basis for the high resolution TEM (HRTEM). TEM images are two-dimensional projections of 3-D objects. The data obtained averages the whole examined volume and thus it is not suitable for surface analysis. TEM can be used in studying the internal structure of specimens down to its atomic levels. It should be noted that the high electron beam used in the electron microscopy can completely destroy the specimen by amorphisizing, melting or evaporating it.[143]

1.11.3 Energy Dispersive X-ray Spectroscopy (EDS)

Energy Dispersive Spectroscopy X-ray (EDS) makes use of the X-ray spectrum emitted by a solid sample bombarded with a focused beam of electrons to obtain a localized chemical analysis. All elements from atomic number 4 (Be) to 92 (U) can be detected in principle, though not all instruments are equipped for 'light' elements ($Z < 10$). Qualitative analysis involves the identification of the lines in the spectrum and is fairly straightforward owing to the simplicity of X-ray spectra. Quantitative analysis (determination of the concentrations of the elements

present) entails measuring line intensities for each element in the sample and for the same elements in calibration standards of known composition[144].

1.11.4 X ray Powder Diffraction (XRD)

X-ray powder diffraction (XRD) is a rapid non-destructive analytical technique primarily used for phase identification of a crystalline material and can provide information on unit cell dimensions. It can also provide structural properties of materials like the lattice parameters, grain size, strain etc. The analysed material is finely ground, and homogenized, for the analysis. The X-rays are generated by a cathode ray tube, filtered to produce monochromatic radiation, collimated to concentrate, and directed toward the sample[145]. The interaction of the incident rays with the sample produces constructive interference (and a diffracted ray) when conditions satisfy Bragg Law ($n\lambda=2d\sin\theta$ where d is the spacing between diffracting planes, θ is the incident angle, n is any integer, and λ is the wavelength of the beam.). This law gives a simple relationship between the different diffraction pattern and the crystalline structure of the material. The Scherrer equation ($\tau = K\lambda/\beta \cos\theta$ where τ is the mean size of the crystalline domains which may be smaller or equal to the grain size, K is a dimensionless shape factor, with a value close to unity, λ is the X-ray wavelength, β the line broadening at half max (FWHM) in radians, and θ is the Bragg angle) is used in the determination of size particles of crystals in powder form. It is a formula that relates the size of the crystallite, in a solid to the broadening of a peak in a diffraction pattern[145].

1.11.5 Raman Spectroscopy

Raman spectroscopic technique is used in observing vibrational, rotational and other low-frequency modes in a system. (Fig 1.18). It relies on inelastic scattering or Raman scattering of monochromatic light usually from a laser in the visible, near infra-red or near ultra violet range. The

laser light interacts with molecular vibrations, phonons or other excitations in the system, resulting in the energy of the laser photons being shifted up or down. The shift in energy gives information about the vibrational modes in the system. Infrared spectroscopy yields similar, but complementary information[146]

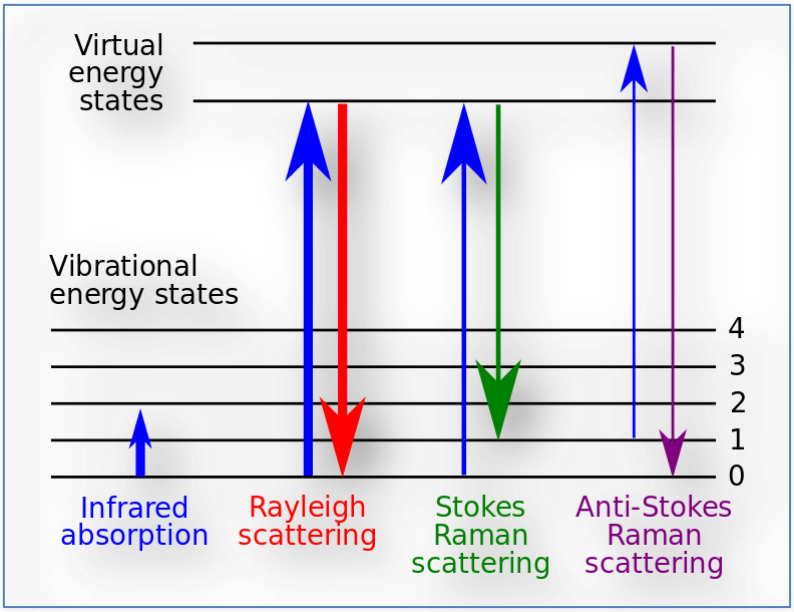

Figure 1.18: The Raman energy levels[146].

1.11.6 Infra-red Spectroscopy

Infrared spectroscopy (IR spectroscopy) is the spectroscopy that deals with the infra-red region of the electromagnetic spectrum i.e. light with a longer wavelength and lower frequency than visible light. IR spectroscopy exploits the fact that molecules have specific frequencies at which they rotate or vibrate corresponding to discreet energy levels or vibrational modes. Thus, it is often used to identify structures because functional groups give rise to characteristic bands both in terms of intensity and position (frequency). The positions of these bands are summarized in a correlation diagram as shown in Fig 1.19. As with all spectroscopic techniques, it can be used to identify and study chemicals. A common

laboratory instrument that uses this technique is a Fourier transform infrared spectrometer[146].

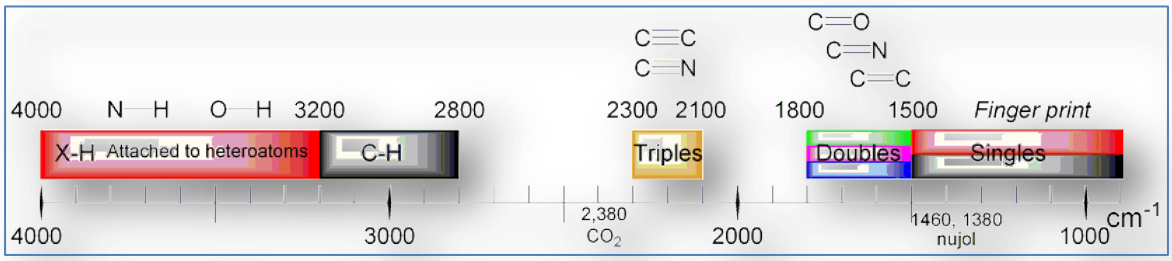

Figure 1.19 The positions of IR characteristic bands of different functional groups[146]**.**

1.11.7 Ultraviolet-Visible Spectroscopy

Ultraviolet-visible (UV-vis) spectroscopy involves the spectroscopy of photons in the UV-visible region. In this region of the electromagnetic spectrum, molecules undergo electronic transitions. Absorption of photons of light measures transitions from the ground state to the excited state. Most absorption by organic compounds results from the presence of Π (i.e. unsaturated) bonds. A chromosphere is a molecular group usually containing a Π bond. When inserted into a saturated hydrocarbon (which exhibits no UV absorbance spectrum), it produces a compound with absorption between 185 and 1000 nm. Transition metal ions also have electronic energy levels that cause absorption at 400–700 nm in the visible region[147]

1.11.8 Nuclear Magnetic Resonance Spectroscopy

Nuclear magnetic resonance spectroscopy, most commonly known as NMR spectroscopy, is a research technique that exploits the magnetic properties of certain atomic nuclei. It relies on the phenomenon of nuclear magnetic resonance and can provide detailed information about the structure, dynamics, reaction state, and chemical environment of molecules. Most frequently, NMR spectroscopy is also used to investigate

the properties of organic molecules, although it is applicable to any kind of sample that contains nuclei possessing spin. Suitable samples range from small compounds analysed with 1-dimensional proton or carbon -13 NMR spectroscopy to large proteins or nucleic acids using 3 or 4-dimensional techniques. NMR spectra are highly unique, well-resolved, analytically tractable and often highly predictable. Thus, in organic chemistry practice, NMR analysis is used in confirming the identity of a substance. Different functional groups have their distinguishable signals and identical functional groups with differing neighbouring substituents also give signals distinguishing one from the other in the NMR spectra. Two-dimensional techniques are used to determine the structure of more complicated molecules. Time domain NMR spectroscopic techniques are used to probe molecular dynamics in solutions and solid state NMR spectroscopy is used to determine the molecular structure of solids[148].

1.12 Scope of Research

Palladium is regarded as the most Pt-like metal. Just like Pt, its activity as anode or cathode catalyst in fuel cells can be effectively enhanced by alloying with other metals. It has also been established that core shell electrocatalyst approach deliberately deposits high cost, high activity precious metal component as a thin layer on the surface of lower cost substrate/nanoparticles /nano alloy core as the only atoms at the nano particle surface actively participating in the electrochemical reactions. High activities have also been reported for core shell catalysts but many are yet to be investigated for their high performances in the membrane electrode assemblies (MEAs).

This research looks into the following in the first three chapters of the study:

- The design and synthesis of a Pd based ternary core shell nano catalyst (FeCo@Fe@Pd) using a fast and facile microwave-assisted technique;
- The study of the core shell nanocatalysts as possible electrocatalyst for both anodic and cathodic reactions in four direct alkaline alcohol fuel cells using methanol, ethanol, ethylene glycol and glycerol as fuels.
- Various microwave assisted synthetic routes (so as to come up with a favourable and reproducible procedure) for the synthesis of the core shell catalyst and the physical and chemical characterisation to ascertain the core shell nature of the catalysts.

The next three chapters - Chapters four to six cover:

- The deposition of FeCo@Fe@Pd nano catalysts on carbon, and tests of its catalytic activity for ORR and methanol, ethanol ethylene glycol and glycerol oxidation in alkali medium.
- The analyses of the results obtained from the studies carried out above.

Chapters' seven to nine deals with:

- The re-synthesis of the core shell catalysts on functionalised multi walled carbon nanotubes substrates (as a way to further enhance their catalytic properties) and the tests of their catalytic performance as both anodes and cathode catalysts using the four fuels listed above.
- The results obtained from these new sets of findings and their analyses

Chapters eleven and twelve cover:

- The preliminary MEA studies of the FeCo@Fe@Pd nano catalysts on their various substrates as anode catalysts in real direct alkaline alcohol fuel cells (Passive DAAFCs) and also on Active DAAFCS operating at diferent temperatures utilising the four different alcohols previously listed.

The last chapter deals with the:

- Synthesis of a novel hydrophobic form of iron (II) phthalocyanine and its characterisation.
- Study of this compound as a potential electro catalyst for oxygen reduction reaction in alkaline media.

1.13 References

(1) Mcconnell, R.; Licht, S.; Rajeshwar, K.; Harrison, K. *Solar Hydrogen Generation*; Rajeshwar, K.; McConnell, R.; Licht, S., Eds.; Springer New York: New York, NY, 2008; pp. 1–315.

(2) Veziroğlu, T. N.; Şahi˙N, S. *Energy Convers. Manag.* **2008**, *49*, 1820–1831.

(3) Momirlan, M.; Veziroglu, T. *Int. J. Hydrogen Energy* **2005**, *30*, 795–802.

(4) Jain, I. P. *Int. J. Hydrogen Energy* **2009**, *34*, 7368–7378.

(5) Winter, C.-J. *Int. J. Hydrogen Energy* **2009**, *34*, S1–S52.

(6) Haile, S. M. *Acta Mater.* **2003**, *51*, 5981–6000.

(7) Andújar, J. M.; Segura, F. *Renew. Sustain. Energy Rev.* **2009**, *13*, 2309–2322.

(8) European Reserch Unit. Site - Fuel cell wheel, 2004.

(9) Ball, M.; Wietschel, M. *Int. J. Hydrogen Energy* **2009**, *34*, 615–627.

(10) Pilatowsky, I.; Romero, R. J.; Isaza, C. a.; Gamboa, S. a.; Sebastian, P. J.; Rivera, W. *Cogeneration Fuel Cell-Sorption Air Conditioning Systems*; Green Energy and Technology; Springer London: London, 2011; pp. 1–155.

(11) Atkins P, J. de P. *Physical Chemistry*; 2011; pp. 1–1085.

(12) Ramani, V. *Electrochem. Soc. Interface* **2006**, 41–44.

(13) Basu, S. *Recent Trends in Fuel Cell Science and Technology*; Springer New Yorkr, 2007; p. 375.

(14) Carrette, L.; Friedrich, K. a.; Stimming, U. *Fuel Cells* **2001**, *1*, 5–39.

(15) Kamarudin, S. K.; Hashim, N. *Renew. Sustain. Energy Rev.* **2012**, *16*, 2494–2515.

(16) Basu, S. *Recent Trends in Fuel Cell Science and Technology*; Springer New Yorkr, 2007; p. 375.

(17) About Fuel Cells New & Renewable Energy Systems Group - TKK AES, 2007.

(18) Mclean, G. F.; Niet, T.; Djilali, N. **2002**, *27*, 507–526.

(19) Markovic, N.; Gasteiger, H.; Ross, P. N.; Berkeley, L.; Division, M. S. **1997**, *144*, 1591–1597.

(20) Blizanac, B. B.; Ross, P. N.; Markovic, N. M. *Electrochim. Acta* **2007**, *52*, 2264–2271.

(21) Gouérec, P.; Poletto, L.; Denizot, J.; Sanchez-Cortezon, E.; Miners, J. H. *J. Power Sources* **2004**, *129*, 193–204.

(22) Gülzow, E.; Schulze, M.; Gerke, U. *J. Power Sources* **2006**, *156*, 1–7.

(23) Lin, B. Y. S.; Kirk, D. W.; Thorpe, S. J. *J. Power Sources* **2006**, *161*, 474–483.

(24) Matsuoka, K.; Iriyama, Y.; Abe, T.; Matsuoka, M.; Ogumi, Z. *J. Power Sources* **2005**, *150*, 27–31.

(25) Varcoe, J. R.; Slade, R. C. T.; Lam How Yee, E. *Chem. Commun. (Camb).* **2006**, 1428–1429.

(26) Yang, C.-C.; Chiu, S.-J.; Chien, W.-C. *J. Power Sources* **2006**, *162*, 21–29.

(27) Bidault, F.; Brett, D. J. L.; Middleton, P. H.; Brandon, N. P. *J. Power Sources* **2009**, *187*, 39–48.

(28) Dillon, R.; Srinivasan, S.; Aricò, a. S.; Antonucci, V. *J. Power Sources* **2004**, *127*, 112–126.

(29) Liu, H.; Song, C.; Zhang, L.; Zhang, J.; Wang, H.; Wilkinson, D. P. *J. Power Sources* **2006**, *155*, 95–110.

(30) Zhao, X.; Yin, M.; Ma, L.; Liang, L.; Liu, C.; Liao, J.; Lu, T.; Xing, W. *Energy Environ. Sci.* **2011**, *4*, 2736.

(31) Zainoodin, a. M.; Kamarudin, S. K.; Daud, W. R. W. *Int. J. Hydrogen Energy* **2010**, *35*, 4606–4621.

(32) Kamarudin, S. K.; Achmad, F.; Daud, W. R. W. *Int. J. Hydrogen Energy* **2009**, *34*, 6902–6916.

(33) Antolini, E. *J. Power Sources* **2007**, *170*, 1–12.

(34) Kamarudin, M. Z. F.; Kamarudin, S. K.; Masdar, M. S.; Daud, W. R. W. *Int. J. Hydrogen Energy* **2013**, *38*, 9438–9453.

(35) Peled, E.; Livshits, V.; Duvdevani, T. *J. Power Sources* **2002**, *106*, 245–248.

(36) Livshits, V.; Philosoph, M.; Peled, E. *J. Power Sources* **2008**, *178*, 687–691.

(37) Antolini, E.; Gonzalez, E. R. *J. Power Sources* **2010**, *195*, 3431–3450.

(38) Tripkovic, A. V; Popovic, K. D.; Grgur, B.; Blizanac, B.; Ross, P.; Maekovic, N. *Electrochim. Acta* **2002**, *47,* 3707-3714.

(39) Yu, E.; Scott, K. *J. Power Sources* **2004**, *137*, 248–256.

(40) Coutanceau, C.; Demarconnay, L.; Lamy, C.; Léger, J.-M. *J. Power Sources* **2006**, *156*, 14–19.

(41) Yu, E.; Scott, K. *J. Power Sources* **2004**, *137*, 248–256.

(42) Scott, K.; Yu, E.; Vlachogiannopoulos, G.; Shivare, M.; Duteanu, N. *J. Power Sources* **2008**, *175*, 452–457.

(43) Yu, E. H.; Krewer, U.; Scott, K. *Energies* **2010**, *3*, 1499–1528.

(44) Chen, C. .; Yang, P. *J. Power Sources* **2003**, *123*, 37–42.

(45) Tang, H.; Wang, S.; Pan, M.; Jiang, S. P.; Ruan, Y. *Electrochim. Acta* **2007**, *52*, 3714–3718.

(46) Wen, Z.; Liu, J.; Li, J. *Adv. Mater.* **2008**, *20*, 743–747.

(47) Liu, Z.; Zhao, B.; Guo, C.; Sun, Y.; Shi, Y.; Yang, H.; Li, Z. *J. Colloid Interface Sci.* **2010**, *351*, 233–238.

(48) Weber, A. Z.; Newman, J. *Modeling transport in polymer-electrolyte fuel cells.*; **2004**; Vol. 104, pp. 4679–4726.

(49) Koenigsmann, C.; Wong, S. S. *Energy Environ. Sci.* **2011**, *4*, 1161-1176.

(50) Long, N. V.; Duy Hien, T.; Asaka, T.; Ohtaki, M.; Nogami, M. *Int. J. Hydrogen Energy* **2011**, *36*, 8478–8491.

(51) Chen, C. Y.; Liu, D. H.; Huang, C. L.; Chang, C. L. *J. Power Sources* **2007**, *167*, 442–449.

(52) Teng, X. W.; Liang, X. Y.; Rahman, S.; Yang, H. *Adv. Mater.* **2005**, *17*, 2237–2241.

(53) Cao, L.; Scheiba, F.; Roth, C.; Schweiger, F.; Cremers, C.; Stimming, U.; Fuess, H.; Chen, L.; Zhu, W.; Qiu, X. *Angew. Chem. Int. Ed. Engl.* **2006**, *45*, 5315–5319.

(54) Qiao, Y.; Li, C. M. *J. Mater. Chem.* **2011**, *21*, 4027.

(55) Shen, P. K.; Xu, C. *Electrochem. commun.* **2006**, *8*, 184–188.

(56) Xu, C.; Liu, Y.; Yuan, D. *Int. J. Electrochem. Sci.* **2007**, *2*, 674–680.

(57) Antolini, E. *Energy Environ. Sci.* **2009**, *2*, 915-931.

(58) Bianchini, C.; Shen, P. K. *Chem. Rev.* **2009**, *109*, 4183–4206.

(59) Wang, X.; Wang, W.; Qi, Z.; Zhao, C.; Ji, H.; Zhang, Z. *J. Power Sources* **2010**, *195*, 6740–6747.

(60) Wei, W.; Chen, W. *J. Power Sources* **2012**, *204*, 85–88.

(61) Yin, Z.; Zheng, H.; Ma, D.; Bao, X. *J. Phys. Chem. C* **2009**, *113*, 1001–1005.

(62) Miao, F.; Tao, B.; Sun, L.; Liu, T.; You, J.; Wang, L.; Chu, P. K. *J. Power Sources* **2010**, *195*, 146–150.

(63) Zhao, Y.; Nie, S.; Wang, H.; Tian, J.; Ning, Z.; Li, X. *J. Power Sources* **2012**, *218*, 320–330.

(64) Wang, Y.; Wang, X.; Li, C. M. *Appl. Catal. B Environ.* **2010**, *99*, 229–234.

(65) Lu, Y.; Jiang, Y.; Wu, H.; Chen, W. *J. Phys. Chem. C* **2013,** *177*, 2926-2938.

(66) Zhao, Y.; Yang, X.; Tian, J.; Wang, F.; Zhan, L. *Int. J. Hydrogen Energy* **2010**, *35*, 3249–3257.

(67) Wang, R.; Li, H.; Feng, H.; Wang, H.; Lei, Z. *J. Power Sources* **2010**, *195*, 1099–1102.

(68) An, L.; Zhao, T. S.; Shen, S. Y.; Wu, Q. X.; Chen, R. *J. Power Sources* **2011**, *196*, 186–190.

(69) An, L.; Zhao, T. S. *Int. J. Hydrogen Energy* **2011**, *36*, 9994–9999.

(70) Kamarudin, M. Z. F.; Kamarudin, S. K.; Masdar, M. S.; Daud, W. R. W. *Int. J. Hydrogen Energy* **2013**, *38*, 9438–9453.

(71) Mann, J.; Yao, N.; Bocarsly, A. B. *Langmuir* **2006**, *22*, 10432–10436.

(72) Chetty, R.; Scott, K. *Electrochim. Acta* **2007**, *52*, 4073–4081.

(73) Sun, S.; Jusys, Z.; Behm, R. J. *J. Power Sources* **2013**, *231*, 122–133.

(74) Ksar, F.; Ramos, L.; Keita, B.; Nadjo, L.; Beaunier, P.; Remita, H. *Chem. Mater.* **2009**, *21*, 3677–3683.

(75) Pandey, R. K.; Lakshminarayanan, V. *J. Phys. Chem. C* **2009**, *113*, 21596–21603.

(76) Xu, C.; Shen, P. K.; Liu, Y. *J. Power Sources* **2007**, *164*, 527–531.

(77) Modibedi, R. M.; Masombuka, T.; Mathe, M. K. *Int. J. Hydrogen Energy* **2011**, *36*, 4664–4672.

(78) Hong, W.; Liu, Y.; Wang, J.; Wang, E. *J. Power Sources* **2013**, *241*, 1–5.

(79) Zhu, C.; Guo, S.; Dong, S. *J. Mater. Chem.* **2012**, *22*, 14851.

(80) Gao, H.; Liao, S.; Liang, Z.; Liang, H.; Luo, F. *J. Power Sources* **2011**, *196*, 6138–6143.

(81) Serov, A.; Kwak, C. *Appl. Catal. B Environ.* **2010**, *97*, 1–12.

(82) Dalbay, N.; Kadirgan, F. *Electrochim. Acta* **1991**, *36*, 353–356.

(83) Demarconnay, L.; Brimaud, S.; Coutanceau, C.; Léger, J.-M. *J. Electroanal. Chem.* **2007**, *601*, 169–180.

(84) Bambagioni, V.; Bevilacqua, M.; Bianchini, C.; Filippi, J.; Marchionni, a.; Vizza, F.; Wang, L. Q.; Shen, P. K. *Fuel Cells* **2010**, *10*, 582–590.

(85) Marchionni, A.; Bevilacqua, M.; Bianchini, C.; Chen, Y.-X.; Filippi, J.; Fornasiero, P.; Lavacchi, A.; Miller, H.; Wang, L.; Vizza, F. *ChemSusChem* **2013**, *6*, 518–528.

(86) Simões, M.; Baranton, S.; Coutanceau, C. *Appl. Catal. B Environ.* **2010**, *93*, 354–362.

(87) Ilie, a.; Simoes, M.; Baranton, S.; Coutanceau, C.; Martemianov, S. *J. Power Sources* **2011**, *196*, 4965–4971.

(88) Hu, W.; Lowry, B.; Varma, A. *Appl. Catal. B Environ.* **2011**, *106*, 123–132.

(89) Bambagioni, V.; Bianchini, C.; Marchionni, A.; Filippi, J.; Vizza, F.; Teddy, J.; Serp, P.; Zhiani, M. *J. Power Sources* **2009**, *190*, 241–251.

(90) Matsuoka, K.; Inaba, M.; Iriyama, Y.; Abe, T.; Ogumi, Z.; Matsuoka, M. *Fuel Cells* **2002**, *2*, 35–39.

(91) Liang, D.; Gao, J.; Wang, J.; Chen, P.; Wei, Y.; Hou, Z. *Catal. Commun.* **2011**, *12*, 1059–1062.

(92) Zhang, Z.; Xin, L.; Li, W. *Int. J. Hydrogen Energy* **2012**, *37*, 9393–9401.

(93) Zhang, J.; Liang, Y.; Li, N.; Li, Z.; Xu, C.; Jiang, S. P. *Electrochim. Acta* **2012**, *59*, 156–159.

(94) Mougenot, M.; Caillard, a.; Simoes, M.; Baranton, S.; Coutanceau, C.; Brault, P. *Appl. Catal. B Environ.* **2011**, *107*, 372–379.

(95) Simões, M.; Baranton, S.; Coutanceau, C. *Appl. Catal. B Environ.* **2011**, *110*, 40–49.

(96) Fordham, P.; Besson, M.; Gallezot, P. *Appl. Catal. A Gen.* **1995**, *133*, L179–L184.

(97) Besson, M.; Gallezot, P. *Catal. Today* **2000**, *57*, 127–141.

(98) Carrettin, S.; McMorn, P.; Johnston, P.; Griffin, K.; Kiely, C. J.; Hutchings, G. J. *Phys. Chem. Chem. Phys.* **2003**, *5*, 1329–1336.

(99) Katryniok, B.; Kimura, H.; Skrzyńska, E.; Girardon, J.-S.; Fongarland, P.; Capron, M.; Ducoulombier, R.; Mimura, N.; Paul, S.; Dumeignil, F. *Green Chem.* **2011**, *13*, 1960.

(100) Zhang, Z.; Xin, L.; Qi, J.; Wang, Z.; Li, W. *Green Chem.* **2012**, *14*, 2150.

(101) Spendelow, J. S.; Wieckowski, A. *Phys. Chem. Chem. Phys.* **2007**, *9*, 2654–2675.

(102) Song, C.; Zhang, J. *PEM Fuel Cell Electrocatalysis and Catalyst Layers: Fundamentals and Applications*; Ed.; Springer, 2008; p. 1159.

(103) Yeager, E. *Electrochim. Acta* **1984**, *29*, 1527–1537.

(104) Gupta, S.; Savinell, R. F. *J. Electroanal. Chem.* **1999**, *29*, 63–72.

(105) Baker, R.; Wilkinson, D. P.; Zhang, J. *Electrochim. Acta* **2008**, *53*, 6906–6919.

(106) Yang, H. *Angew. Chem. Int. Ed. Engl.* **2011**, *50*, 2674–2676.

(107) Suo, Y.; Zhuang, L.; Lu, J. *Angew. Chem. Int. Ed. Engl.* **2007**, *46*, 2862–2864.

(108) Kitchin, J. R.; Nørskov, J. K.; Barteau, M. A.; Chen, J. G. *Phys. Rev. Lett.* **2004**, 4–7.

(109) Shao, M. H.; Huang, T.; Liu, P.; Zhang, J.; Sasaki, K.; Vukmirovic, M. B.; Adzic, R. R. *Langmuir* **2006**, *22*, 10409–10415.

(110) Mavrikakis, M.; Hammer, B.; Nørskov, J. K. *Phys. Rev. Lett.* **1998**, *81*, 2819–2822.

(111) (a)Galema, S.A. *Chem. Soc. Rev.* **1997**, *26*, 233-238; (b) Anton Paar, Synthos 3000, '*Enhanced microwave - assisted synthesis*' handbook / manual.

(112) Adzic, R. R.; Zhang, J.; Sasaki, K.; Vukmirovic, M. B.; Shao, M.; Wang, J. X.; Nilekar, a. U.; Mavrikakis, M.; Valerio, J. a.; Uribe, F. *Top. Catal.* **2007**, *46*, 249–262.

(113) Zhang, J.; Mo, Y.; Vukmirovic, M. B.; Klie, R.; Sasaki, K.; Adzic, R. R. *J. Phys. Chem. B* **2004**, *108*, 10955–10964.

(114) Shao, M.; Sasaki, K.; Marinkovic, N.; Zhang, L.; Adzic, R. *Electrochem. commun.* **2007**, *9*, 2848–2853.

(115) Xing, Y.; Cai, Y.; Vukmirovic, M. B.; Zhou, W.-P.; Karan, H.; Wang, J. X.; Adzic, R. R. *J. Phys. Chem. Lett.* **2010**, *1*, 3238–3242.

(116) Sasaki, K.; Naohara, H.; Cai, Y.; Choi, Y. M.; Liu, P.; Vukmirovic, M. B.; Wang, J. X.; Adzic, R. R. *Angew. Chem. Int. Ed. Engl.* **2010**, *49*, 8602–8607.

(117) Mayrhofer, K. J. J.; Juhart, V.; Hartl, K.; Hanzlik, M.; Arenz, M. *Angew. Chem. Int. Ed. Engl.* **2009**, *48*, 3529–3531.

(118) Wang, D.; Xin, H. L.; Yu, Y.; Wang, H.; Rus, E.; Muller, D. a; Abruña, H. D. *J. Am. Chem. Soc.* **2010**, *132*, 17664–17666.

(119) Wang, L.; Nemoto, Y.; Yamauchi, Y. *J. Am. Chem. Soc.* **2011**, *133*, 9674–9677.

(120) Kuai, L.; Yu, X.; Wang, S.; Sang, Y.; Geng, B. *Langmuir* **2012**, *28*, 7168–7173.

(121) Lee, Y. W.; Kim, M.; Kim, Z. H.; Han, S. W. *J. Am. Chem. Soc.* **2009**, *131*, 17036–17037.

(122) Li, H.; Wu, H.; Zhai, Y.; Xu, X.; Jin, Y. *ACS Catal.* **2013**, *3*, 2045-2051.

(123) Mazumder, V.; Chi, M.; More, K. L.; Sun, S. *J. Am. Chem. Soc.* **2010**, *132*, 7848–7849.

(124) Malik, M. A.; Wani, M. Y.; Hashim, M. A. *Arab. J. Chem.* **2012**, *5*, 397–417.

(125) Sekol, R. C.; Li, X.; Cohen, P.; Doubek, G.; Carmo, M.; Taylor, A. D. *Appl. Catal. B Environ.* **2013**, *138-139*, 285–293.

(126) Wilde, G. *Nanostructured materials*; Elsevier, 2009; Vol. 1, p. 384.

(127) Bard, Allen J, Faukner, L. R. *Electrochemical Methods:Fundamentals and Applications*; 2nd ed.; Wiley, New York: New York, 2001; p. 864 Pages.

(128) Bagotsky V. *Fundamentals of Electrochemistry;* 2nd ed;John Wiley and Sons, 2005, p. 1–640.

(129) Wang, .Joseph. *Analytical Electrochemistry*; 3rd ed.; Wiley-VCH, 2006; p. 272.

(130) Compton, RG, B. C. *Understanding Voltammetry*; 2007; pp. 249–253.

(131) Brainina, K. Z.; Malakhova, N. a; Stojko, N. Y. *Fresenius. J. Anal. Chem.* **2000**, *368*, 307–325.

(132) Kounaves, S. P. In *Handbook of Instrumental Techniques for Analytical Chemistry*; pp. 709–726.

(133) Rubi, J. M.; Kjelstrup, S. *J. Phys. Chem. B* **2003**, *107*, 13471–13477.

(134) Otles, S. *Handbook of food analysis instruments*; CRC Press, 2008.

(135) Harnisch, F.; Freguia, S. *Chem. Asian J.* **2012**, *7*, 466–475.

(136) Ball, S. C. *Platin. Met. Rev.* **2005**, *49*, 27–32.

(137) Gasteiger, H. a.; Kocha, S. S.; Sompalli, B.; Wagner, F. T. *Appl. Catal. B Environ.* **2005**, *56*, 9–35.

(138) Coutanceau, C.; Croissant, M. .; Napporn, T.; Lamy, C. *Electrochim. Acta* **2000**, *46*, 579–588.

(139) Schmidt, T. J.; Gasteiger, H. A.; Behm, R. J. *J. Electrochem. Soc.* **1999**, *146*, 1296–1304.

(140) Inzelt, G. *Conducting polymers. A New Era in Electrochemistry*; Springer, 2008; p. 282.

(141) Pacios, M.; Villa, R.; Godignon, P.; Martín-Fernández, I.; Del Valle, M.; Bartrolí, J.; Esplandiu, M. In *Nanotechnology and Nanomaterials Carbon Nanotubes growth and applications"*; 2011.

(142) Gervasi, C. a.; Alvarez, P. E.; Fiori Bimbi, M. V.; Folquer, M. E. *J. Electroanal. Chem.* **2007**, *601*, 194–204.

(143) Williams, D.; Carter, C. *Transmission Electron Microscopy*; 2009; p. 758.

(144) Joseph Goldstein, D E. Newbury, D C. Joy, C E. Lyman, P Echlin, E LIfshin, L Sawyer, and J. R. M. *Scanning Electron Microscopy and X-Ray Microanalysis*; Springer New York, 2003; Vol. 34, p. 453.

(145) He, B. B. *Two-dimensional X-ray Diffraction*; John Wiley & Sons, 2011, 2011; p. 426.

(146) Hazle, M. a.; Mehicic, M.; Gardiner, D. J.; Graves, P. R. *Vib. Spectrosc.* **1990**, *1*, 104.

(147) Owen, T. *Fundamentals of Modern UV-visisble Spectroscopy*; 2000; p. 133.

(148) Pohmann, R. In *In vivo NMR Imaging*; Springer, 2011; pp. 3–21.

Chapter 2

EXPERIMENTAL SECTION

2.1 Materials and Reagents

Table 2. 1: The list of reagents and chemicals used for syntheses of catalysts and their electrochemical analyses

Reagents/Chemicals	Purity (%)	Source
Multiwall carbon nanotubes	96 wt. %	Cheap Tubes Inc. VT USA
Vulcan XC-72Carbon	98	Sigma- Aldrich
Tokuyama anion-exchange membrane A-006 (OH-type)		Tokuyama Corporation
Nafion perfluorinated ion exchange fluorinated resin (5%).		Sigma- Aldrich
$FeCl_2.4H_2O$	98	Sigma- Aldrich
$CoCl_2.6H_2O$	98	Sigma- Aldrich
$PdCl_2$	98	Sigma- Aldrich
Polyvinylpyrolidone (PVP)		Sigma- Aldrich
KOH	99	Merck
KCl	99	Merck
Alumina oxide Nano powder (50nm)	98.5%	Sigma- Aldrich
DMF	99	Merck
Methanol	99.5	Merck
Ethylene Glycol	99	Merck
Glycerol	99.5	Merck
HNO_3	64.66	Merck
H_2SO_4	98	Merck
HCl	99	Merck
Acetic acid anhydride	98.5	Sigma- Aldrich

2.2 Synthesis of Catalysts

Multi-walled Carbon nanotubes (MWCNTs) were functionalized using a microwave assisted solvothermal technique (MW-ST). This was done using a 2-step procedure. Firstly, 1 g of pristine multi walled carbon nanotubes was added to 20 ml 65% HNO_3. After stirring for 5 mins on a magnetic stirrer, the mixture was transferred in to an Anton Paar microwave reactor. It was microwaved for 15 mins at 85^0C. The metallic impurities in the MWCNT are oxidised during this process, they are later removed after the reaction during centrifuging. A 3:1 mixture of H_2SO_4:HNO_3 was added to the treated MWCNTs. The mixture was sonicated for 30 mins and microwaved for a second time for another 10 mins. The microwave reaction was conducted at 500W power and 160°C. Ramp/steady-reaction/cooling time was 10/15/45 mins. The evaporation of acidic reagents in closed vessels of microwave causes a high pressure and simulates reflux conditions. Thus, a longer time is needed for cooling to ensure adequate condensation of acidic fumes after the reaction.The viscous and almost miscible mixture was separated by centrifuging.

Etching of the MWCNTs was carried out by addition of a mixture of 4:1 ratio of H_2SO_4:H_2O_2 to the suspension. This was done in a fume hood as both reagents are oxidizing agents. The mixture was stirred in the fume hood for 30 mins at 70°C. The resulting carboxylate multiwalled carbon nanotubes (CNT-OH) was centrifuged and washed continuously with deionised water until the pH of the residual water was 7. It was then dried overnight in an oven at 120°C.

For the functionalization with sulfonate groups; $(SO_3)^{2-}$ 500 mg of CNT-OH was added to a mixture of 1:15 H_2SO_4 : acetic acid anhydride in a beaker. The mixture was stirred in a fume hood for 2 h at 50°C. The resulting suspension was then centrifuged and washed several times with deionised water until the pH of the residual water was 7. The black solid was dried overnight at 120°C [1–3].

2.2.1 a Characterisation of Functionalized Carbon Nanotubes

Both carboxylate (CNT-OH) and sulfonate (CNT-SO_3) functionalised carbon nanotubes were characterised using FESEM, TEM, FTIR, and Raman spectroscopy. This was necessary as they were used as alternate substrates for the bulk of the research carried out in this study.

Fig 2.1 shows the FESEM and TEM images of the MWCNTs in their pristine form and after functionalization with both carboxyl and sulfonate groups were done. The first 3 sets represent the FESEM images while the last set of 3 images below represent their equivalent TEM images. Carboxylate functionalised MWCNTs are represented as o-MWCNTs (or CNT-OH / oCNTs) while sulfonate functionalised MWCNTs are denoted s-MWCNTs (or CNT-SO_3 /sCNTs). MWCNTs appear very tangled in the SEM images of the pristine CNTs in Fig 2.1. The initial functionalizing to produce carboxyl functionalised CNTs (CNT-OH) resulted in shorter forms of the CNTs. Further treatment to produce the sulfonate functionalised CNTs (CNT-SO_3) resulted in the formation of aggregates in form of lumps or clusters.

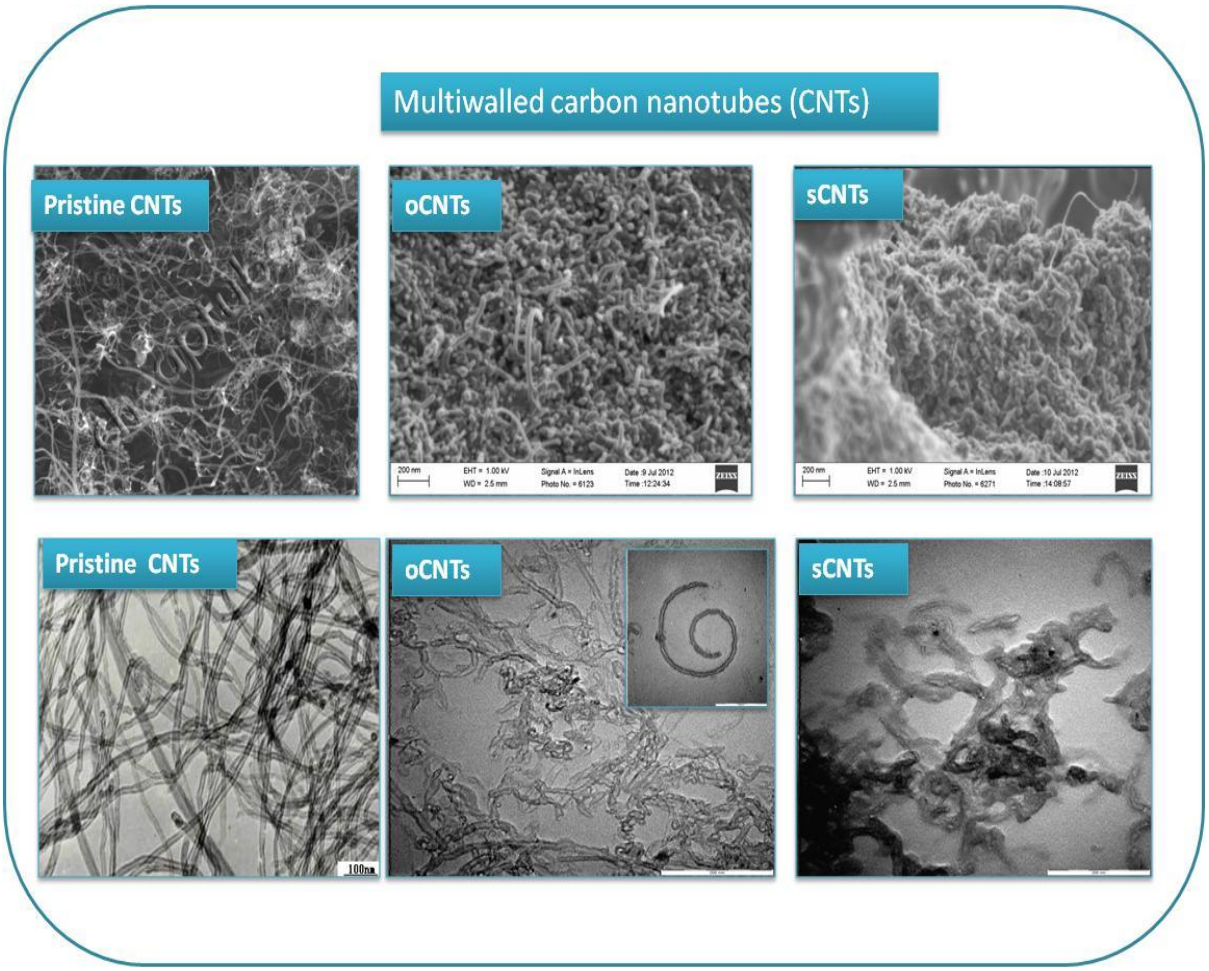

Figure 2.1: FESEM images of Pristine, carboxylate functionalised, and sulfonate functionalised MWCNTs produced by Cheap tubes Inc, USA (above) and the equivalent TEM images (below).

2.2.1b FTIR Spectra

The Fourier transform infrared spectroscopy (FTIR) data for both carboxylate (a) and sulfonate (b) functionalised nanotubes are shown in Figures 2.2 a and b. Figures 2.2 a clearly shows the characteristic features of the oxygen containing groups present on the nanotubes. The broad intense band 3447 cm^{-1} can be attributed to the stretching vibrational modes of the O-H group. The very weak bands at ~2888 and ~2333 cm^{-1} are signals of both symmetric and asymmetric C-H of aryl groups. The band at 1719 and 1587 cm^{-1} might result from C=O stretching vibrations from carboxylic and carbonyl groups. Aromatic or Aryl unsaturated rings are also attributed to these signals. The strong

band at 1225 cm^{-1} is O-H bending deformation in –COOH[4,5]. The peak at 1056 cm^{-1} is assigned to C-O stretching vibrations of epoxides, or cyclic ethers. Thus, FTIR clearly confirms the presence of oxygen containing groups like hydroxyl, carboxyl, and epoxy, firmly anchored on the carboxylate functionalised nanotubes.

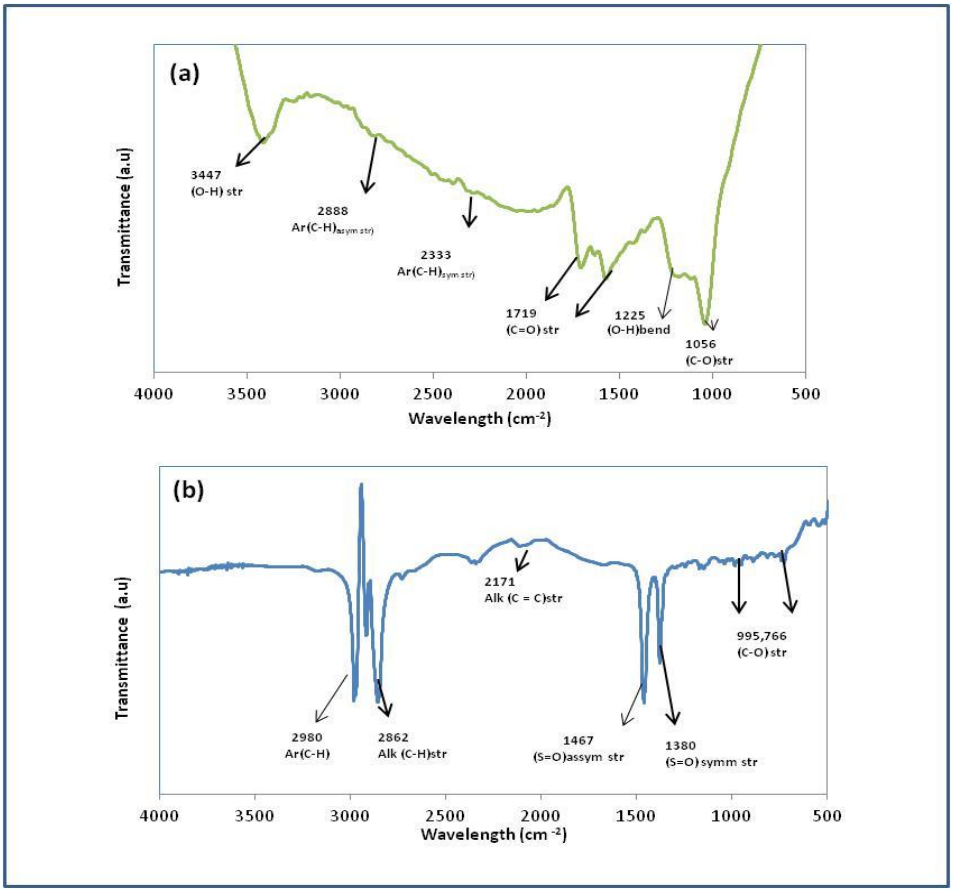

Figure 2.2: Infra-red spectra of carboxylate-functionalised (a) and sulfonated (b) MWCNTs.

Figure 2.2 b. shows two strong bands at 1467 and 1380 cm^{-1} which are the characteristic absorption bands of organic sulfonate groups; the bands correspond to the O=S=O asymmetric and O=S=O symmetric stretching motions respectively[6,7]. The intense bands at 2980 and 2862 cm^{-1} are attributed to C-H stretching motions of aromatic and unsaturated alkyl groups. The group of bands at 995, 888, 766 cm^{-1} are assigned to the C-O stretching vibrations of substituted pyridines or aromatic rings[4]

2.2.1c Raman Spectra

Figure 2.3 displays the Raman spectra of pristine MWCNT, o-MWCNT, and s-MWCNT. The tangential G- band and D- band of carbon nanotubes were observed in both the functionalised MWCNTs. The D-band reflects the disorder in the carbon nanotubes, thus increase in the intensity of the D-band is an indication of the rise in the defect density (amount of defects) in the CNTs or a decrease in the structural order of the carbon nanotubes bundles [8]. These defects can be brought about as a result of added functional groups, missing carbon atoms in the walls of the carbon nanotubes or the inhomogeneous decoration of the tube wall by functional groups [9].

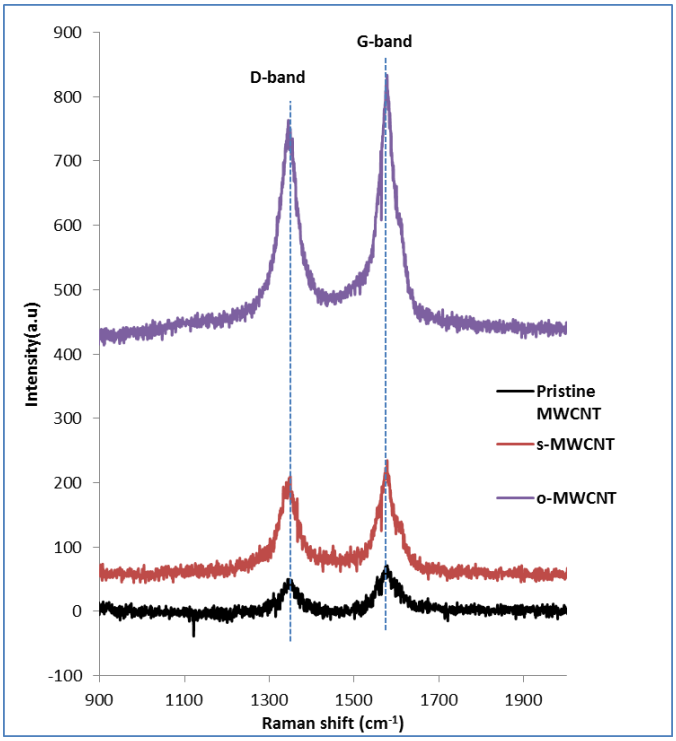

Figure 2.3: Raman spectra of Pristine MWCNT, carboxylate functionalised MWCNT (o-MWCNT) and sulfonate functionalised MWCNTs (s-MWCNTs).

From the spectra above, the D bands appear at ~1344 cm^{-1} for all three of the MWCNTs. There is an increase in the intensities of the two functionalized MWCNT bands compared with the raw pristine MWCNT, though the D-band intensity of the o-MWCNT is more intense than that of

s-MWCNT. Thus we can rightly deduce that there are more anionic surface groups anchored on the walls of the o-MWCNT than s-MWCNTs. G-band is the graphite band and appears at ~1577 cm^{-1} in all the spectra. A lack of change in the positions of G band in all the spectra means the electronic characteristics of both s-MWCNTs and o-MWCNTs are almost intact after functionalization procedures.

The degree of functionalization of the MWCNT walls can also be quantified using the D to G band intensity ratio (I_D/I_G). An increase in the (I_D/I_G) indicates an increase in number of defects[10]. o-MWCNT and s-MWCNT have 0.84 and 0.83 (I_D/I_G) ratios respectively. Both functionalized MWCNTs appear to have the same degree of functionalization, though a further increase of roughness of s-MWCNTs was expected as a result of the second acid treatment involved in its synthetic procedure.

2.2.2a FeCo@Fe supported on Carbon.

Although all the catalysts were synthesized by the microwave assisted techniques. Four different methods using different solvents, procedures and preparation time schemes were utilized to reduce Fe and Co salts for the synthesis of the precursor core alloy, FeCo@Fe. The various reduction techniques were modifications of synthetic procedures in literature.

Method A (Hydrogenation)

This technique involves a simple reduction method by hydrogenation[11]. 0.3650 g of $CoCl_2 \cdot 6H_2O$ (1.53 mmol) and 0.5302 g of $FeCl_2.4H_2O$ (2.7 mmol) were dissolved in 20 mL of triply-distilled deionized water, and then 150 mg of Vulcan XC-72 carbon support were dispersed in it. The suspension was ultrasonicated for about 30 mins, and then subjected to heating under continuous magnetic stirring until the solvent was completely evaporated to give smooth, thick slurry. The slurry was oven-

dried at 60°C, and then ground in an agate mortar to produce a fine dark and free-flowing powder. The FeCo/C powder was heated in a tube furnace at 300 °C under flowing H_2/Ar for 2 h to reduce the solid salt mixture, (Ar was initially purged into the furnace at 6cc/min for 15 mins before the start of the reduction process) and then annealed at 500 °C for 2 h to achieve the core-shell structure (FeCo@Fe/C). The fine powder was left to cool to room temperature under Ar atmosphere.

Method B (Seed mediated MW-ST)

This technique involves reduction of the reactants by microwave with EG as reductant and NaOH as a seeding agent[12]. 0.642 g of $CoCl_2 \cdot 6H_2O$ and 1.060 g of $FeCl_2.4H_2O$, mixed in a 1:2 mmol ratio were dissolved in 40 mL of EG solvent. 150 mg of Vulcan XC-72 carbon support was dispersed in the resulting solution. The suspension was ultra sonicated for about 30 min while 1.5 ml 1 M NaOH was added drop wise. The resulting suspension was poured into a microwave reactor vessel (quartz tube) and bubbled with argon for 15 mins before being capped and transferred into the microwave for the reduction reaction. The microwave equipped with a magnetic stirrer was operated at a maximum power of 800W and 80 bar pressure at 200 °C. Ramp/reaction/cooling times were 15/15/30 mins. The suspension was centrifuged and the resulting precipitate was repeatedly washed with deionised water to remove traces of unreacted EG and other impurities. The solid was dried in a vacuum oven at 150 °C. The dried FeCo alloy was then annealed under flowing Ar/H_2 gas at 500 °C for 2 h to achieve the core-shell structure (FeCo@Fe/C). The fine powder was left to cool to room temperature under Ar atmosphere.

Method C (MW-ST with PVP)

This technique also involves reduction by microwave but with EG as reductant and PVP as a capping agent and stabilizer[13]. 0.642 g of $CoCl_2 \cdot 6H_2O$ (2.7 mmol) and 1.060 g of $FeCl_2.4H_2O$ (5.3 mmol) were

dissolved in 40 mL of EG solvent and 150 mg of Vulcan XC-72 carbon support was dispersed in it. 0.26g PVP was then added as a stabiliser. The suspension was ultrasonicated for about 30 min. The resulting suspension was poured into a microwave reactor vessel (quartz tube) and bubbled with argon for 15 minss before being capped and transferred into the microwave for the reduction reaction. The microwave equipped with a magnetic stirrer was operated at a maximum power of 800W and 80 bar pressure at 200 ^{o}C. Ramp/reaction/cooling times were 15/10/30 mins. The suspension was centrifuged and the resulting precipitate was suspended in acetone under magnetic stirring for 15 mins, the resulting blue-colored acetone (indicating presence of excess PVP) was decanted after centrifuging. The procedure was repeated until clear acetone was obtained after decanting. A last washing was done with ether to completely remove acetone traces. The solid was dried then in a vacuum oven at 150 ^{o}C. The dried FeCo alloy was annealed under flowing Ar/H_2 gas at 500 ^{o}C for 2 h to achieve the core-shell structure and was left to cool to room temperature under Ar atmosphere.

Method D (MW-ST with PVP)

The same procedure in Method C above was used. The only difference was in the microwave reaction time for reduction which was increased to 15 minutes. Thus the ramp/reaction/cooling times were 15/15/30 minutes[13].

For clarification purpose, the core alloy obtained from hydrogenation will be denoted as FeCo@Fe/$C_{(H)}$, those obtained with micro wave irradiation with seeding agent using NaOH will be denoted as FeCo@Fe/$C_{(NaOH)}$ and those at 10 and 15 minutes microwave irradiation with PVP stabilizer will be denoted as FeCo@Fe/$C_{(PVP\ 10)}$ and FeCo@Fe/$C_{(PVP\ 15)}$ respectively.

2.2.2b FeCo@Fe@Pd Supported on Carbon

All nano core shell Pd catalyst samples (FeCo@Fe@Pd/C) were synthesized from their core alloys using the same microwave assisted solvothermal procedure. A different component was added to the mixture when using the core alloy from the 'seed mediated' technique.

Method A: **(MW-ST with PVP)**

To synthesize the FeCo@Fe@Pd/C nanoparticles, the as-prepared carbon supported of FeCo@Fe (0.2g) was thoroughly mixed with $PdCl_2$ (0.35g),- mixture of 1:3 mass ratio- in 40 ml EG. 0.26 g polyvinylpyrolidone (PVP) was added to the mixture. It was magnetically stirred for 30 mins in a sealed vessel under a layer of Ar. The black viscous mixture was then transferred into a microwave quartz vessel and subjected to rapid microwave irradiation using the microwave reactor which was operated at 500 W, 80 bars, and ~198 ^{o}C for 15 minutes. The ramp/reaction/cooling times were 15/15/30 minutes. The resulting product was repeatedly washed with acetone and deionised water to remove traces of ethylene glycol and other impurities, and then dried at 100 ^{o}C.

Method B: **(Seed mediated MW-ST)**

FeCo@Fe@Pd/C nanoparticles were prepared as described in Method B in 2.2.2a. The as-prepared carbon supported FeCo@Fe was thoroughly mixed with $PdCl_2$ (1:3) in 40 ml EG. The mixture was subjected to magnetic stirring while 1.5ml 1 M NaOH solution was added to it drop-wise. The mixture was bubbled with Ar, sealed and magnetically stirred for 30 minutes under a layer of Ar. The black viscous mixture was then transferred into a microwave quartz vessel and subjected to rapid microwave irradiation using the microwave reactor which was operated at 500 W, 80 bars, and ~198^{o}C for 15 mins. The ramp/reaction/cooling times were 15/15/30 mins. The resulting product was repeatedly washed with acetone and deionised water to remove traces of EG and other impurities, and then dried at 100 ^{o}C.

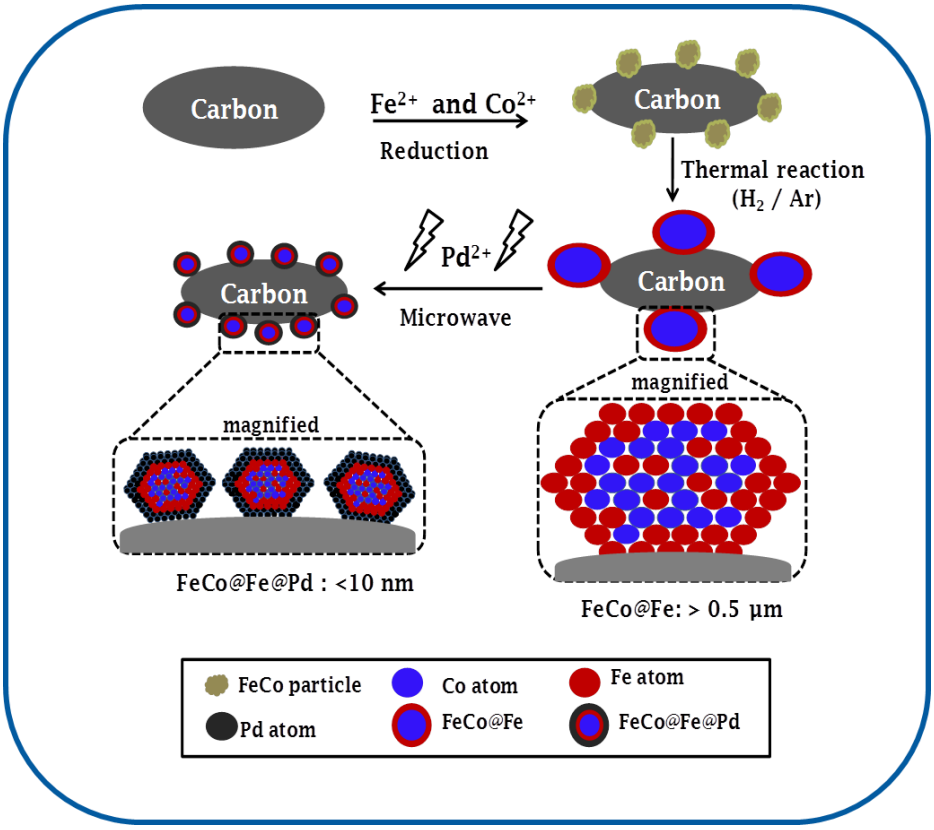

Scheme 2.1: General synthesis scheme of FeCo@Fe@Pd/C core shell nano catalysts.

2.2.3a FeCo@Fe Supported on Carbon Nanotubes

The reduction method by hydrogenation was used in synthesizing the Pd based nano core shell catalysts on both the hydroxyl (CNT-OH) and sulfonate (CNT-SO_3) functionalised carbon nanotubes. Equimolar mixture of $CoCl_2 \cdot 6H_2O$ (0.6424 g) and $FeCl_2.4H_2O$ (0.5302 g) were dispersed in hydroxyl functionalised carbon nanotubes (CNT-OH) and sulphonate carbon nanotubes (CNT-SO_3) respectively. The suspension was ultrasonicated for about 30 min, and then subjected to heating under continuous magnetic stirring until the solvent was completely evaporated to give smooth, thick slurry. The slurry was oven-dried at 60° C, and then ground in an agate mortar to give a fine dark and free-flowing powder. The obtained FeCo/CNT –OH and FeCo/CNT –SO_3 powder was heated in a tube furnace at 300 °C under flowing H_2/Ar for 2 h, and then annealed at

500°C for 2 h, and then cooled to room temperature under Ar atmosphere to achieve the core-shell structure FeCo@Fe/CNT-OH and FeCo@Fe/CNT-SO_3 respectively.

2.2.3b FeCo@Fe@Pd Supported on Carbon Nanotubes

The palladium decorated core shell alloys FeCo@Fe@Pd/CNT-OH and FeCo@Fe@Pd/CNT-SO_3 were obtained using a mixture of the as-prepared FeCo@Fe/CNT-OH or FeCo@Fe/CNT-SO_3 and $PdCl_2$ in a 1:3 mass ratio. 40 ml EG was added to the mixture with 0.26g PVP. The black suspension was magnetically stirred for 30 minutes and subjected to rapid microwave irradiation using the Anton Parr Synthos 3000 microwave reactor which was operated at 500 W, 80 bars, and ~198°C for 15 mins. The resulting product was repeatedly washed with acetone and deionised water to remove traces of ethylene glycol and other impurities, and then dried at 100 °C. Pd/CNT-OH and Pd/CNT-SO_3 nanoparticles of same Pd mass loading as the core-shell were also synthesized using the same microwave procedure. The dried catalysts were used without further treatment. These catalysts were used as 'control catalysts' in the experiments.

2.2.4 NanoFeTSPc Supported on Carbon Nanotubes

The procedure for the nanoFeTSPc was a modification of a previous work using DODA for making organo-soluble metallophthalocyanines[14]. 123g (0.34 mol) of CTAB was dissolved in 5 mL of deionised water and subjected to ultra-sonication for about 1 h. 80g (0.08mol) of Na_4FeTSPc was then dissolved in 2 mL 10^{-3} M NaOH solution, and both solutions were mixed and stirred over a magnetic stirrer at ~ 50 °C for 1 h. The resulting hot paste-like crude product was dispersed with 20 mL warm water (~ 40 °C), suction-filtered and washed with copious amount of warm water several times, and finally with pentane. The dark-green colored crystalline product was oven-dried at 70 °C, to obtain hydrophobic FeTSPc nanoparticles, abbreviated as nanoFeTSPc (Scheme 2.2). 2 mg of the as

prepared nanoFeTSPc was dissolved in 50 mL ethylene glycol in a 250 ml Erlenmeyer flask. 40 mg of hydroxyl and sulfonate functionalised-MWCNTs was then added respectively. The mixtures were ultrasonically dispersed for 1 h. Each of the solution was poured in a quartz vessel and transferred into a microwave reactor which was operated at 800W and at a temperature of 190 °C for 60 s (Scheme 2.3). The ramp/reaction/cooling time was 15/1/45 mins. The resulting suspension was separated by filtration and the obtained residue was washed with acetone and deionised water. It was then dried at 110 °C overnight in an oven. The final products have been abbreviated as *o*MWCNT-nanoFeTSPc (nanoFeTSPc on CNT-OH) and *s*MWCNT (nanoFeTSPc on CNT-SO_3).

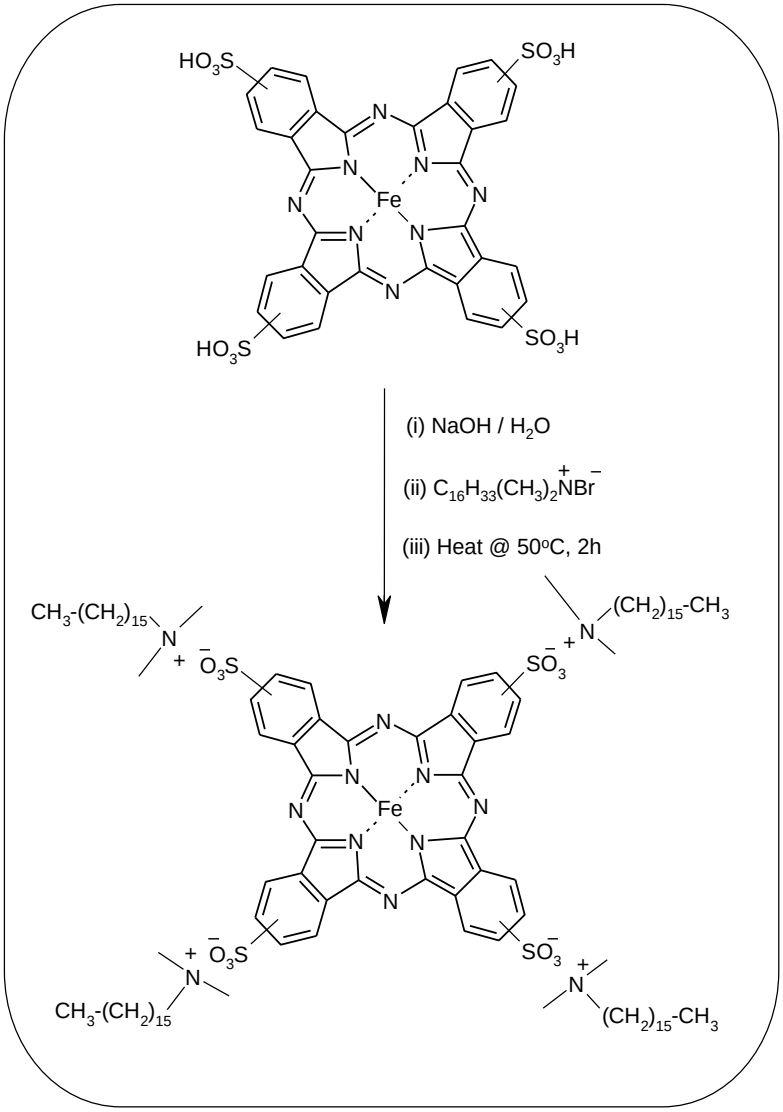

Scheme 2.2: Synthesis of Hydrophobic nanoFeTSPc

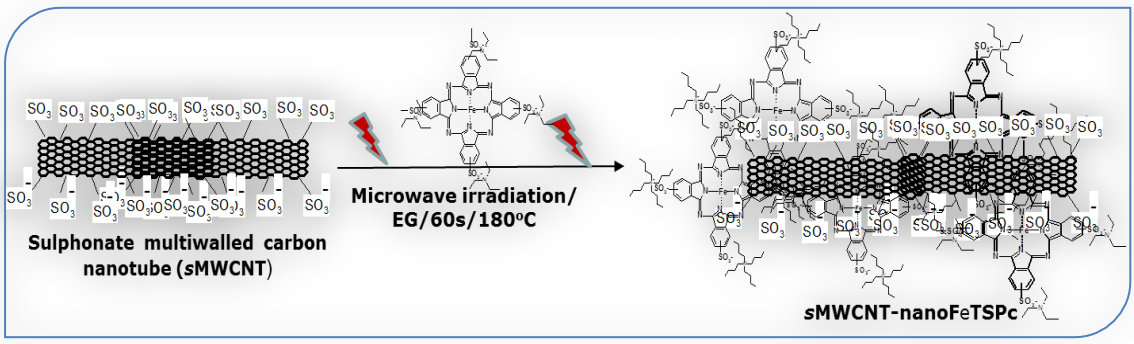

Scheme 2.3: Incorporation of nanoFeTSPc on *s*MWCNT

2.3 Instruments and procedures.

2.3.1 UV Visible

The UV–visible spectra were recorded using a Cary 300 UV–Visible Spectrophotometer, driven by Varian software version 3.0.

Few granules of the samples were dissolved in organic solvents and transferred into UV quartz corvettes. They were placed in allocated compartments in the UV spectrophotometer and measured against the pure organic solvents (which act as the references).

2.3.2 Raman

Raman spectroscopy data were collected using a Jobin–Yvon Horiba TX 6400 micro-Raman spectrometer equipped with a triple monochromatic system to eliminate contributions from Rayleigh scattering. The samples were analysed with a 514-nm argon excitation laser (1.5 mW laser power on the sample to avoid thermal effects), using a 509 objective with acquisition time of 120 s. The Raman wavelength range was from 1200 – 3200 cm^{-1}.

2.3.3 FTIR

Fourier transmission infrared spectroscopy (FTIR) analyses were carried out using a Bomem (Hartmann & Braun), model MB-102 spectrophotometer. The functionalised MWCNTs –CNT-OH and CNT-SO_3, FeTsPc and nanoFeTSPc were analysed as KBr pellets. For the KBR pellet preparation, a few granules of the samples were mixed with well dried KBr crystals (0.15 g). The mixture was ground until a smooth powder is formed. The resulting powder was then scooped in the mould to cast them into transparent discs.

2.3.4 XRD

Catalysts were analysed on a PANalytical X'Pert Pro powder diffractometer X' Celerator and a variable divergence and receiving slits with Fe filtered Co Kα radiation. The phases were identified using X'Pert Highscore plus software. The crystallite size and lattice parameter of the nano catalysts

were calculated from the Pd (220) diffraction peak fitted with the Gaussian function. The nanoparticles were prepared for X-ray diffraction (XRD) analysis using a back loading preparation method. Samples with smaller quantities were prepared using a zero background sample disc with a top loading preparation method.

2.3.5 HRTEM

Transmission electron microscopy (TEM) images were taken on a JEOL JEM 2000EX microscope at an accelerating voltage of 200kV. High resolution transmission electron microscopy (HRTEM) images and selected area electron diffraction (SAED) patterns were obtained on a Tecnai F-20 instrument equipped with Gatan high-angle annular dark field detector (HAADF) field emission high-resolution scanning transmission electron microscope (STEM) operated at an accelerating voltage of 200kV, Gun extraction voltage was 4500V. Energy dispersive spectroscopy (EDS) line scan was also performed using this instrument in the STEM mode. Specimens for all of the TEM analyses were prepared by dispersing the nanoparticles in methanol, sonicating for 1 min in order to ensure adequate dispersion of the nanostructures, evaporating one drop of the solution onto 300 mesh Cu grid, coated with a lacey carbon film. For specimens incorporated or embedded on carbon nanotubes, HRTEM images were taken using another instrument: High resolution transmission electron microscopy (HRTEM) images were taken on JEOL ARM200F double aberration corrected high resolution transmission electron microscope (HRTEM) with field emission gun (FEG), and energy dispersive X-ray spectrometry system (EDS), with a scanning transmission electron microscopy (STEM) attachment, high angle annular dark-field STEM detector (HAADF), electron energy loss spectroscopy (EELS) system and two spherical aberration corrected (Cs) lenses giving the HRTEM a point resolution of 0.11nm and a STEM resolution of 0.08nm. Specimens for all of the HRTEM analyses were prepared by dispersing the nanoparticles in methanol, sonicating for about 2 min in

order to ensure adequate dispersion of the nanostructures. A 300 mesh Cu grid, coated with a lacy carbon film was carefully dipped into each suspension of nanoparticles and air dried. This was done to avoid an excessive agglomeration of the nanoparticles on the grids.

2.3.6 FESEM

A field emission scanning electron microscope (FESEM Zeiss-Leo DSM982) was used in obtaining scanning electron microscopy (SEM) images. Images were obtained at a low accelerating voltage (EHT - 1.00kV) and a working distance (WD) of 2-5 mm using the 'IN-LENS' detector. The nanoparticle were coated with 2/3 layers of carbon before the images were taken.

2.3.7 ICP-AES

Inductively coupled plasma atomic emission spectroscopy (ICP-AES) was carried out with an Intrepid Iris instrument (Thermo Elemental). Each sample (50 mg) was treated in a microwave heated digestion bomb in sealed PTFE vessels with concentrated HNO_3 (2.0 mL) and 98% H_2SO_4 (2 mL). The heating program comprised some preheating steps and a final 10 min digestion step at 220 °C. The resulting residual solutions were diluted with water to constant volume. The solutions were then analysed for the metal content.

2.3.8 NMR

$^{13}C\{^{1}H\}$-Nuclear magnetic resonance (NMR) spectroscopy was carried out using Bruker Avance DRX-400 Mhz NMR spectrometer with chemical shifts relative to external tetramethylsilane. The calibration curves for the quantitative analysis were obtained using authentic samples of the various products in the appropriate range of concentrations with 1, 4-dioxane as internal standard. 40.5 µL 1, 4-dioxane was added to 2 ml fuel cell exhausts in a clean test tube. 500 µL was extracted from the mixture with a micro syringe and transferred into NMR tube. The cover tube was

properly sealed to avoid contact with air before being transferred to the NMR spectrometer for analysis.

2.3.9 Half Cell Electrochemical Experiments

All half-cell electrochemical experiments were carried out using an Autolab Potentiostat PGSTAT 100 (Eco Chemie, Utrecht, and The Netherlands) driven by version 4.9 of GPES and FRA software. A glassy carbon working electrode (GCE) was used for cyclic and linear voltammetry (CV and LSV) testing, (Bioanalytical Systems (BAS), active area 3 mm).

Cyclic voltammograms of the modified electrodes may display mixed diffusion (a mixture of thin layer and semi-infinite diffusion) as a result of the diffusion through the Nafion film present in the catalyst ink and due to the presence of MWCNTs used as substrates in some of the catalysts. This has been termed the "thin layer effect" and has also been observed by other authors[15,16]. The thin layer effect will result in a double shift position of the CV and may affect the observed onset potentials or peak potentials exhibited in the voltammograms. But as equal microliters of each catalyst ink were deposited on the electrode surface for each test, the layers of ink have fairly the same thickness and one can infer that the observed peak positions of the voltammograms reflect the relative activity of each catalyst.

Scan rate studies of the catalysts were performed with CVs at increasing scan rate speed. The Randles-Sevčik analysis was carried out using the raw CV data obtained at each scan rate with no background correction. Hence, the observed points from the plots do not trace back to the zero origin but all exhibited a positive intercept.

Low concentration of the electrolyte was used in some of the experiments (e.g., 0.5 M KOH/0.5 alcohol) which means that migration could also be playing a role in the kinetic studies.

The test for the ORR activity of the catalysts was done using a rotating disk electrode (RDE) (Autolab Netherlands, active areas 5mm). A Pt rod and Ag|AgCl (saturated 3 M KCl) were used as a counter and reference electrode, respectively.

Electrochemical impedance spectroscopy (EIS) measurements were performed with Autolab Frequency Response Analyser (FRA) software between 100 kHz and 10 mHz with the amplitude (rms value) of the AC signal as 10 mV. All the tests for alcohol oxidation were performed in high purity de aerated saturated electrolyte solutions by bubbling with high purity nitrogen gas. For the ORR activity test, linear scans were conducted at different rotatory speeds in 0.1 M KOH electrolyte solutions bubbled with high purity O_2.

2.4 Fuel Cell Experiments

2.4.1 Passive Fuel Cells

A home-made, oxygen-breathing DAFC was used in this study. The device is shown in Fig 2.4. The fuel cell hardware was made from *Plexiglas* and the electricity collectors were plated with gold. The volume of the anode compartment was ca. 20–25 mL for an actual fuel solution of 13–15 mL. For a reliable evaluation of the oxidation products, the anode compartment was sealed under a nitrogen atmosphere, whereas the cathode was exposed to air. The operating temperatures were in the range of 15 ^{o}C – 18 ^{o}C. The anode catalysts cell performance was evaluated by means of an ARBIN BT-2000 5A four channels instrument.

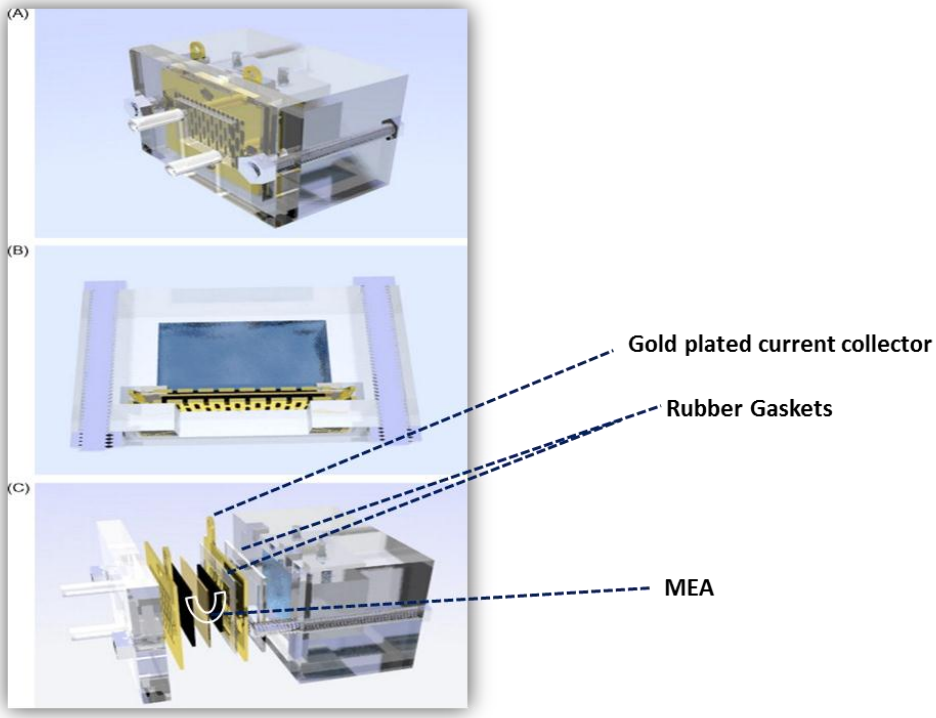

Figure 2.4: Home-made oxygen-breathing DAFC used showing the complete view (A), Top view showing the anode compartment (B) and the expanded view showing the Membrane electrode assembly (MEA) (C)[20] (copy right ICCOM)

2.4.2 Active Fuel Cells

The active DAFC were purchased from Scribner-Associates (USA) (25 cm^2 fuel cell fixture) and were modified with gold-plated current collectors and titanium end plates to tolerate the alkaline conditions used in this work. The effective electrode area was 1 cm^2. The fuel (solutions containing 10 wt. % MeOH/EtOH or 5 wt. % EG/GLY in 2 M KOH) was delivered to the anode at 4 mL min^{-1} by a micro pump. The oxygen flow rate was 200 mL min^{-1} and a relative humidity (RH) of 100%. The temperature of the cell under working conditions was controlled at (25, 40, 60, and 80) ^oC, respectively, by a thermocouple positioned inside the end plates.

The stages of the fuel cell assembly are shown in a pictorial scheme in the images of Fig 2.5. Steps (i) to (vi) correspond to:

(i) Placing anode CL with GDL, (i.e. catalyst on nickel foam) on the Titanium (serpentine) flow field plates.

(ii) Overlaying the Anion exchange membrane A-201 Tokouyama (gasket is placed in between the layer (i) and (ii))

(iii) Completing the MEA assembly by overlaying the cathode CL with GDL (FeCo catalysts on carbon cloth) on the membrane.

(iv) Sealing up the fuel cell fixture (another flow field plate was placed over the cathode before sealing).

(v) Attaching the other operating accessories to the fixtures, the heating rods, temperature regulators, oxygen in lets, and fuel inlet into the anode through the micro pump etc.

(vi) Connecting the whole set up to the DAFC to run the experiment.

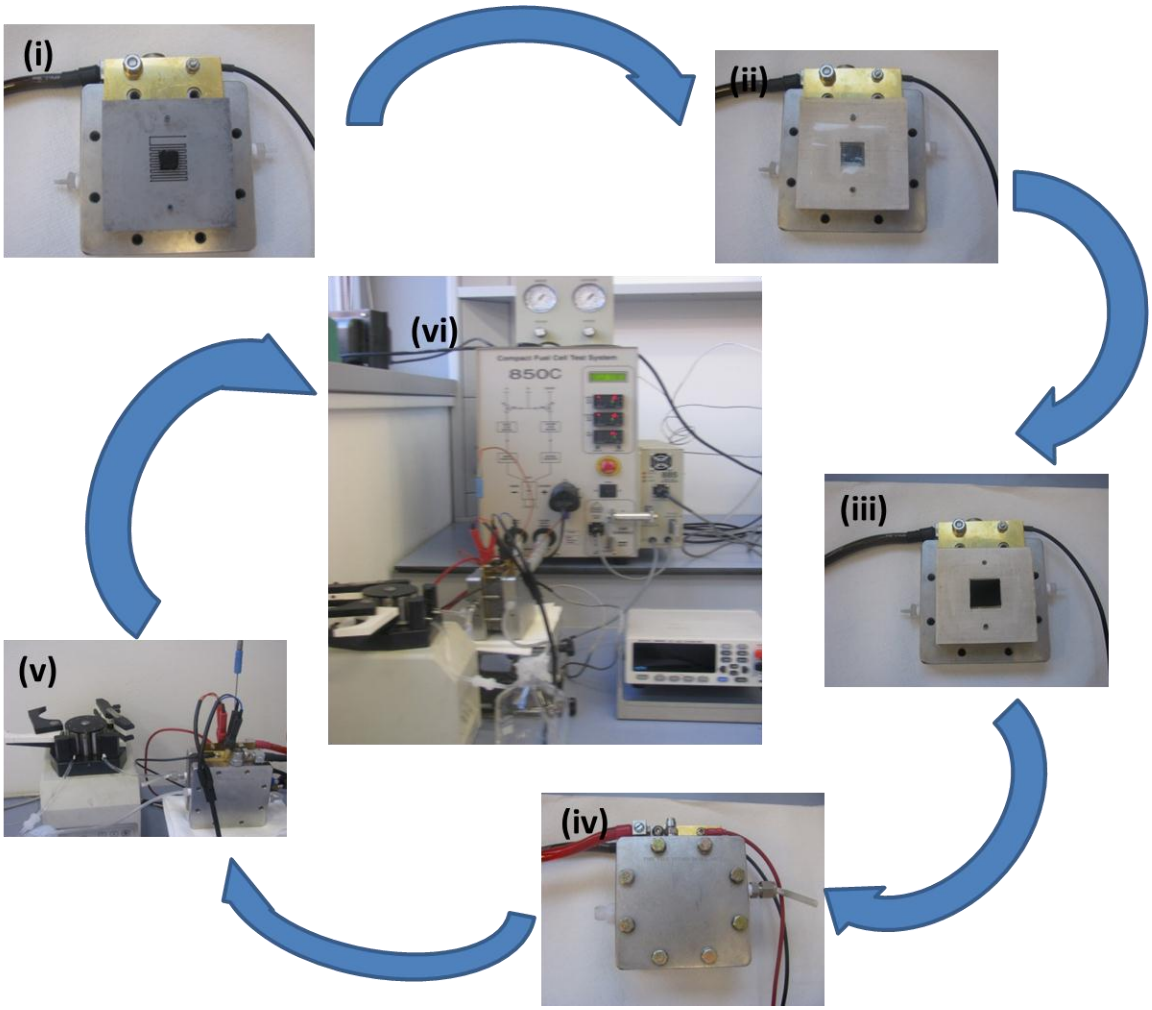

Figure 2.5: Stages of assembly of components for the Active fuel cell tests

2.5 Electrode Modification Processes

2.5.1 Glassy Carbon Electrode (GCE)

1.0mg of the nanoparticle was dispersed in 1.0ml of EtOH and 100µL of 5% Nafion was added. The mixture was ultrasonicated for 3 min to make a uniform ink. The working electrode was prepared by dropping 10 µL of the catalyst ink on the GCE and allowing it to dry in an oven at 60^{o}C. The Pd loading on each electrode was maintained at 1.3±1µg. Before each measurement the glassy carbon working electrode was polished to a mirror finish using Alumina slurry (nanopowder Aldrich) and then cleaned by ultrasonic stirring in ethanol and acetone for 3 mins respectively.

2.5.2 Rotatory Disc Electrode (RDE)

A rotating disk GCE (Autolab Netherlands, 5 mm diameter) was used for all RDE experiments. The same pre-treatment procedures for the use of the glassy carbon electrode (GCE) are followed while using the RDE. 0.1 M KOH solution used for all the ORR experiments were also initially de aerated with high purity N_2 and later aerated with high purity O_2 to carry out the experiments.

2.6 MEA

2.6.1 Passive MEA

The MEAs (membrane electrode assembly) for the passive monoplanar cells were fabricated using a commercial Tokuyama A-201 anion-exchange membrane and cathodes containing a proprietary Fe-Co/C electro catalyst on carbon cloth[21] . The anode was made using a 5.13 cm^2 nickel foam plate onto which was deposited the appropriate amount of a dense catalyst prepared by dispersing the solid catalyst into minimum amount of water (no binder was added). The membrane was conditioned in a saturated KOH solution for 1 min before assembling the MEA. The MEA was then assembled by mechanically pressing anode, cathode, and membrane[22]. Some FESEM images of the Gas diffusion layer (GDL) of the MEA comprising core shell nanocatalysts, FeCo@Fe@Pd, incorporated on carbon and carbon nanotubes can be seen in Figs 2.6 (a,b) and (a',b') respectively and their equivalent monometallic Pd nanocatalysts incorporated on the same substrates in Figs 2.7 (a,b) and (a',b') are also shown.

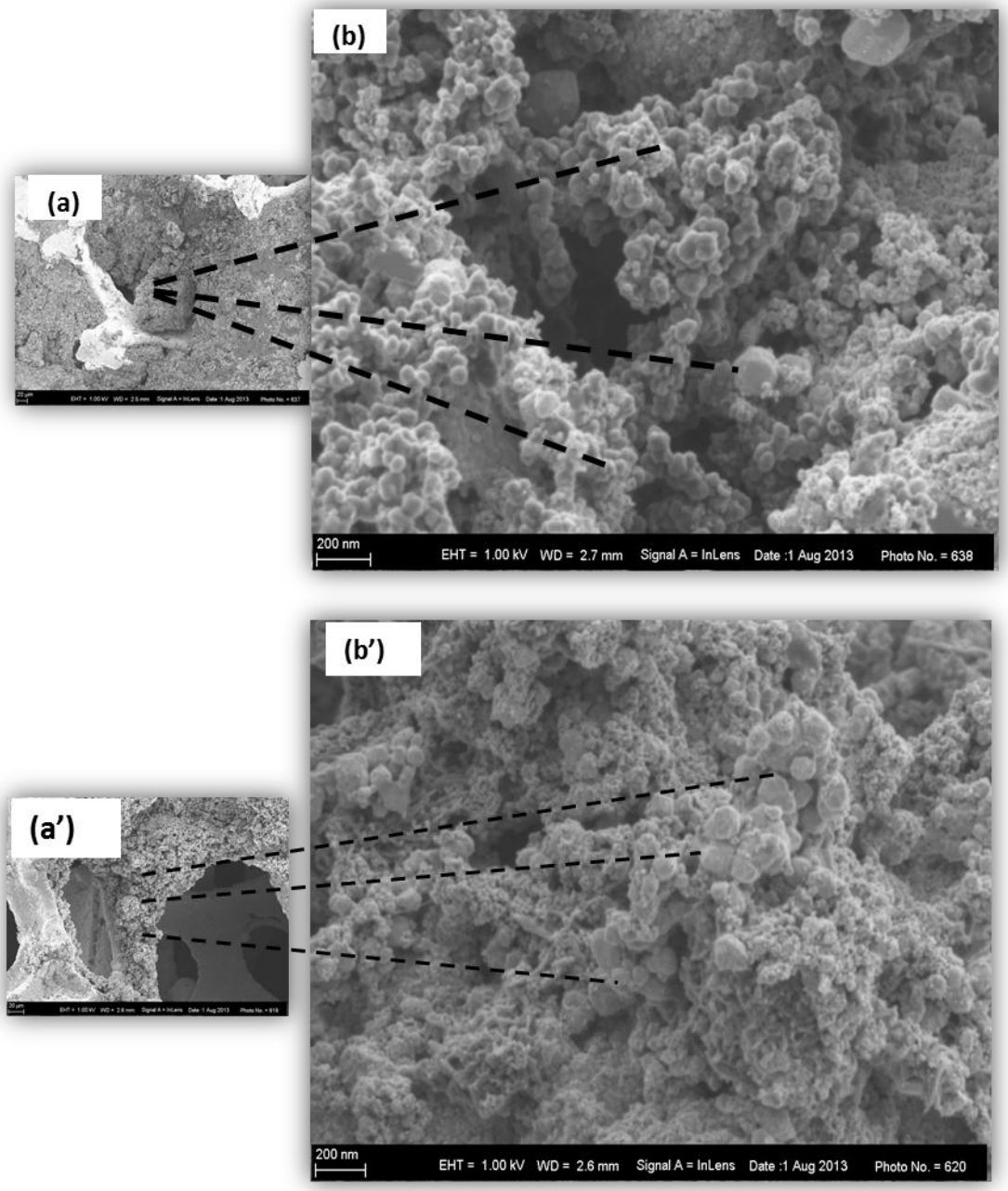

Figure 2.6: FESEM images of the MEA anode catalysts [CL on GDLs] of Passive Fuel cells – FeCo@Fe@Pd/C on nickel foam (a and b) and FeCo@Fe@Pd/CNT-OH on nickel foam (a' and b')

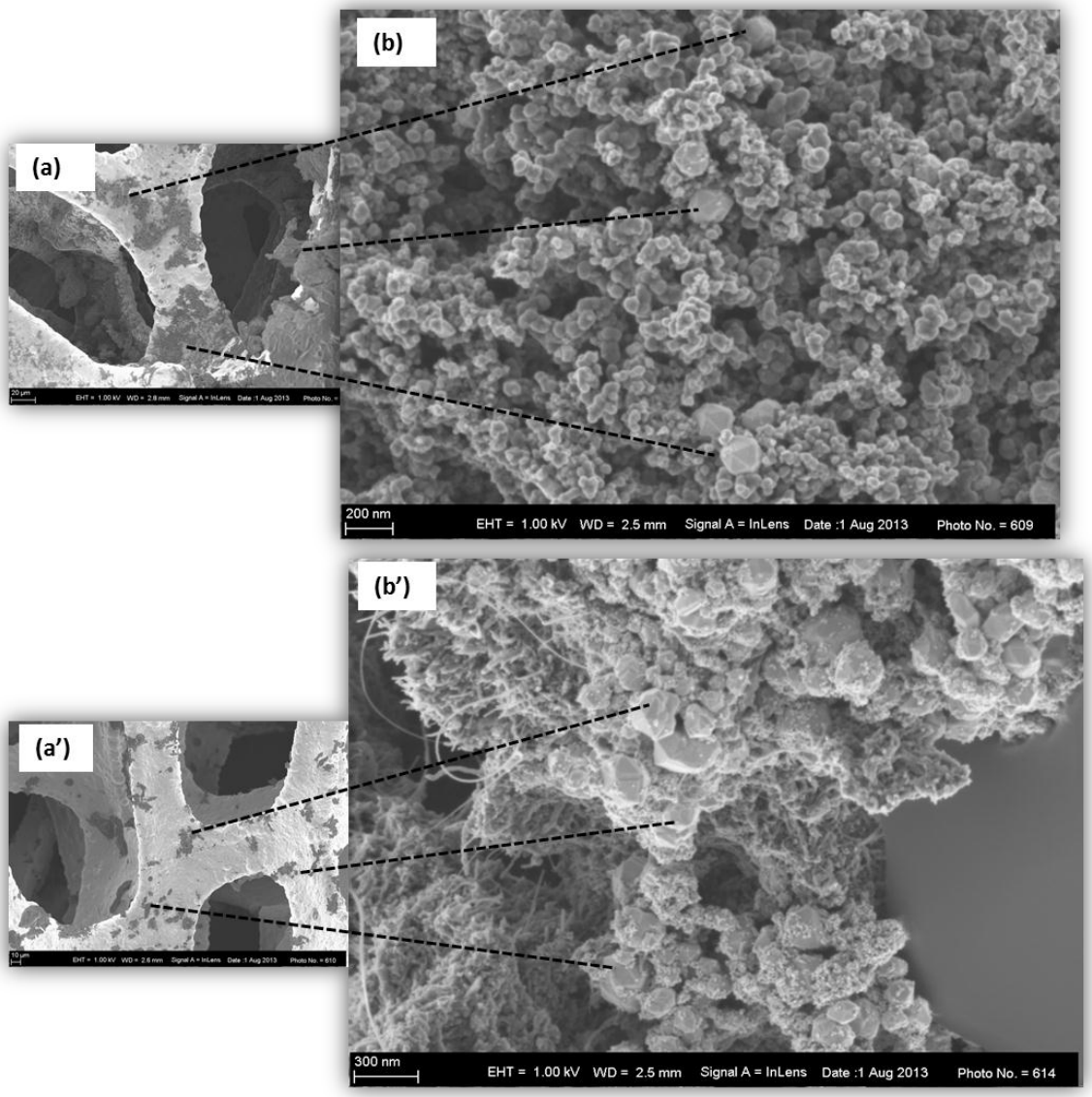

Figure 2.7: FESEM images of the MEA anode catalysts [GDLs] of Passive Fuel cells – Pd/C on nickel foam (a and b) and Pd/CNT-OH on nickel foam (a' and b')

2.6.2 Active MEA

The active MEA was fabricated by mechanically pressing the anode (nano catalysts on nickel foam with an area of 1 cm^2), commercial Tokuyama A-006 anion-exchange membrane and cathodes (Fe–Co/C electrocatalyst on carbon cloth). A dense anode ink was prepared by mixing the powdered catalyst with an aqueous dispersion of polytetrafluoroethylene (PTFE) to produce a binder loading of 5 wt.%. Some FESEM images of GDL

comprising core shell nanocatalysts FeCo@Fe@Pd/CNT-OH and Pd/OH respectively on Nickel foam used in the Active Fuel cell tests are shown in Figures 2.8 and 2.9 below:

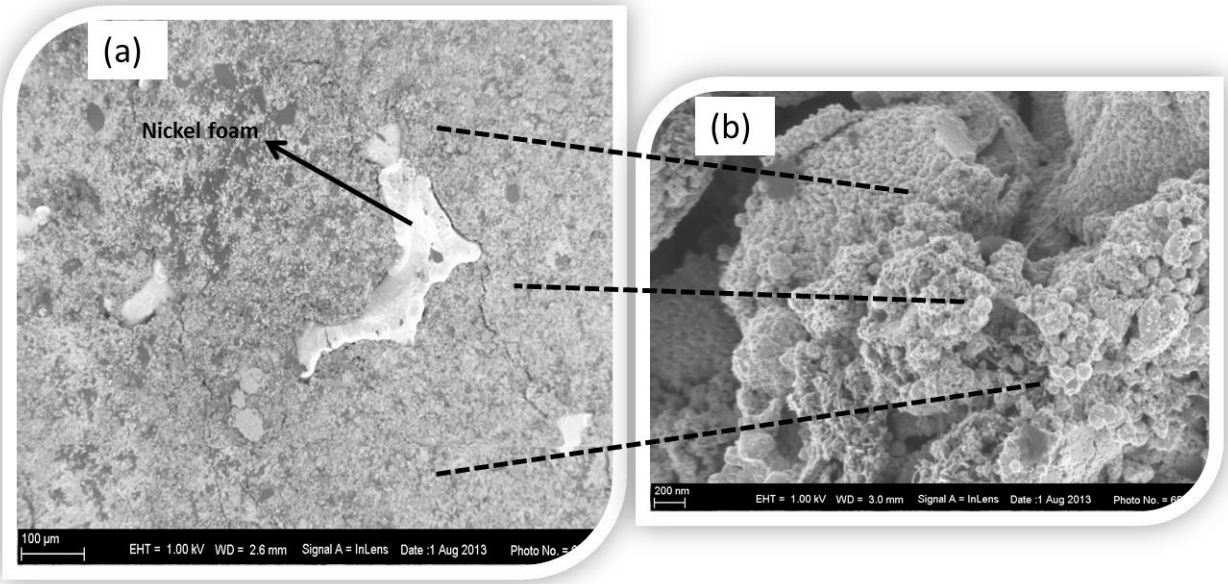

Figure 2.8: FESEM images of CL on GDLs for active fuel cell - Nickel foam containing FeCo@Fe@Pd/CNT-OH catalysts mixed with PTFE binder

One sees a very compact GDL with the anode catalysts well filled in all the orifices of the Nickel foam in Fig 2.8 a. The core shell nanocatalysts are mostly of small sizes and are seen to be properly incorporated with the nanotubes and well bound with the PTFE binder (Fig 2.8 b). Some loose parts reveal the icosahedral shape of palladium.

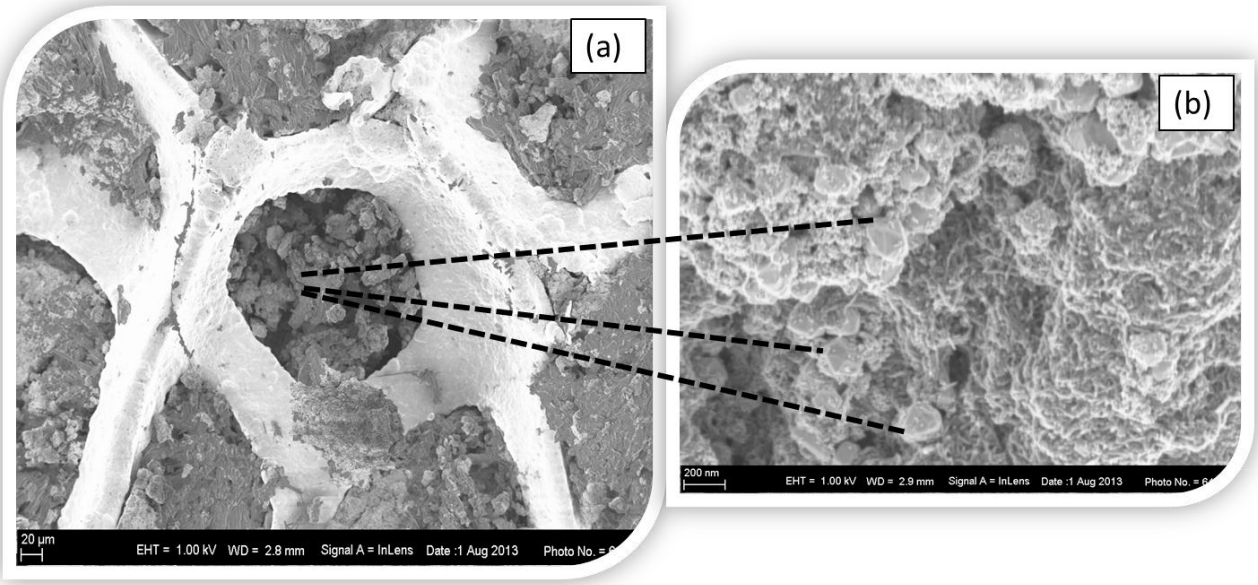

Figure 2.9: FESEM images of GDLs for active fuel cell-Nickel foam containing Pd/CNT-OH catalysts mixed with PTFE binder.

The big sizes of the Palladium nanocatalysts are very obvious in Fig 2.9 b. Their icosahedral morphologies are also well highlighted. The particles also appear quite lose in spite of the PTFE binder mixed with it (Fig 2.9 a). This may be as a result of the big sizes of the particles (> 100nm)

2.7 References

(1) Siswana, M. P.; Ozoemena, K. I.; Nyokong, T. *Electrochim. Acta* **2006**, *52*, 114–122.

(2) Sun, Z.-P.; Zhang, X.-G.; Liang, Y.-Y.; Li, H.-L. *J. Power Sources* **2009**, *191*, 366–370.

(3) Morozan, A.; Campidelli, S.; Filoramo, A.; Jousselme, B.; Palacin, S. *Carbon N. Y.* **2011**, *49*, 4839–4847.

(4) Günzler, H.; Gremlich, H.-U. *IR spectroscopy: an introduction*; 1st ed.; Wiley-VCH, 2002; p. 361.

(5) Gao, B.; Yuan, C.; Su, L.; Chen, S.; Zhang, X. *Electrochim. Acta* **2009**, *54*, 3561–3567.

(6) Silverstein, R. M.; Webster, F. X.; Kiemle, D. *Infrared spectrometry*; 7th ed.; Wiley New York, 2005; Vol. 7, p. 512.

(7) Solomons, T. W. G.; Fryhle, C. B. *Organic chemistry*; 10th ed.; John Wiley & Sons, Inc., USA, 2010; p. 1280.

(8) Zhang, R.; Wang, X. *Chem.MaterMater* **2007**, *19*, 976–978.

(9) Kim, U. J.; Furtado, C. a; Liu, X.; Chen, G.; Eklund, P. C. *J. Am. Chem. Soc.* **2005**, *127*, 15437–15445.

(10) Jeong, Y.; Kim, J.; Lee, G. **2010**, 1–6.

(11) Wang, D.; Xin, H. L.; Yu, Y.; Wang, H.; Rus, E.; Muller, D. a; Abruña, H. D. *J. Am. Chem. Soc.* **2010**, *132*, 17664–17666.

(12) Sarkar, a.; Vadivel Murugan, a.; Manthiram, a. *Fuel Cells* **2010**, *10*, 375–383.

(13) Galletti, A. M. R.; Antonetti, C.; Venezia, A. M.; Giambastiani, G. *Appl. Catal. A Gen.* **2010**, *386*, 124–131.

(14) Sanchez, M.; Fache, E.; Bonnet, D.; Meunier, B. *J. Porphyr. Phthalocyanines* **2001**, *05*, 867–872.

(15) Sims, M. J.; Rees, N. V.; Dickinson, E. J. F.; Compton, R. G. *Sensors Actuators B Chem.* **2010**, *144*, 153–158.

(16) Kozub, B. R.; Rees, N. V.; Compton, R. G. *Sensors Actuators B Chem.* **2010**, *143*, 539–546.

(17) Compton, RG, B. C. *Understanding Voltammetry*; 2007; pp. 249–253.

(18) Coutanceau, C.; Croissant, M. .; Napporn, T.; Lamy, C. *Electrochim. Acta* **2000**, *46*, 579–588.

(19) Schmidt, T. J.; Gasteiger, H. A.; Behm, R. J. *J. Electrochem. Soc.* **1999**, *146*, 1296–1304.

(20) Bambagioni, V.; Bianchini, C.; Marchionni, A.; Filippi, J.; Vizza, F.; Teddy, J.; Serp, P.; Zhiani, M. *J. Power Sources* **2009**, *190*, 241–251.

(21) Bambagioni, V.; Bianchini, C.; Filippi, J.; Lavacchi, A.; Oberhauser, W.; Marchionni, A.; Moneti, S.; Vizza, F.; Psaro, R.; Dal Santo, V.; Gallo, A.; Recchia, S.; Sordelli, L. *J. Power Sources* **2011**, *196*, 2519–2529.

(22) Marchionni, A.; Bevilacqua, M.; Bianchini, C.; Chen, Y.-X.; Filippi, J.; Fornasiero, P.; Lavacchi, A.; Miller, H.; Wang, L.; Vizza, F. *ChemSusChem* **2013**, *6*, 518–528.

PART II: RESULTS AND DISCUSSION

Chapter 3*

EXPLORING THE SYNTHETIC TECHNIQUES OF FeCo@Fe@Pd CORE-SHELL NANOCATALYSTS

* The following publication resulted from part of the research work presented in this chapter and it is not referenced further.

1. O.O. Fashedemi, Basil Julies and K.I. Ozoemena, "Synthesis of Pd-coated FeCo@Fe/C core-shell nanoparticles: microwave-induced 'top-down' nanostructuring and decoration". *Chem. Commun,* **2013**, 49, 2034-2036.

3.1 Synthetic Methods for FeCo@Fe and FeCo@Fe@Pd Nanocatalysts

Three main techniques were studied for the reduction of the mixture of iron and cobalt salts for the synthesis of FeCo alloy. A summary of the procedures for reduction are:

i) Hydrogenation: This involved direct heating of the dried slurry of the liquid mixture of the two salts with Vulcan carbon over H_2/Ar gas.

ii) Seed mediated microwave induced solvothermal reduction (MW-ST): NaOH served as the seeding agent and was added to a mixture of the two salts and Vulcan carbon in water.

iii) Microwave induced solvothermal (MW-ST) with PVP as stabilizers: This procedure also involved reduction by microwave irradiation. In this case, the salts and Vulcan carbon are mixed in EG solvent which served as the reducing agent, while PVP served as a capping agent and stabilizer.

iv) The fourth procedure was a modification of (iii). The difference is in the microwave irradiation period. It was carried out for 15 mins as against 10 mins in the previous process.

All the three main procedures were modifications of established techniques in literature[1–3].

The as-synthesised reduced FeCo alloys were further subjected to annealing under the same conditions to produce FeCo@Fe/C core shell alloys. For clarification purpose, the core–alloy obtained from hydrogenation will be denoted as FeCo@Fe@/C $_{(H)}$, those obtained with microwave irradiation with seeding using NaOH will be denoted as FeCo@Fe/C$_{(NaOH)}$ and those at 10 and 15 mins microwave irradiation with PVP will be denoted as FeCo@Fe/C$_{(PVP\ 10)}$ and FeCo@Fe/C$_{(PVP\ 15)}$, respectively. The Pd based FeCo@Fe@Pd core shell nanocatalysts were all synthesized using the microwave assisted technique.

The capping agents and/ stabilisers added to the solvents were also different depending on the origin of the FeCo@Fe core shell alloy. FeCo@Fe@Pd/C core shell nanocatalysts from FeCo@Fe@/$C_{(H)}$, FeCo@Fe/$C_{(PVP\ 10)}$ and FeCo@Fe/$C_{(PVP\ 15)}$ cores were all synthesized using a mixture of the core alloys and Pd chloride salts in EG with PVP as capping agent and exposed to 15 mins microwave irradiation. FeCo@Fe@Pd/C core shell nanocatalysts from FeCo@Fe/$C_{(NaOH)}$ was synthesized in EG with NaOH without the addition of any capping agent. It was also exposed to 15 mins microwave irradiation. The FeCo@Fe@Pd/C core shell nano catalysts were also abbreviated corresponding to the origin of their core alloys.

Pd has been alloyed with a number of non-noble elements. By using density functional theory (DFT) Shao et al[4] established a 'volcano' relationship between ORR activity and a variety of Pd and Pt based alloy in acidic medium where a 'Pd –skin on Pd_3Fe' alloy was found to be at the top of the volcano. The lattice contraction induced on Pd overlayer on the Pd_3Fe alloy as a result of the lattice mismatch between Pd and Fe originated the enhanced catalytic activity of the 'Pd –skin on Pd_3Fe' alloy with respect to other alloys tested. A similar principle has informed the choice of the core – alloys (FeCo) used in this study. A smaller atom (Co) has been incorporated into Fe lattice to form a 'Fe-skin on FeCo' alloy (FeCo@Fe); this alloy is expected to have an enhanced Fe surface. FeCo@Fe alloy incorporated in Pd lattice through the decoration of the alloy with Pd will give a Pd shell with an alloy core – FeCo@Fe@Pd. The Pd shell formed on this core shell alloy (Fe@FeCo) is expected to exhibit a very significant catalytic improvement, as it takes advantage of a better electronic and catalytically improved Fe surface.

3.2 Physical Characterisation of the Four FeCo@Fe@Pd/C Catalysts

The four core-shell alloy catalysts (FeCo@Fe/C) and their corresponding Pd-core shell nanocatalysts (FeCo@Fe@Pd/C) were characterised by FESEM and TEM and HRTEM. All the catalysts were found to be well dispersed on the Vulcan carbon substrate. Much information could not be deduced from the FESEM images as the particles vibrated a lot under the beam. This was thought to be the effect of the magnetic iron based alloy (FeCo@Fe) core on the Pd outer shell. The TEM images however revealed a number of information about the morphology, and size ranges of the catalysts. The reducing effect of microwave irradiation from the micron-sized core alloys to the nano-sized core shell catalysts was obviously noticed too. HRTEM images of the core shell catalysts alone were also taken to confirm their core shell particle sizes, thus confirming the effectiveness of what can be described as the *microwave induced top-down nanostructuring and decoration* (*MITNAD*) procedure used for the Pd based core shell synthesis. Figs 3.1 (a –d) show the FESEM images of the four core shell nano catalysts. All the catalysts appear to have uneven sizes and a somewhat spherical and pseudo spherical shapes.

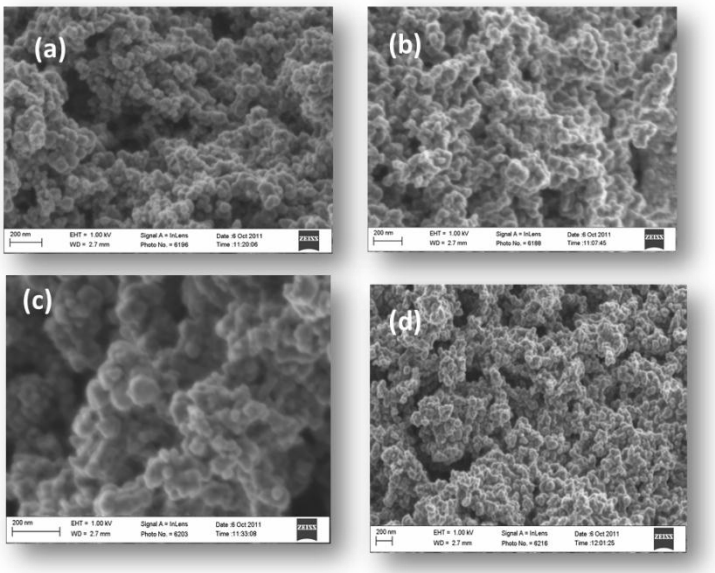

Figure 3. 1: FESEM images of FeCo@Fe@Pd/$C_{(H)}$ (a), FeCo@Fe@Pd /$C_{(NaOH)}$ (b), FeCo@Fe@Pd/$C_{(PVP\ 10)}$ (c), and FeCo@Fe@Pd/$C_{(PVP\ 15)}$ (d).

Fig 3.2 displays the TEM images of the four core alloys (a – d) and their corresponding core shell catalysts (a'-d'). All the palladium based core shell nano catalysts exhibited a remarkable reduction in size in comparison to their originating core alloys. FeCo@Fe@Pd/C$_{\textbf{(PVP 10)}}$ did not show a reduction comparable to the other catalysts. It should be noted also that it had the least exposure to the microwave irradiation during its synthetic procedure.

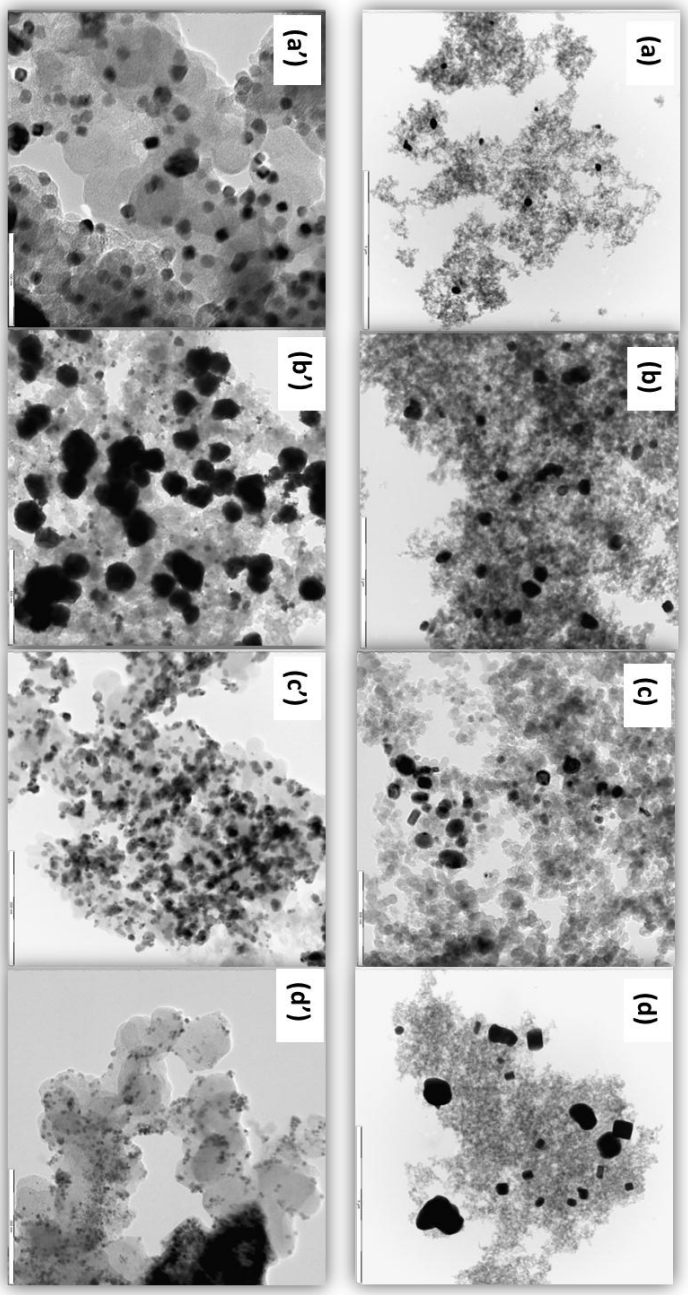

Figure 3. 2: TEM images of of core shell alloys- FeCo@Fe@/$C_{(PVP\ 15)}$ (a), FeCo@Fe /$C_{(PVP\ 10)}$ (b), FeCo@Fe/$C_{(NaOH)}$, (c) and FeCo@Fe/$C_{(H)}$ (d) and TEM images of core shell nanocatlysts- FeCo@Fe@Pd /$C_{(PVP\ 15)}$ (a'), FeCo@Fe@Pd /$C_{(PVP\ 10)}$ (b') FeCo@Fe@Pd /$C_{(NaOH)}$, (c') and FeCo@Fe@Pd/$C_{(H)}$ (d').

Table 3.1: A summary of the physical characteristic parameters of the 8 catalysts as observed in the TEM images in Fig 3.2

Physical Characteristics	Core alloy catalysts	Core shell nano catalysts
	(a) FeCo@Fe/$C_{(PVP\ 15)}$	**(a') FeCo@Fe@Pd /$C_{(PVP\ 15)}$**
Size range	74-186 nm	11-18 nm
Morphology	Octahedral, cubes	Octahedral
Magnification	2 µm	500 nm
	(b) FeCo@Fe/$C_{(PVP\ 10)}$	**(b') FeCo@Fe@Pd /$C_{(PVP\ 10)}$**
Size range	137-205 nm	97-149 nm
Morphology	Pseudo – ocathedral	Cubes, triangles, octahedral
Magnification	5 µm	100 nm
	(c) FeCo@Fe/$C_{(NaOH)}$	**(c') FeCo@Fe@Pd /$C_{(NaOH)}$**
Size range	40-90 nm	11-17 nm
Morphology	Cubes, rectangular	Icosahedral
Magnification	500 nm	200 nm
	(d) FeCo@Fe/$C_{(H)}$	**(d') FeCo@Fe@Pd /$C_{(H)}$**
Size range	208 – 634 nm	4-7 nm
Morphology	Cubes, octahedral	Icosahedral, octahedral
Magnification	5 µm	200 nm

HRTEM images (Fig 3.3) of the Pd core shell nanocatalysts showed a confirmation of the results obtained in Table 3.1. The uneven sizes of FeCo@Fe@Pd/$C_{\mathbf{(PVP\ 10)}}$ are obvious , though they are fewer in number than the other much reduced sized nanoparticles seen in the image.

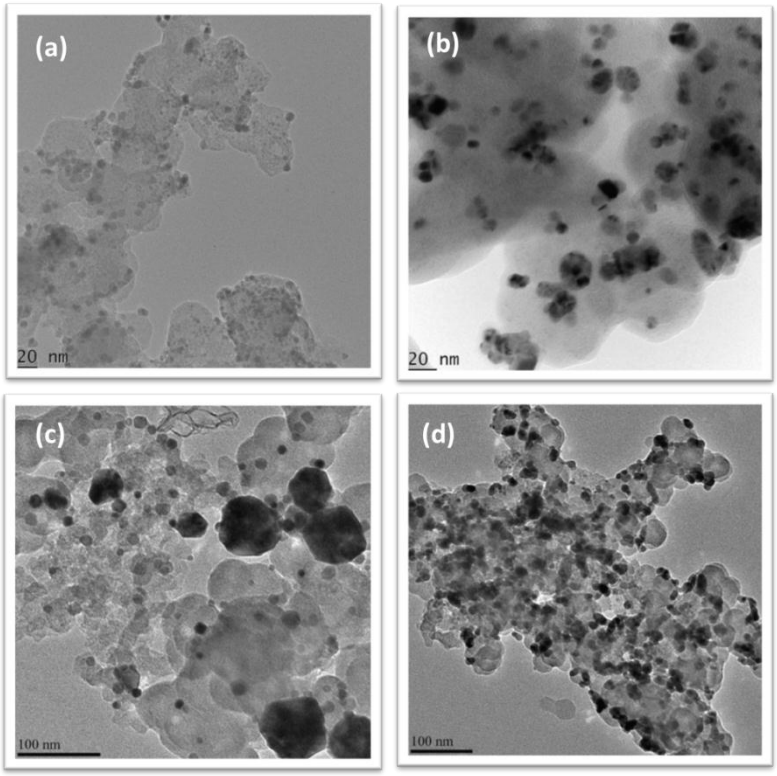

Figure 3. 3: HRTEM images of core shell nano catalysts- FeCo@Fe@Pd /$C_{(H)}$ (a), FeCo@Fe@Pd /$C_{(NaOH)}$, (b), FeCo@Fe @Pd /$C_{(PVP\ 10)}$, (c) and core shell nano catalysts- FeCo@Fe @Pd /$C_{(PVP\ 1)}$

3.3 Electrochemical Characterisation of Nanocatalysts: Oxygen Reduction Reaction (ORR) as a Model for Screening

The electrochemical properties of the catalysts were obtained using cyclic voltammetry. The experiments were carried out in 0.1 M KOH solution saturated with nitrogen gas. The core alloys (i.e., FeCo@Fe/C) did not give any appreciable current responses, except that of the FeCo@Fe/C$_{(H)}$ (Fig 3.4). Interestingly, however, upon incorporation of Pd onto the core FeCo@Fe, one observes an enhanced current response (Fig 3.5).

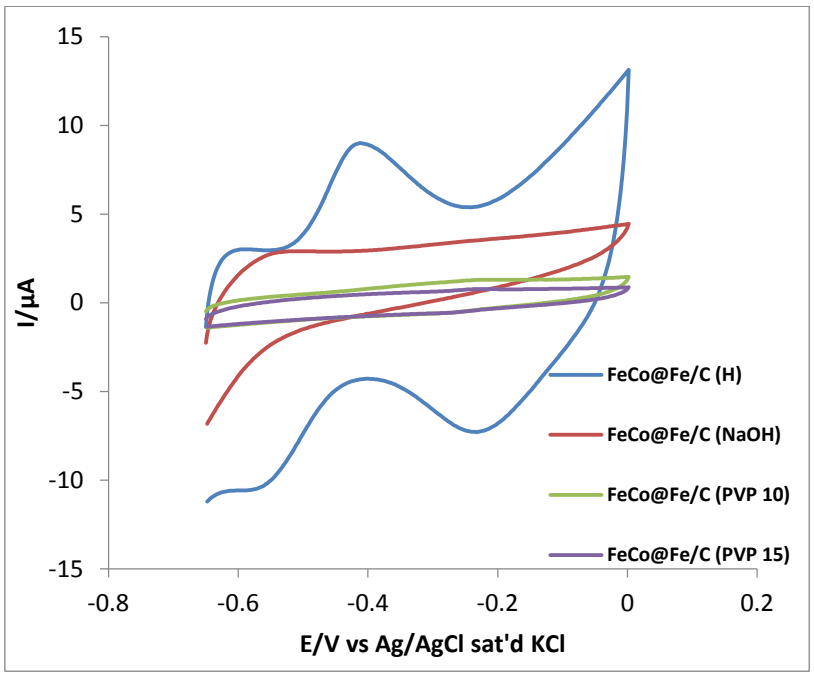

Figure 3. 4: CVs of FeCo@Fe/C$_{(H)}$, FeCo@Fe/C$_{(NaOH)}$, , FeCo@Fe /C$_{(PVP\ 10)}$ and FeCo@Fe/C$_{(PVP\ 15)}$ in 0.1 M KOH sat'd N_2 gas at 25 mVs^{-1}.

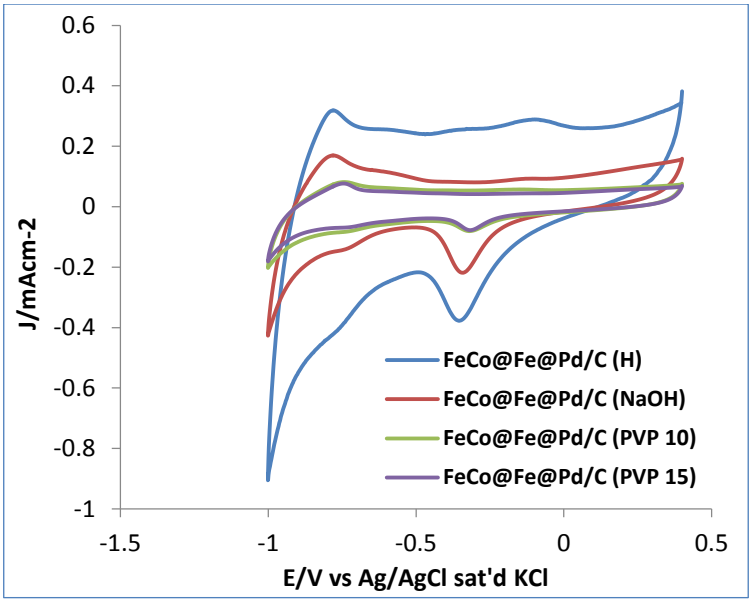

Figure 3. 5: Comparative CVs of FeCo@Fe@Pd/$C_{(H)}$ FeCo@Fe@Pd/$C_{(NaOH)}$, FeCo@Fe @Pd/$C_{(PVP\ 10)}$, and FeCo@Fe @Pd/$C_{(PVP\ 15)}$ in 0.1 M KOH saturated N_2 gas at 25 mVs^{-1}.

The four catalysts exhibited the typical CV voltammograms of Pd based material in alkaline medium. The H_2 desorption peak was noticeable at -0.78 V for FeCo@Fe@Pd/$C_{\mathbf{(H)}}$ and FeCo@Fe@Pd/$C_{\mathbf{(NaOH)}}$, the peaks appeared later at -0.74 V for both FeCo@Fe@Pd/$C_{\mathbf{(PVP(10)}}$, and FeCo@Fe@Pd/$C_{\mathbf{(PVP(15)}}$. The PdO oxide peak was very prominent in FeCo@Fe@Pd/$C_{\mathbf{(H)}}$ CV (at -0.1 V), a less appreciable peak was noticed in FeCo@Fe@Pd/$C_{\mathbf{(NaOH)}}$, and no PdO peaks were observed in CVs of both FeCo@Fe@Pd/$C_{\mathbf{(PVP(10)}}$, and FeCo@Fe@Pd/$C_{\mathbf{(PVP(15)}}$. The reverse scans revealed the main peak attributed to PdO reduction at about -0.32 V to -0.35 V. FeCo@Fe@Pd/$C_{\mathbf{(H)}}$ exhibited the latest reduction peak at -0.35 V. The columbic amount (Q) was obtained from the PdO reduction peak, it is associated with the peak area and is employed in calculating the electrochemically active surface area (EASA) of catalysts[5]. The larger the Q value the larger the EASA of the catalysts. As seen in Fig 3.5, FeCo@Fe@Pd /$C_{\mathbf{(H)}}$ is expected to have the largest Q value out of the 4 catalysts. The exact numeric values are summarised in Table 3.2.

Table 3.2: A summary of electrochemical parameters of the catalysts based on the CVs in Fig 3.5

Catalyst	PdO_{red} /(V)	Q/mC
$FeCo@Fe@Pd/C_{(H)}$	-0.3726	0.4335
$FeCo@Fe@Pd/C_{(NaOH)}$	-0.3604	0.2455
$FeCo@Fe@Pd/C_{(PVP\ 10)}$	-0.3360	0.04470
$FeCo@Fe@Pd/C_{(PVP\ 15)}$	-0.3384	0.05796

The catalysts were further screened for their ORR catalytic activity. The CVs obtained in 0.1 M KOH saturated with O_2 at 25 mVs^{-1} can be seen in Figure 3.6. The cyclic voltammograms results obtained under the same experimental conditions was in good agreement with the previous performances of the nanocatalysts. The electrochemical data from the ORR has been summarised in Table 3.3. $FeCo@Fe@Pd/C_{(H)}$ gave both the earliest onset reduction potential (E_{onset}) at the positive region (0.048 V) and the best current density response (1.13 $mAcm^{-2}$) out of the four catalysts screened. Its E_{onset} was found to be 140mV earlier than those obtained for both $FeCo@Fe@Pd/C_{(PVP\ 10)}$, and $FeCo@Fe@Pd/C_{(PVP\ 15)}$ (-0.09079 V). The value was also 100mV earlier than that of $FeCo@Fe@Pd/C_{(NaOH)}$. Its current response was also twice the value exhibited by $FeCo@Fe@Pd/C_{(PVP(10)}$ and $FeCo@Fe@Pd/C_{(PVP(15)}$.

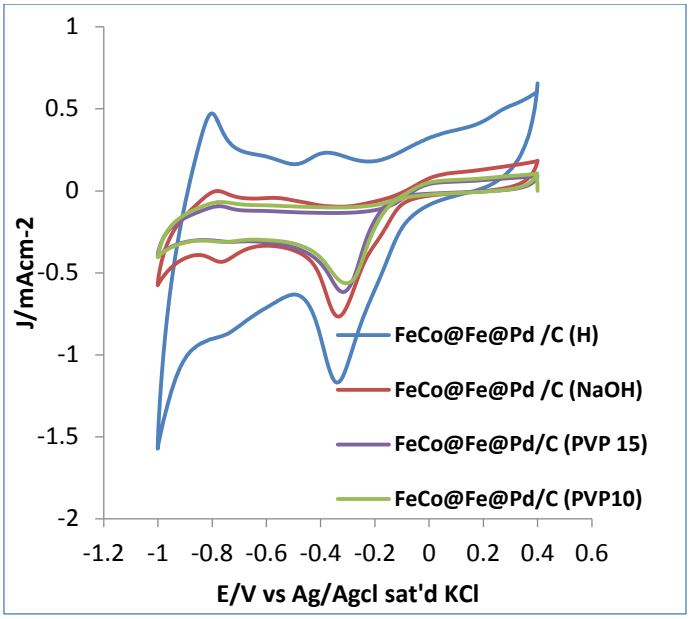

Figure 3. 6: Comparative CVs of FeCo@Fe@Pd/$C_{(H)}$ FeCo@Fe@Pd/$C_{(NaOH)}$, FeCo@Fe @Pd/$C_{(PVP\ 10)}$, and FeCo@Fe @Pd/$C_{(PVP\ 15)}$ in 0.1 M KOH saturated O_2 at 25 mVs^{-1}

Table 3.3: Summary of electro catalytic parameters of catalysts from CVs in Fig 3.6

Catalyst	E_{onset} /V	E (PdO_{red})/V	J (PdO_{red}) /mAcm $^{-2}$
FeCo@Fe@Pd/$C_{(H)}$	0.0484	-0.3178	1.130
FeCo@Fe@Pd/$C_{(NaOH)}$	-0.0541	-0.3105	0.729
FeCo@Fe@Pd/$C_{(PVP10)}$	-0.0908	-0.2837	0.549
FeCo@Fe@Pd/$C_{(PVP15)}$	-0.0908	-0.2959	0.561

As all the catalysts are of core shell nature, the smaller and evenly distributed nanoparticle sizes of FeCo@Fe@Pd/$C_{(H)}$ has been attributed as one of the main factors contributing to the better catalytic response of the catalyst. Its smaller nano sizes also informed its larger EASA as deduced from Table 3.2.

3.4 Morphology and Electrochemical Activity of nanocatalysts - 'MITNAD' explained

The technique used in the synthesis of the Pd based nanocatalysts for this study has been hinged on the use of microwave as an eco- friendly synthesis procedure. Although three of the core alloys, FeCo@Fe, were synthesised by microwave induced technique, while the four palladium-based core shell catalysts, FeCo@Fe@Pd, were all made through *MITNAD* procedure; nonetheless the catalysts have shown a number of differences with respect to their physical and electrochemical properties. The reduction to the nano level i.e. nano-sizing of the micron-sized core alloys to nano-sized Pd core shell catalysts, led to the coinage of the term *'MITNAD'*. *MITNAD* explains the microwave induced top–down nano structuring and decoration (using Pd) of the core shell alloys FeCo@Fe to give FeCo@Fe@Pd nanocatalysts. FeCo@Fe@Pd/$C_{(H)}$ catalysts which gave the best electrocatalytic performance of the four catalysts had its core alloy synthesised through hydrogenation of its component salts, involving a solvent-less technique before being subjected to the *MITNAD* procedure. Its good catalytic response has earlier been attributed to its smallest nanoparticle sizes though other reasons will be expounded later. Thus, the basic scheme of this procedure is best illustrated using the samples of this catalyst as seen in Scheme 3.1

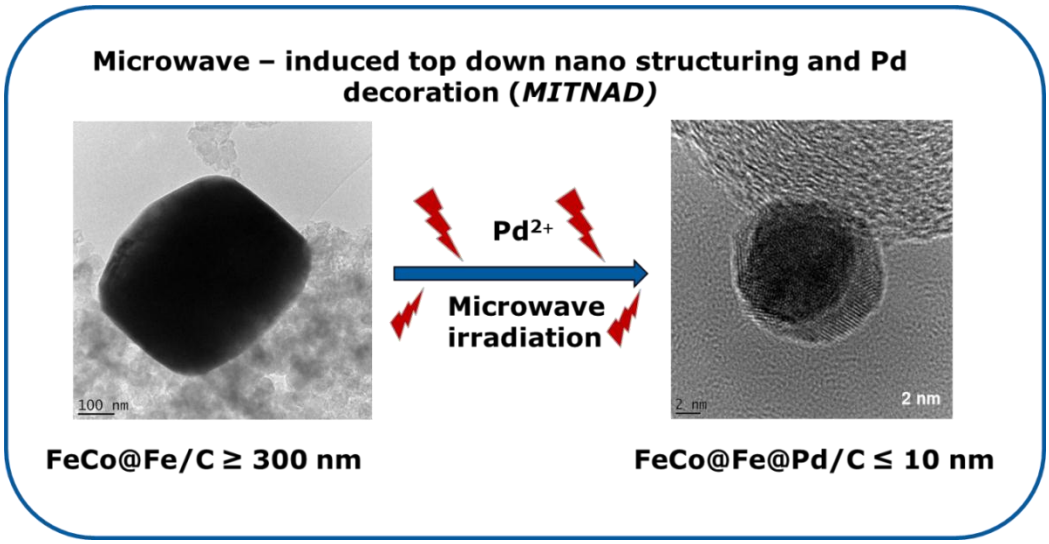

Scheme 3.1: MITNAD synthetic route using FeCo@Fe@Pd/$C_{(H)}$ catalysts

The second best performing catalyst, FeCo@Fe@Pd/C$_{(NaOH)}$, was also synthesized via a 2-step process, both involving the use of solvents. EG was used and it is a non-toxic solvent with a very high 'loss tangent' (tan δ> 0.5). Loss tangent is the ability of a material to convert electromagnetic energy to heat energy at a given frequency and temperature. The presence of NaOH was to act as seeding agent for the precipitation of the metal with the lower reducing potential, Co, which would subsequently serve as nuclei spots for the growth of Fe during the synthesis of the FeCo@Fe/C core alloy. The same mixture of solvents was used during *MITNAD*. The result showed a fairly larger particle size and an electrochemical activity comparable to that of FeCo@Fe@Pd/C$_{(H)}$. For both FeCo@Fe@Pd/C$_{(PVP\ 10)}$, and FeCo@Fe@Pd/C$_{(PVP\ 15)}$ catalysts, the first step of their synthesis procedure (formation of FeCo@Fe/C alloy) was also via MW-ST. In this case, however, besides the reducing agent which is EG, PVP was also added to the mixture as a capping agent to prevent agglomeration of the nanoparticles after their formation. They exhibited the worst electrocatalytic activity for ORR. Their particle sizes were not that desirable for catalysis either as they came out larger than expected.

An excessive presence of PVP might be a main contribution to the poor performance of the catalysts. As there was no post-annealing treatment after *MITNAD* process (annealing is a good way of removing excess and unreacted polymer stabilizers like PVP), the possibility of having more PVP in the system cannot be ruled out although the washing process was done as thoroughly as possible. In terms of accessibility for catalysis, the presence of residual strong stabilisers used in synthesis could affect the catalytic performance of the nanoparticles. Strong binding stabilizers used in synthesis could also be the barrier blocking the adsorption of reactants onto the catalyst surface, thus blocking active sites in nanocatalysts[6,7].

In view of all of these observations and results, procedure for the synthesis of FeCo@Fe@Pd/C$_{(H)}$ (reduction by hydrogenation and nano-

sizing by *MITNAD*) was chosen as the standard synthetic route for all other catalysts used in the course of this research studies. The design of FeCo@Fe@Pd/$C_{(H)}$ can be considered based on some main factors underlining its core shell nature. These principles are also related to its enhanced catalytic activity as will be explained below.

The prediction trends of core shell preferences for late transition metals (TS metal) alloy nanoparticles were explained by Wang and Johnson[8]. Their findings have been used in the design of the chosen synthetic route of the core shells in these studies. A Core shell particle design seen as a relative enrichment of a shell by one metal over another will entail the study of ground state structures and configurations of different metal alloy combinations e g. pure shell, mixed core, pure shell single metal core structures etc. Thus, there is a need to identify general trends through calculations that reflect some underlying principles in core shell configuration.

Generally, factors most often mentioned as determinants for core shell preferences are cohesive energy, surface energy, atomic radii, and electro negativity[9]. There is an interplay among these factors which is generally overlooked, but was taken into consideration by Wang and Johnson. The surface energies calculated from Density Functional theory (DFT) are shown in Table 3.4.

Table 3.4: DFT-PW91 Calculated Segregation Energies in eV for 55-Atom Binary Alloy Nanoparticles. Note that the row is for ***Core*** while column is for the ***shell*** [8].

	Au	**Ag**	**Cu**	**Pt**	**Pd**	**Ni**	**Ir**	**Rh**	**Co**	**Os**	**Ru**	**Fe**
Au	0	−0.06	−0.67	−1.77	−0.67	−2.02	−3.36	−2.22	−2.05	−2.93	−1.90	−4.70
Ag	0.07	0	−0.77	−1.99	−0.82	−2.29	−3.54	−2.41	−2.15	−3.03	−1.96	−5.20
Cu	0.47	0.08	0	−0.24	0.26	−0.81	−1.93	−0.99	−0.71	−1.61	−0.72	−2.58
Pt	1.01	0.84	0.41	0	0.51	−0.61	−1.37	−0.70	−0.95	−1.45	−0.66	−2.71
Pd	0.89	0.70	0.13	−0.44	0	−1.09	−1.71	−1.13	−1.29	−1.67	−0.84	−3.26
Ni	0.95	0.67	0.72	0.42	0.46	0	−0.67	−0.17	−0.20	−0.48	0.04	−2.02
Ir	1.48	1.51	1.22	1.48	1.34	0.33	0	0.23	−0.04	−0.40	0.07	−1.97
Rh	1.28	1.33	0.90	0.75	0.79	−0.23	−0.36	0	−0.53	−0.66	−0.12	−2.87
Co	0.52	0.36	0.73	0.94	0.75	0.15	0.04	0.16	0	0.13	0.11	−2.24
Os	1.54	1.68	1.71	2.52	1.95	0.92	0.65	0.54	0.72	0	0.14	−0.34
Ru	1.43	1.46	1.30	1.76	1.14	0.19	0.38	0.42	0.07	−0.18	0	−2.24
Fe	0.77	0.60	1.83	0.82	0.74	−0.10	0.00	−0.02	0.07	−0.08	−0.29	0

Segregation Energy (SE) was obtained from the energy difference $\Delta E_{(A)B}$ (after full atomic relaxations) between a nanoparticle with *m* A atoms in the core (denoted within parentheses) and *n* B atoms in the shell (a complete equation of the calculation can be found in the above cited

article). Clearly, a positive $\Delta E_{(A)B}$ indicates a core–shell structure that prefers A in the core and B in the shell; the larger the magnitude, the greater the tendency. In contrast, a negative $\Delta E_{(A)B}$ indicates the opposite preference i.e. A in the shell and B in the core. Considering the core alloy used in this study, the two metals involved being Fe and Co; $\Delta E_{\mathbf{(Co)Fe}}$ has a calculated SE value of +0.07 eV, thus yielding a mixed alloy with a preferential Fe shell coverage (FeCo@Fe). A further combination of a tertiary alloy with a Fe-rich surface and Pd gives an SE value of +0.74 eV for $\Delta E_{\mathbf{(Fe)Pd}}$ this means that the present configuration of Fe-core and Pd-shell is preferred. Assuming a swap in the positions of the metals with $\Delta E_{\mathbf{(Pd)Fe}}$, SE value will be -0.36 eV which still confirms the preferential position of Pd as the shell and Fe in the core. Thus, the Pd based core shell nanocatalyst has a FeCo@Fe@Pd structure. The Table was also illustrated in a colour coded form as seen in Fig 3.7.

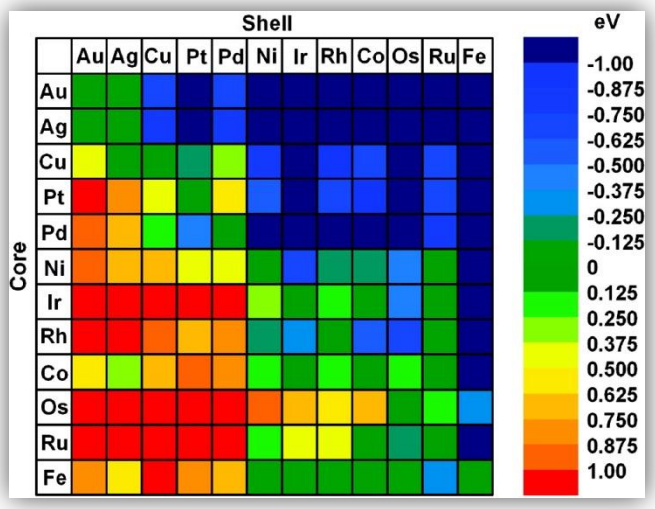

Figure 3. 7: Color-coded matrix of DFT-PW91 segregation energies for impurity in 55-atom nanoparticle composed of 12 late-transition metals (132 binaries)[8]

There also exists a strong correlation of SE and alloying core–shell preferences when atoms are aligned according to their cohesive energy – smallest to largest cohesive energy (group by group going from late to middle TS Metals) and by atomic sizes – largest to smallest WS radius (that is size within the group from 5d,4d to 3d).The Wigner–Seitz (WS)

radius is the better parameter to use than the atomic radius as it directly determines the atomic size, the band width and energy[10]. For binary atoms formed by metals from different groups the two factors, cohesive energy and WS radius act co-operatively. Metals, going from late to middle TS metals of both larger cohesive energy and smaller radius, prefer to be in the core region. On the other hand, for nanoparticles formed by metals within a group going from 5d to 3d, the cohesive energy gets smaller and the WS radius gets smaller too. Thus, there is a competition between the two factors and the WS radius dominates most of the time where the atom with the smaller radius goes into the core to relieve the compressive strain. Exceptions are found in the diagonal 4d and 5d where cohesive energy dominates as the WS radii are too small. This analysis can be applied to reveal the core preferences for multi component nanoparticles.

Using the tertiary core shell Pd based nanoparticle developed in this study, the different core shell preferences can also be explained using the cohesive and WS radius factors. The three metals are in different groups, so both the cohesive energy and WS radius are considered. Moving from 3d to 5d, Co with the largest cohesive energy of 4.5 eV will have a core preference with respect to Fe, 4.4 eV; while Fe will prefer the core with respect to Pd which has a cohesive energy of 3.5 eV. The WS radii of the three metals are 1.4 Å, 1.45 Å, and 1.55 Å, respectively. Thus, Co will prefer the core position when alloyed with Fe and the Fe surface will prefer the core position when alloyed with Pd. All of these in effect explain the positions of the metals comprising the nanocatalysts used in this study according to their core-shell design.

Regarding the enhanced catalytic surface of catalysts with core shell architecture, many authors have written on this. It is well known that the incorporation of smaller atoms into larger TS metals induces a lattice

contraction and thus causing a strain on the surface of the TS metal rich surface. This lattice – strain effect has been well expounded by the Nørskov d- band theory. This Nørskov model is based on shifts of the d-band centre, increasing or decreasing the interaction of the surface metal catalysts with the adsorbates. This is because the d-bands are narrow and small changes in their environment can change the d-states and their interaction with the adsorbates state significantly. The shift of the d-band centre has been calculated for alloys with two or more metals, and for surface segregated phases of a given metal on a metal nanoparticle. This shift is mainly caused by the lattice mismatch and the electronic interaction between the metals[11–15]. According to these studies, if the lattice constants of two metals differ, strained over layers (shell layers) with chemical properties that are significantly different from those of the pure over layer metals are formed. Such strain has been shown to modify the chemisorption properties of the metal considerably.

In other words, scientific investigations have proved that strain generally induces changes in the ability of a surface to form bonds to adsorbed atoms or molecules, thus one can use this to manipulate the reactivity of a metal. And as this strain can be induced by incorporation of metals into one another, the reactivity of the Pd surfaces of the core shell catalysts fabricated in this study is envisaged to be much better than the ordinary pure Pd metallic surface. Thus, as a result of this, one of the main reason for the enhanced catalytic activities of the surface of FeCo@Fe@Pd core shell nano catalysts in both ORR and Alcohol oxidation reactions carried out in these studies have been explained using the lattice strain effect explained by the d-band theory

3.5 Palladium Core –Shell Nanocatayst Supported on Vulcan Carbon (FeCo@Fe@Pd/$C_{(H)}$)

3.5.1 Introduction

The physical and electrochemical properties of FeCo@Fe@Pd/C will be discussed in this section. XRD patterns and ultimately the STEM-EDS line scan confirmed the core-shell structure of both the FeCo@Fe/C core alloy and FeC@Fe@Pd/C nano catalyst. The electrochemical characterisation was carried out using cyclic voltammetry. The experiment was carried out in a nitrogen saturated 0.1 M KOH electrolyte at 50 mVs^{-1}.

3.5.2 XRD Characterisation

The XRD patterns of FeCo@Fe/C and FeCo@Fe@Pd/C are shown in Fig 3.8. The diffraction pattern of FeCo@Fe/C can be indexed to the body-centered cubic (bcc) structure (space group *Pm*3*m*) (JCPDS card: No. 03-065-6829). The intense peaks of the spectrum indicate the crystallinity and large sizes of the alloy. FeCo@Fe@Pd/C and Pd/C both display diffraction peaks at 2θ (hkl) values of 46.9° (111), 54.7° (200), 81.1° (220) and 99.4° (311) corresponding to a typical face-centered cubic structure of Pd. The shift in the diffraction lines of Pd in FeCo@Fe@Pd/C to higher 2θ positions compared to those of Pd/C reflects a lattice contraction as a result of the substitution of the Pd lattice by the FeCo alloy. The lattice strain effect has already been observed on Pd alloys with the Pd-rich surface incorporated with smaller atoms[1,16,17]

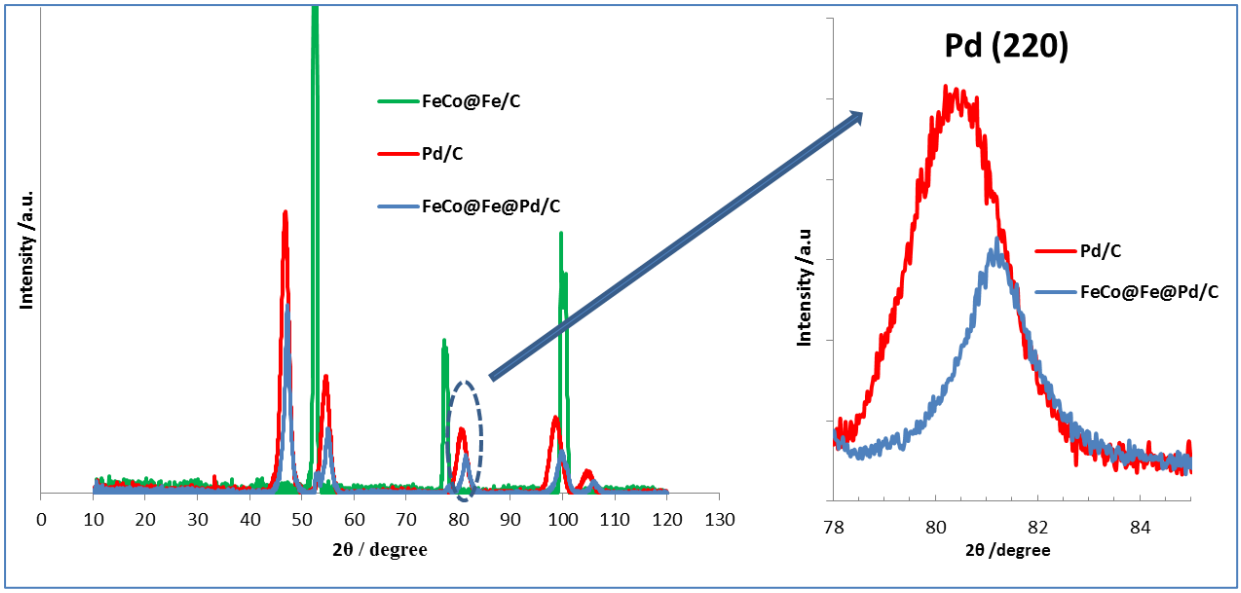

Figure 3. 8: XRD patterns of FeCo@Fe/C. Pd/C and FeCo@Fe@Pd/C catalysts with Pd (220) diffraction peaks of Pd/C and FeCo@Fe@Pd/C as inset**.**

The Scherrer formula and Vergard's law were used in estimating the average particle sizes of the core shell nanoparticles (*d*) and the lattice parameter (*a*). The values were estimated from the Gaussian fitted (220) peak. Particles size values (*d*) were calculated as nm while lattice parameters values were estimated as Å.

$$d = \frac{k\lambda}{\beta Cos\,\theta} \qquad (3.1)$$

$$a = \frac{\sqrt{2}\lambda}{Sin\theta} \qquad (3.2)$$

Where λ represents the wavelength of X-ray (1.79026 Å), θ is the angle of the (2 2 0) peak (Bragg angle), *K* (0.89) is the Scherrer constant and β is its half peak width or full width at half maximum/integral breadth.

Particle sizes (*d*) were estimated as 8 nm for FeCo@Fe@Pd/C while Pd/C was 10.5 nm. Lattice parameter (*a*) values were and 3.8971 Å and 3.9271 Å for FeCo@Fe@Pd/C and Pd/C respectively. A lattice mismatch of about 2.85 % can already be estimated between the Pd core shell catalyst and the single Pd metal catalyst. This also confirms the lattice contraction.

3.5.3 TEM and HRTEM

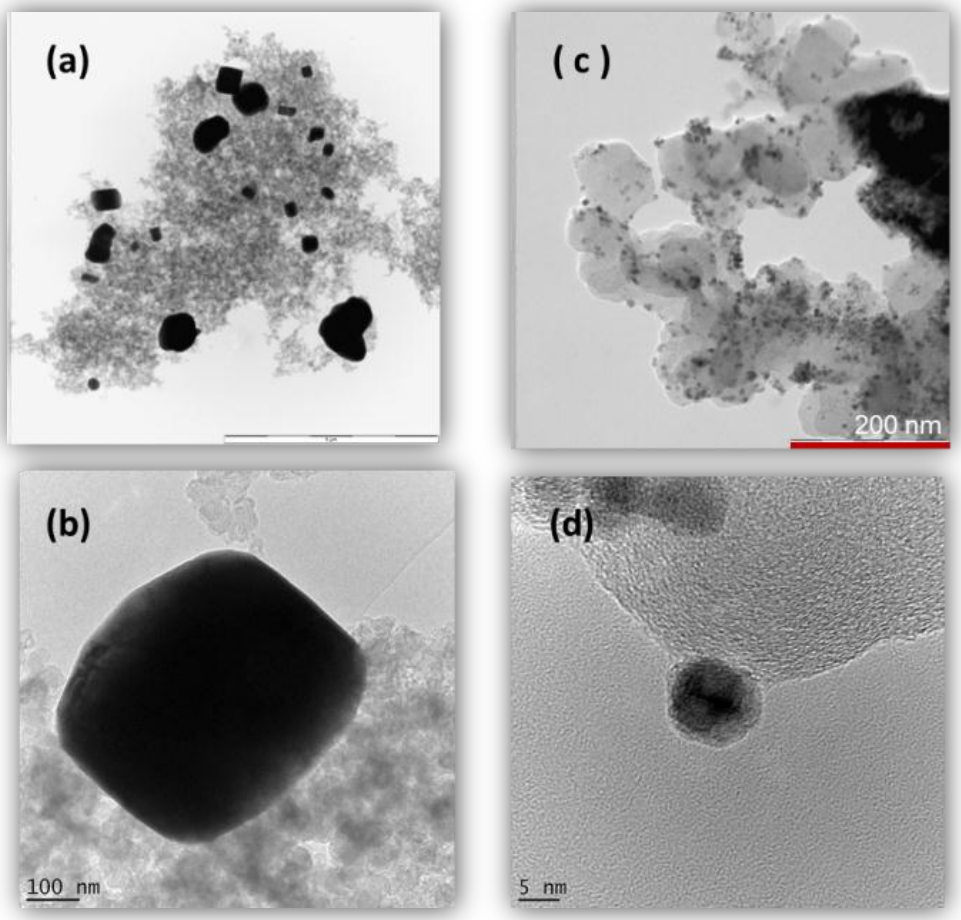

Figure 3. 9: TEM images of FeCo@Fe/C (a) and FeCo@Fe@Pd/C (c) with their corresponding HRTEM images (b) and (d)

Observing the HRTEM images of the nanocatalysts further gives a confirmation of the effectiveness of *MITNAD* synthetic route

3.5.4 FESEM

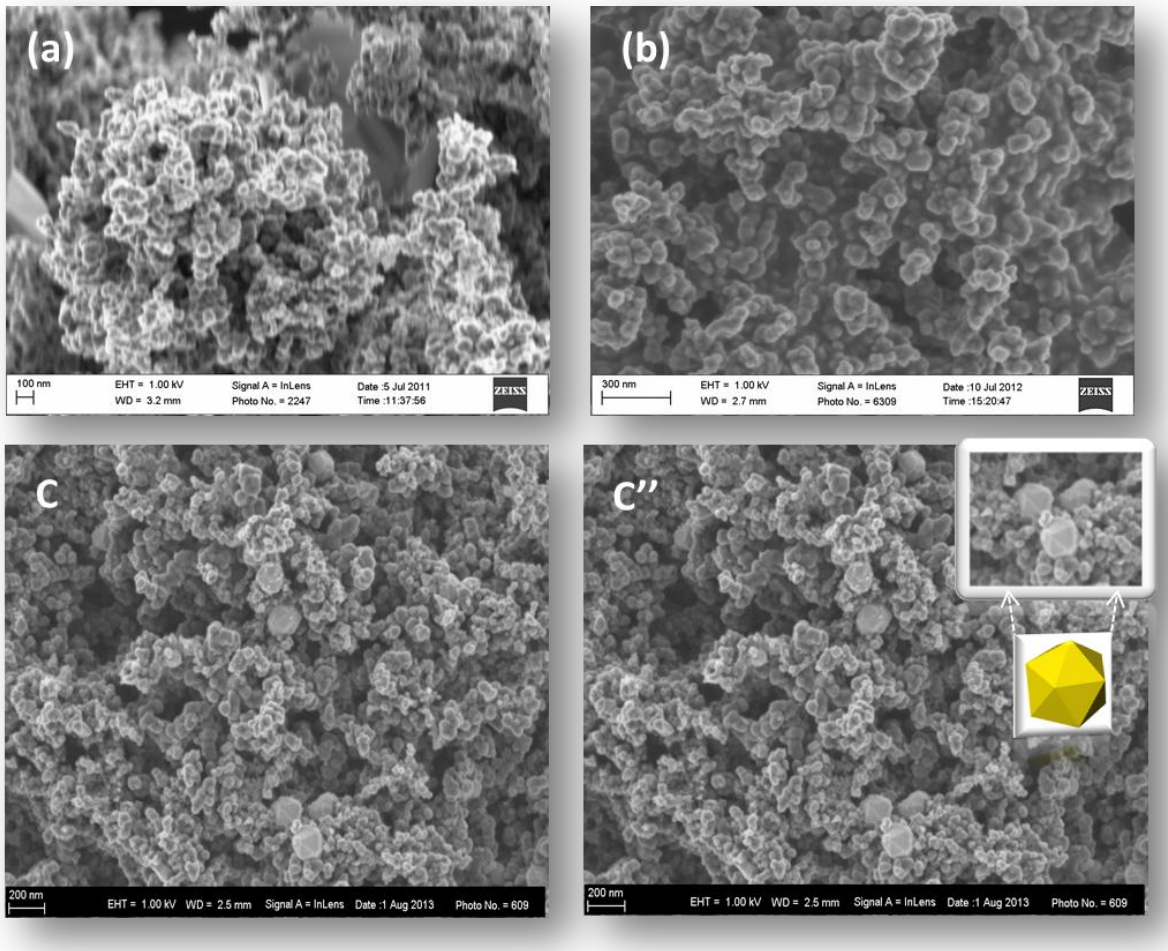

Figure 3. 10: FESEM images of FeCo@Fe/C (a), FeCo@Fe@Pd/C (b) and Pd/C (c' and c'').

The FESEM images of the catalysts are displayed in Fig 3.10. A well-focussed image of the FeCo@Fe/C core alloy could not be obtained as a result of its high magnetic properties. The particles were in constant motion under the beam. FeCo@Fe@Pd/C appears as small spherical nano particles, although its real morphology is an icosahedron and is better seen in the TEM images. Pd/C particles can be seen in Fig 3.10 c. and c''. Both images are the same but the icosahedral shapes of the Pd nanoparticles are highlighted in the inset picture accompanied by a model icosahedron image.

3.5.5 STEM HAADF –EDX

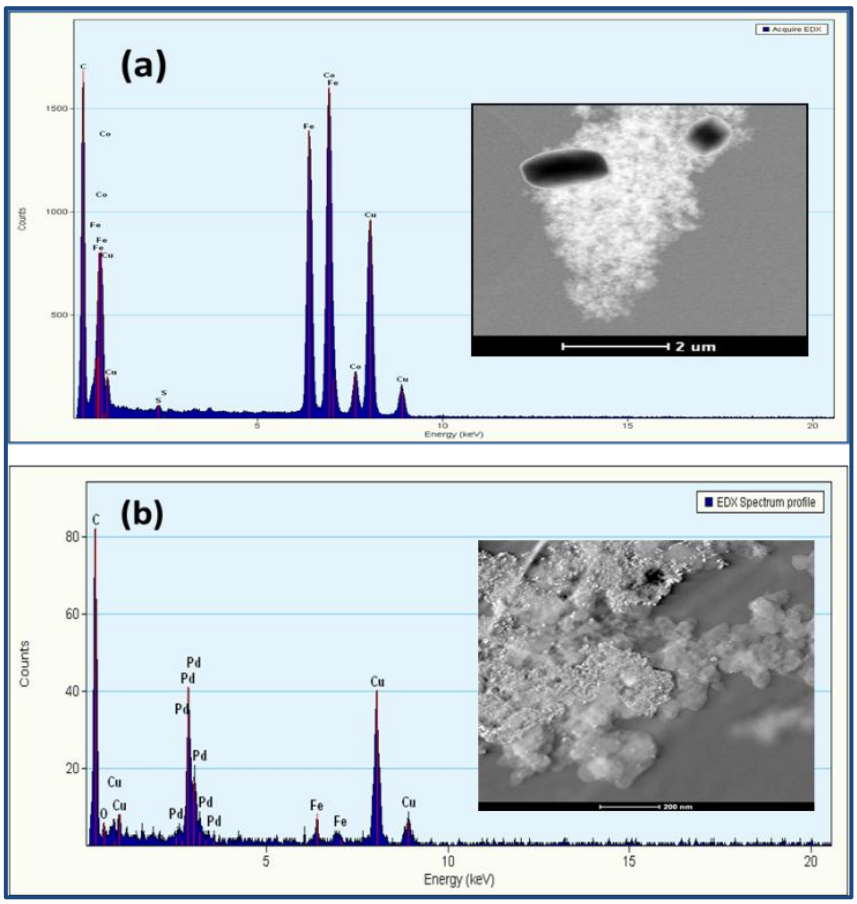

Figure 3. 11: STEM HAADF images (insets) and EDX Spectra of FeCo@Fe/C (a) and FeCo@Fe@Pd/C (b)

HAADF images of the core shell alloys- FeCo@Fe/C and core shell nano catalysts, FeCo@Fe@Pd/C, were taken in the STEM mode, they are represented as insets in images (a) and (b) respectively. The EDX of these particles were also carried out and the spectra reveal an approximate elemental composition of the catalysts. Co is not seen in the EDX spectra of FeCo@Fe@Pd/C owing to its small percentage.

3.5.6 EDX Line Scan

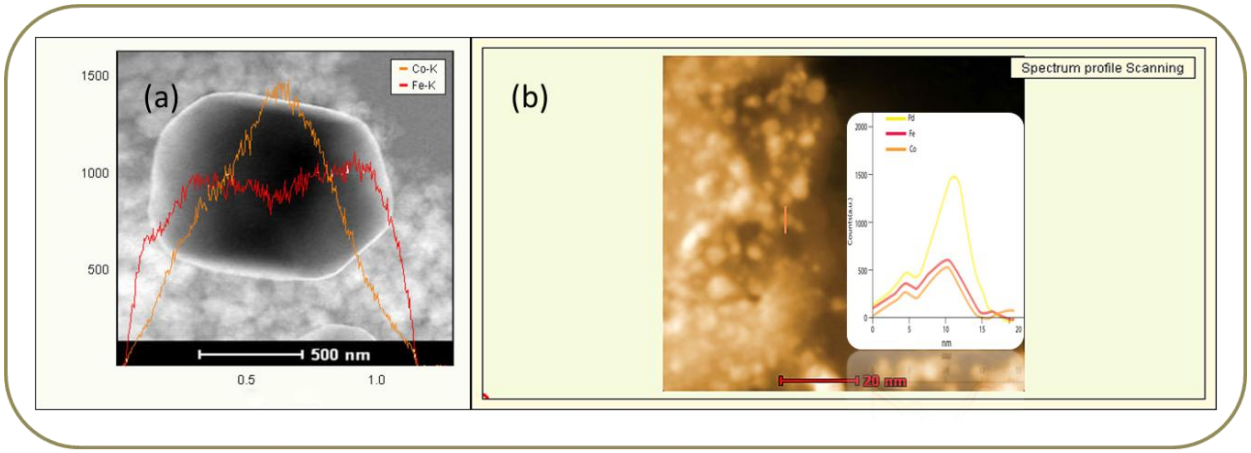

Figure 3. 12: STEM EDX line scans of FeCo@Fe/C (a) and FeCo@Fe@Pd/C (b) overlaid on their HAADF images.

EDX line scan was also performed in the STEM mode. These images revealed the core-shell nature of both the FeCo@Fe/C core alloy (a) and FeCo@Fe@Pd/C core shell nano catalysts (b). Figure 3.12 (a) shows Fe as the outer shell layer while the Co with an obvious mixture of Fe remains generally in the central core. The bright layer surrounding the particle is also indicative of a pure metal covering of the nanoparticle. Palladium is also seen as an outer shell covering in the two nanoparticles chosen for the line scan EDX of FeCo@Fe@Pd/C catalyst while FeCo@Fe alloy remains in the core. As the particles were quite small – sub 10 nm, single particles underwent a lot of vibrations under the beam so line scans were conducted using two or more nanoparticles.

3.5.7 SAED

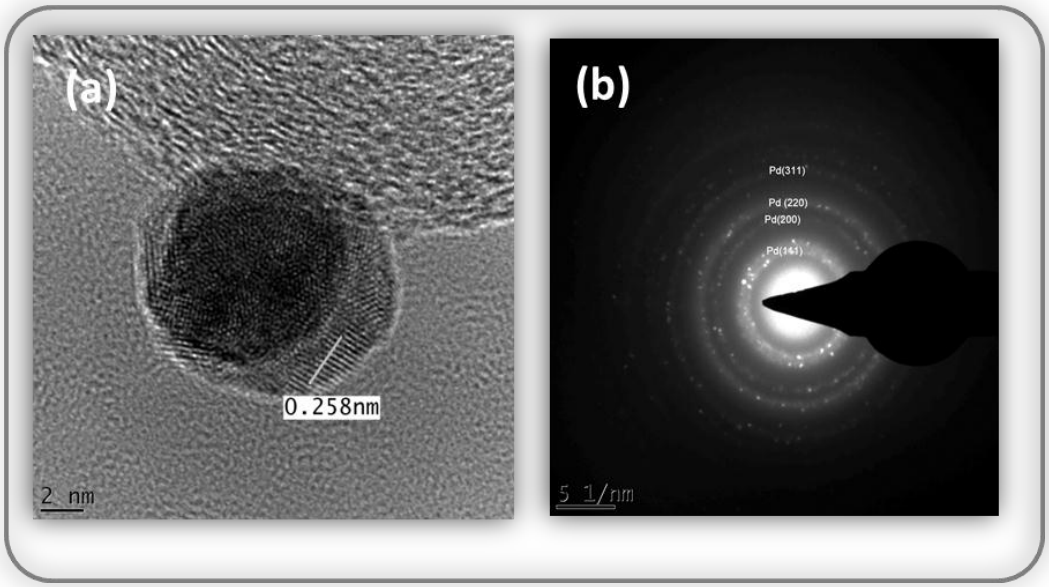

Figure 3. 13: HRTEM and SAED pattern of FeCo@Fe@Pd/C core shell nanoparticle

The lattice resolved HRTEM image (a) and the corresponding SAED pattern (b) of the core shell catalyst can be seen in Fig. 3.13. The icosahedron shape of FeCo@Fe@Pd/C nano catalyst is better appreciated in this image. Its interplanar distances obtained from the lattice fringes of the nanoparticle lie between 0.231 and 0.248 nm which correspond to the (111) plane of the Pd alloy, in close agreement with the d-spacing of 0.225 nm obtained from the XRD data. A well-defined Pd icosahedron has an interplanar distance of about 0.230 nm between its (111) planes[18,19].

3.5.8 Electrochemical Properties (EASA)

Figure 3.14 shows the cyclic voltammograms (CV) of the catalysts dispersed on glassy carbon electrode recorded in a N_2 saturated 0.1M KOH solution. The CV responses show the general features characteristic to palladium. The broad anodic peaks at the potentials of -0.5V to -0.2V are associated with the formation of Pd surface oxides, whereas the reduction of these oxides results in well-defined cathodic peaks between -0.4V to -0.3V. The electrochemically active surface area (EASA) of the Pd catalysts was best estimated using the Pd oxide reduction peak. According to Woods et al.[20] the reduction of the Pd monolayer formed on the Pd surface corresponds to a charge density of 0.424 $mCcm^{-2}$. This provides a convenient method to determine the effective electrochemical surface area (EASA) of Pd, without the complications of using the poor hydrogen absorption peak associated with Pd, or surface contamination as observed in other methods e.g., Cu UPD and CO stripping[21,22]. Thus, from Figure 3.14, the specific EASA of the nanoparticles modified GCE was estimated using the relation:

$$EASA = \frac{Q}{SI} \qquad (3.2)$$

where Q is the columbic charge (0.0707 and 0.1429 mC for Pd/C and FeCo@Fe@Pd/C, respectively), S is a proportionality constant (0.424 $mCcm^{-2}$) and I is the catalyst loading (1.3±1 µg (Pd). EASA value was estimated as 149.10 cm^2mg^{-1} and 245.47 $cm^2\ mg^{-1}$ for Pd/C and FeCo@Fe@Pd/C respectively.

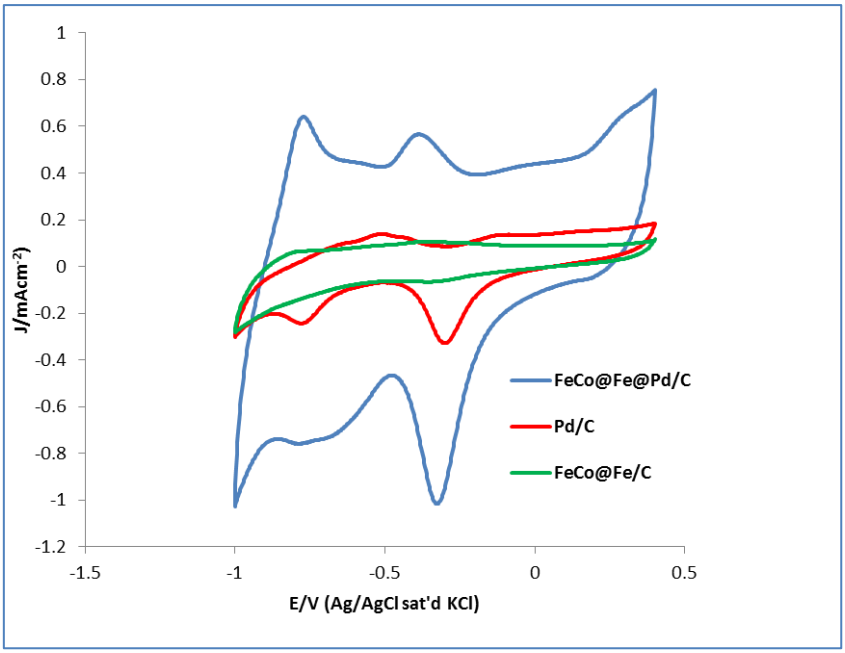

Figure 3. 14: Comparative cyclic voltammograms of FeCo@Fe/C-core, Pd/C-shell and FeCo@Fe@Pd/C-core shell catalysts in 0.1 M KOH solution saturated with N_2

Looking at the voltammograms displayed in Fig 3.14, one sees that the cyclic voltammograms of the FeCo@Fe@Pd/C catalyst exhibits the highest capacitive nature among the three characterised catalysts. The nature of the substrate, Vulcan XC-72 powder, used in its synthesis may have undergone a physical activation as a result of the double thermal treatment involved in the synthetic procedure of FeCo@Fe@Pd/C catalyst. Heat treatment of Vulcan carbon is known to increase its capacitive current[23]. It should be noted that Vulcan XC-72 powder used as substrate for the monometallic Pd/C did not undergo any form of thermal treatment. Also, the possibility of a greater thickness of the catalyst film on the modified electrode may lead to such observations.

3.6 Palladium Core–Shell Nanocatayst Supported on Functionalised Multi-Walled Carbon Nanotubes (FeCo@Fe@Pd/MWCNTS$_{(H)}$)

3.6.1 Introduction

This section describes the characterisation of the core-shell nanocatalysts supported on functionalised MWCNTs i.e., carboxyl-functionalised (CNT-OH) and sulfonate-functionalised (CNT-SO_3). The six nano catalysts FeCo@Fe/CNT-OH$_{(H)}$, FeCo@Fe/CNT-$SO_{3(H)}$, Pd/CNT-OH, Pd/CNT-SO_3, FeCo@Fe/CNT-OH, and FeCo@Fe/CNT-SO_3 were characterised by XRD, FESEM, and HRTEM, and by electrochemical methods. As the emphasis of the study is on the core shell Pd based nano catalysts, STEM HRTEM and STEM-HAADF were used to ascertain the core shell nature of both FeCo@Fe core shell alloys and the FeCo@Fe@Pd on functionalised carbon nanotubes. The electrochemical characterisation was carried out using cyclic voltammetry in a nitrogen saturated 0.1 M KOH electrolyte at 50 mVs^{-1}.

3.6.2 XRD

The powder XRD patterns of FeCo@Fe@Pd/CNT-OH and FeCo@Fe@Pd/CNT-SO_3, are depicted in Fig 3.15 and are compared with the single metal Pd on CNT-OH and CNT-SO_3 respectively. The four palladium based catalysts can be indexed to the face centred cubic (fcc) structure (SP-group Fm-3m) (JCPDS card: 03-065-6174). They all displayed diffraction peaks at 2θ (hkl) values of 46.9°(111), 54.7°(200), 81.1° (220) and 99.4°(311) corresponding to a typical face centred structure of Pd. Particles size values (*d*) estimated from the Gaussian fitted (220) peak were calculated as 15.9 nm, 14.7 nm, 7.4 nm and 10.8 nm while lattice parameters values were estimated as 3.8948 Å, 3.8972 Å, 3.8767 Å and 3.8735 Å for Pd/CNT-SO_3, Pd/CNT-OH, FeCo@Fe@Pd/CNT-OH and FeCo@Fe@Pd/CNT-SO_3 respectively.

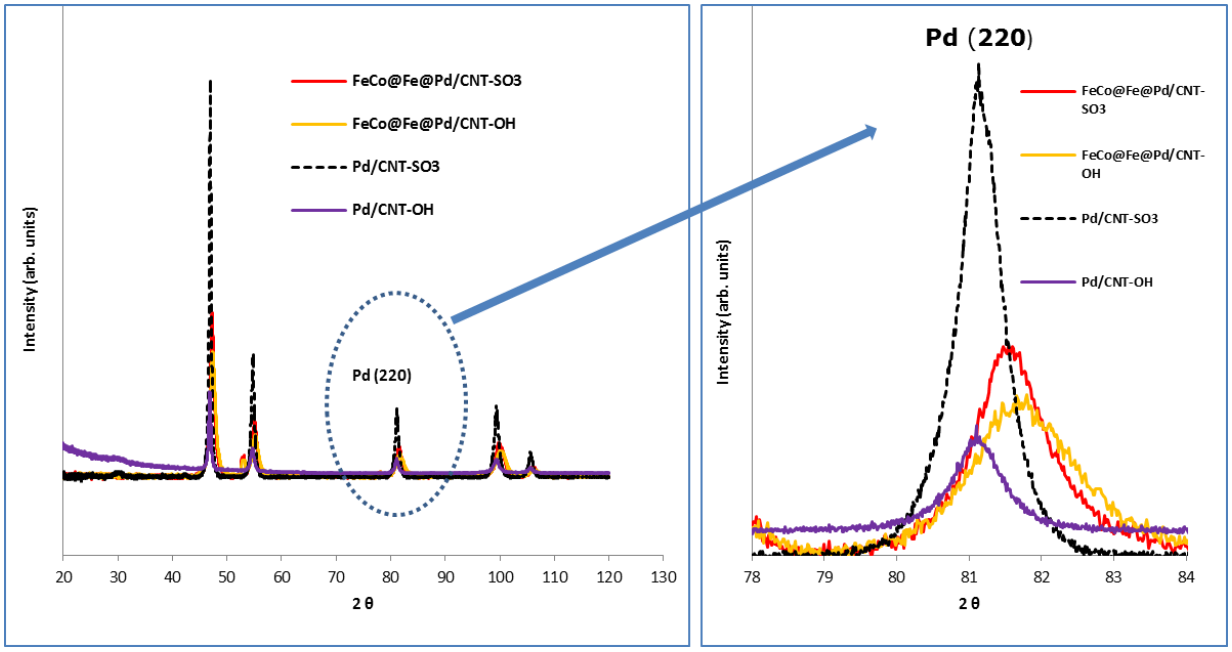

Figure 3. 15: XRD patterns comparing Pd/ on carbon nanotubes with FeCo@Fe@Pd/CNT-OH, FeCo@Fe@Pd/CNT-SO_3 (a) and their detailed Pd (220) diffraction peaks (b).

The intense peaks of the Pd/CNT-OH and Pd/CNT-SO_3 spectra indicate the crystallinity and large sizes of both catalysts. The broader peaks of the core shell Pd based nano catalysts show that they have smaller particle sizes. There are obvious shifts in the diffraction peaks to higher 2θ positions of the two Pd based core shell nano catalysts compared to those of the two single Pd metal on the same substrates. As an example, the 2θ values for the (220) reflection peak (Fig 3.15b) shifts from 81.06° in Pd/CNT-OH and Pd/CNT-SO_3 to 81.55° and 81.63° in FeCo@Fe@Pd/CNT-SO_3 and FeCo@Fe@Pd/CNT-OH respectively. These shifts show a lattice contraction which indicates the substitution of Pd atoms by those of FeCo@Fe alloy in the Pd lattice. This also resulted in the Pd lattice parameter contraction of the core shell catalysts from 3.8898 Å in Pd to 3.8735 Å and3.8767 Å for FeCo@Fe@Pd/CNT-OH and FeCo@Fe@Pd/CNT-SO_3. This lattice strain effect has already been observed on Pd alloys with Pd rich surface incorporated with other atoms[24–26].

3.6.3 HRTEM

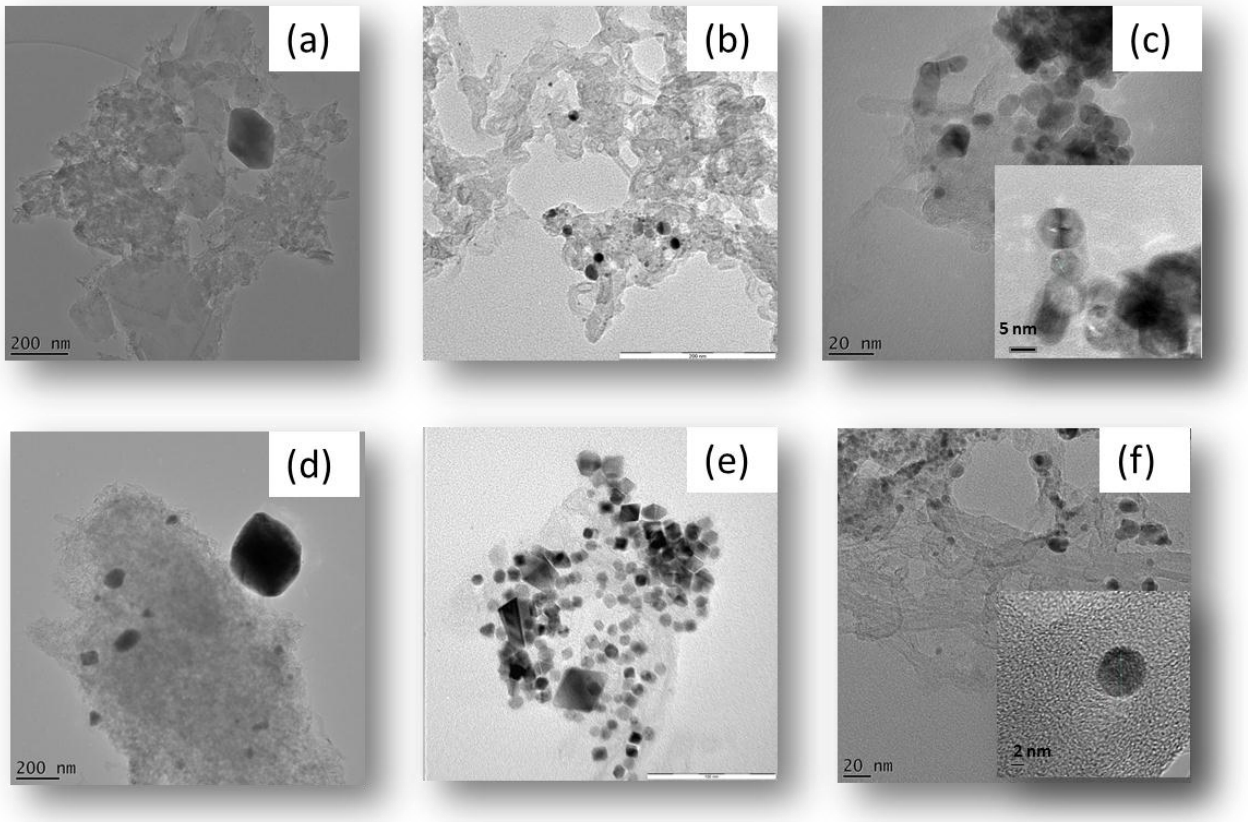

Figure 3. 16: HRTEM images of FeCo@Fe@/CNT-SO_3 (a), Pd/CNT-SO_3, (b) FeCo@Fe@Pd/CNT-SO_3, (c) FeCo@Fe@/CNT-OH (d), Pd/CNT-OH, (e) FeCo@Fe@Pd/CNT-OH (f). The insets in (c) and (f) are the higher magnifications of the HRTEM images of the core shell nano catalysts

The large sizes of the core alloys, FeCo@Fe/CNT-SO_3 and FeCo@Fe/CNT-OH, are obvious in (a) and (d) images, both having a size of about 200 nm with hexagonal shapes with bright edges; indicating the presence of Fe in the outer layer resulting from segregation from the bulk alloy as a result of annealing. The morphologies of Pd on CNT-SO_3 and CNT-OH are depicted in Figs 3.16 (b) and (e) respectively. Pd/CNT-SO_3 exhibit mainly spherical shapes with particles sizes of < 15 nm though one sees a few nanoparticles of > 40 nm. In comparison to its sulfonate counterpart, Pd on carboxyl functionalised nanotubes, Pd/CNT-OH showed a number of polygonal structures ranging from triangular, cubic, and octahedral to hexagonal shapes. This feature has also been observed by other authors using the Polyol mode (with PVP) of synthesizing Pd nanoparticles[27,28].

The nanoparticle sizes are mainly about 30-40 nm but there are a few larger particles of about 150 nm.

Figures 3.16 (c) and (f) show the HRTEM images of FeCo@Fe@Pd/CNT-SO_3 and FeCo@Fe@Pd/CNT-OH respectively. Their higher magnified images showing the Pd lattice fringes are inserted as insets. Both core shell catalysts exhibit the icosahedral morphology. The nanoparticle size of FeCo@Fe@Pd/CNT-SO_3 is about 12-13 nm which is in good agreement with the calculated crystallite size from XRD. The d- spacing of 0.23 nm was obtained from HRTEM image in the inset of Fig 3.16 c and corresponds to that of the Pd (111) plane (0.225 nm) from XRD. The particle sizes of FeCo@Fe@Pd/CNT-OH are smaller, 5 - 6 nm with a few slightly bigger ones. This also correlates well the calculated size obtained from XRD. The higher magnification image (inset of Fig.3.16 f.) reveals a Pd d-spacing of 0.22 nm which also corresponds to the Pd (111) phase (0.224 nm) from the XRD data. Polygonal Pd nanoparticles with dominant (111) facets are mainly formed during Polyol synthetic process; these facets have been known to exhibit high catalytic properties[12,29].

3.6.4 FESEM

The FESEM characterization gave a confirmation of the observations seen in the HRTEM images. The particle sizes and shapes were maintained. This has also proved the effectiveness of the microwave assisted solvothermal technique – *MITNAD*- used in inducing rapid nano structuring and nano sizing of the core alloy (> 200nm size) to the core shell (<10 nm). While FeCo@Fe@Pd/CNT-SO_3 nano particles appear 'clumped' together with the carbon nanotubes there is an even distribution of the FeCo@Fe@Pd/CNT-OH nano particles. The nanoparticles are non-spherical as they appear with sharp edges.

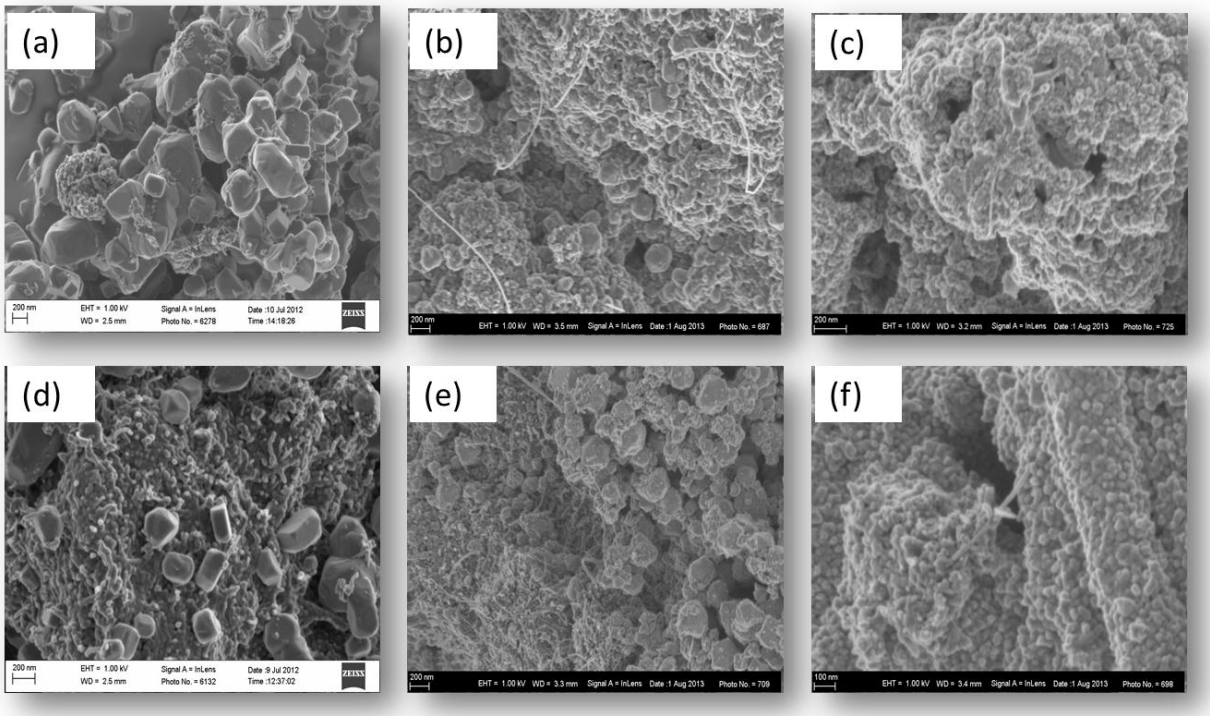

Figure 3. 17: FESEM images of FeCo@Fe@/CNT-SO_3 (a), Pd/CNT-SO_3, (b) FeCo@Fe@Pd/CNT-SO_3, (c) FeCo@Fe@/CNT-OH (d), Pd/CNT-OH, (e) FeCo@Fe@Pd/CNT-OH (f).

3.6.5 STEM HRTEM and HAADF

The catalysts were also characterized using STEM-HAADF imaging. The exceptional resolution of the probe corrected STEM combined with the Z-contrast provides insight into the core-shell nature/structure of core alloy (FeCo@Fe) and core-shell nano catalyst (FeCO@Fe@Pd) deposited on carbon nanotubes. The images are displayed in Figures 3.18, 3.19 and 3.20

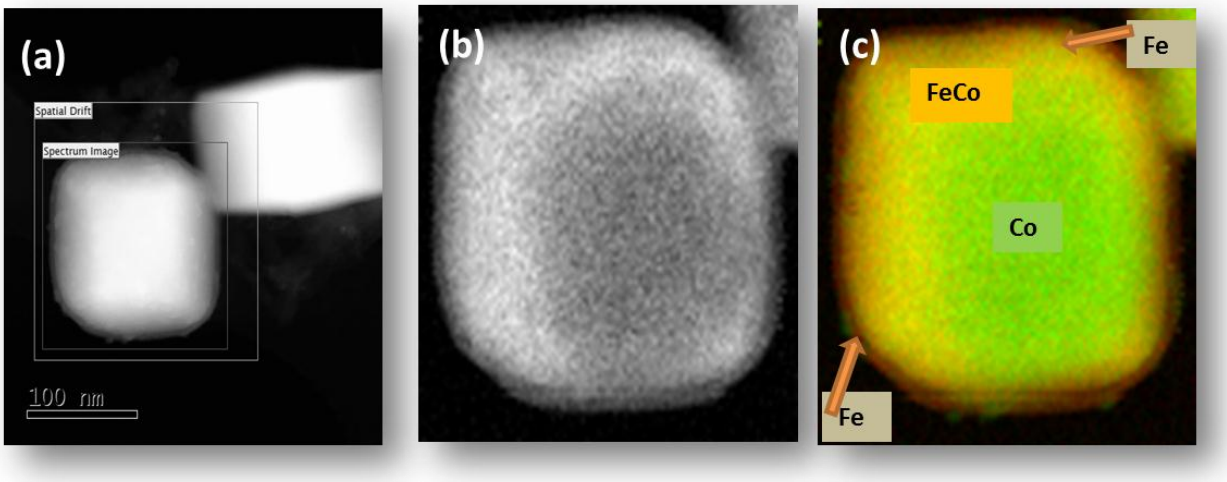

Figure 3. 18: STEM –HAADF (survey) images, (a) EELS spectrum images (b and c) images of the core alloy FeCo@Fe on CNT-OH or CNT-SO_3

Figure 3.18 a shows the STEM-HAADF images of the core alloy FeCo@Fe, the contrast between the inner FeCo core alloy and the segregated Fe shell around the edges of the core alloy was further confirmed by the EELS spectrum images in b and c. This structure had been proposed earlier as a result of the synthetic procedure of the core alloy. The big sizes of FeCo@Fe alloy is also seen in the Fig 3.18 a, as already observed in the Fig 3.16 a and b (HRTEM images) and in Figures 3.17 a and b (FESEM images). These large sizes have prevented the observation of the nanotubes since they are viewed at lower magnifications.

Figures 3.19 show the STEM-HRTEM (a) and STEM-HAADF (b) images of Pd on functionalised carbon nanotubes. The Icosahedral shape of Pd can be clearly seen on the different lattice fringes of the carbon nanotube fibres in the STEM-HRTEM image. A close observation of the STEM-HAADF image reveals the five triangular planar shapes of the icosahedral morphology of the Pd catalyst.

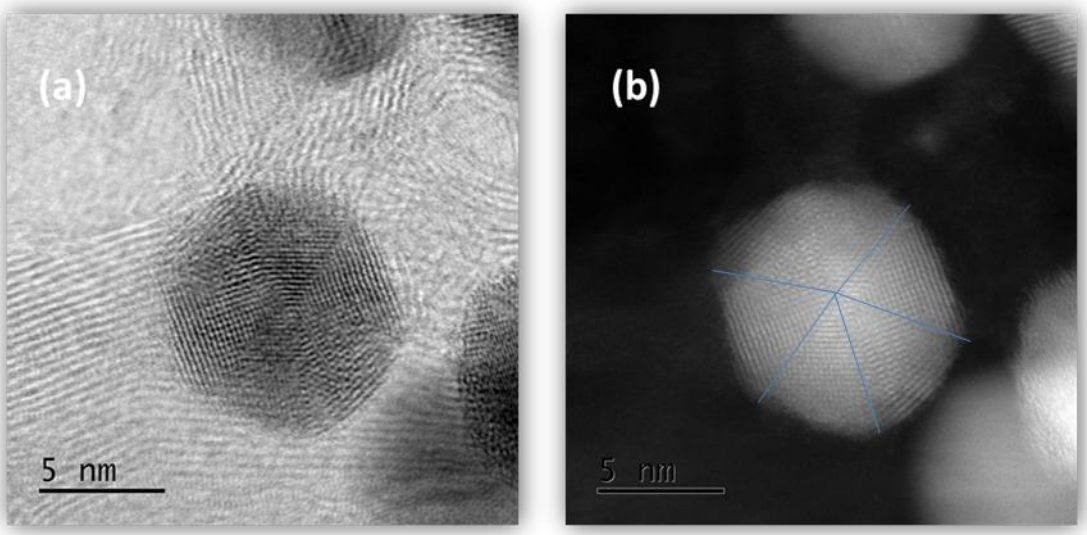

Figure 3. 19: STEM–HRTEM (a) and STEM –HAADF (b) Pd on functionalised carbon nanotubes.

Figures 3.20 display the STEM-HRTEM (a) and STEM-HAADF (b) images of the FeCo@FePd/CNT-OH nano catalyst. The icosahedral shapes of the core shell nano catalysts can be seen. The contrast in the magnitude of the FeCo@Fe core alloy on being decorated by the Pd shell to form FeCo@Fe@Pd core shell nano catalyst is well highlighted in this image. There is a nano-sizing of the former from ≈ 200 – 300 nm to 6.8 – 9 nm sizes in the latter. The carbon nanotube substrates are easily identified all around the core shell nano catalysts. A good scrutiny of the lattice fringes of some of the better magnified core shell nanocatalysts reveal a lack of continuity of the lattice fringes of the Pd shell on the FeCo@Fe core. The core shell images also show the complete segregation of the core alloy from the Pd shell. This contrast is well highlighted in the HAADF-STEM images of the core shell nano catalysts in Fig 3.20 c. Though there are

aggregates of the core shell nano catalysts, the bulk of the nanoparticles reveal a contrast between the core and the Pd shell. The core alloy appears to be centralized in the core shell. The particle size of one of the more prominent nano catalyst seen in the image is 9.3 nm, the FeCo@Fe core is about 6.3 nm, and this gives about 3 nm coverage of the Pd coverage around the core alloy. Some of the other images of the FeCoFe@Pd in the course of this characterisation had the cores situated on the side of the shell and not in the centre as seen below. But the coverage of the core alloy by the Pd-shell was not compromised.

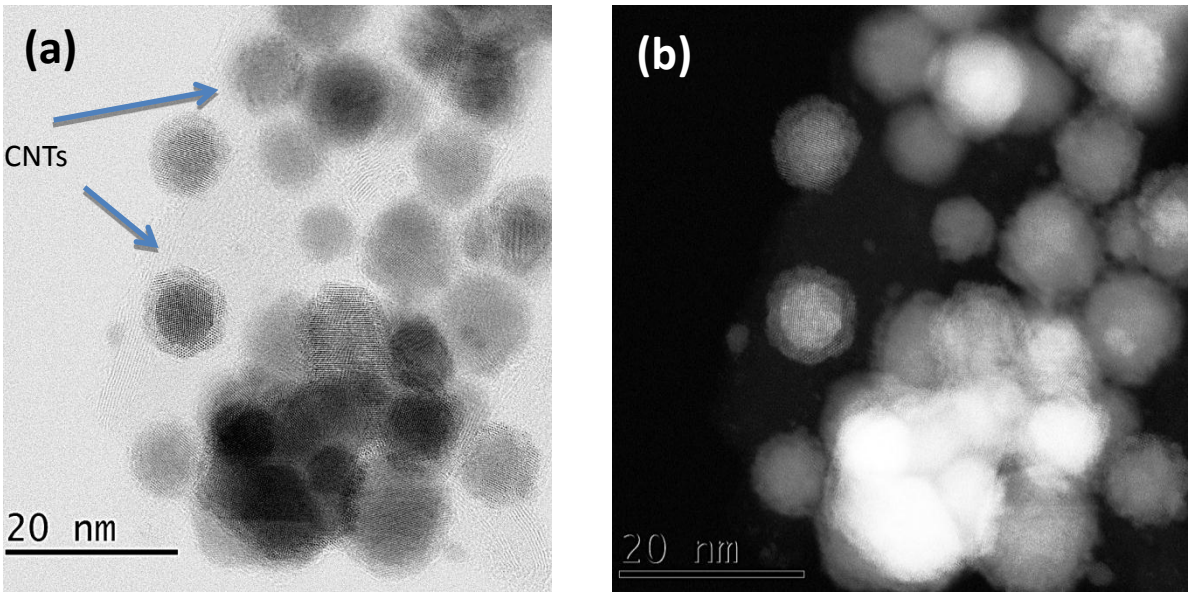

Figure 3. 20: STEM - HRTEM (a) and HAADF images (b) of FeCo@Fe@Pd core-shell nano catalysts on CNT-OH.

3.6.6 Electrochemical Properties (EASA)

Cyclic voltammograms of the Palladium nanocatalysts and FeCo@Fe – core catalysts on functionalised CNTs were done and recorded at 50 mVs^{-1} in a N_2 saturated 1 M KOH solution (Fig 3.21). The CV responses of the palladium nano catalysts show the general features characteristic of palladium. Beginning from the low potential region one can easily distinguish the anodic broad peak at the potentials of about -0.79 V to –0.52 V due to the oxidation of adsorbed and absorbed hydrogen. The formation of the PdO coverage on the surface of the catalysts is accompanied by a small increase in current density and can be seen at about -0.34 V to-0.21 V. The small and broad peak at -0.14 V to 0.02 V can be attributed to the oxidation of quinolic groups comprising carboxyl and ketone groups on the surface of the functionalised multiwalled carbon nanotubes, this has also been observed by other authors[30,31]. The reduction of the Pd oxides to Pd in the reverse scan results in well-defined cathodic peaks at 0.37 V, 0.36 V,0.35 V and 0.33 V for FeCo@Fe@Pd/CNT-OH, FeCo@Fe@Pd/CNT-SO_3, Pd/CNT-OH and Pd/CNT-SO_3 respectively. The appearance of the cathodic PdO reduction peaks of the core shell nanocatalysts in the same voltages as that of Pd mono metals confirms the Pd layer coverage over the core shells. The other less intense and broad cathodic peaks observed between -0.72 V and -0.85 V in all the Pd based catalysts are due to the hydrogen uptake. As the FeCo@Fe core alloys exhibited no electro active response in the medium no further studies were done on them.

The EASA values were estimated using the Pd oxide reduction peaks (Fig. 3.21). The columbic charge, *Q* for the catalysts was 0.2475 mC, 0.1335 mC, 0.0625mC, and 0.0896mC for FeCo@Fe@Pd/CNT-OH, FeCo@Fe@Pd/CNT-SO_3, Pd/CNT-OH and Pd/CNT-SO_3 respectively. Thus ECSA for the four catalysts were calculated as 42.61 m^2g^{-1} (FeCo@Fe@Pd/CNT-OH), 22.66 m^2g^{-1} (FeCo@Fe@Pd/CNT-SO_3), 12.75

m^2g^{-1} (Pd/CNT-OH) and 15.42 m^2g^{-1} (Pd/CNT-SO_3). A summary of the electrochemical properties obtained is found in Table 3.5.

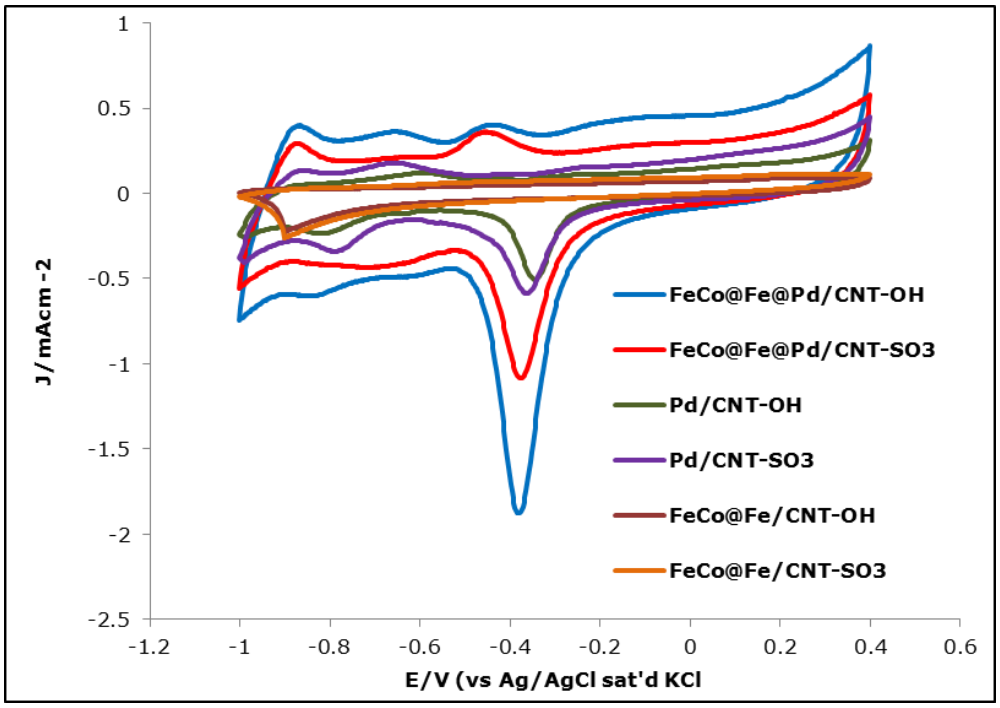

Figure 3. 21: Comparative cyclic voltammograms of FeCo@Fe@Pd/CNT-OH, FeCo@Fe@Pd/CNT-SO_3, Pd/CNT-OH Pd/CNT-SO_3, FeCo@Fe/CNT-SO_3 and FeCo@Fe/CNT-OH catalysts in 0.1 M KOH solution saturated with N_2 at 50 mVs^{-1}.

Table 3.5: Some electrochemical parameters of the four active catalysts on functionalized carbon nanotubes in 1M KOH, sat'd N_2 at 50 mVs^{-1}

Catalyst	PdO $_{red}$ (V)	Q/mC	RSA/cm^2	EASA/ catalyst (cm^2 mg^{-1} Pd)	EASA/ catalyst (m^2g^{-1}Pd)
FeCo@Fe@Pd/CNT-OH	-0.379	0.2475	0.5837	426.05	42.61
FeCo@Fe@Pd/CNT-SO_3	-0.372	0.1335	0.3149	229.85	22.66
Pd/CNT-OH	-0.345	0.0625	0.1747	127.52	12.75
Pd/CNT-SO_3	-0.362	0.0896	0.2113	154.23	15.42

3.7 Conclusion

Various synthetic routes based on microwave wave assisted techniques were investigated in order to choose a most favourable procedure for the synthesis of the nanocatalysts used in this study. Four different methods were explored for the synthesis of core nano alloys of the ”FeCo@Fe series” together with their corresponding four Pd based core shell nano catalysts which were of the “FeCo@Fe@Pd series”. All catalysts were thoroughly characterised to ascertain their morphology, size, and composition. Their electro catalytic activity was tested by using them as cathode materials in ORR in alkaline medium.

The best synthetic method - based on the smaller size, larger surface area and best electro catalytic performance in ORR – was the 2-step synthesis involving the making of the core shell alloy by hydrogen reduction of its salts (FeCo@Fe/C $_{(H)}$) and a subsequent microwave induced top–down nano structuring and decoration –*MITNAD*- (using Pd) to give the Pd based core shell nano catalyst (FeCo@Fe@Pd/C$_{(H)}$). The preferred positions of the component metals (Fe, Co and Pd) in their core shell architecture was also explained using “The prediction trends of core shell preferences” for late transition metals alloy nanoparticles explained by Wang and Johnson[8]. The Norsvok d- band theory was employed to explain the catalytically improved surface of the TS metal comprising the shell (Pd). This was rationalised by the induced contraction of the nano core shell Pd surface as a result of the incorporation of the core alloy into its lattice (as was evident from the XRD studies).

This technique was further used to synthesise the same nano core shell catalysts on two different carbon nanotubes – the carboxylate (o-MWCNTs) and sulfonate (s-MWCNTs) functionalised multi walled carbon nanotubes. Thus, FeCo@Fe@Pd/CNT-OH and FeCo@Fe@Pd/CNT-SO_3 were produced. Their core shell natures even when anchored on the nanotubes were evident from their STEM-HAADF images.

The 2-step route (involving hydrogen reduction and *MITNAD*), used for the synthesis of the ternary Pd based core shell nanocatalysts used in the various studies in the subsequent chapters, has proved to be a very facile, benign, reproducible and economically viable synthetic method for nanocatalysts with core shell design.

3.8 References

(1) Wang, D.; Xin, H. L.; Yu, Y.; Wang, H.; Rus, E.; Muller, D. a; Abruña, H. D. *J. Am. Chem. Soc.* **2010**, *132*, 17664–17666.

(2) Sarkar, a.; Vadivel Murugan, a.; Manthiram, a. *Fuel Cells* **2010**, *10*, 375–383.

(3) Galletti, A. M. R.; Antonetti, C.; Venezia, A. M.; Giambastiani, G. *Appl. Catal. A Gen.* **2010**, *386*, 124–131.

(4) Shao, M.; Liu, P.; Zhang, J.; Adzic, R. *J. Phys. Chem. B* **2007**, *111*, 6772–6775.

(5) Liang, Z. X.; Zhao, T. S.; Xu, J. B.; Zhu, L. D. *Electrochim. Acta* **2009**, *54*, 2203–2208.

(6) Cheong, S.; Watt, J. D.; Tilley, R. D. *Nanoscale* **2010**, *2*, 2045–2053.

(7) Lee, H.; Habas, S. E.; Kweskin, S.; Butcher, D.; Somorjai, G. a.; Yang, P. *Angew. Chemie* **2006**, *118*, 7988–7992.

(8) Wang, L.-L.; Johnson, D. D. *J. Am. Chem. Soc.* **2009**, *131*, 14023–14029.

(9) Ferrando, R.; Jellinek, J.; Johnston, R. L. *Chem. Rev.* **2008**, *108*, 845–910.

(10) Pinski, FJ . Ginatempo, B. Johnson, DD. Staunton, J B. Stocks, GM. Gyorffy, B. *Phys. Rev. Lett.* **1991**, *66*, 766–769.

(11) Hammer, B and Norskov, J. *Surf. Sci.* **1995**, *343*, 211–220.

(12) Mavrikakis, M.; Hammer, B.; Nørskov, J. K. *Phys. Rev. Lett.* **1998**, *81*, 2819–2822.

(13) Kitchin, J. R.; Nørskov, J. K.; Barteau, M. A.; Chen, J. G. *Phys. Rev. Lett.* **2004**, 4–7.

(14) Greeley, J.; Nørskov, J. K. *Surf. Sci.* **2005**, *592*, 104–111.

(15) Greeley, J.; Nørskov, J. K.; Mavrikakis, M. *Annu. Rev. Phys. Chem.* **2002**, *53*, 319–348.

(16) Zhao, J.; Sarkar, A.; Manthiram, A. *Electrochim. Acta* **2010**, *55*, 1756–1765.

(17) Chen, L.; Guo, H.; Fujita, T.; Hirata, A.; Zhang, W.; Inoue, A.; Chen, M. *Adv. Funct. Mater.* **2011**, *21*, 4364–4370.

(18) Yu, Y.; Zhao, Y.; Huang, T.; Liu, H. *Pure Appl. Chem.* **2009**, *81*, 2377–2385.

(19) Chen, Y.; He, B.; Huang, T.; Liu, H. *Colloids Surfaces A Physicochem. Eng. Asp.* **2009**, *348*, 145–150.

(20) Rand, D. A. J.; Woods, R. *J. Electroanal. …Electroanalytical Chem. Interfacial Electrochem.* **1971**, *31*, 29–38.

(21) Zhou, W.; Lee, J. Y. *J. Phys. Chem. C* **2008**, 3789–3793.

(22) Zhong, C.-J.; Luo, J.; Fang, B.; Wanjala, B. N.; Njoki, P. N.; Loukrakpam, R.; Yin, J. *Nanotechnology* **2010**, *21*, 062001.

(23) Antolini, E. *Appl. Catal. B Environ.* **2009**, *88*, 1–24.

(24) Li, R.; Mao, H.; Zhang, J.; Huang, T.; Yu, A. *J. Power Sources* **2013**, *241*, 660–667.

(25) Yang, X.; Yang, Q.; Xu, J.; Lee, C.-S. *J. Mater. Chem.* **2012**, *22*, 8057.

(26) Suo, Y.; Zhuang, L.; Lu, J. *Angew. Chem. Int. Ed. Engl.* **2007**, *46*, 2862–2864.

(27) Xiang, D.; Yin, L. *J. Mater. Chem.* **2012**, *22*, 9584.

(28) Kristian, N.; Yu, Y.; Gunawan, P.; Xu, R.; Deng, W.; Liu, X.; Wang, X. *Electrochim. Acta* **2009**, *54*, 4916–4924.

(29) Jiang, Y.; Lu, Y.; Li, F.; Wu, T.; Niu, L.; Chen, W. *Electrochem. commun.* **2012**, *19*, 21–24.

(30) Jürmann, G.; Tammeveski, K. *J. Electroanal. Chem.* **2006**, *597*, 119–126.

(31) Zhu, C.; Guo, S.; Dong, S. *J. Mater. Chem.* **2012**, *22*, 14851.

Chapter 4*

OXYGEN REDUCTION REACTION AT FeCo@Fe@Pd/C

* The following publications resulted from part of the research work presented in this chapter and they are not referenced further.

1. O.O. Fashedemi, Basil Julies and K.I. Ozoemena, "Synthesis of Pd-coated FeCo@Fe/C core-shell nanoparticles: microwave-induced 'top-down' nanostructuring and decoration". *Chem. Commun.,* **2013**, 49, 2034-2036.
2. Omobosede O. Fashedemi and Kenneth I. Ozoemena, "Enhanced methanol oxidation and oxygen reduction reactions on palladium-decorated FeCo@Fe/C core–shell nanocatalysts in alkaline medium", *Phys. Chem. Chem. Phys.*, **2013**,**15**, 20982-20991

4.1 Introduction

Palladium (Pd)-based electrocatalysts have continued to be a subject of major research interest for application in direct alkaline alcohol fuel cells (DAAFC)[1–3]. There are several reasons for such research interest and they include (i) Pd is more abundant in nature and so stands a better chance of replacing the expensive platinum (Pt), (ii) Pd exhibits better kinetics for DAAFC than Pt catalysts, (iii) reaction dynamics are best facilitated in alkaline media compared to the acidic media, (iv) alcohol cross-over from anode to cathode may be minimised since cell conductance is affected by the electro-osmotic drag of hydrated hydroxyl ions. In low temperature DAAFC, cathode performance losses associated with alcohol crossover arise from the fact that most Pt-based cathode systems are catalytically active to alcohol oxidation under cell operating conditions, leading to a mixed cathode potential. This represents a serious problem as it also influences the ORR negatively[4]. Without doubt, one possible solution to the problem will be found in the development of alternative oxygen reduction catalysts that are inactive to methanol oxidation through modified cathode structure and component.

In the above context, the need for a Pd-based electrocatalyst that permits efficient alcohol oxidation reaction (AOR) kinetics, oxygen reduction reaction (ORR) kinetics and, importantly, tolerates the presence of alcohol in the cathode side should alcohol cross-over occurs during cell operation. Pd-based core shell nanocatalysts are known to enhance ORR activities.
This catalyst is easy to fabricate, and for ORR, it exhibits fast kinetics which can be judged by its high exchange current density value and low Tafel value and it also shows a very high resistance to methanol cross over at high concentrations in the cathode region.

4.2 Comparative Cyclic Voltammetric Evolutions

The activities of the Pd-based nanocatalysts were investigated for ORR in 0.5 M KOH at Pd/C, FeCo@Fe/C and FeCo@Fe@Pd/C. From Fig. 4.1, it is evident that FeCo@Fe@Pd/C showed the best ORR activity in terms of onset potential and reduction current density. The onset potentials are -0.07 V (FeCo@Fe@Pd/C), –0.15 V (Pd/C) and –0.2 V (FeCo@Fe/C), meaning that FeCo@Fe@Pd/C requires the least energy for ORR to occur. Also, the current densities decrease as FeCo@Fe@Pd/C (1.150 mA cm^{-2}) > Pd/C (0.669 mA cm^{-2}) > FeCo@Fe/C (0.046 mA cm^{-2}). Kuai et al[5] recorded an onset potential of about 0.185mV with a current density of 0.285mAcm^{-2} using 1M KOH for Au@Pd/C catalyst. FeCo@Fe@Pd/C outperforms this catalyst at much less alkaline concentrations.

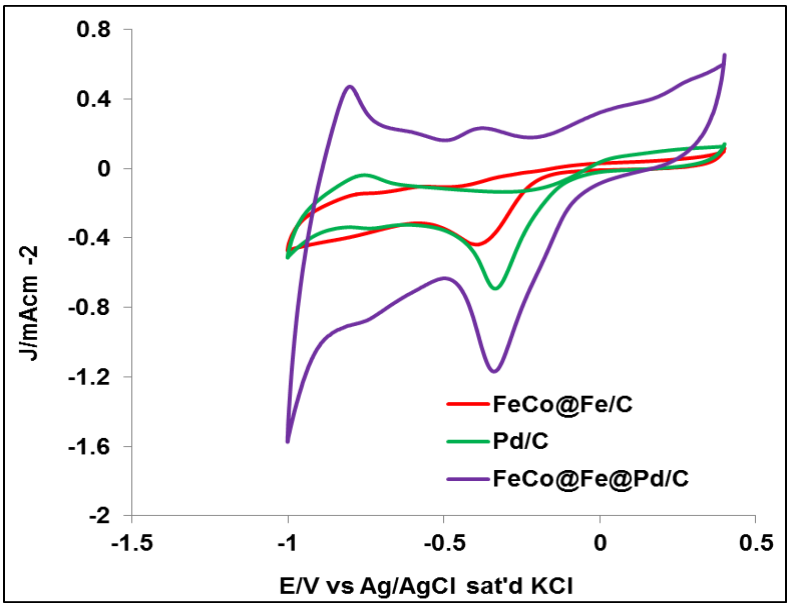

Figure 4. 1: Comparative cyclic voltammograms of FeCo@Fe/C, Pd/C and FeCo@Fe@Pd/C catalysts in 0.1M KOH solution saturated with Oxygen. Sweep rate is 25 mVs^{-1}

Despite the fact that the voltammogram of FeCo@Fe@Pd/C is the most capacitive, this does not compromise its ORR catalytic activity as highlighted above. The thickness of the catalyst film on the modified electrode or nature of the carbon substrate after the two annealing process may have contributed to this observation.

4.3 Rotatory Disc Electrode Experiments

Considering the high performance of the FeCo@Fe@Pd/C, rotating disk electrode (RDE) experiments were done to unravel its electro-kinetic properties towards ORR. Figure 4.2a compares the hydrodynamic plots of the FeCo@Fe@Pd/C modified GCE in an oxygen-saturated 0.1 M KOH solution at different rotation rates (from 200 to 2800 rpm), with the current density increasing with increasing rotation rates. RDE of Pd/C was also done for comparison. The number of electrons involved in the ORR can be obtained from the Koutecky-Levich equation (Equation 1)[6]

$$\frac{1}{j} = \frac{1}{j_d} + \frac{1}{j_k} = \frac{1}{0.21nFD^{2/3}\gamma^{-\frac{1}{6}}C_{O_2}\omega^{\frac{1}{2}}} + \frac{1}{nFkC_{O_2}} \qquad (4.1)$$

where j is the measured current density, j_d is the diffusion-limiting current density, j_k is the kinetic current density, n is the number of electrons transferred, F is the Faraday constant, D is the diffusion coefficient (1.95×10^{-5} cm^2s^{-1}), γ is the kinematic viscosity ($8.98 \times 10^{-3} cm^2s^{-1}$), C_{O2} is the oxygen concentration (1.15×10^{-3} $moldm^{-3}$), ω is the rotation speed, and k is the kinetic rate constant. The linearity of the Koutecky–Levich plot (j^{-1} vs $\omega^{-1/2}$, Fig.4. 2b) is indicative that the reaction is first order, and controlled by kinetics at the electrode surface as well as mass transport of oxygen species. From the slope of the plot, the number of electrons (n) transferred per oxygen molecule was calculated as 3.98, suggesting that the ORR process goes through the direct 4-electron reduction mechanism to produce water as observed in other Palladium based alloy. The good linearity and parallelism of the plots is indicative of the first order reaction kinetics with respect to dissolved oxygen. The 4-electron process was also confirmed by the comparison to the slopes of the Koutecky–Levich plot with the theoretical values of 4- and 2- electron reduction processes. Fig.4. 2 c displays the Hydrodynamic RDE plots of Pd/C, its equivalent K-L plots are shown in Fig 4.2 d. The number of electrons transferred (n) was calculated as 3.6.

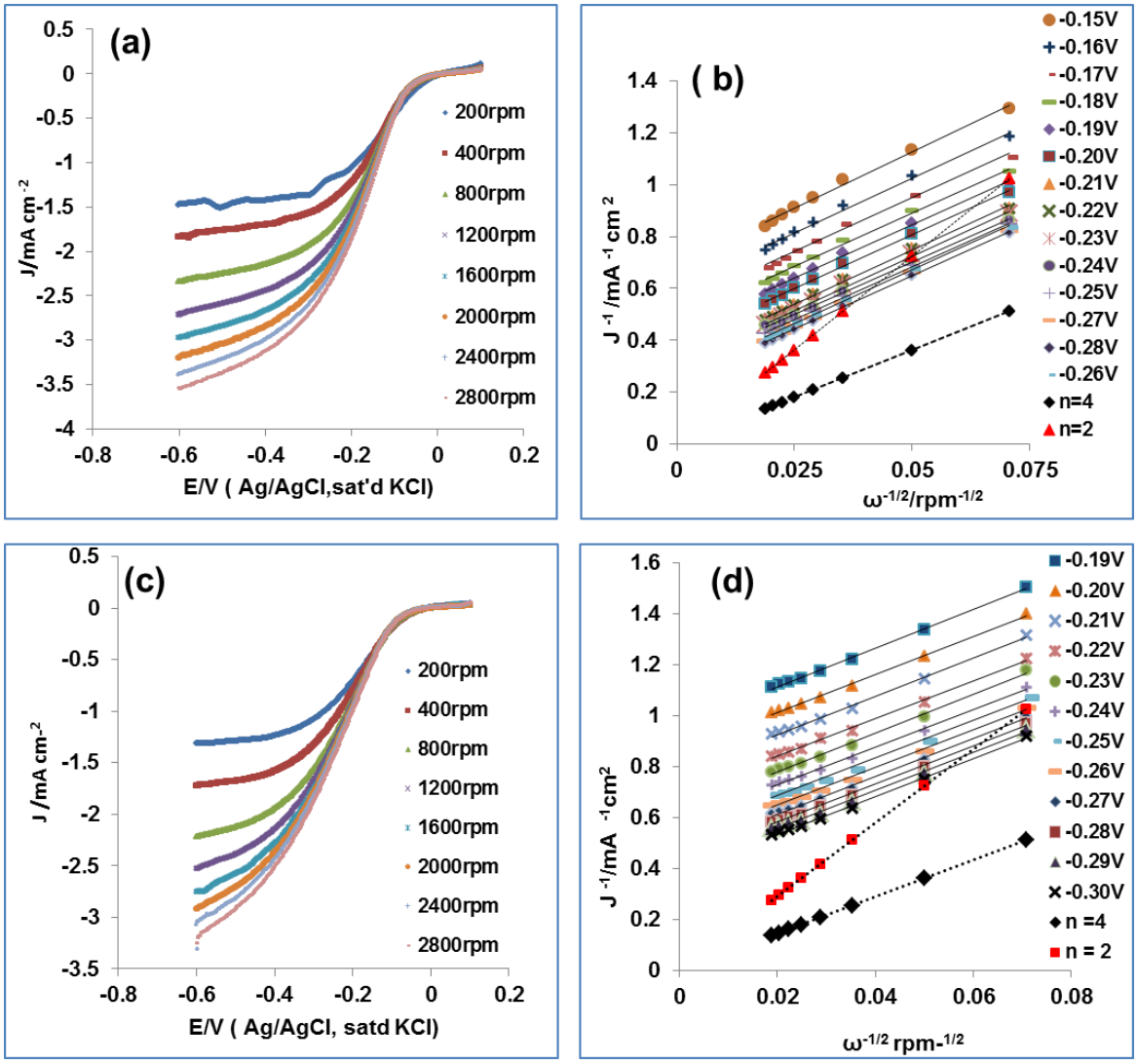

Figure 4. 2: Hydrodynamic voltammograms of FeCo@Fe@Pd/C and Pd/C (a and c) and their equivalent K-L plots (b and d), in 0.1 M KOH saturated O_2.

Although, Pd/C also displayed an appreciable oxygen reduction mechanism, FeCo@Fe@Pd/C still proved to be the better catalyst as can be seen in the analysis below. Figure 4.3 shows the RDE curves of both FeCo@Fe@Pd/C and Pd/C at 1600 rpm (4.3a) and the current responses at voltages in the ORR diffusion controlled range (4.3b). A higher current is generated at every active voltage by FeCo@Fe@Pd/C, also the $E_{1/2}$ is shifted about 0.7 V more positive in core shell nano catalyst. This corroborates the findings in the CV test.

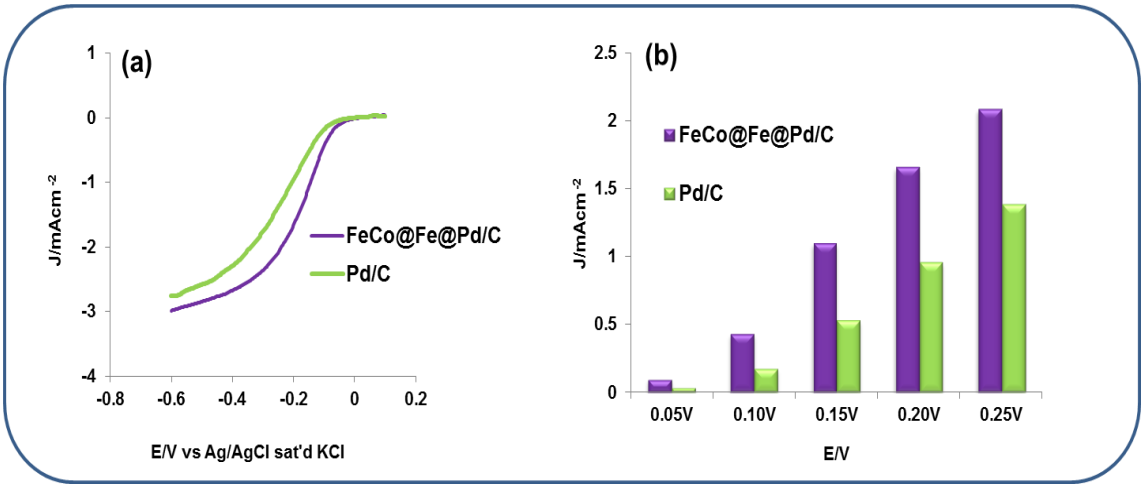

Figure 4. 3: RDE curves of FeCo@Fe@Pd/C and Pd/C at 1600 rpm (a) and the current responses at voltages in the ORR diffusion controlled range (b)

4.4 Stability Studies

The stability or durability of the FeCo@Fe@Pd/C core shell nano catalyst was evaluated by cycling the electrode potential between 0.4 V to -0.1 V versus Ag/AgCl (sat'd KCl) in a 0.1 M KOH solution saturated with N_2 gas. Fig 4.4 gives the cyclic voltammograms of FeCo@Fe@Pd/C from the 5th to the 1,500th cycle. The polarization curves of the 5th and 1,500th cycle are displayed as insets.

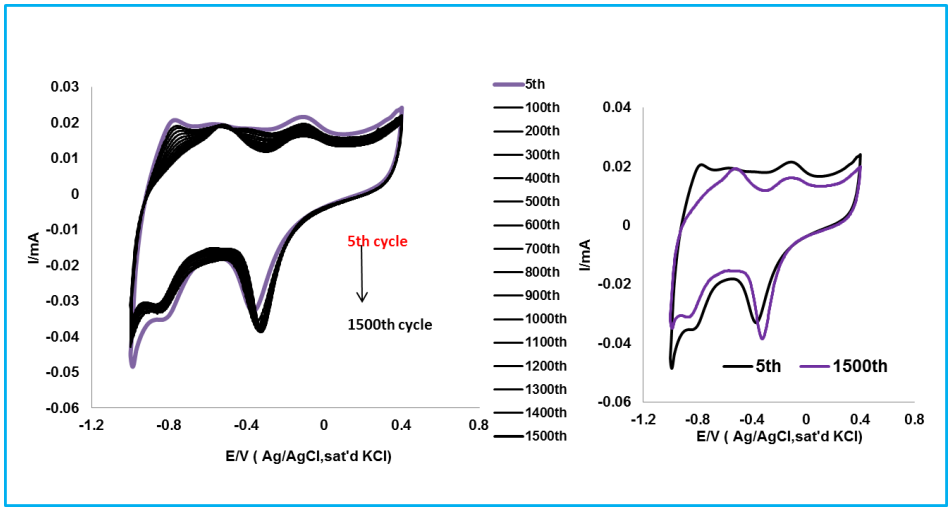

Figure 4. 4: CV polarization curves of FeCo@Fe@Pd/C from the 5th to the 1,500th cycle. The cyclic voltammograms of the 5th and 1,500th cycle are displayed as insets.

It can be seen that the catalyst shows an increased PdO reduction current, which can also be interpreted as an increase in ECSA, in the first few cycles till the 1500th cycle. This can be attributed to surface roughening and removal of contaminants from the surfaces of the catalysts[7]. Since the start of the decrease of the PdO reduction peak was not observed in the first 1,500 potential cycles, one can assume a relative stability of the catalyst on the electrode surface for ORR in alkaline medium.

4.5 ORR Kinetic Parameters

Having ascertained the better catalytic performance of core shell FeCo@Fe@Pd/C catalysts, further studies were done to study its kinetics during the ORR process. The RDE polarization curves (Fig 4.2a) are characteristic of mixed kinetic- and diffusion-controlled currents with no well-defined mass transport–limited current. Similar shapes of polarization curves were observed in Pd –Ni nanoalloys[8] and Pd_3Fe@Pt /C nano catalysts[9]. This is a feature observed in porous electrode in which the depth of O_2 penetration inside the electrode structure changes with potential. Such features have been attributed to the presence of a polymer or Nafion thin film. Thus the kinetic parameters can be estimated from the Koutecky-Levich equation (Equation 4.1), assuming the so-called *'two-layer model'* (i.e., diffusion in both the polymer/Nafion film used as catalyst binder and in the hydrodynamic boundary layer)[10,11].The kinetic current (j_k) can then be evaluated as seen in equations 4.2–4.4:

$$\frac{1}{j_k} = \frac{1}{|j_o| \exp^{|\eta/b|}} + \frac{1}{j_l^{f-ad}} \tag{4.2}$$

$$\eta = E - E_{eq} = -b\left(\ln\left|\frac{j_k}{j_l^{f-ad} - j_k}\right| + \ln\left|\frac{j_l^{f-ad}}{j_o}\right|\right) \tag{4.3}$$

$$\eta = E - E_{eq} = -\frac{1}{\alpha n f}\left(\ln\left|\frac{j_k}{j_l^{f-ad} - j_k}\right| + \ln\left|\frac{j_l^{f-ad}}{j_o}\right|\right) \tag{4.4}$$

Where j_k is the kinetic current density, j_l^{f-ad} is the limiting current density due to diffusion through the Nafion film and adsorption on the catalyst particles (it is difficult to separate their individual contribution, but the value can be easily estimated from the plot of j_k^{-1} vs η,- see typical representative plot in Figure 4.5a). Having obtained the value of the limiting current density (i.e., $j_l^{f-ad} = j_l = 3.23$ mAcm^{-2}) a graph of ln ($|j_k/(j_l-j_k)|$) vs the overpotential (η) was plotted, which gave a straight line (4.5b), the slope of which the Tafel slope b was obtained (59.7 mVdec^{-1}), and from the intercept of which the exchange current density j_o was calculated as 8.23 x 10^{-2} mAcm^{-2}. The low Tafel slope b *(ca.* 60 mVdec^{-1}, i.e. RT/F) may be due to adsorption isotherm of the oxygenated species (Temkin behaviour) as observed by other authors[12].

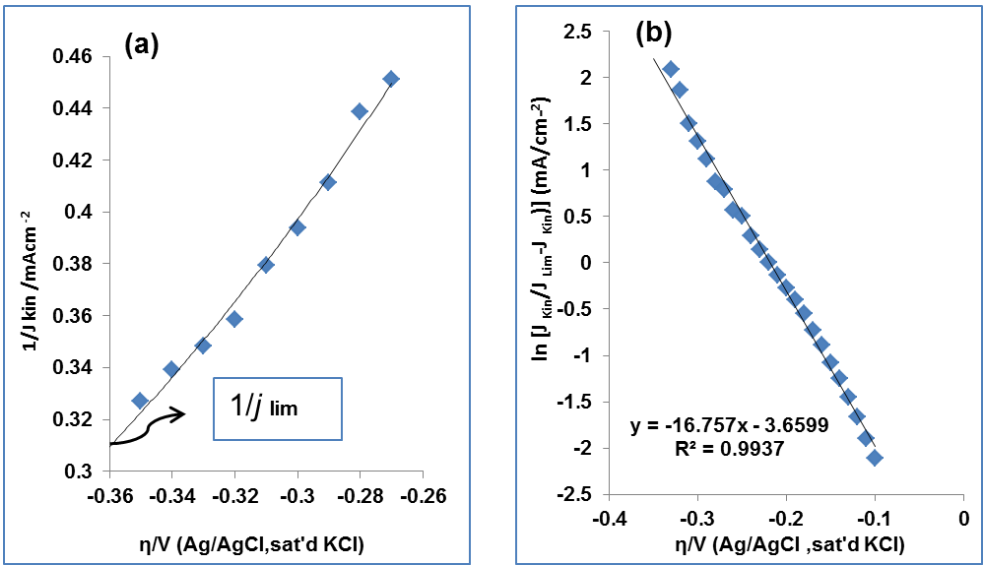

Figure 4. 5: (a) Plot of J^{-1} vs η and (b) Plot of ln($|j_k/(j_l-j_k)|$) vs η

Apparently, on thin –film Pd electrodes the Pd oxides are reduced in more negative potentials than the range of Tafel analysis which results in a single Tafel slope. The exchange current density is an important kinetic parameter representing the electrochemical reaction rate at equilibrium. The magnitude of the exchange current density determines how rapidly the electrochemical reaction can occur. A high effective surface area is known to be a major contributor to high exchange density[13]. This further

proves the high ORR catalytic capabilities of the FeCo@Fe@Pd/C catalyst with j_o value of about two orders higher in magnitude than some Platinum based catalysts[14–16].

Table 4.1 gives a summary of the performance of FeCo@Fe@Pd/C core-shell alloy in comparison to other Pd based alloys for ORR. Its better onset potential for ORR is noticeable at very low alkaline concentrations compared to some of the other catalysts. Its oxygen reduction process also goes through the 4-electron direct pathway which is the highly preferred pathway for ORR in fuel cell processes. Pd-Sn/C which is the other catalyst undergoing this pathway begins its ORR at a later potential. Its Tafel value is also comparable to the other Pd based catalysts.

Table 4.1: Comparative table showing onset reduction potential (E_{red} onset), number of overall electrons transferred and Tafel values of FeCo@Fe@Pd/C and other catalysts in ORR

Pd-based catalyst	**Electrolyte**	***E* red onset[1] (V)**	**No of ès**	**Tafel slope (mVdec^{-1})**	**Reference**
FeCo@Fe@Pd/C	0.1M KOH	-0.07 Vs Ag/AgCl	3.98	59.8	This work
Pd-Ni/C (3:1)	0.1M KOH	-0.125 Vs Hg/HgO	3.4	48/110	17
Ag_1Pd_1/CNT	1 M NaOH	≈-0.1 Vs Ag/AgCl	2.11	n/a	18
Ag_2Pd_1/CNT	1 M NaOH	≈-0.1 Vs Ag/AgCl	1.88	n/a	18
Ag_4Pd_1/CNT	1 M NaOH	≈-0.1 Vs Ag/AgCl	2.25	70/ 136	18
Pd-Sn/C	0.5M KOH	0.9 vs RHE (-0.19 vs Ag/AgCl)	3.8	48/110	19
Pd@Ag/C	0.1 NaOH	0.0 vs Hg/HgO	n/a	60/120	20

4.6 MeOH Tolerance

Methanol cross-over in fuel cells is a very serious problem as it leads to high overvoltage, influences the ORR negatively, and competes with ORR mechanism[21], hence the need to understand the impact of methanol in ORR. The ORR activity at FeCo@Fe@Pd/C catalysts was evaluated in the presence of different molar concentrations of methanol (Fig 4.6). There was no obvious negative shift in the onset potentials or in the current density in the presence of 2 M and 3 M methanol. This shows there is no negative influence of methanol on the catalyst as it exhibits a good tolerance to the presence of high concentrations of methanol.

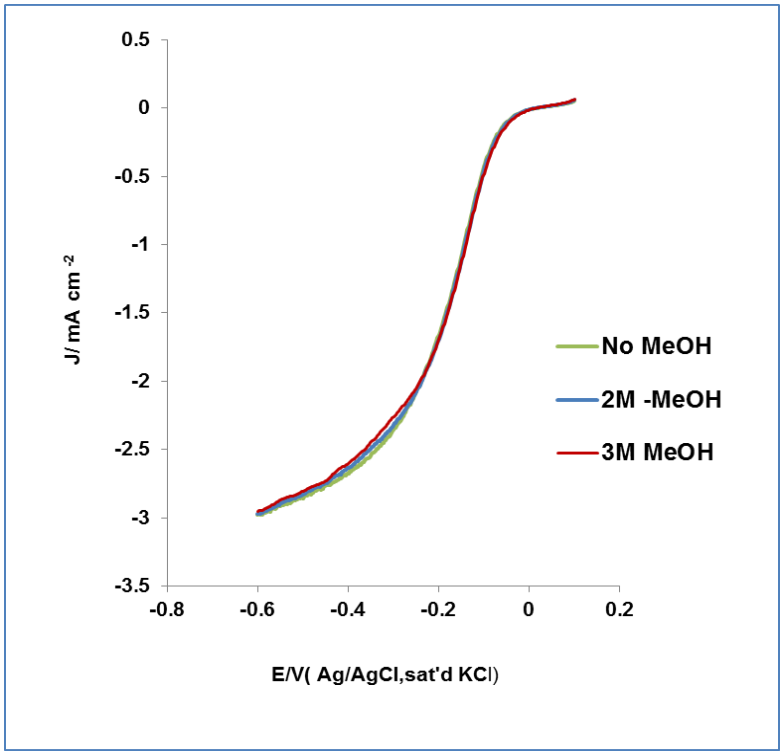

Figure 4. 6: ORR at 1600rpm in 0.1 M KOH sat'd O_2 in the presence of, 2M and 3M, methanol.

4.7 Conclusion

Though a considerable controversy still exists about the detailed reaction mechanism in ORR, two main steps governing ORR are: (i) the first electron transfer to the adsorbed oxygen molecule – molecular oxygen dissociation - and (ii) the removal of the adsorbed intermediates (mainly O and OH) formed after the O-O bond rupture[21,22]. The better ORR activity of FeCo@Fe@Pd/C core-shell nanocatalysts can be explained as a result of the combination of both ligand and geometric effects. Here, an electronic shift and geometric strain in the shell due to the underlying core favourably modify the binding energies of reaction intermediates. This occurs particularly in the direct four-electron transfer. The presence of a nano alloy of Fe-rich surface, embedded in Pd (with a mole ratio of 1:3) will cause a lowering of its oxygen binding energy and thus result in a weak Pd-O/ Pd-OH bond. This will improve its ORR activity as a result of the faster kinetics in breaking these bonds. This is consistent with the findings of other authors. Shao et al [23]conducted a study on some Pd based alloy using the density functional theory (DFT). Their findings revealed that Pd monolayer on Pd_3Fe (111) has different electronic properties from pure Pd, which causes a large difference in ORR activity between the two surfaces. The latter has its BE_o (bindng enery of atomic oxygen) shifted down by 0.25eV compared to Pd (111) which significantly lowers the binding energy of O and/or OH to the surface causing a weakening of Pd-O/ Pd-OH bonds and thus a faster removal of O and OH. Pd alloys which bind strongly with O or OH atoms are not expected to be very catalytically active towards ORR because of their slow kinetics in breaking O-O bonds. Additionally, the sluggishness of this step also impedes the adsorption of O_2 as the adsorption sites are occupied with O/OH. The large ECSA of FeCo@Fe@Pd/C can also not be left out in explaining its higher ORR catalytic performance. This is attributed to its smaller size and even distribution on the substrate as seen from its physical characterisations.

4.8 References

(1) Mazumder, V.; Chi, M.; Mankin, M. N.; Liu, Y.; Metin, Ö.; Sun, D.; More, K. L.; Sun, S. *Nano Lett.* **2012**, *12*, 1102–6.

(2) Kim, J. S.; Yu, J. K.; Lee, H. S.; Kim, J. Y.; Kim, Y. C.; Han, J. H.; Oh, I. H.; Rhee, Y. W. *Korean J. Chem. Eng.* **2005**, *22*, 661–665.

(3) Zhu, C.; Guo, S.; Dong, S. *Adv. Mater.* **2012**, *24*, 2326–31.

(4) Jeyabharathi, C.; Venkateshkumar, P.; Mathiyarasu, J.; Phani, K. L. N. *J. Electrochem. Soc.* **2010**, *157*, B1740.

(5) Kuai, L.; Yu, X.; Wang, S.; Sang, Y.; Geng, B. *Langmuir* **2012**, *28*, 7168–73.

(6) Bard, Allen J, Faukner, L. R. *Electrochemical Methods:Fundamentals and Applications*; 2nd ed.; Wiley, New York: New York, 2001; p. 864 Pages.

(7) Wang, D.; Xin, H. L.; Yu, Y.; Wang, H.; Rus, E.; Muller, D. a; Abruña, H. D. *J. Am. Chem. Soc.* **2010**, *132*, 17664–6.

(8) Zhao, J.; Sarkar, A.; Manthiram, A. *Electrochim. Acta* **2010**, *55*, 1756–1765.

(9) Wang, R.; Zhou, T.; Qiu, X.; Wang, H.; Wang, Q.; Feng, H.; Linkov, V.; Ji, S. *Int. J. Hydrogen Energy* **2013**, *38*, 10381–10388.

(10) Schmidt, T. J.; Gasteiger, H. A.; Behm, R. J. *J. Electrochem. Soc.* **1999**, *146*, 1296–1304.

(11) Coutanceau, C.; Croissant, M. .; Napporn, T.; Lamy, C. *Electrochim. Acta* **2000**, *46*, 579–588.

(12) Erikson, H.; Kasikov, A.; Johans, C.; Kontturi, K.; Tammeveski, K.; Sarapuu, A. *J. Electroanal. Chem.* **2011**, *652*, 1–7.

(13) Wang, J. X.; Markovic, N. M.; Adzic, R. R. *J. Phys. Chem. B* **2004**, *108*, 4127–4133.

(14) Parthasarathy, A.; Srinivasan, S.; Appleby, A. J.; Martin, C. R. *J. Electrochem. Soc.* **1992**, *139*, 2530–2537.

(15) Stassi, a.; D'urso, C.; Baglio, V.; Blasi, a.; Antonucci, V.; Arico, a. S.; Castro Luna, a. M.; Bonesi, a.; Triaca, W. E. *J. Appl. Electrochem.* **2006**, *36*, 1143–1149.

(16) Meng, H.; Shen, P. K. *J. Phys. Chem. B* **2005**, *109*, 22705–9.

(17) Li, B.; Prakash, J. *Electrochem. commun.* **2009**, *11*, 1162–1165.

(18) Lee, C.-L.; Chiou, H.-P.; Chang, K.-C.; Huang, C.-H. *Int. J. Hydrogen Energy* **2011**, *36*, 2759–2764.

(19) Kim, J.; Momma, T.; Osaka, T. *J. Power Sources* **2009**, *189*, 909–915.

(20) Wen, Z.; Liu, J.; Li, J. *Adv. Mater.* **2008**, *20*, 743–747.

(21) Song, C.; Zhang, J. *PEM Fuel Cell Electrocatalysis and Catalyst Layers: Fundamentals and Applications*; Song, C., Ed.; Springer, 2008; p. 1159.

(22) Yang, X.; Hu, J.; Fu, J.; Wu, R.; Koel, B. E. *Angew. Chemie* **2011**, *123*, 10364–10367.

(23) Shao, M.; Liu, P.; Zhang, J.; Adzic, R. *J. Phys. Chem. B* **2007**, *111*, 6772–5.

Chapter 5*

ELECTROCATALYTIC OXIDATION OF MONOHYDRIC ALCOHOLS AT FeCo@Fe@Pd/C

* The following publications resulted from part of the research work presented in this chapter and they are not referenced further.

1. Omobosede O. Fashedemi and Kenneth I. Ozoemena. "Enhanced methanol oxidation and oxygen reduction reactions on palladium-decorated FeCo@Fe/C core–shell nanocatalysts in alkaline medium" *Phys. Chem. Chem. Phys.*, **2013**,**15**, 20982-20991
2. Omobosede O. Fashedemi and Kenneth I. Ozoemena. "Comparative electrocatalytic oxidation of ethanol, ethylene glycol and glycerol in alkaline medium at Pd-decorated FeCo@Fe/C core-shell nanocatalysts." *Electrochimica. Acta*, **2014**, 128, 279-286

5.1 Introduction

Development of novel catalysts with high electrocatalytic activity for methanol and ethanol oxidation has been receiving much attention. This is as a result of the fact that alcohols of lower molar mass are widely proposed as possible fuels for mobile applications[1,2]. As methanol (MeOH) is the simplest alcohol and its C-C bond is not broken during its oxidation process, the electrochemical reaction kinetics is faster than those of other alcohol fuels. Methanol also has a high energy density (6100 Wh kg^{-1}), and coupled with its being a safe fuel for storage. Direct methanol fuel cells (DMFCs) have been extensively studied over the decades. Toxicity of methanol however limits its widespread use by consumers. On the other hand ethanol (EtOH) is more attractive as it is less toxic, thus more environmentally friendly; it also has a higher energy density than methanol (8,000 Wh kg^{-1}) and can be produced in large quantities through green fermentation process. Additionally ethanol has been proven to have a lower cross over rate and affects the cathode performance less severely than methanol. Thus, direct ethanol fuel cells (DEFCs) have also been receiving great attention[3,4].

However, research on development of electrocatalysts for Direct Alcohol fuel cells (DAFCs) have been focussed on Pt based catalysts. These catalyst are recognized as the best catalysts for low temperature fuel cells[5,6]. But apart from its high cost and limited resource, Pt gets easily poisoned due to surface coverage by poisonous intermediates like Pt-CO during oxidation of alcohols. Pd is a better candidate as it is less expensive, more abundant and can also overcome the CO poisoning effect[7,8]. In comparison with monometallic Pd nanostructures, Pd based alloy nanostructures show enhanced electrocatalytic activities due to the synergetic and electronic effect. Based on this a lot of Pd based alloy nanoparticles have been successfully prepared[9–12]. Multi metallic Pd based alloys have also been widely explored and have been found to have great advantages as catalysts in fuel cells[11,13–15].

As one of the challenges of DAFC development is to reduce the Pt loading and also to have catalyst superior to CO poisoning tolerance, this designed tertiary Palladium nanocatalysts (using some very common and cheap transition metals) in the form of a core shell - FeCo@Fe@Pd/C synthesised in this study can emerge as a better alternative to Pt /C. It has already been noted that for requirements of electrocatalytic activity and durability, core-shell like catalysts seem to be most promising for practical application[16]. The electro-oxidative activity of FeCo@Fe@Pd/C in both methanol and ethanol has been found to be comparable to some platinum based catalysts. The catalyst also exhibits a high tolerance to CO poisoning in both alcohols at low potential.

5.2 Comparative Cyclic Voltammetry Experiments

Figure 5.1a compares the cyclic voltammetric (CV) responses of methanol oxidation reaction (MOR) at GCE modified with FeCo@Fe/C, Pd/C and FeCo@Fe@Pd/C. The data show that unlike Pd/C and FeCo@Fe@Pd/C; FeCo@Fe/C nanocatalysts did not have any activity towards MOR. FeCo@Fe@Pd/C showed excellent electrochemical performance compared to Pd/C. It had a more negative onset potential (E_{onset}) –0.5 V compared to –0.2 V for the Pd/C, meaning that it requires lower energy for MOR to occur at the FeCo@Fe@Pd/C surface than at the Pd/C. The FeCo@Fe@Pd/C catalyst yielded a higher current response (~ 4 times) than the Pd/C. The ratio of the forward anodic peak current density (J_f) to the reverse anodic peak current density (J_b) i.e., (J_f/J_b) is indicative of the ability of the catalyst to tolerate the accumulation of carbonaceous species[17–22]. The J_f/J_b ratios were estimated as 4.2 and 2.7 for FeCo@Fe@Pd/C and Pd/C, respectively, indicating excellent poisoning tolerance during MOR at the core-shell nanocatalyst platform.

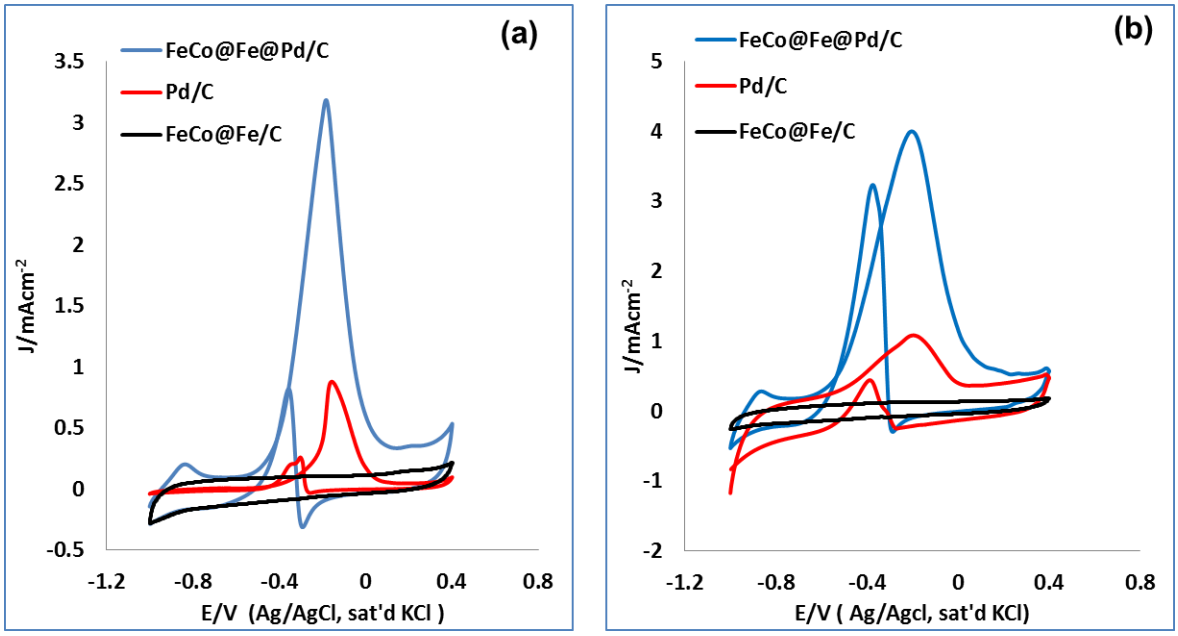

Figure 5. 1: Comparative CVs of FeCo@Fe@Pd/C, Pd/C and FeCo@Fe/C in 0.5 M MeOH/ 0.5 M KOH (a) and 0.5 M EtOH/0.5 M KOH (b) saturated with N_2 respectively, at a scan rate of 25 mVs^{-}

Figure 5.1b displays the comparative CV responses of ethanol oxidation reaction (EOR) on the three catalysts analysed in the MOR studies. The results also showed that FeCo@Fe/C gave no appreciable catalytic activity to ethanol oxidation. Thus no studies were performed on this catalyst again. FeCo@Fe@Pd/C exhibited an outstanding performance with respect to the monometallic Pd/C in EOR with a 70 mV earlier ethanol oxidation onset potential than Pd/C which had an E_{onset} of 640 mV. The current oxidative response (J_p) of FeCo@Fe@Pd/C is also 4 times higher than that of Pd/C. However both catalysts showed almost the same value of $J_f/J_{b,}$ i.e., 1.28 and 1.09 for FeCo@Fe@Pd/C and Pd/C respectively. A summary of the catalytic performances of the nanocatalysts of the oxidation of both MEOH and EtOH are given in Table 5.1.

Table 5.1: Summary of the catalytic oxidative performances from CV studies of FeCo@Fe@Pd/C and Pd/C in both methanol and ethanol**.**

Electrocatalyst	Alcohol	E_{onset} / V	J_p / mAcm^{-2}	J_f/J_b
FeCo@Fe@Pd/C	Methanol	-0.50	3.14	4.2
Pd/C		-0.20	0.83	2.7
FeCo@Fe@Pd/C	Ethanol	-0.71	3.93	1.28
Pd/C		-0.64	0.97	1.09

5.3 Scan Rate Studies

Considering the good performance of the FeCo@Fe@Pd/C in both alcohols further studies on the electrocatalytic behaviour of the FeCo@Fe@Pd/C were performed. To understand the nature of mass transport behaviour of FeCo@Fe@Pd/C, a series of cyclic voltammograms were recorded at different scan rates (25 – 800 mVs^{-1}). The polarisation curves of the different scan rates are seen in Figs 5.2 a and b for MOR and EOR respectively. Their corresponding plots of peak current densities (J_p) vs. square root scan rate ($\nu^{-1/2}$) are shown as insets.

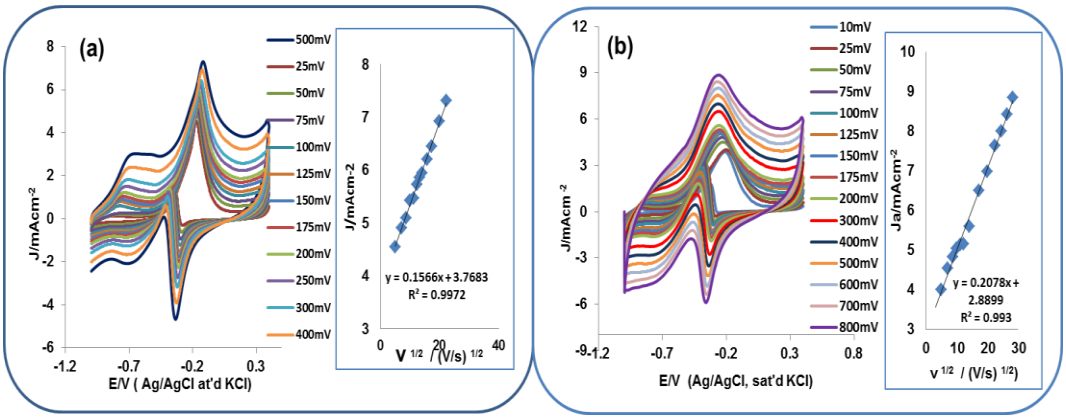

Figure 5. 2: Scan rate studies of FeCo@Fe@Pd/C in MeOH (a) and EtOH (b). The corresponding plots of peak current densities (J_p) vs. square root scan rate ($v^{-1/2}$) are the insets in both diagrams.

The peak current densities were seen to increase with increasing scan rates in both alcohols with little or no shifts in the anodic alcohol oxidation peak potential during each scan. The corresponding plots of the peak current versus the square root of the scan rates gave linear relations with linear regression equation having correlation coefficient (R^2) values of > 0.990. This indicates a diffusion-controlled reaction processes.

5.4 Electrochemical Impedance Spectroscopy

EIS experiments were performed at –0.2 V (vs Ag/AgCl sat'd KCl) to provide further insights into the activities of both FeCo@Fe@Pd/C and Pd/C catalysts in both alcohols. The Nyquist plots obtained are shown in Figs 5.3 (a) and (b) and the equivalent circuit -Rs[(R_{CT} CPE)]-used in fitting the plots is shown as inset. The values of the circuit parameters (R_s- electrolyte solution resistance, R_{CT}-charge transfer resistance and CPE-constant phase element) for the oxidation of each of the alcohol can be seen in Table 5.2.

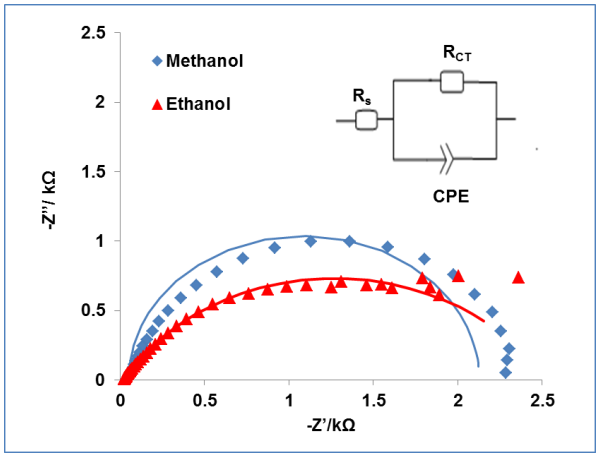

Figure 5. 3: Nyquist plots of FeCo@Fe@Pd/C in 0.5 M [MeOH/EtOH]/0.5 M KOH at 0.2 V vs (Ag/AgCl sat'KCl)

R_{CT} is the most important parameter as it indicates the ease of charge transfer by the catalysts during the electro oxidation reaction. The smaller the value of R_{CT} (the size of semicircle gives a good indication of this) the

faster the electron transport and hence the oxidation reaction process at the modified electrode.

Table 5.2: The values of the components of the circuit (Rs [(R_{CT} CPE)]) used in fitting the Nyquist plots in Fig 5.3.

Alcohol	**Electrochemical Impedance Parameters**			
	***R_s* /Ω**	***R_{ct}* /kΩ**	**CPE / μF**	***n***
Methanol	23.05±0.37	8.10±0.04	45.24±1.73	0.82±0.01
Ethanol	19.80±0.38	6.39±0.05	73.80±1.75	0.76±0.01

The core shell nanocatalyst, FeCo@Fe@Pd/C exhibited good electron transport in oxidation of both alcohols as can be seen from the R_{CT} values which fall within the same range.

5.5 Tafel Analysis

The effect of alcohol concentrations on the electrocatalysis of FeCo@Fe@Pd/C studied at concentrations ranging from 0.5 to 3.0 M alcohol in 0.5 M KOH using linear sweep voltammetry at a rate of 1 mVs^{-1} was also done (Figs 5.4 a and b). A graphical representation of these findings is shown below in Fig 5.4 c. A steady increase in current density was observed with an increase in concentration of the alcohols, and with no significant shift in potential upon increase in the alcohol concentration. This confirms facile mass transport phenomenon as a result of minimal build-up of adsorbates on the catalysts' surface. A decline of the peak current density sets in after 1.25 M in EtOH oxidation and after 1.50 M MeOH oxidation.

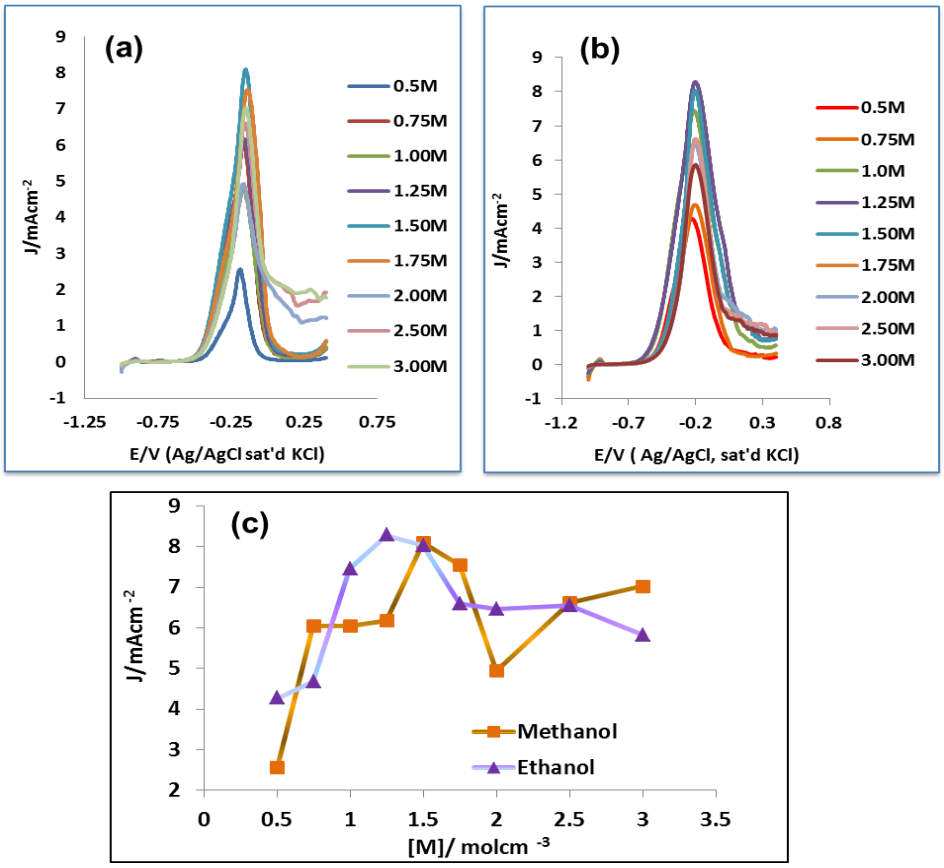

Figure 5. 4: Concentration studies showing LSV plots of FeCo@Fe@Pd/C in 0.5M MeOH/0.5M KOH at 1 mV s^{-1} (a), and in ethanol (b). Graphical representations of plots 5.4 a and b (c)

The conventional Tafel equation for oxidation processes[23–25]; equations (5.1) and (5.2) were used to determine the kinetic parameters.

$$\eta = a + b \log j \qquad (5.1)$$

$$b = \frac{2.303RT}{(1-\alpha)nF} \qquad (5.2)$$

where η is the over potential (difference between the applied potential and open circuit potential), j is the current density , b is the Tafel slope, a is the Tafel constant relating to the exchange current density,α is the transfer coefficient , n is the number of electrons involved in the rate determining step , while other symbols retain their usual meaning. Figures 5.5 (a) and (b) show the plots of η vs log j in both MeOH and EtOH while the attached tables give the kinetic parameters of the alcohols for the molar concentrations studied (0.5 M-3.0 M). The Tafel (b) and

transfer coefficient (*a*) values were obtained at each alcohol concentration studied. Generally, the higher the Tafel slope, the faster the overpotential increases with the current density. Thus, for an electrochemical reaction to obtain a high current at low over potential, the reaction should exhibit a low Tafel value. The transfer coefficient (α) is the fraction of the potential energy that is transferred to the reaction. It is inversely proportional to the Tafel slope. According to Soderberg et al.[26], the minimum α value for any reaction mechanism (ignoring adsorption effects) should be 0.5 and highest b value is 118 $mVdec^{-1}$. Thus, any standard reaction mechanism with α value larger than this is an indication of a better electrocatalytic mechanism.

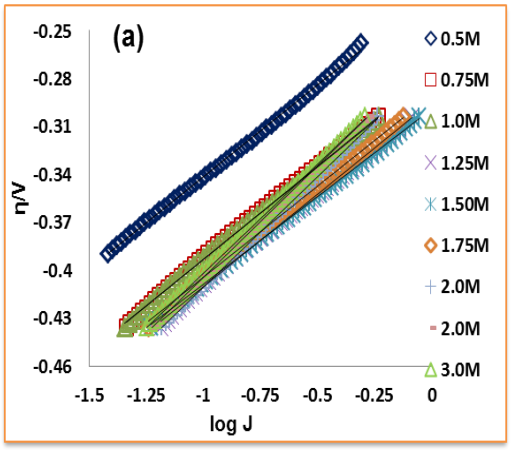

[METHANOL] (M)	Tafel slope (2.303RT/ αnF)	α	a (-RT/αnF) log Jo	R^2
0.5	115.2	0.513	0.2264	0.9987
0.75	117.3	0.504	0.2762	0.9992
1.00	116.0	0.510	0.2773	0.9993
1.25	116.0	0.510	0.2944	0.9988
1.50	109.7	0.539	0.2992	0.9995
1.75	114.5	0.516	0.2901	0.9987
2.00	138.5	0.427	0.2723	0.999
2.50	139.7	0.423	0.2651	1.000
3.00	136.4	0.434	0.2656	0.9998

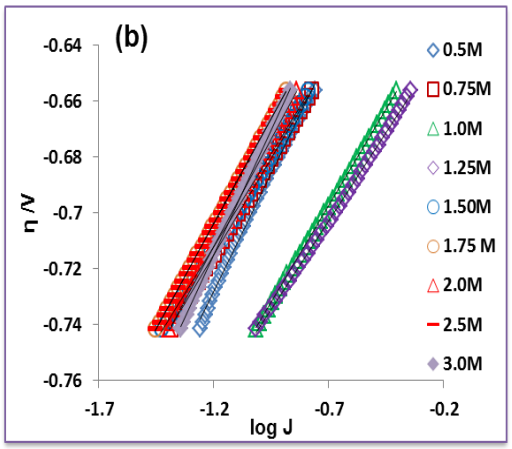

[ETHANOL] (M)	Tafel slope (2.303RT/α nF)	α	a (-RT/αnF) log Jo	R^2
0.5	168.9	0.350	0.5252	0.9965
0.75	138.7	0.426	0.5486	0.9999
1.00	138.5	0.427	0.6003	0.9999
1.25	126.2	0.467	0.6144	0.9991
1.50	133.5	0.443	0.5220	0.9995
1.75	149.5	0.395	0.5239	0.9998
2.00	153.8	0.385	0.5273	0.9998
2.50	149.9	0.395	0.5239	0.9998
3.00	178.5	0.331	0.5007	0.9997

Figure 5. 5: Tafel plots of FeCo@Fe@Pd/C obtained at each of the concentrations of MeOH (a) and EtOH (b) with tables showing the kinetic parameters (*b*) and (*a*) at each of the concentrations studied.

The average Tafel value obtained with FeCo@Fe@Pd/C in MeOH oxidation was found to be 122.59±11.93 with a transfer coefficient value (*a*) of 0.49±0.05. For EtOH oxidation, the average value of *b* was 148.66±16.83 and with a transfer coefficient value (*a*) of 0.40±0.04. Although the Tafel values obtained for the oxidation of both EtOH and MeOH at the FeCo@Fe@Pd/C modified electrode are higher than the expected values, they still fall within the experimental range. The *a* values on the other hand are perfectly within the range expected for a good catalytic reaction. The difference in the two Tafel values for both alcohols is not very significant so one can readily assume a similar kinetic pathway for the oxidation of FeCo@Fe@Pd.CNT-OH in both MeOH and EtOH.

5.6 Chronoamperometry Studies.

Stability and durability of the catalysts during the oxidation processes in both alcohols was studied using chronomperometry (CA) .The CA curves for both MeOH and EtOH oxidation are shown in Fig 5.6.

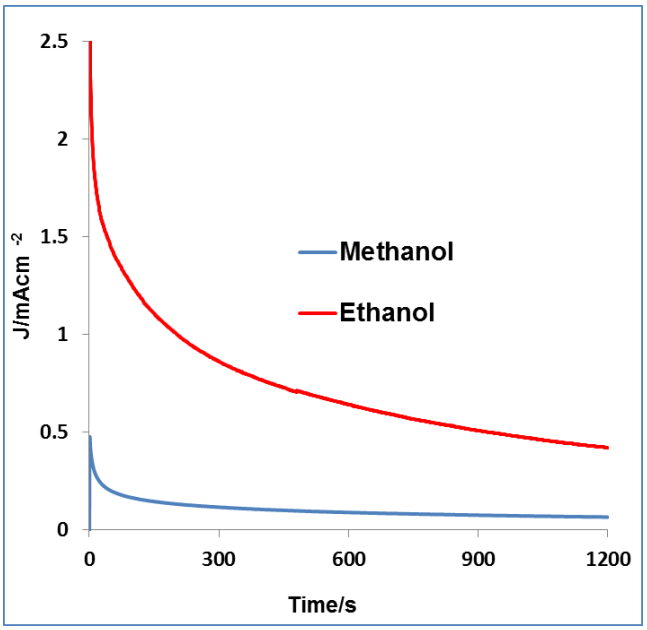

Figure 5. 6: Chronoamperometry curves at 0.5 M [MeOH/EtOH]/ 0.5 M KOH at a constant voltage of -0.2 V.

A higher kinetic current was observed during the EtOH oxidation process. This was maintained throughout the duration of the reaction process. Half

way through the reaction, at 600s, the current exhibited by FeCo@Fe@Pd/C in MeOH and EtOH oxidation were 0.0892 and 0.6408 $mAcm^{-2}$ respectively. The quasi steady current at the end of the reaction followed the same trend with the current at MeOH being 0.0658 mA cm^{-2} and that of EtOH was 0.4212 mA cm^{-2}. It should be noted that this was the first test carried out highlighting a major difference in activities between the alcohol oxidative properties of FeCo@Fe@Pd/C in MeOH and EtOH respectively.

5.7 Electrocatalytic Rate Constant

The catalytic rate of the oxidation of MeOH and EtOH by FeCo@Fe@Pd/C was then obtained using the chronoamperometry data. The electrocatalytic rate constant (K_{cat}) was obtained by employing the conventional equation below:

$$\frac{J_{cat}}{J_{buff}} = \pi^{1/2}\left(kC_o t\right)^{1/2} \tag{5.3}$$

Where J_{cat} and J_{buff} are the current densities in the presence and absence of the alcohols, C_o is the bulk concentration and t is the time. The plots obtained and results are shown in Fig 5.7.

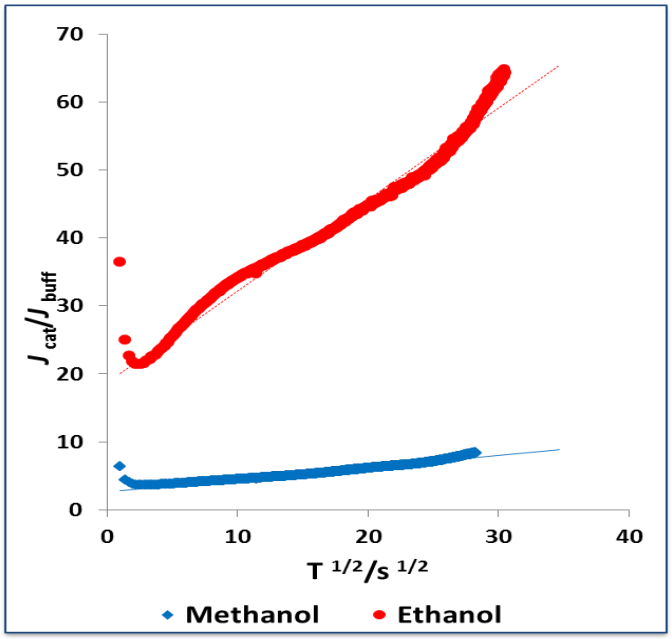

Figure 5. 7: Plots of J_{cat}/J_{buff} vs $t^{1/2}$ for MEOH and EtOH oxidation by FeCo@Fe@Pd/C

K_{cat} values of 2.09 x 10^4 $cm^3mol^{-1}s^{-1}$ and 1.15 x 10^6 $cm^3mol^{-1}s^{-1}$ were obtained as catalytic rate constants in both MeOH and EtOH oxidation respectively. From the values obtained, it is seen that FeCo@Fe@Pd/C core shell nanocatalysts display a high rate of oxidation of both alcohols, but it is evident that its oxidation of ethanol is faster than that of methanol. Its rate of catalysing EtOH is at least two orders higher than that of MeOH.

5.8 Tables of Comparison

It is very evident from the various electrochemical tests carried out so far that the novel FeCo@Fe@Pd/C core shell catalyst will surely serve as a highly efficient anode catalyst in DAAFC like DMFCs and DEFCs. To further boost this argument some comparison was done between FeCo@Fe@Pd/C and other Pd based catalyst used as anodes for the oxidation of MeOH and EtOH in half cell fuel cell studies. This can be seen in Tables 5.3.and 5.4.

Table 5. 3: Comparative table showing the catalyst loading, ECSA, onset potential (E onset), methanol oxidation potential (E peak) and j_f/j_b values of FeCo@Fe@Pd/C and other catalysts

Catalyst	Electrolyte	Pd loading (µg)	ECSA (m^2/g)	E onset (V)	E peak (V)	J_f/J_b	Reference
FeCo@Fe@Pd/C	0.5 M MEOH/ 0.5 M KOH	1.3(24%)	24.57	-0.585 vs Ag/AgCl	-0.19	4.20	This work
Ni-Pd/Si-MCP	1 M MEOH/ 2 M KOH	n/a	9.16	-0.55 vs SCE	-0.06	1.89	[44]
Ni-Pd/Si	1 M MEOH/ 2 M KOH	n/a	3.04	-0.51 vs SCE	-0.05	n/a	[44]
Pd-Mn_3O_4/MWCNT	1 M MEOH/ 0.5 M NaOH	20 wt %	76.19	-0.69 vs SCE	n/a	2.60	[45]
Pd/C- nanodots	1 M MEOH/ 1 M KOH	n/a	n/a	-0.62 vs Ag/AgCl	≈1.08	≈1.08	[46]]
Pd/HCNF	1 M MEOH/ 1 M KOH	20.5 wt %	n/a	≈-0.55 vs SCE	-0.224	≈3.30	[47]
Pd/Pani	1 M MEOH/ 0.5 M NaOH	40	n/a	-0.62 vs SCE	-0.20V	≈2.01	[48]
Pd-Co/CNT (8:1)	1 M MEOH/ 1 M KOH	n/a	n/a	≈-0.35 vs Hg/HgO	≈-0.10	1.20	[49]
CHPN	0.5 M MEOH/ 0.5 M KOH	1	n/a	≈-0.50 vs Ag/AgCl	-0.16V	3.25	[50]
PD XC-72 – (commercial)	1M MEOH/ 1M NaOH	n/a	n/a	-0.45 vs Ag/AgCl	≈-0.30	2.50	[51]
Pd nano flowers	0.5M MEOH/0.5M KOH	500 (0.5mg)	n/a	≈-0.19 vs RHE	0.19	≈5.00	[52]
Au@Pd/C	0.5M MEOH/0.5M KOH	10 metal loading	n/a	≈-0.50 vs Ag/AgCl	-0.12	≈3.00	[53]

Note: CNT-carbon nanotubes, MWCNT –multiwalled carbon nanotubes, Si-MCP- silicon micro channel plates, HCNF- Helical carbon nanofibres, PANI –polyaniline nanofibres film, CHPN- carbon nanotube raspberry hollow Pd nanospheres

Table 5. 4: Comparative table showing the catalyst Pd loading, onset potential (E_{onset}), ethanol oxidation potential (E_{peak}) and j_f/j_b values of FeCo@Fe@Pd/C and other catalysts.

Electrocatalyst	Alcohol solution	Pd loading (µg)	E_{onset} / V	ΔE_p / V	J_p / mAcm^{-2}	J_f/J_b	Ref
FeCo@Fe@Pd/C	0.5 M EtOH /0.5 M KOH	1.3	-0.71 (vs Ag/AgCl)	0.14 (vs Ag/AgCl)	3.93 (214 mAmg^{-1})	1.24	This work
np-$Pd_{75}Au_{25}$	0.5 M EtOH /1.0 M KOH	n/a	-0.58 (vs Ag/AgCl)	≈-0.35 (vs Ag/AgCl)	6.95	1.18	[39]
CHPNs	0.5 M EtOH /0.5 M KOH	1 0	-0.55 (vs Ag/AgCl)	-0.191 (vs Ag/AgCl)	n/a	0.5	[40]
PdNi/CeO/C	1.0 M EtOH /1.0 M KOH	7.6 (PdNi)	≈-0.4	≈0.15	5.3(mAcm^{-2} µg^{-1}PdNi)	1.4	[41]
Pd-PANI nanofibres	1 0M EtOH /0.5 M KOH	40	-0.70 (vs SCE)	-0.17 (vs SCE)	≈1.25	≈1.4	[42]
Pd-TiN	0.5 M EtOH /1 0 M KOH	4.4	-0.572 (vs MMO)	-0.076 (vs MMO)	2.87	0.51	[31]
Ru@PtPd/C	1.0 M EtOH /1.0 M KOH	n/a	≈-0.56 (vs MMO)	-0.1 (vs MMO)	3.6(mAmg^{-1})	1.5	[43]
Pd/HCN-F	0.5 M EtOH /1.0 M KOH	20.5 wt %	≈-0.65 (vs SCE)	-0.273 (vs SCE)	≈52(mAcm^{-2} µg^{-1}Pd)	≈0.8	[44]
NiNWA/PdNP	1.0 M EtOH /0.5 M KOH	n/a	-0.5 (vs MMO)	-0.09 (vs MMO)	0.15	0.25	[45]
NiNWA/PdNF	1.0 M EtOH /0.5 M KOH	n/a	-0.6 (vs MMO)	0.75 (vs MMO)	1.7	1.2	[45]
Pd-CeO_2/C	1.0 M EtOH /1.0 M KOH	300	-0.6 (vs MMO)	-0.09 (vs MMO)	39	0.9	[46]

5.9 Conclusion

Palladium based core shell catalyst -FeCo@Fe@Pd/C - has been used for the electrocatalytic oxidation of two monohydric alcohols, methanol and ethanol. The catalyst showed high oxidative catalytic properties of both alcohols. However, a higher ease of ethanol oxidation was evident from the values of its catalytic rate in constant for ethanol oxidation which was two orders higher than in methanol. This was corroborated by its higher current density values for ethanol after 1,800 seconds of oxidation of both alcohols using chronoamperometry. Its quasi steady current density after the ethanol oxidation process was six times more than that of methanol oxidation.

5.10 References

(1) Ganesan, R.; Lee, J. S. *Angew. Chem. Int. Ed. Engl.* **2005**, *44*, 6557–60.

(2) Rousseau, S.; Coutanceau, C.; Lamy, C. *J. Power Sources* **2006**, *158*, 18–24.

(3) Song, S.; Zhou, W.; Zhou, Z.; Jiang, L.; Sun, G.; Xin, Q.; Leontidis, V.; Kontou, S.; Tsiakaras, P. *Int. J. Hydrogen Energy* **2005**, *30*, 995–1001.

(4) Jiang, L.; Sun, G.; Zhou, Z.; Zhou, W.; Xin, Q. *Catal. Today* **2004**, *93-95*, 665–670.

(5) Wang, C.; Hou, Y.; Kim, J.; Sun, S. *Angew. Chem. Int. Ed. Engl.* **2007**, *46*, 6333–5.

(6) Schnaidt, J.; Heinen, M.; Jusys, Z.; Behm, R. J. *J. Phys. Chem. C* **2013**, *117*, 12689–12701.

(7) Ha, S.; Larsen, R.; Masel, R. I. *J. Power Sources* **2005**, *144*, 28–34.

(8) Roy, P. S.; Bagchi, J.; Bhattacharya, S. K. *Catal. Sci. Technol.* **2012**, *2*, 2302-2310.

(9) Guo, S.; Dong, S.; Wang, E. *Energy Environ. Sci.* **2010**, *3*, 1307.

(10) Chai, J.; Li, F.; Hu, Y.; Zhang, Q.; Han, D.; Niu, L. *J. Mater. Chem.* **2011**, *21*, 17922-17929

(11) Zhao, J.; Jarvis, K.; Ferreira, P.; Manthiram, A. *J. Power Sources* **2011**, *196*, 4515–4523.

(12) Guo, S.; Wang, E. *Acc. Chem. Res.* **2011**, *44*, 491–500.

(13) Guo, S.; Zhang, S.; Sun, X.; Sun, S. *J. Am. Chem.* **2011**, 15354–15357.

(14) Antolini, E.; Colmati, F.; Gonzalez, E. R. *Electrochem. commun.* **2007**, *9*, 398–404.

(15) Spinacé, E. V.; Linardi, M.; Neto, A. O. *Electrochem. commun.* **2005**, *7*, 365–369.

(16) Zhao, X.; Yin, M.; Ma, L.; Liang, L.; Liu, C.; Liao, J.; Lu, T.; Xing, W. *Energy Environ. Sci.* **2011**, *4*, 2736.

(17) Lee, C.-L.; Chiou, H.-P.; Syu, C.-M.; Liu, C.-R.; Yang, C.-C.; Syu, C.-C. *Int. J. Hydrogen Energy* **2011**, *36*, 12706–12714.

(18) Liu, W.; Herrmann, A.-K.; Geiger, D.; Borchardt, L.; Simon, F.; Kaskel, S.; Gaponik, N.; Eychmüller, A. *Angew. Chem. Int. Ed. Engl.* **2012**, *51*, 5743–7.

(19) Maxakato, N. W.; Ozoemena, K. I.; Arendse, C. J. *Electroanalysis* **2010**, *22*, 519–529.

(20) Qiu, C.; Shang, R.; Xie, Y.; Bu, Y.; Li, C.; Ma, H. *Mater. Chem. Phys.* **2010**, *120*, 323–330.

(21) Mayrhofer, K. J. J.; Juhart, V.; Hartl, K.; Hanzlik, M.; Arenz, M. *Angew. Chem. Int. Ed. Engl.* **2009**, *48*, 3529–31.

(22) Mayrhofer, K. J. J.; Strmcnik, D.; Blizanac, B. B.; Stamenkovic, V.; Arenz, M.; Markovic, N. M. *Electrochim. Acta* **2008**, *53*, 3181–3188.

(23) Compton, RG, Banks. C. *Understanding Voltammetry*; 2007; pp. 249–253.

(24) Bard, Allen J, Faukner, L. R. *Electrochemical Methods:Fundamentals and Applications*; 2nd ed.; Wiley, New York: New York, 2001; p. 864 Pages.

(25) Song, C.; Zhang, J. *PEM Fuel Cell Electrocatalysis and Catalyst Layers: Fundamentals and Applications*; Song, C., Ed.; Springer, 2008; p. 1159.

(26) Soderberg, J. N.; Co, A. C.; Sirk, A. H. C.; Birss, V. I. *J. Phys. Chem. B* **2006**, *5*, 10401–10410.

(27) Chen, L. Y.; Chen, N.; Hou, Y.; Wang, Z. C.; Lv, S. H.; Fujita, T.; Jiang, J. H.; Hirata, a.; Chen, M. W. *ACS Catal.* **2013**, *3*, 1220–1230.

(28) Liu, Z.; Zhao, B.; Guo, C.; Sun, Y.; Shi, Y.; Yang, H.; Li, Z. *J. Colloid Interface Sci.* **2010**, *351*, 233–8.

(29) Wei, Y.-C.; Liu, C.-W.; Kang, W.-D.; Lai, C.-M.; Tsai, L.-D.; Wang, K.-W. *J. Electroanal. Chem.* **2011**, *660*, 64–70.

(30) Pandey, R. K.; Lakshminarayanan, V. *J. Phys. Chem. C* **2009**, *113*, 21596–21603.

(31) Thotiyl, M. M. O.; Kumar, T. R.; Sampath, S. *J. Phys. Chem. C* **2010**, *114*, 17934–17941.

(32) Gao, H.; Liao, S.; Liang, Z.; Liang, H.; Luo, F. *J. Power Sources* **2011**, *196*, 6138–6143.

(33) Hu, G.; Nitze, F.; Barzegar, H. R.; Sharifi, T.; Mikołajczuk, A.; Tai, C.-W.; Borodzinski, A.; Wågberg, T. *J. Power Sources* **2012**, *209*, 236–242.

(34) Hasan, M.; Newcomb, S. B.; Rohan, J. F.; Razeeb, K. M. *J. Power Sources* **2012**, *218*, 148–156.

(35) Xu, C.; Shen, P. K.; Liu, Y. *J. Power Sources* **2007**, *164*, 527–531.

Chapter 6*

ELECTROCATALYTIC OXIDATION OF POLYHYDRIC ALCOHOLS AT FeCo@Fe@Pd/C

* The following publication resulted from part of the research work presented in this chapter and it is not referenced further.

Omobosede O. Fashedemi and Kenneth I. Ozoemena. "Comparative electrocatalytic oxidation of ethanol, ethylene glycol and glycerol in alkaline medium at Pd-decorated FeCo@Fe/C core-shell nanocatalysts." *Electrochimica. Acta*, **2014,** 128, 279-286.

6.1 Introduction

Among the alcohols used in Direct Alcohol Fuel Cell (DAFC) applications, the polyhydric alcohols such as Ethylene glycol (EG) and Glycerol (Gly) have been appearing as preferable alternative fuels in DAFCs. They can be electrochemically oxidized and are much less volatile [boiling points: 198^{o}C-EG; 290^{o}C–Gly][1,2]. They display relatively high theoretical energy density (5.2 kWhkg^{-1} and 5.0 kWhkg^{-1} for EG and Gly respectively), furthermore they are biomass derived fuel cells (GLY from methanolysis of vegetable oils and EG from oxidation of ethylene) and thus they can be produced in renewable and environmentally friendly ways[3–5]. A number of studies have been devoted to Pd based catalysts for the electro oxidation of EG and Gly in alkaline medium. The binary systems have been quite popular, M. Simoes et al[3] demonstrated the use of PdAu and PdNi alloys in the electro oxidation of glycerol, and they discovered an improved catalytic activity. L. Su et al showed that Pd/TiO_2 nanofibres had excellent catalytic activity for glycerol, ethylene glycol and propane 1, 2- diol, with glycerol giving the highest activity. A high potential was found to remove poisoning species[6].

This study looks into the use of Pd ternary nanocatalysts in the form of a core shell. FeCo@Fe@Pd/C modified glassy carbon electrode (GCE) was investigated for EG and Gly electro oxidation in alkaline medium. The results obtained show the potential applicability of the as-prepared nanocatalysts as effective low cost catalyst in DAFCs with polyhydric alcohol fuel, especially in direct ethylene glycol fuel cells (DEGFCs).

6.2 Comparative Cyclic Voltammetry Studies

Cyclic voltammetry (CV) remains the most important electrochemical technique for screening catalysts for alcohol oxidation. The CV is unique in its ability to provide some crucial but basic information regarding the energetics (thermodynamics) and kinetics of the electro oxidation reaction as well as the ability of the catalyst to resist fouling arising from intermediate oxidation products. Some of these information are obtained in terms of the onset potential (E_{onset}), peak potential separation (ΔE_p), forward current density (J_p), and ratio of forward to reverse peak current densities (J_f/J_b). Fig 6.1 shows the comparative cyclic voltammetric responses of GCE modified FeCo@Fe/C, Pd/C and FeCo@Fe@Pd/C in EG (a) and Gly (b). The voltammograms are characterized by two well-defined anodic peaks: one in the forward scan (i.e., anodic condition) and the other in the reverse scan (i.e., cathodic condition). The core alloy catalyst (i.e., FeCo@Fe/C) did not give any appreciable catalytic activity in any of the two alcohols, thus no further studies were done on it. The electrocatalytic performances of the other two catalysts, Pd/C and FeCo@Fe@Pd/C, as obtained from the cyclic voltammetry are summarized in Table 6.1. The electrocatalytic parameters are established in terms of the: (i) E_{onset}, indicating the ease of electrocatalysis (the more negative the value the easier the electrocatalysis); (ii) the ΔE_p, indicating the ease at which accumulated intermediates are removed from the catalyst's surface (the lower the value the more efficient the catalyst)[7]; (iii) forward peak current density (J_f), indicating the catalyst's maximum current generation; and (iv) the J_f/J_b, which reflects the tolerance ability to carbonaceous species accumulated on the modified electrode surface (the higher the value the more tolerant to poisoning the catalyst becomes)[8].

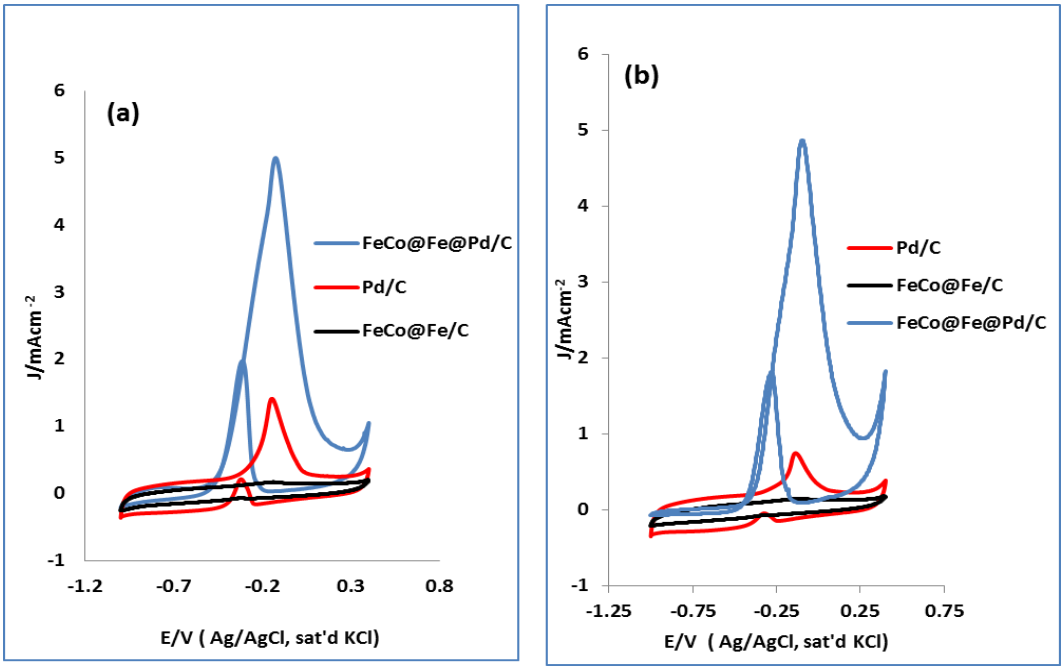

Figure 6.1: Comparable polarisation curves for the oxidation of EG (a) and GLY (b).in 0.5 M/0.5M KOH, at scan rate 25 mVs^{-1}

The CV data as depicted in Table 6.1 clearly show that the FeCo@Fe@Pd/C is a better catalyst for alcohol oxidation reaction than the Pd/C (at the same Pd loading); the onset potential at the FeCo@Fe@Pd/C is about 200 mV more negative, while the current density is about four times higher than seen at the Pd/C. These observations are in good correlation with other remarkable improvements shown in literature by core-shell catalysts in fuel cell catalysis over their bulk mono-metallic counterparts. In all the alcohols, the EG oxidation exhibited higher catalytic current densities suggesting that the catalysts are more tolerant to the poisoning generated by EG than from GLY. Although Pd/C gave higher J_f/J_p value for the GLY oxidation compared to the FeCo@Fe@Pd/C, all its other electro catalytic parameters were poor.

Table 6.1 shows the Comparative electro catalytic properties of the Pd-nanocatalysts towards two polyhydric alcohol oxidation reaction in alkaline electrolyte (0.5 M alcohol / 0.5 M KOH) in terms of onset potential (E_{onset}), peak potential separation (ΔE_p), forward current density (J_p), and ratio of

forward to reverse peak current densities (J_f/J_b) at the same Pd loading (~ 1.3 µg).

Table 6.1: Comparative electrocatalytic properties of the Pd-nanocatalysts towards EG and GLY oxidation reaction in alkaline electrolyte (0.5 M alcohol / 0.5 M KOH)

Electrocatalyst	Alcohol	E_{onset} / V	ΔE_p / V	J_p / mAcm^{-2}	J_f/J_b
FeCo@Fe@Pd/C	**Ethylene glycol**	- 0.60	0.17	5.01	2.81
Pd/C		- 0.41	0.20	1.29	2.74
FeCo@Fe@Pd/C	**Glycerol**	- 0.48	0.17	4.50	2.33
Pd/C		- 0.37	0.22	0.96	4.73

Table 6.1 suggests that the catalytic reaction may be more facile at the EG than at the GLY. The J_f/J_p values are higher than the values obtained for EG (1.67) and GLY (1.62) oxidation recently reported in literature using Pt binary and tertiary alloys (Pt_5Ru_4Sn/C) as anode catalysts[9].

6.3 Scan Rate Studies

Considering the overall high performance of the FeCo@Fe@Pd/C over the Pd/C catalysts, further studies on the electro catalytic behaviour of the FeCo@Fe@Pd/C were performed. Scan rate studies involving the performance of series of cyclic voltammograms were recorded at 10–800 mVs^{-1} were done to have an insight into the nature of mass transport behaviour at the FeCo@Fe@Pd/C modified electrode during the electro oxidation of the two alcohols. Their peak current densities were found to increase with increasing scan rates in the both alcohols. The corresponding plots of the peak current versus the square root of the scan rates gave linear relations with linear regression equation having

correlation coefficient (R^2) values of > 0.990, thus indicating near perfect diffusion-controlled reaction processes in oxidation of both alcohols at the modified FeCo@Fe@Pd/C surfaces. (Figs 6.2 a and b).

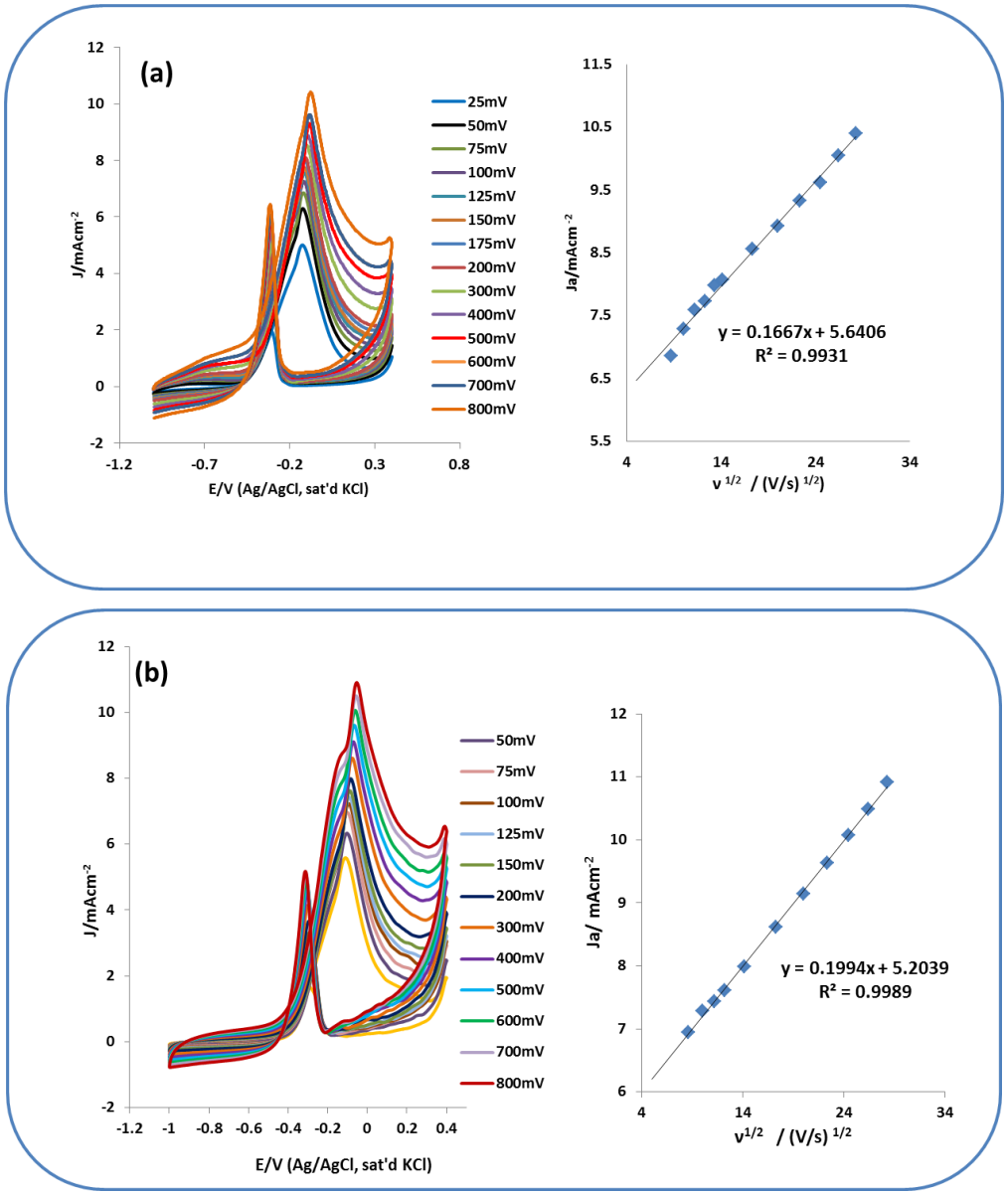

Figure 6. 2 : CV voltammograms at scan rates 25-800 $mVs^{-1}$of FeCo@Fe@Pd/C in N_2 saturated 0.5 M [EG (a) /GLY (b)] /0 5 M [KOH] with their equivalent plots of j_a vs $v^{1/2.}$

6.4 Chronoamperometry

Chronamperometry studies were carried out to further investigate the stability and CO poisoning tolerance of the catalysts in both alcohols. A good fuel cell catalyst should exhibit high current densities at low over potentials, and retain such current at a long period of time. The stability of current generated by the electro catalysts was tested by performing chronoamperometric experiments. Figures 6.3 a and b compare the chronoamperometric curves of FeCo@Fe@Pd/C and Pd/C respectively in alkaline solutions of the two alcohols. As was observed in the CV data, the FeCo@Fe@Pd/C gave higher current response than the Pd/C. The current densities dropped at ≈ 1.98 $mAcm^{-2}$ in both alcohols for FeCo@Fe@Pd/C. The approximate steady current values after 50 s alcohol oxidation period were found to be 1.66 and 1.61 $mAcm^{-2}$ in EG and GLY, respectively. The quasi-stable current densities at the end of the test after 1200 s was 0.80 and 0.65 $mAcm^{-2}$ in EG and GLY, respectively. FeCo@Fe@Pd/C gave the highest stable current response in oxidation of EG. For the Pd/C electrode, one observes the same trend but with stability at the end of the reaction occurring at extremely low current density values of 0.13 $mAcm^{-2}$, in EG and 0.03 $mAcm^{-2}$ in GLY.

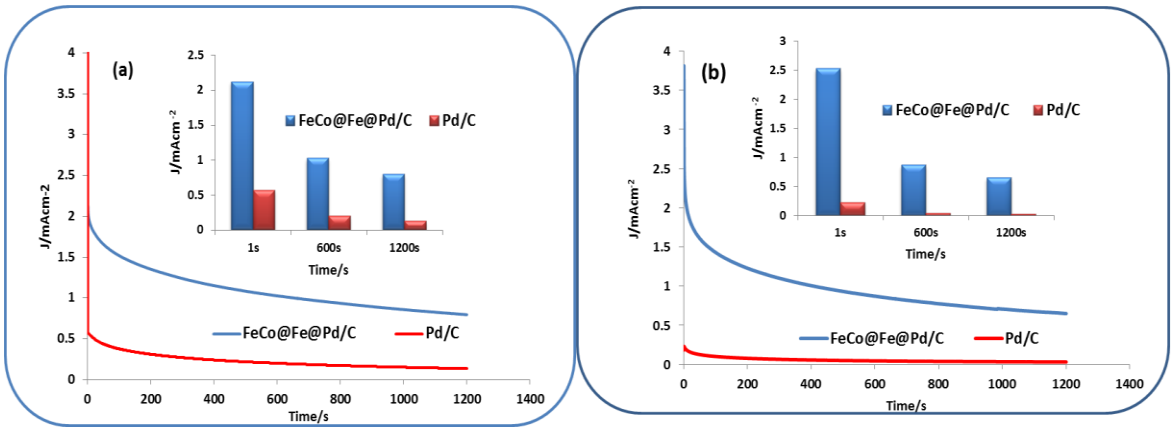

Figure 6. 3: Chonoamperommetry curves of FeCo@Fe@Pd/C and Pd/C at -0.2 V in 0.5 M EG/ 0.5 M KOH (a) and 0.5 M GLY/0.5 M KOH (b).Insets are bar chart representations of the current responses at 1s, 600 s, and 1,200 s respectively in both alcohols.

The stability of FeCo@Fe@Pd/C at the higher current densities indicates better alcohol oxidation than Pd/C in the alcohols. The higher current density exhibited by FeCo@Fe@Pd/C in EG (a) also shows better oxidation in this alcohol than in GLY (b). These results corroborate our observation from the cyclic voltammetry.

Chronopotentiometry experiments were carried out at a fixed current density of 0.3mAcm^{-2}. Figs 6 4a and b show the chronopotentiometric curves of both GCE-FeCo@Pd/C and GCE- Pd $_{nano}$/C during EG and Gly oxidation respectively. A slight increase in polarisation potential with polarisation time is a good indication of little poisoning at electrode surface[4]. While a combination of higher potential polarizations accompanied by oscillations are indicative of a poisoning of the electro catalyst[10]. The polarisation potential in EG oxidation increased for about 20 mins and occurred at a higher potential of ≈ 1.14V on the FeCo@Fe@Pd/C electrode. Slight oscillations were also observed during the polarization process. Though there is an indication of presence of poisoned electrode surface by CO_{ads}, the resistance of the catalyst to poisoning at its surface is also noticed as this did not overly affected its catalytic performance towards EG oxidation.

On the other hand a steady polarization curve was observed at ≈ 1.04V (lower than EG) for the oxidation of GLY at the same modified electrode, no noticeable time increase was observed with increase in potential. Little poisoning of the electrode surface during GLY oxidation, the stability of FeCo@Fe@Pd/C in both EG and GLY oxidation and its tolerance to CO can thus be inferred from this study. Pd/C exhibited significant oscillations throughout the polarization process, especially in GLY oxidation. The potential oscillation frequency increased with polarization time. This is a clear indication of accumulation of poisoning species on the electrode surface and the unstable nature of the catalyst during the oxidation of both alcohols.

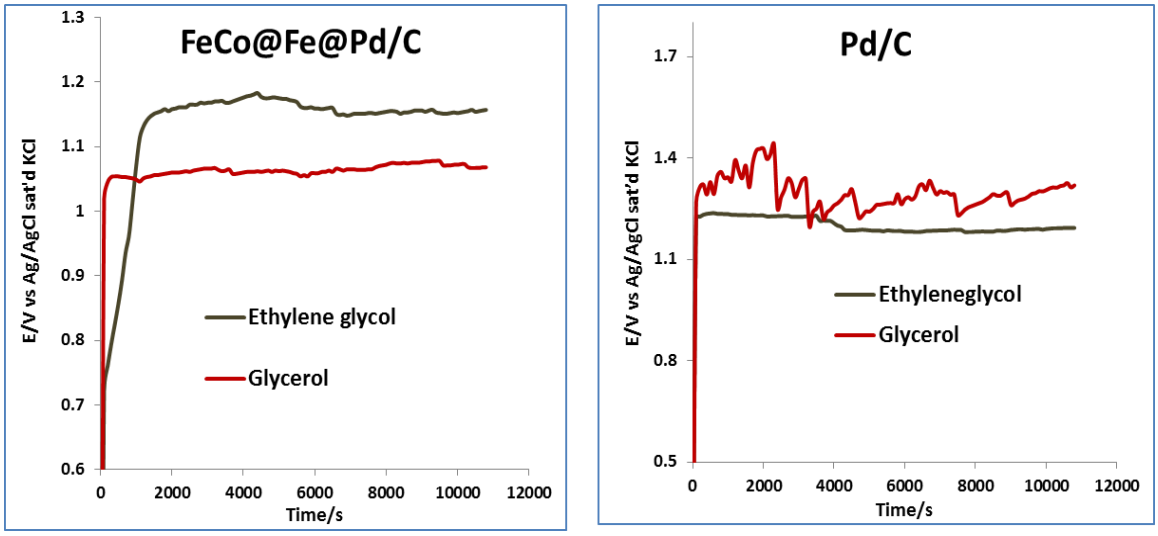

Figure 6. 4: Chronopotentiometry polarizations of FeCo@Fe@Pd/C and Pd/C in both 0.5 M [EG/ GLY] / 0.5 M KOH.

6.5 Electrochemical Impedance Spectroscopy

As the core shell nanocatalyst–FeCo@Fe@Pd/C has given superior catalytic performances in all the pervious experiments carried out, further insights into its electrocatalytic activity towards EG and GLY oxidation were done using the electrochemical impedance spectroscopy(EIS). EIS is a sensitive technique used in determining the heterogeneous kinetics as well as the electrocatalytic oxidation kinetics in fuel cells[11,12]. Figs 6.5 a and b represent the Nyquist plots at a fixed active potential at different voltages of -0.2 V and -0.4 V (vs Ag/AgCl, sat'd KCl) measured in 0.5 M alcohol in 0.5 M KOH solutions. It can be seen that the least semi-circular curves were obtained at -0.2 V making it the voltage with the least resistance to electron or charge transfer in the oxidation of both alcohols. The equivalent circuit used in fitting the plot is the same for the two alcohols [$R_s(R_{ct}CPE)$], where R_s is the electrolyte (solution) resistance, R_{ct} is the charge transfer resistance, and CPE is the constant phase element.

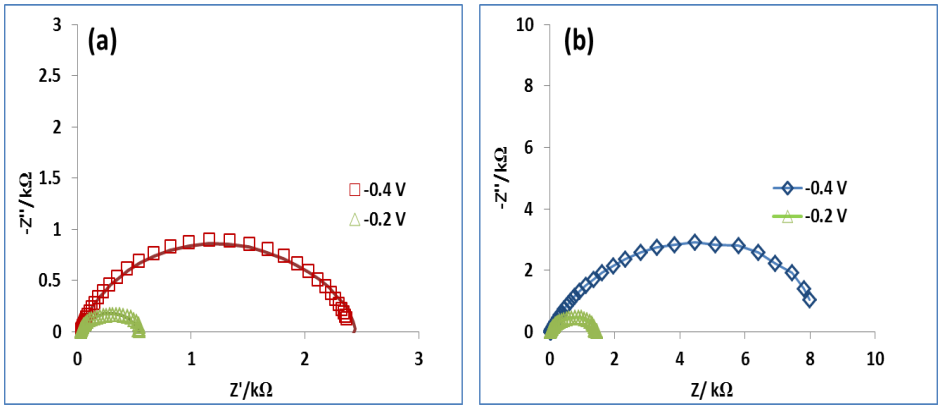

Figure 6. 5: EIS of FeCo@Fe@Pd/C at -0.2 V and -0.4 V in 0.5 M EG /0.5 M KOH (a) and 0.5 M GLY / 0.5 M KOH (b)

Table 6.2: Electrochemical impedance data obtained from the Nyquist plots at -0.2 V vs Ag/AgCl.

Alcohol	**Electrochemical Impedance Parameters**			
	R_s **/Ω**	R_{ct} **/kΩ**	**CPE / µF**	**n**
Ethylene glycol	27.71±0.53	0.52±0.01	58.10±3.25	0.78±0.01
Glycerol	27.82±0.45	1.40±0.22	41.90±1.46	0.77±0.01

Table 6.2 gives a summary of the data obtained from the EIS experiments. The R_s values are the same for the alcohols at the voltages studied, this implies the solution does not affect the oxidation reaction. The R_{ct} values give the interpretation of the rate of electron transfer at the electrode / solution interface. Comparing the R_{ct} values obtained for the modified electrodes in the alcohols showed lower values in EG oxidation (0.5170 kΩ) at -0.2V compared to GLY (1.409 kΩ). This shows an increased rate of electron/charge transfer during electro oxidation of EG compared to GLY.

6.6 Kinetics

The kinetics at the electrode surface in the two alcohols was studied by analysing the kinetic parameters –Tafel slope value (*b*) and the transfer coefficient (*a*) and the electro catalytic rate constant (k_{cat}).

6.6.1 Tafel Values

LSV scans were obtained at various increasing concentrations at a slow scan rate ($1mVs^{-1}$) to obtain the Tafel values (*b*) and transfer coefficients (*a*). The effect of alcohol concentration on electro catalysis of FeCo@@Fe@Pd/C was studied at concentrations ranging from 0.5 to 3.0 M alcohol (EG and Gly) in 0.5 M KOH solution. Figures 6.6 a and b show the responses at the different concentrations using linear sweep voltammetry at a rate of 1 mVs^{-1}. A steady increase in current density is observed with an increase in concentration of the alcohols. But a decrease in current density is seen after 1.25 M concentration in GLY and after 1.50 M concentration in EG. This is a remarkably high concentration for electro catalytic oxidation in both alcohols. Su et al[6] studied the effect of increased alcohol concentration for glycerol oxidation at palladium titanium oxide (Pd/TiO_2) nano fibres. A drop in oxidation current density was observed after a 0.5 M concentration. This was attributed to excessive adsorbed glycerol on the electrode surface, thus blocking the access of OH^- to the active sites on Pd resulting in an insufficient coverage of $(OH)_{ads}$ and leading to a decrease of the peak current accordingly .

This shows the availability of active sites on the FeCo@Fe@Pd/C in high concentrations of the alcohols especially EG. It should be noted that one of the characteristics of a direct alcohol fuel cell is its ability to operate at high fuel concentrations especially if it is to be used for portable power applications.

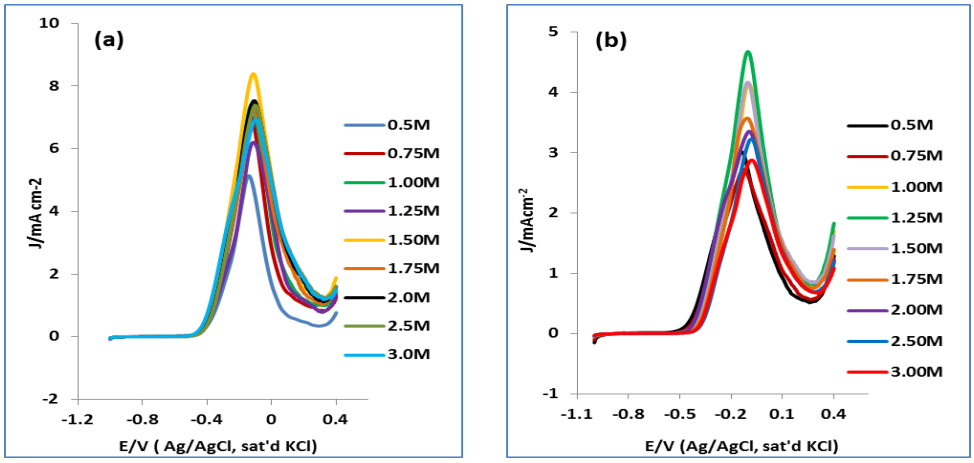

Figure 6. 6: Linear sweep voltammograms of FeCo@Fe@Pd/C in EG (a) and GLY (b), 0.5 M [alcohol]/ 0.5 M KOH, scan rate = 1 mVs^{-1}

The conventional equations (6.1) and (6.2) were used to obtain the Tafel values and the transfer coefficient values[13–15].

$$\eta = a + b \log j \qquad (6.1)$$

$$b = \frac{2.303RT}{(1-\alpha)nF} \qquad (6.2)$$

where η is the overpotential (difference between the applied potential and open circuit potential), j is the current density , b is the Tafel slope, $a$is the Tafel constant relating to the exchange current density, α is the transfer coefficient , n is the number of electrons involved in the rate determining step , while other symbols retain their usual meaning.

Figures 6.7 (a) and (b) depict the plots of η vs log j in both EG and Gly respectively. Attached to the plots are the tables of the kinetic parameters for each one of the molar concentrations studied (0.5 M–3.0 M) while the average values of the Tafel slope, b and the corresponding transfer coefficient, α values for both alcohols are given in Table 6.3

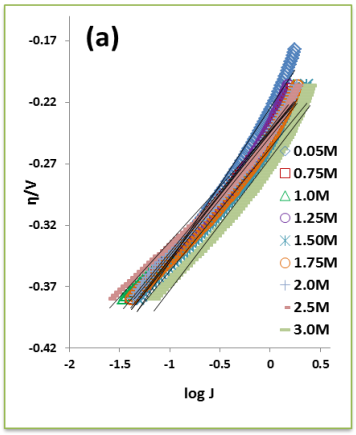

[Ethylene glycol]/M	Tafel slope (2.303RT/αnF)	α	a (-RT/αnF) log Jo	J_o	R^2
0.5	117.1	0.505	0.231	0.094	0.9932
0.75	103.1	0.574	0.2443	0.234	0.9899
1.00	99.4	0.595	0.2427	0.307	0.9892
1.25	106.5	0.555	0.2415	0.185	0.9843
1.50	100.1	0.591	0.2573	0.372	0.9860
1.75	101.6	0.582	0.2478	0.275	0.9867
2.00	100.2	0.590	0.2444	0.275	0.9935
2.50	89.7	0.660	0.2435	0.518	0.9869
3.00	107.4	0.551	0.2655	0.297	0.9821

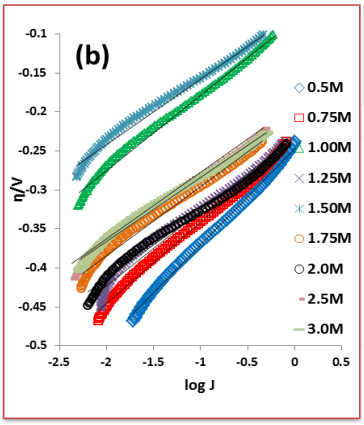

[GLYCEROL] /M	Tafel slope (2.303RT/ αnF)	α	a (-RT/αnF) log Jo	J_o	R^2
0.5	122.7	0.482	0.2476	0.102	0.9932
0.75	104.2	0.568	0.2369	0.188	0.9899
1.00	96.4	0.614	0.0825	0.007	0.9892
1.25	89.8	0.659	0.2347	0.411	0.9843
1.50	84.0	0.704	0.0736	0.007	0.9860
1.75	88.3	0.670	0.2072	0.222	0.9867
2.00	86.5	0.684	0.2404	0.601	0.9935
2.50	85.4	0.692	0.1924	0.179	0.9869
3.00	81.5	0.726	0.2023	0.303	0.9821

Figure 6. 7: Plots of η vs log j in EG (a) and Gly (b) respectively. Attached to the plots are the tables of the kinetic parameters for each one of the molar concentrations studied (0.5 M – 3.0 M)

For an electrochemical reaction to obtain a high current at low over potential, the reaction should exhibit a low Tafel slope[15]. The transfer coefficient (a) is the fraction of the potential energy that is transferred to the reaction and is inversely proportional to the Tafel slope (equation 6.2). In a research conducted by Soderberg et al[16] it was found that the minimum a value for any reaction mechanism (ignoring adsorption effects) should be 0.05 and the highest b value is 118mVdec^{-1}.

A look at Table 6.3 and considering the value of the Tafel slopes (b) and transfer coefficient (α), obtained for the oxidation of EG and GLY alcohols using FeCo@Fe@Pd/C, it is clear that the reaction mechanisms at the modified electrode in both alcohols are virtually the same.

Table 6.3: The average values of the Tafel slope, *b* and corresponding transfer coefficient, *a* values for both EG and GLY oxidation.

Alcohol	**Tafel Slope(*b*)**	***a***
Ethylene glycol	102.80±7.40	0.5778 ± 0.0419
Glycerol	93.19±13.05	0.6442 ± 0.7750

Tafel slope (*b*) values of 102.8 $mVdec^{-1}$ and 93.19 $mVdec^{-1}$ were calculated for EG and Gly oxidation respectively. These values are also much lower than Pt and Pd modified electrodes reported in literature for alcohol oxidation[17,18]. The electrode surface does not exhibit any form of porosity as this is attributed to very high Tafel values. The mechanism for the electrocatalytic oxidation of both alcohols at the modified electrode is also very favourable. The calculated average values of *a* were 0.58 and 0.64 for EG and GLY oxidation respectively.

6.6.2 Electrocatalytic Rate Constant

The catalytic rate of the oxidation of EG and GLY at GCE-FeCo@Fe@Pd/C was obtained using the chronoamperometry data. The electrocatalytic rate constant (K_{cat}) was obtained by employing the conventional equation below:

$$\frac{J_{cat}}{J_{buff}} = \pi^{1/2}\left(kC_o t\right)^{1/2} \qquad (6.3)$$

Where J_{cat} and J_{buff} are the current densities in the presence and absence of the alcohols, C_o is the bulk concentration and *t* is the time. Values of (4.32±0.03) x 10^3 and (2.65±0.23) x 10^3 $mol^{-1}s^{-1}$ were obtained for both EG and GLY oxidation respectively. This shows the very fast speed of the

oxidation of both alcohols by the catalyst. It further indicates the effectiveness of such catalyst in fuel cell application. Fig 6.8 shows the plots of J_{cat}/J_{buff} vs $t^{1/2}$; insets are the values of the calculated catalytic rate constants $K_{cat.}$

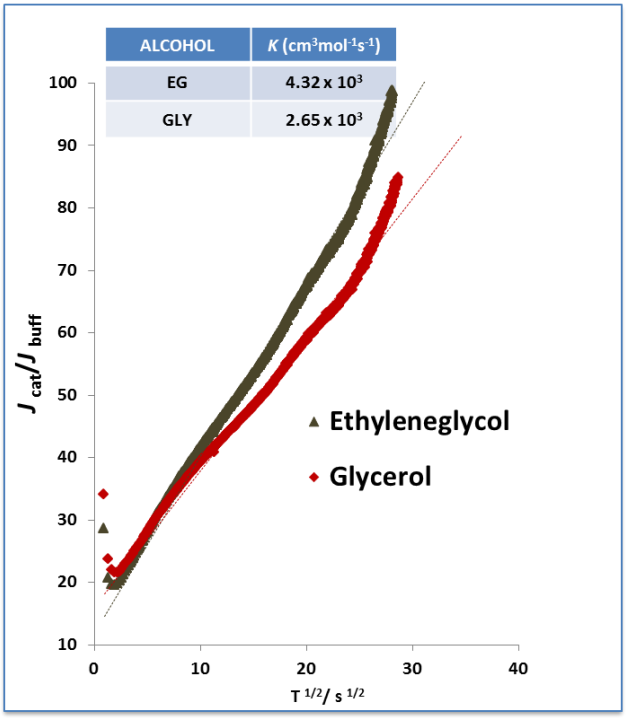

Figure 6. 8: Plots of J_{cat}/J_{buff} vs $t^{1/2}$, inset are the values of the calculated catalytic rate constants $K_{cat.}$ in both 0.5 M [EG / GLY]/ 0.5 KOH

6.7 Table of Comparison

Table 6.4 displays comparative electrocatalytic properties of the Pd-nanocatalysts towards EG and GLY oxidation reaction in alkaline electrolyte with respect to other Pd based catalyst in literature, in terms of onset potential (E_{onset}), peak potential separation (ΔE_p), forward peak current density (J_p), and ratio of forward to reverse peak current densities (J_f/J_b)

Table 6.4: Comparative electrocatalytic properties of the Pd-nanocatalysts towards EG and GLY oxidation reaction in alkaline electrolyte

Electrocatalyst	Alcohol solution	Pd loading (µg)	E_{onset} (V)	ΔE_p (V)	J_p ($mAcm^{-2}$)	J_f/J_b	Ref
FeCo@Fe@Pd/C	0.5 M EG /0.5 M KOH	1.3	-0.60 (vs Ag/AgCl)	0.17 (vs Ag/AgCl)	5.01 /272 $mAmg^{-1}$	2.64	This work
Pd-CeO_2	1.0 M EG /1.0 M KOH	300	-0.40 (vs MMO)	-0.05 (vs MMO)	68	≈2.72	19
Pd-NiO	1.0 M EG /1.0 M KOH	300	-0.42 (vs MMO)	-0.07 (vs MMO)	104	≈1.73	19
Pd-Co_3O_4	1.0 M EG /1.0 M KOH	300	-0.49 (vs MMO)	-0.07 (vs MMO)	98	≈1.66	19
Pd-Mn_3O_4	1.0 M EG /1.0 M KOH	300	-0.49 (vs MMO)	-0.07 (vs MMO)	98	≈2.3	19
P-MWCNT/Pd	0.5 M EG /2.0 M KOH	n/a	-0.40 (vs SCE)	≈-0.04 (vs SCE)	146.2 $mAmg^{-1}$	1.04	20
F-MWCNT/Pd	0.5 M EG /2.0 M KOH	n/a	-0.40 (vs SCE)	≈-0.04 (vs SCE)	98.3 $mAmg^{-1}$	1.30	20
S-MWCNT/Pd	0.5 M EG /2.0 M KOH	n/a	-0.40 (vs SCE)	≈-0.04 (vs SCE)	177.2 $mAmg^{-1}$	1.94	20
Pd-CMS	1.0 M EG /1.0 M KOH	100	-0.35 (vs MMO)	-0.04 (vs MMO)	110	2	21
FeCo@Fe@Pd/C	0.5 M Gly /0.5 M KOH	1.3	-0.48 (vs Ag/AgCl)	0.17 (vs Ag/AgCl)	4.50/259 $mAmg^{-1}$	2.80	This work
Pd-CeO_2	1.0 M Gly /1.0 M KOH	300	-0.33 (vs MMO)	-0.05 (vs MMO)	50	≈2.5	19
Pd-NiO	1.0 M Gly /1.0 M KOH	300	-0.32 (vs MMO)	-0.03 (vs MMO)	88	≈2.2	19
Pd-Co_3O_4	1.0 M Gly /1.0 M KOH	300	-0.38 (vs MMO)	-0.05 (vs MMO)	70	≈2.3	19

P-MWCNT: Pristine Multiwalled carbon nanotubes; F-MWCNT: Acid functionalised Multiwalled carbon nanotubes; S-MWCNT: Sulfonated Multiwalled carbon nanotubes; ; Pd-CMS: Palladium carbon microspheres

6.8 Conclusion

The novel (FeCo@Fe@Pd/C) core shell nano catalyst has shown a remarkable activity in the electro oxidation of EG and Gly in alkaline media. It has already been established from the studies carried out in this work that the core shell catalysts have shown outstanding catalytic performance compared to the monometallic Pd nano catalysts. Some of the other significant findings related to the electro catalytic activities of FeCo@Fe@Pd/C in both alcohols studied include: (i) that at the core-shell, the onset potential for EG oxidation is 120 mV higher than seen for GLY, (ii) the j_f/j_b values are 2.81 and 2.33 for EG and Gly, respectively, (iii) the peak current density of the core-shell is 5.01 and 4.5 $mAcm^{-2}$ for EG and GLY oxidation which is between 3.9 and 4.7 higher than that observed at the Pd monometallic catalyst; (iv) the values of the resistance to charge transfer (Rct) are 0.52 and 1.40 kΩ during oxidation of EG and Gly respectively and (v) that FeCo@Fe@Pd/C (despite its low Pd loading) exhibits better catalytic performance than some literature reports to date.

In general, the Pd core-shell nano catalyst is very stable as it is tolerant to carbonaceous poisoning generated during the alcohol oxidation processes. It is more effective for alcohol oxidation than the single metal counterpart Pd/C catalysts with the same mass loading and operating under same experimental conditions. This behaviour has been attributed to its smaller nanoparticle size, higher EASA and the positive strain effect on its active surface due to the incorporation of the core alloy in its Pd lattice. Its best alcohol oxidation activity has been in ethylene glycol, due its more favourable kinetics which was shown by its high catalytic rate constant. The promising results seen here have opened doors for further exploration of this catalyst for application in DAAFC devices, especially in direct alkaline ethylene glycol fuel cell (DEGFC).

6.9 References

(1) Matsuoka, K.; Inaba, M.; Iriyama, Y.; Abe, T.; Ogumi, Z.; Matsuoka, M. *Fuel Cells* **2002**, *2*, 35–39.

(2) Yue, H.; Zhao, Y.; Ma, X.; Gong, J. *Chem. Soc. Rev.* **2012**, *41*, 4218–44.

(3) Simões, M.; Baranton, S.; Coutanceau, C. *Appl. Catal. B Environ.* **2011**, *110*, 40–49.

(4) Zhang, J.; Liang, Y.; Li, N.; Li, Z.; Xu, C.; Jiang, S. P. *Electrochim. Acta* **2012**, *59*, 156–159.

(5) Serov, A.; Kwak, C. *Appl. Catal. B Environ.* **2010**, *97*, 1–12.

(6) Su, L.; Jia, W.; Schempf, A.; Ding, Y.; Lei, Y. *J. Phys. Chem. C* **2009**, *113*, 16174–16180.

(7) Thotiyl, M. M. O.; Kumar, T. R.; Sampath, S. *J. Phys. Chem. C* **2010**, *114*, 17934–17941.

(8) Liu, Z.; Hong, L. *J. Appl. Electrochem.* **2007**, *37*, 505–510.

(9) Kim, H. J.; Choi, S. M.; Green, S.; Tompsett, G. a.; Lee, S. H.; Huber, G. W.; Kim, W. B. *Appl. Catal. B Environ.* **2011**, *101*, 366–375.

(10) Shih, Z.-Y.; Wang, C.-W.; Xu, G.; Chang, H.-T. *J. Mater. Chem. A* **2013**, *1*, 4773.

(11) Maxakato, N. W.; Ozoemena, K. I.; Arendse, C. J. *Electroanalysis* **2010**, *22*, 519–529.

(12) Chen, W.; Kim, J.; Sun, S.; Chen, S. *Langmuir* **2007**, 11303–11310.

(13) Compton, RG, Banks. C. *Understanding Voltammetry*; 2007; pp. 249–253.

(14) Bard, Allen J, Faukner, L. R. *Electrochemical Methods:Fundamentals and Applications*; 2nd ed.; Wiley, New York: New York, 2001; p. 864 Pages.

(15) Song, C.; Zhang, J. *PEM Fuel Cell Electrocatalysis and Catalyst Layers: Fundamentals and Applications*; Ed.; Springer, 2008; p. 1159.

(16) Soderberg, J. N.; Co, A. C.; Sirk, A. H. C.; Birss, V. I. *J. Phys. Chem. B* **2006**, *5*, 10401–10410.

(17) Shen, P. K.; Xu, C. *Electrochem. commun.* **2006**, *8*, 184–188.

(18) Popovic, K. D.; Lovic, J. D. *Electrochim. Acta* **2001**, *46*, 3163–3173.

(19) Xu, C.; Tian, Z.; Shen, P.; Jiang, S. P. *Electrochim. Acta* **2008**, *53*, 2610–2618.

(20) Sun, Z.-P.; Zhang, X.-G.; Liu, R.-L.; Liang, Y.-Y.; Li, H.-L. *J. Power Sources* **2008**, *185*, 801–806.

(21) Xu, C.; Liu, Y.; Yuan, D. *Int. J. Electrochem. Sci.* **2007**, *2*, 674–680.

Chapter 7*

OXYGEN REDUCTION REACTION AT FeCo@Fe@Pd/MWCNTS

*The following manuscript is in preparation for publication and resulted from part of the research work presented in this chapter

O.O. Fashedemi and K.I. Ozoemena "The Effects of Carbon Supports on the Oxygen Reduction Reactions at Palladium Nanocatalysts in Alkaline Medium".

7.1 Introduction.

It has already been introduced in Chapter 4 that considerable attention is drawn to oxygen reduction reaction (ORR) in alkaline media because of its importance in energy conversion technologies such as alkaline fuel cells. However unlike Chapter 4, this chapter deals with the use of carboxylated- and sulphonated-functionalised multi-walled carbon nanotubes (MWCNTS) as support for the core-shell nanocatalysts, i.e., FeCo@Fe@Pd/CNT-OH and FeCo@Fe@Pd/CNT-SO_3. It is important to note that for practical fuel cell applications, electrocatalysts are dispersed on carbon materials that display high electrical conductivity, high stability and a large surface area for high dispersion of the catalysts. Commonly used carbon supports include the traditional carbon black, carbon nanotubes (CNTs)[1–3] and carbon nanofibres (CNF)[4–6]. On the other hand, these carbon materials (used alone) are highly selective towards the two-electron pathway but their activity is quite low. For quinolic grafted carbon surfaces (such as the carboxylated functionalised CNT-OH), the electrochemical reduction of O_2 proceeds by a 2-electron mechanism to yield hydrogen peroxide[7–9]. Thus, the use of CNTs (with high porosity and electronic conductivity)[10–12] as support for the core shell FeCo@Fe@Pd nanocatalysts may facilitate the more favourable four–electron ORR pathway.

7.2 Comparative Cyclic Voltammetry Experiments

The initial studies of the activities of the Pd-based nanocatalysts on functionalised multi-walled carbon nanotubes (MWCNTS) were investigated for ORR in 1.0 M KOH using cyclic voltammetry. From Fig 7.1, it is evident that FeCo@Fe@Pd/CNT-OH showed the best ORR activity in terms of onset potential and reduction current density.

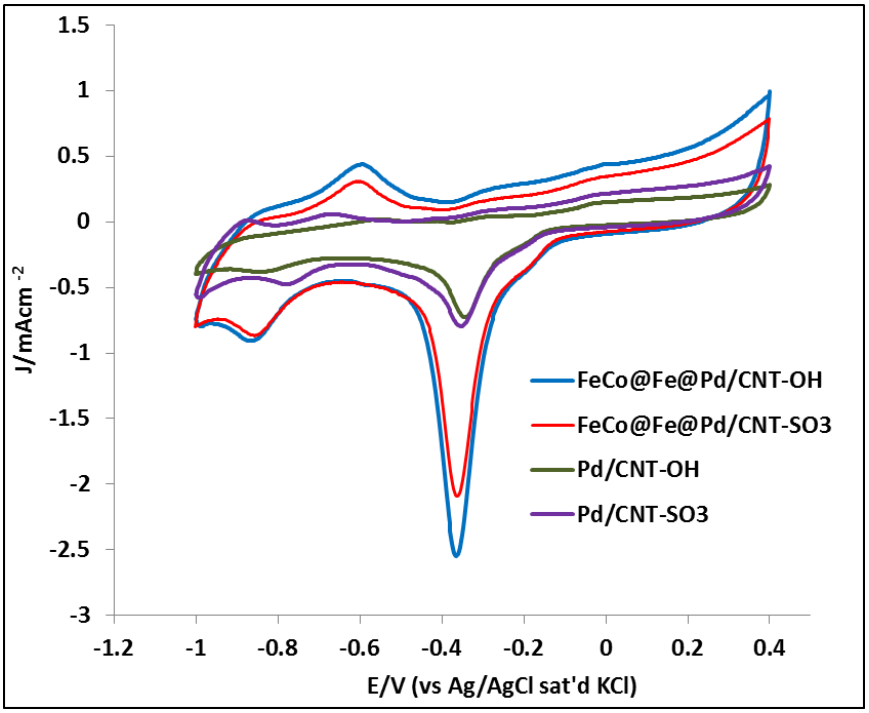

Figure 7.1: Comparative cyclic voltammograms of FeCo@Fe@Pd/CNT-OH, FeCo@Fe@Pd/CNT-SO_3, Pd/CNT-OH and Pd/CNT-SO_3 catalysts in 0.1M KOH solution saturated with Oxygen. (Sweep rate = 50 mVs^{-1})

The FeCo@Fe@Pd core shell nanocatalysts supported on both CNT-OH and CNT-SO_3 had the same oxygen reduction onset potential of -0.0981 V but FeCo@Fe@Pd/CNT-OH gave the best activity with respect to current density response to reduction of oxygen with a value of 2.50 $mAcm^{-2}$ compared to FeCo@Fe@Pd/CNT-SO_3 having a value of 2.04 $mAcm^{-2}$. The current was normalized by the geometric area of the electrode (0.07065 cm^{-2}). The single metal -palladium -catalysts on CNT-OH and CNT-SO_3 exhibited almost the same catalytic responses to molecular oxygen

reduction irrespective of their different carbon supports. Both had the same onset oxygen reduction potential of 0.139 V and current densities of 0.068 mA cm^{-2} and 0.073 mA cm^{-2} for Pd/CNT-OH and Pd/CNT-SO_3 respectively. Also, both core-shell nanocatalysts showed about 42 mV earlier onset potential than their single Pd metal counterparts and FeCo@Fe@Pd/CNT-OH had an increase of 2.43 mA cm^{-2} in current which is about 35 times more of ORR current density compared to Pd metal alone. FeCo@Fe@Pd/ CNT-SO_3 gave an increase of 1.97 mA cm^{-2}; this is about 29 times more than the single Pd metal catalyst on the same substrate. A summary of the ORR electro catalytic performance of the catalysts from the CV is shown in Table 7.1:

Table 7.1: ORR electrocatalytic performance (CV) of the Pd based nanocatalysts

Catalysts	**E_{onset} (V)**	**E_{peak} (V)**	**J_{peak} ($mAcm^{-2}$)**
FeCo@Fe@Pd/CNT-OH	-0.0981	0.3569	2.51
FeCo@Fe@Pd/CNT-SO_3	-0.9811	-0.3545	2.040
Pd/CNT-OH	-0.1396	-0.3276	0.0678
Pd/CNT-SO_3	-0.1396	-0.3349	0.0734

7.3 ORR Mechanism

RDE Hydrodynamic voltammetry curves were obtained at different rotation rates as shown in Figures 7.2 a, b, c and d. The Koutecky-Levich plots, j^{-1} vs $\omega^{-1/2}$ are shown as insets. From the slopes of the K-L plots of the catalysts, the number of electrons (n) transferred per oxygen molecule was calculated and the average n value was 3.6, 3.2, 2.8 and 2.8 for FeCo@Fe@Pd/CNT-OH, FeCo@Fe@Pd/CNT-SO_3, Pd/CNT-OH and Pd/CNT-SO_3 respectively. This suggests that the ORR process goes through the 4-electron reduction mechanism to produce water using the FeCo@Fe@Pd/CNT-OH as catalyst, while the other three catalysts exhibit the 3-electron reduction pathway which is an indication of the occurrence of both the 2-electron (a two-step pathway with H_2O_2 produced as an intermediate) and the 4- electron pathways occurring during their oxygen reduction mechanisms[13].

The results (n values) obtained from these experiments could also be an indication that the two types of functionalised carbon nanotubes support (CNT-OH and CNT-SO_3) actually take part in the oxygen reduction reaction following a 2 electron pathway as earlier suggested (this has also been confirmed by other earlier cited authors) while the Pd based catalysts (Pd and FeCo@Fe@Pd) undergo the 4 electron pathway as also observed by other authors[10,14–16].

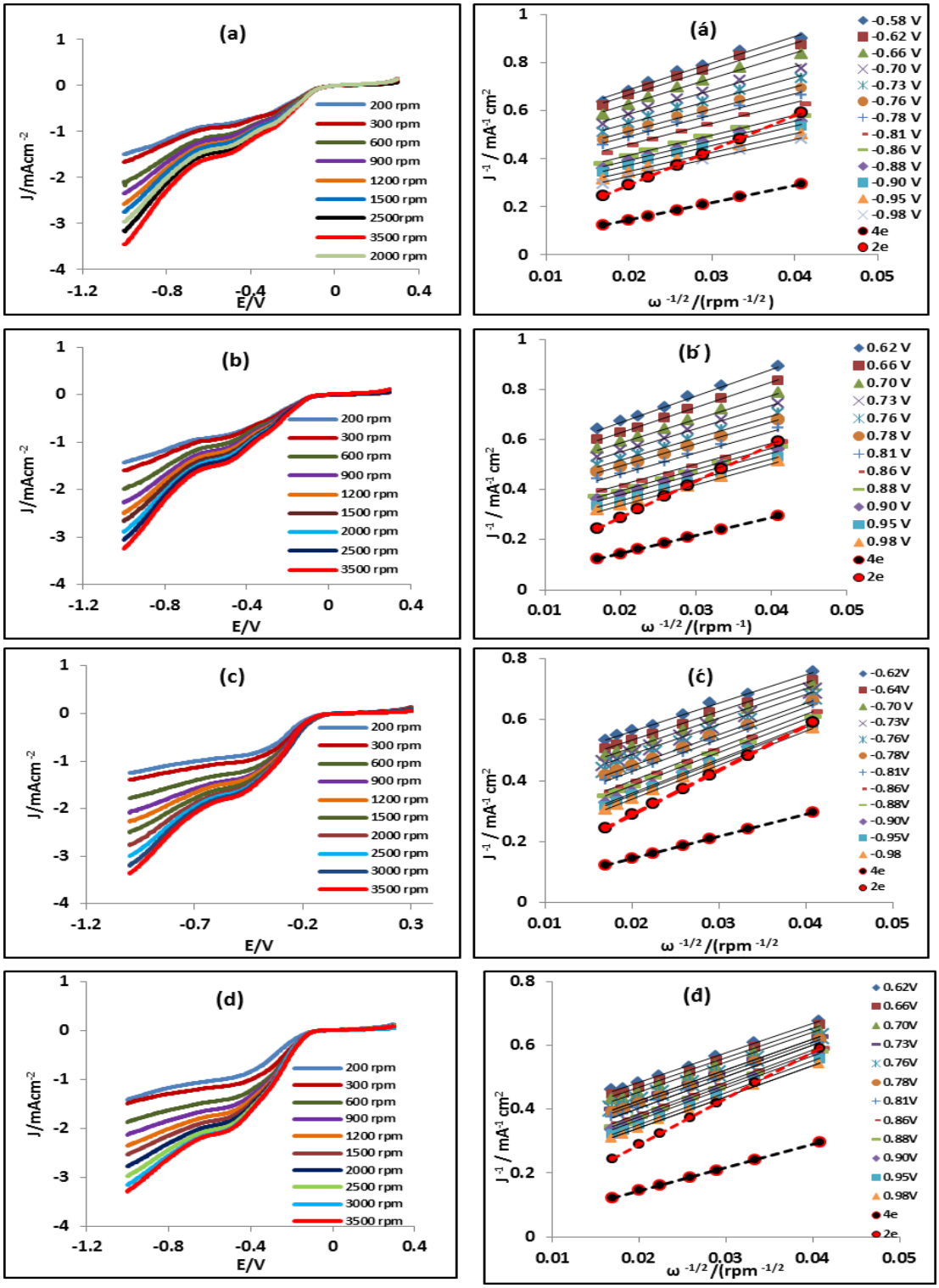

Figure 7.2: RDE Hydrodynamic polarization curves of FeCo@Fe@Pd/CNT-OH (a), FeCo@Fe@Pd/CNT-SO_3 (b), Pd/CNT-OH (c) and Pd/CNT-SO_3 (d) in oxygen saturated 0.1 M KOH solution at different rotation rates. (á, b́, ć and d́) are the Koutecky-Levich plots derived from the Hydrodynamic polarization curves of each catalyst.

To provide some insights into the reasons for the different number of electrons transferred in the ORR, it is necessary to have a look at the overall scheme for ORR on metals as shown in Figure 7.3[17–19]. The mechanisms give the number of possible reaction pathways of oxygen reduction. O_2 can be reduced directly to water, (rate constant k_1), this is the direct 4-electron reduction pathway. A second possible pathway is the two electron reduction of O_2 to adsorbed $H_2O_{2\ (ad)}$ (rate constant k_2), which can then be further reduced to water (rate constant k_3); this makes up the serial four-electron pathway. A third possibility is that $H_2O_{2\ (ad)}$ can also be either a final product which is desorbed into the electrolyte solution (rate constant k_5) or it can be chemically decomposed on the electrode surface (rate constant k_4). In these latter cases H_2O_2 is the final oxygen reduction reaction product.

The shapes of the Hydrodynamic voltammograms of the catalysts showed some 'rest periods' around -0.25 V and -0.55 V during the ORR using the core shell catalysts in the mixed kinetic-diffusion controlled region. These became less pronounced at the faster rotatory speeds. These double steps may be ascribed to the generation of trace amounts of H_2O_2[20,21]. This observation can be seen as suggesting an initial oxygen reduction at the carbon nanotubes support sites (producing some H_2O_2) which later culminates in the complete oxygen reduction at the metal catalyst site.

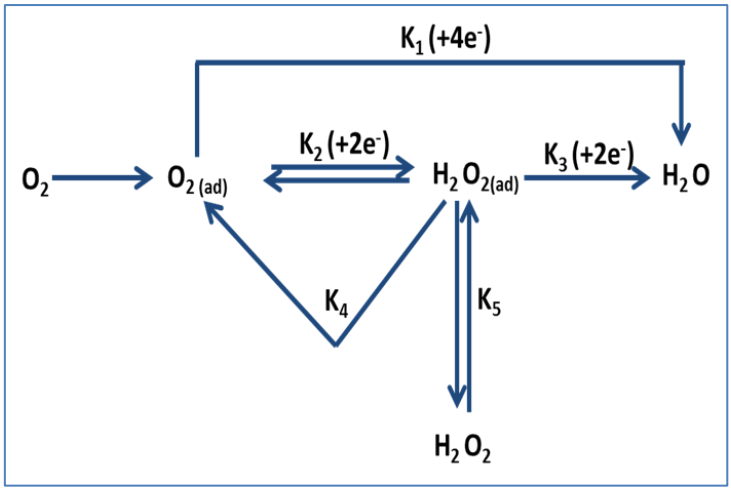

Figure 7.3: ORR reaction pathways[17–19]. (Note that a few adaptations have been made on the scheme to suite this present study).

Thus, a serial 4-electron oxygen reduction pathway leading to water is proposed for the FeCo@Fe@Pd/CNT-OH core shell catalyst, while FeCo@Fe@Pd/CNT-SO_3 begins with the serial oxygen reduction pathway but ends with a mixture of products (OH^- and HO_2^-) of both the 4- electron and 2-electron pathways. The 4-electron and 3-electron O_2 reduction pathways were also confirmed by the comparison to the slopes of the Koutecky–Levich plot with the theoretical values of 4- and 2-electron reduction processes (Fig 7.2 á, ḅ,).

7.4 ORR Kinetics

As observed for nanocatalysts supported on the Vulcan carbons (Chapter 4), the MWCNTs-supported catalysts also present features of ill-defined diffusion limiting regions (Fig 7.2). Thus, the kinetic parameters can be estimated from the Koutecky-Levich equation, assuming the so-called *'two-layer model'* (i.e., diffusion in both the polymer/Nafion film used as catalyst binder and in the hydrodynamic boundary layer[22–24]. The Tafel plots i.e. the Plot of ln ($|j_k / (j_l - j_k)|$) vs η for the catalysts studied are shown in Figures 7.4 a, b, c, and d. The kinetic parameters are summarised in Table 7.2

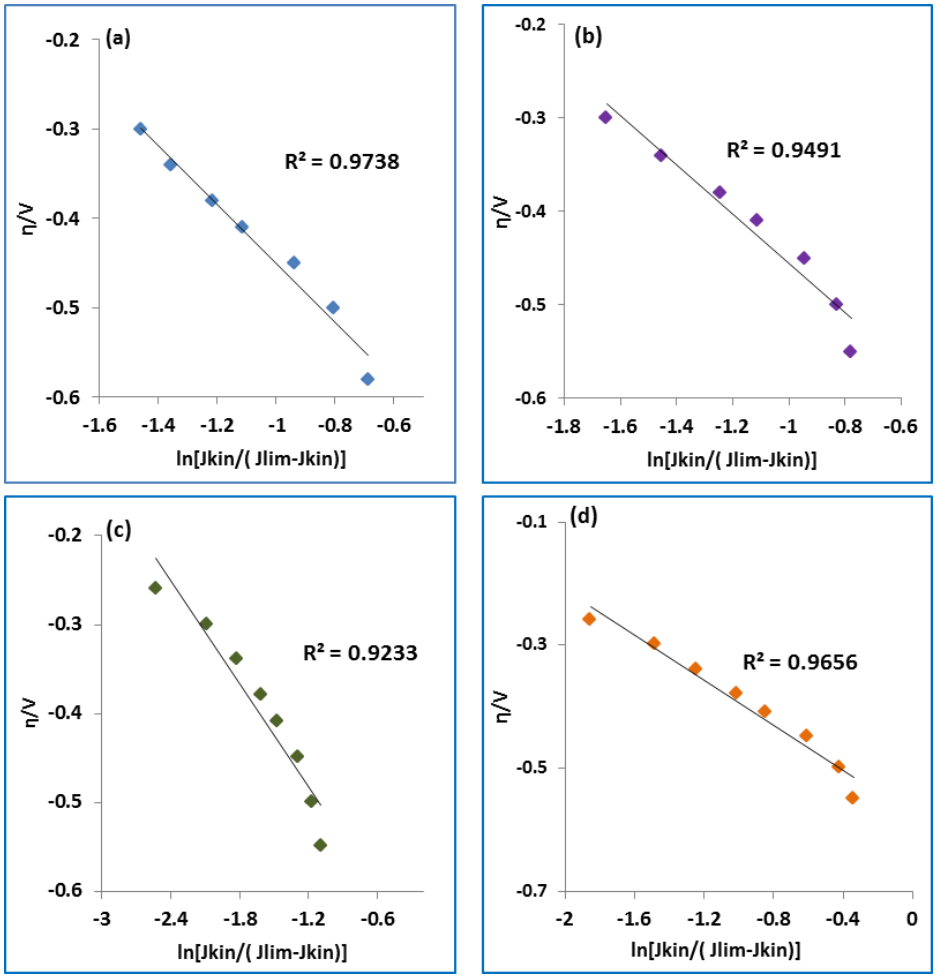

Figure 7.4: Tafel plots of FeCo@Fe@Pd/CNT-OH (a), FeCo@Fe@Pd/CNT-SO_3 (b) Pd/CNT-OH (c) and Pd/CNT-SO_3(d)

Table 7.2: Kinetic parameters, *b* and j_o for the ORR

Catalyst	**Tafel Slope *b*** **($mVdec^{-1}$)**	**j_{lim}** **($mAcm^{-2}$)**	**$10^4 j_o$** **($mAcm^{-2}$)**
FeCo@Fe@Pd/CNT-OH	331.20	6.45	6.10
FeCo@Fe@Pd/CNT-SO_3	262.80	6.62	4.43
Pd/CNT-OH	193.50	10.00	2.48
Pd/CNT-SO_3	182.30	6.65	3.29

The Tafel values are very high for the core shell catalysts. It is known that porous electrodes undergoing irreversible ORR, and obeying the Tafel kinetics can result in a Tafel slope twice the value of the normal Tafel slope[25,26]. Zhang et al observed values of 10-11 times the normal Tafel values in high over potential for acid treated PtNi alloys on graphene used as electro catalysts for ORR in alkaline medium. The untreated equivalent alloys yielded 7-9 times the 120mV Tafel values[27]. The four catalysts studied have the ion exchange current density in the same magnitude though FeCo@FeCoPd/CNT-OH is slightly higher than the rest. The magnitude of the ion exchange current density determines how rapidly the electrochemical reaction can occur. The ORR exchange current density values obtained are in the same magnitude but higher values than some Pt based catalysts used for ORR in acidic medium[28,29].

7.5 Methanol Tolerance.

The alcohol tolerant ability is very important for cathode electro catalysts intending to be used for practical fuel cell applications, especially in direct alcohol fuel cells. Thus a methanol tolerance of the four catalysts was studied in O_2-saturated 0.1 M KOH with 2 M methanol at a scan rate of 10 mV s^{-1} and 1500 rpm. The plots are depicted in Figures.7.5.

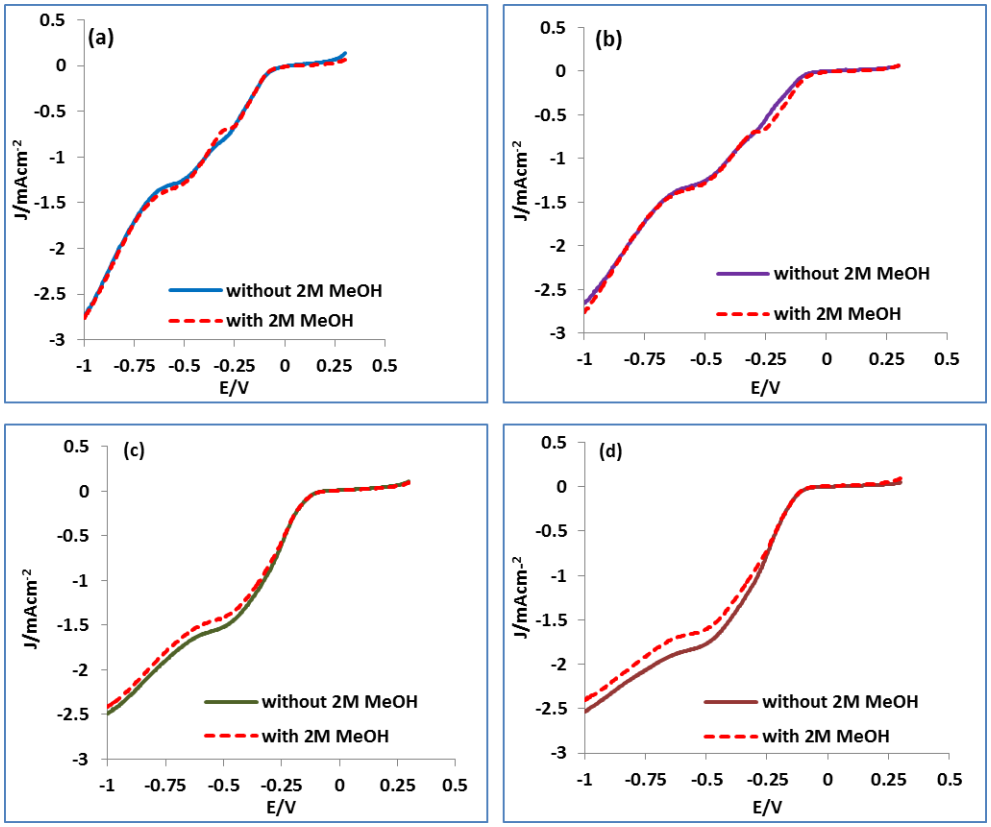

Figure 7.5: ORR polarization curves for FeCo@Fe@Pd/CNT-OH, (a) FeCo@Fe@Pd/CNT-SO_3, (b) Pd/CNT-OH (c) and Pd/CNT-SO_3 (d) in O_2 saturated 0.1 M KOH solutions with 2 M CH_3OH, at 1500 rpm and 10 mV s^{-1}.The broken lines depict the ORR curves with CH_3OH.

The onset potential values and current density responses are maintained at both FeCo@Fe@Pd/CNT-OH and FeCo@Fe@Pd/CNT-SO_3 modified electrodes during ORR with and without the presence of methanol. The 'first step' in the mixed kinetic-diffusion control region attributed to the production of hydrogen peroxide is very slightly pronounced in both catalysts. The two catalysts appear not to be affected by the presence of alcohol. On the contrary, Pd/CNT-OH and (d) Pd/CNT-SO_3 exhibit a reduced shift in their current density response. Though the onset potential for ORR is still the same with or without alcohol, there is a reduced $E_{1/2}$ potential in their ORR curves in the presence of methanol. The negative $E_{1/2}$ shift is more pronounced in Pd/CNT-SO_3, than Pd/CNT-OH. This gives a confirmation of the excellent alcohol tolerant ability of the core shell Pd based catalysts.

7.6 Stability

As the core shell catalysts have proved to be the better of the four catalysts studied, they were tested for their stability at the oxygen reduction potentials. They were subjected to a repetitive and continuous potential cycling between 0.4 V to -1.0 V at a scan rate of 50 mVs^{-1} in 0.1 M KOH to evaluate their durability. Figure 7.6 shows the electrochemical surface area (ECSA, obtained from the integrated coulometric charge of the oxide reduction peaks) as a function of the number of potential cycles for FeCo@Fe@Pd/CNT-OH and FeCo@Fe@Pd/CNT-SO_3 catalysts. It can be seen that each catalyst show an increased ECSA in the first few cycles, which could be attributed to surface roughening and removal of contaminants from the sample surface. However, the ECSA of both catalysts decreased gradually at 700 cycles and stabilised after 1200 cycles. This is a good indication of their durability. A recently reported Au decorated Pd-Co alloy exhibited complete degradation after 300 cycles[30].

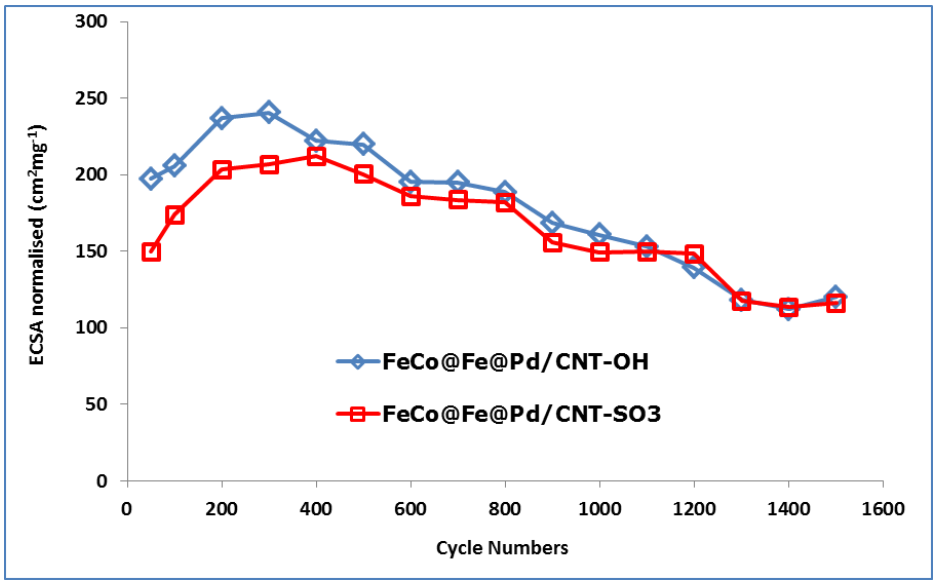

Figure 7.6: Electrochemical surface area as a function of the number of potential cycles for FeCo@Fe@Pd/CNT-OH and FeCo@Fe@Pd/CNT-SO_3 catalysts

7.7 Comparative Studies with other Pd based Catalysts

Table 7.3 shows a short comparative assessment of the ORR performance and kinetics of the catalysts studied in comparison with other Pd based catalysts published in recent literature.

Table 7.3: Comparative table showing onset reduction potential (E_{red} onset), number of electrons transferred and Tafel slope (b) values of Pd-based catalysts in ORR.

Pd-based catalyst	Electrolyte	E_{red} onset[1] (V)	No of e-s	b /mVdec^{-1}	Ref
FeCo@Fe@Pd/CNT-OH	0.1 M KOH	0.04vs Ag/AgCl	4	331.2	This work
FeCo@Fe@Pd/CNT-SO_3	0.1 M KOH	-0.03vs Ag/AgCl	3	262.8	This work
Pd/CNT-OH	0.1 M KOH	-0.08 vs Ag/AgCl	3	193.5	This work
Pd/CNT-SO_3	0.1 M KOH	-0.06 vs Ag/AgCl	3	182.3	This work
Pd/CNT-acid treated	0.1 M KOH	0.90 vs RHE	4	63/80	31
Pd_3-Ni/C	0.1M KOH	-0.13 vs Hg/HgO	3.40	48/110	32
Ag_1Pd_1/CNT	1 M NaOH	-0.10 vs Ag/AgCl	2.11	n/a	33
Ag_2Pd_1/CNT	1 M NaOH	-0.10 vs Ag/AgCl	1.88	n/a	33
Ag_4Pd_1/CNT	1 M NaOH	-0.10 vs Ag/AgCl	2.25	70/ 136	33
Pd-Sn/C	0.5 M KOH	-0.19 vs Ag/AgCl	3.8	48/110	34
Pd@Ag/C	0.1M NaOH	0.00 vs Hg/HgO	n/a	60/120	13
PdNP/CNT -sputtered	0.1 M KOH	0.90 vs RHE	4	60/107	35
Pd Bulk	0.1 M KOH	0.90 vs RHE	4	52/111	35
Ag@Pd/CNT	1.0 M KOH	-0.09 vs MMO	2.8	n/a	14

Note: [1] Onset potential obtained from RDE at 1600 rpm. CNT-carbon nanotube; PdNP- Palladium nanoparticles

7.8 Conclusion

Palladium decorated core shell nanocatalysts supported on carboxylate and sulfonate functionalised multi walled carbon nanotubes, FeCo@Fe@Pd/CNT-OH and FeCo@Fe@Pd/CNT-SO_3, exhibited a superior ORR activity in alkaline medium compared to their Pd monometallic counterparts incorporated on the same substrates. The improved ORR activity of the core shell nano catalysts can be attributed to the compressive strain experienced by the Pd skin of the core shell catalysts. XRD analyses already show that the Pd interatomic distance in the core shell nano catalysts are smaller than that of pure Pd nanoparticles with a mismatch of about 1.35 % and 1.01 % in FeCo@Fe@Pd/CNT-OH and FeCo@Fe@Pd/ CNT-SO_3 respectively. This compressive strain is expected to shift the d-band centre to a lower energy level, thus weakening the adsorption energy of the adsorbates on their surfaces and leading to an enhanced ORR performance. It has been well determined that the electronic structure (d-band centre, relative to the Fermi level) governs the strength of bonding of OH and O to a metal surface and thus, in turn, controls the ORR kinetics[36–39]. The smaller nanoparticle sizes of the core shell nanocatalysts also resulted in an increased surface area for ORR catalysis. The effect of the different substrates used was noticeable in the kinetics of the core shell nano catalysts. FeCo@Fe@Pd/CNT-OH exhibited a more favourable ORR pathway than its sulfonate counterpart, thus coupled with its high ethanol tolerance in alkaline medium and its metal composition it may be another preferred alternative as a cheap cathode catalyst in direct alkaline alcohol fuel cells.

7.9 References

(1) Liu, Z.; Zhao, B.; Guo, C.; Sun, Y.; Shi, Y.; Yang, H.; Li, Z. *J. Colloid Interface Sci.* **2010**, *351*, 233–8.

(2) Hu, F.; Cui, X.; Chen, W. *J. Phys. Chem. C* **2010**, 20284–20289.

(3) Murugesan, S.; Myers, K.; Subramanian, V. (Ravi). *Appl. Catal. B Environ.* **2011**, *103*, 266–274.

(4) Hu, G.; Nitze, F.; Barzegar, H. R.; Sharifi, T.; Mikołajczuk, A.; Tai, C.-W.; Borodzinski, A.; Wågberg, T. *J. Power Sources* **2012**, *209*, 236–242.

(5) Lee, C.-L. *J. Solid State Electrochem.* **2007**, *11*, 1313–1317.

(6) Zheng, J.-S.; Wang, M.-X.; Zhang, X.-S.; Wu, Y.-X.; Li, P.; Zhou, X.-G.; Yuan, W.-K. *J. Power Sources* **2008**, *175*, 211–216.

(7) Jirkovský, J. S.; Panas, I.; Ahlberg, E.; Halasa, M.; Romani, S.; Schiffrin, D. J. *J. Am. Chem. Soc.* **2011**, *133*, 19432–41.

(8) Campos, M.; Siriwatcharapiboon, W.; Potter, R. J.; Horswell, S. L. *Catal. Today* **2013**, *202*, 135–143.

(9) Jürmann, G.; Tammeveski, K. *J. Electroanal. Chem.* **2006**, *597*, 119–126.

(10) Antolini, E. *Energy Environ. Sci.* **2009**, *2*, 915.

(11) Slanac, D. A.; Hardin, W. G.; Johnston, K. P.; Stevenson, K. J. *J. Am. Chem. Soc.* **2012**, *134*, 9812–9.

(12) Burchardt, T. *J. Power Sources* **2004**, *135*, 192–197.

(13) Jiang, L.; Hsu, A.; Chu, D.; Chen, R. *Electrochim. Acta* **2010**, *55*, 4506–4511.

(14) Sekol, R. C.; Li, X.; Cohen, P.; Doubek, G.; Carmo, M.; Taylor, A. D. *Appl. Catal. B Environ.* **2013**, *138-139*, 285–293.

(15) Wei, Y.-C.; Liu, C.-W.; Chang, Y.-W.; Lai, C.-M.; Lim, P.-Y.; Tsai, L.-D.; Wang, K.-W. *Int. J. Hydrogen Energy* **2010**, *35*, 1864–1871.

(16) Diabate, D.; Napporn, T. W.; Servat, K.; Habrioux, a.; Arrii-Clacens, S.; Trokourey, a.; Kokoh, K. B. *J. Electrochem. Soc.* **2013**, *160*, H302–H308.

(17) Song, C.; Zhang, J. *PEM Fuel Cell Electrocatalysis and Catalyst Layers: Fundamentals and Applications*; Ed.; Springer, 2008; p. 1159.

(18) Blizanac, B. B.; Ross, P. N.; Markovic, N. M. *Electrochim. Acta* **2007**, *52*, 2264–2271.

(19) Mustain, W. E.; Prakash, J. *J. Power Sources* **2007**, *170*, 28–37.

(20) Fu, G.; Jiang, X.; Tao, L.; Chen, Y.; Lin, J.; Zhou, Y.; Tang, Y.; Lu, T. *Langmuir* **2013**, *29*, 4413–20.

(21) Yeager Ernest. *J. Mol. Catal.* **1986**, *38*, 5–25.

(22) Demarconnay, L.; Coutanceau, C.; Léger, J.-M. *Electrochim. Acta* **2004**, *49*, 4513–4521.

(23) Coutanceau, C.; Croissant, M. .; Napporn, T.; Lamy, C. *Electrochim. Acta* **2000**, *46*, 579–588.

(24) Schmidt, T. J.; Gasteiger, H. A.; Behm, R. J. *J. Electrochem. Soc.* **1999**, *146*, 1296–1304.

(25) Soderberg, J. N.; Co, A. C.; Sirk, A. H. C.; Birss, V. I. *J. Phys. Chem. B* **2006**, *5*, 10401–10410.

(26) Perry, M.; Newman, J.; Cairns, E. J. **1998**, *145*, 5–15.

(27) Zhang, K.; Yue, Q.; Chen, G.; Zhai, Y.; Wang, L.; Wang, H.; Zhao, J.; Liu, J.; Jia, J.; Li, H. **2011**, 379–389.

(28) Meng, H.; Shen, P. K. *J. Phys. Chem. B* **2005**, *109*, 22705–9.

(29) Stassi, a.; D'urso, C.; Baglio, V.; Blasi, a.; Antonucci, V.; Arico, a. S.; Castro Luna, a. M.; Bonesi, a.; Triaca, W. E. *J. Appl. Electrochem.* **2006**, *36*, 1143–1149.

(30) Wei, Y.-C.; Chen, T.-Y.; Liu, C.-W.; Chan, T.-S.; Lee, J.-F.; Lee, C.-H.; Lin, T.-L.; Wang, K.-W. *Catal. Sci. Technol.* **2012**, *2*, 1654.

(31) Jukk, K.; Alexeyeva, N.; Johans, C.; Kontturi, K.; Tammeveski, K. *J. Electroanal. Chem.* **2012**, *666*, 67–75.

(32) Li, B.; Prakash, J. *Electrochem. commun.* **2009**, *11*, 1162–1165.

(33) Lee, C.-L.; Chiou, H.-P.; Chang, K.-C.; Huang, C.-H. *Int. J. Hydrogen Energy* **2011**, *36*, 2759–2764.

(34) Kim, J.; Momma, T.; Osaka, T. *J. Power Sources* **2009**, *189*, 909–915.

(35) Jukk, K.; Alexeyeva, N.; Sarapuu, A.; Ritslaid, P.; Kozlova, J.; Sammelselg, V.; Tammeveski, K. *Int. J. Hydrogen Energy* **2013**, *38*, 3614–3620.

(36) Shao, M. H.; Huang, T.; Liu, P.; Zhang, J.; Sasaki, K.; Vukmirovic, M. B.; Adzic, R. R. *Langmuir* **2006**, *22*, 10409–15.

(37) Mavrikakis, M.; Hammer, B.; Nørskov, J. K. *Phys. Rev. Lett.* **1998**, *81*, 2819–2822.

(38) Nanoparticles, E. S.; Tian, N.; Zhou, Z.; Sun, S. *J. Phys. Chem. C* **2008**, *112*, 19801–19817.

(39) Zhang, Z.; More, K. L.; Sun, K.; Wu, Z.; Li, W. *Chem. Mater.* **2011**, 1570–4577.

Chapter 8*

ELECTROCATALYTIC OXIDATION OF MONOHYDRIC ALCOHOLS AT FeCo@Fe@Pd/MWCNTS

* The following manuscript is in preparation for publication and resulted from part of the research work presented in this chapter.

O.O. Fashedemi and K.I. Ozoemena, "Palladium decorated FeCo@Fe core-shell (FeCo@Fe@Pd) supported on carbon nanotubes for Methanol and Ethanol oxidation in Alkaline Medium".

8.1 Introduction

A lot of extensive research has gone into the study of direct methanol fuel cells (DMFCs). This is because the methanol (MeOH) is the simplest alcohol and its electrochemical reaction kinetics is faster than those of other alcohol fuels during its electrocatalytic oxidation process. On the other hand, ethanol (EtOH) is less toxic, more environmentally friendly and also has a higher energy density than methanol; it can also be produced in large quantities through green fermentation process[1,2]. Thus, direct ethanol fuel cells (DEFCs) have also been receiving great attention in direct alcohol fuel cell (DAFC) technology. Although Pt is the favourite choice of catalyst for alcohol oxidation, it gets easily poisoned due to surface coverage by intermediates like Pt-CO during oxidation of alcohols. Pd is a better candidate as it is less expensive, 50 times more abundant on earth and can also overcome the CO poisoning effect[3–5]. Another important advantage of Pd based catalysts is the superior stability and corrosion resistance in alkaline media[6]. One of the main points for future studies is to improve their catalytic performances in DAFCs.

In comparison with monometallic Pd nanostructures, Pd-based alloy nanostructures show enhanced electrocatalytic activities due to the synergetic and electronic effect. Based on this a lot of Pd based alloy nanoparticles have been successfully synthesized and showing an enhanced performance in electrocatalytic applications[7–10]. Among these are the core shell nanocatalysts which are emerging as effective nanocatalysts aimed at efficient utilization of the precious metals since the precious or noble metal can be highly dispersed on a core formed of relative inexpensive metals. This study looks into the use of the ternary core-shell FeCo@Fe@Pd incorporated on carboxyl- and sulfonate-functionalised carbon nanotubes (CNT-OH and CNT-SO_3) as anode catalysts for the oxidation of two monohydric alcohols, MeOH and EtOH. A comparison with monometallic Pd on both substrates, Pd/CNT-OH and Pd/CNT-SO_3, was also done.

8.2 Comparative Cyclic Voltammetry Experiments

The first test for the monohydric alcohol oxidation reaction performance of the four catalysts was carried out using CV. From Figures 8.1 and 8.2 it can be seen that at potentials below negative 0.75 V, the oxidation current is negligible in all the voltammograms but with increasing potential, the oxidation current takes off rapidly, signifying the oxidation of the alcohols. The alcohol oxidation onset potential (E_{onset}) and current density *(j)* response are the two main parameters to evaluate catalytic activity of electro catalysts while employing CV. Two anodic peaks can be observed in all the CV scans, the oxidation peak in the forward scan is related to the oxidation of freshly chemisorbed alcohol species while the reverse oxidation peak corresponds to the removal of carbonaceous species partially oxidised in the forward scan, rather than that caused by newly adsorbed species[11,12]. The anodic forward scan actually measures the alcohol oxidation and the magnitude of this scan gives the electro catalytic activity of the electro catalyst for alcohol oxidation.

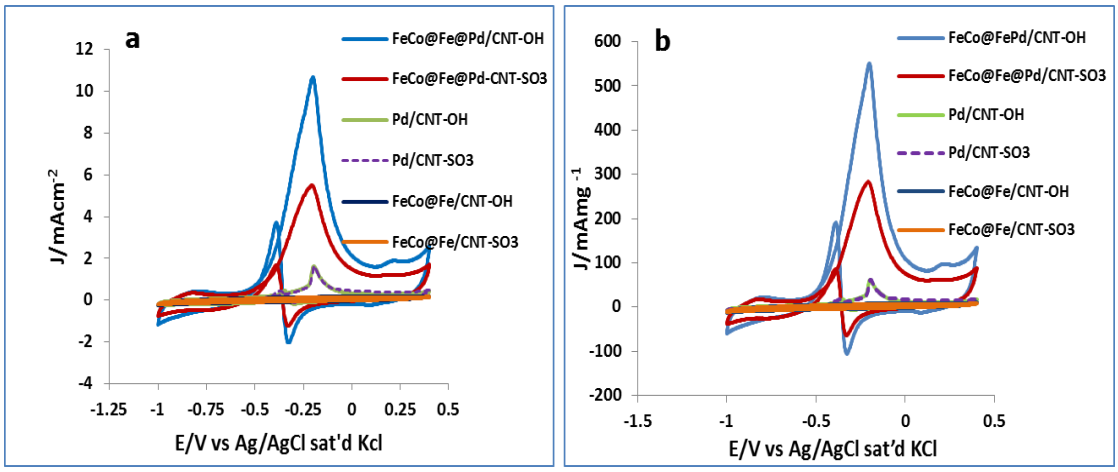

Figure 8. 1: Comparative cyclic voltammograms of the six catalysts in 0.5 M MeOH/1M KOH (Scan rate-50mVs^{-1}); [current response in current density (a) and in mass density (b)]

Figures 8.1a and 8.1b correspond to the performances of the catalysts in methanol. A good observation of the voltammograms shows that the core shell incorporated on sulfonate nanotube FeCo@Fe@Pd/CNT-SO_3 exhibits the highest negative onset potential value of -0.65V. This value is about

30mV earlier than that of FeCo@Fe@Pd/CNT-OH which is -0.62 V. However, although FeCo@Fe@Pd/CNT-SO_3 shows the earliest onset potential for MeOH oxidation, the corresponding potential of methanol oxidation on FeCo@Fe@Pd/CNT-OH at every other given oxidation current density is obviously lower than the other three catalysts, indicating the ease of methanol oxidation reaction on this catalyst though it had a slightly late start in oxidation. Monometallic nano Pd incorporated on CNT-OH and CNT-SO3 both exhibit the same onset potential at -0.38 V, thus beginning their catalytic oxidation of methanol at about 250mV later than the core shell nanocatalysts.The methanol oxidation peak potentials values of the four catalysts were all around -0.2 V. Their specific values were -0.21V, -0.22 V, and -0.19 V for FeCo@Fe@Pd/CNT-OH, FeCo@Fe@Pd/CNT-SO_3, Pd /CNT-OH and Pd/CNT-SO_3, respectively.

Evaluating the current responses for methanol oxidation by the four catalysts one sees that FeCo@Fe@Pd/CNT-OH gave the highest current density value of 10.40mAcm^{-2} (552 Ag^{-1}), which is twice that of FeCo@Fe@Pd/CNT-SO_3:5.25 mAcm-^{2} (283 Ag^{-1}) and more than six times greater than that of the mono metallic nanoparticles of Pd/CNT-OH and Pd/CNT-SO_3 which both have a value of 1.63 mAcm^{-2} (60.8 Ag^{-1}).

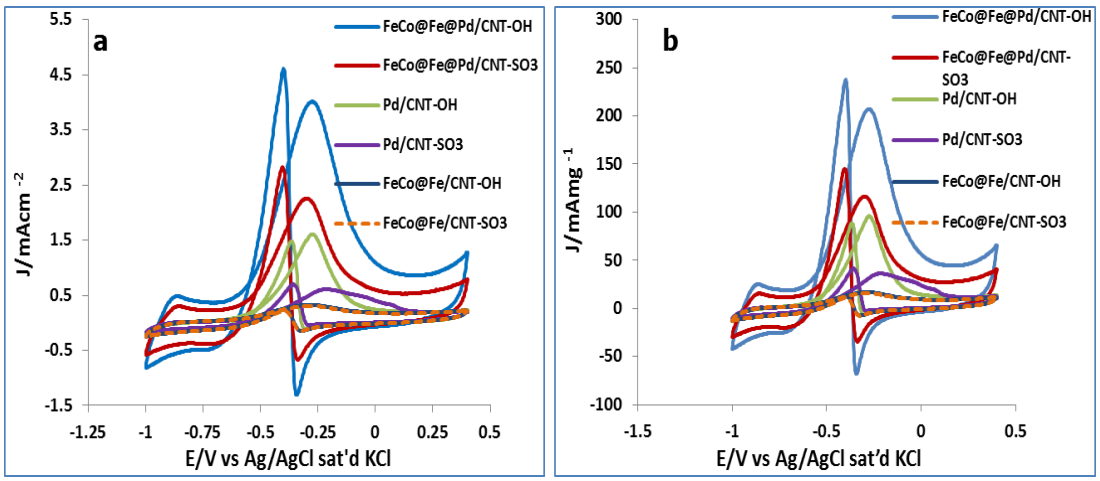

Figure 8. 2: Comparative cyclic voltamograms of the six catalysts in 0.5 M EtOH/1M KOH (Scan rate-50mVs^{-1}); [current response in current density (a) and in mass density (b)]

The same trends observed in methanol oxidation are seen at comparing the electro catalytic performances of the catalysts for ethanol oxidation. Cyclic voltammograms for the oxidation of ethanol is shown in Figure 8.2. FeCo@Fe@Pd/CNT-OH gave the best and earliest onset potential at -0.692 V, which is about 20 mV earlier than that of FeCo@Fe@Pd/CNT-SO_3 with -0.673 V. Pd/CNT-OH and Pd/CNT-SO_3 both had onset potentials of -0.0580 V and -0.5668 V, respectively. All the catalysts exhibited their ethanol oxidation peak potentials at about -0.30 V. FeCo@Fe@Pd/CNT-OH still showed the highest current density of 3.98 $mAcm^{-2}$ (220 Ag^{-1}); FeCo@Fe@Pd/CNT-SO_3 was 2.22 $mAcm^{-2}$ (110 Ag^{-1}), Pd/CNT-OH was 1.46 $mAcm^{-2}$(98 Ag^{-1}) and Pd/CNT-SO_3, 0.64 $mAcm^{-2}$ (28 Ag^{-1})

It is generally accepted that during alcohol oxidation at noble metal catalysts surface some poisonous intermediates, such as CHO_{ads}, CH_3Co_{ads}, and CO_{ads} can be strongly adsorbed on the metal surface as a result of oxidation of chemisorbed alcohols, leading to a self-poisoning of the catalysts. The ratio of the forward anodic peak current density (j_f) to the reverse anodic peak current density (j_b) i.e., j_f/j_b can be used to evaluate the poisoning tolerance of the catalyst. A larger j_f/j_b value, is attributed to a more effective removal of the poisoning species on the catalysts' surface during the anodic forward scan as well as less accumulation of carbonaceous residues on the modified electrode surface[13–15]

The j_f/j_b ratios calculated for the four catalysts studied during methanol oxidation are greater than 2. This means the modified electrodes have a high tolerance to CO_{ads} species in methanol oxidation. The marked increase of the backward scan peak observed during ethanol oxidation is already suggestive of the formation of more strongly adsorbed carbonaceous species being oxidised/removed as compared to those generated during methanol oxidation. The result of this is seen in the generally lower j_f/j_b values during ethanol oxidation.

Comparing the activities of the catalysts in the oxidation of the two alcohols (from their cyclic voltammograms); one observes that the onset potential for the catalytic oxidation of methanol and ethanol begins at practically the same voltages (≈-0.6 V /-0.7 V) for all the catalysts, but the peak potential value for ethanol oxidation (-0.30 V) is 10 mV earlier than that of the oxidation of methanol (-0.20 V) on all the catalysts. However, the four catalysts also showed lower values of anodic forward current responses in ethanol oxidation compared to their anodic current responses in methanol oxidation.

It can be reasonably concluded that although the catalysts generally exhibited an initial ease of ethanol oxidation, the kinetics of methanol oxidation on the catalysts appear to be better considering the current response and values of j_f/j_b ratio. Table 8.1 below gives a summary of the electrocatalytic performance of the catalysts in methanol and ethanol oxidation in terms of the onset potential and current densities and the J_f/J_b ratio from the data obtained from the cyclic voltammograms.

Table 8.1: Summary of the electrocatalytic activities of the catalysts in 0.5 M [alcohol]/1.0 M KOH solution.

	0.5M MeOH/ 1 M KOH				**0.5M EtOH/ 1 M KOH**			
Catalysts	**E_s (V)**	**E_p (V)**	**J_f / (mAcm^{-2})**	**J_f/J_b**	**E_s (V)**	**E_p(V)**	**J_f/ (mAcm^{-2})**	**J_f/J_b**
FeCo@Fe@Pd/CNT-OH	-0.6002	-0.2066	10.40	3.42	-0.6924	-0.2969	3.98	0.85
FeCo@Fe@Pd/CNT-SO_3	-0.5801	-0.2164	5.25	3.52	-0.6729	-0.3214	2.22	0.80
Pd-CNT-OH	-0.3751	-0.1944	1.63	3.82	-0.5801	-0.2896	1.56	1.07
Pd-CNT-SO_3	-0.3751	-0.1944	1.63	3.47	-0.5582	-0.2335	0.61	0.95

8.3 Electrochemical Impedance Spectroscopy

Further insights into the electrocatalytic activity of the catalysts towards oxidation of MEOH and ETOH were obtained using the electrochemical impedance spectroscopy (EIS). Figures 8.3a and 8.3b represent the Nyquist plots at active negative potentials (-0.29V) measured in 0.5M MeOH/1.0 M KOH solution and at -0.30 V measured in 0.5M EtOH/1.0 M KOH solution. The equivalent circuit used in fitting the plot is the same for both alcohols [$R_s(R_{ct}CPE)$], where R_s is the electrolyte solution resistance, R_{ct} is the charge transfer resistance, and CPE is the constant phase element. The electrochemical impedance data is summarized in Table 8.2. The R_s values are the same for the alcohols at the voltages studied, this implies the electrolyte solution does not affect the oxidation reaction.

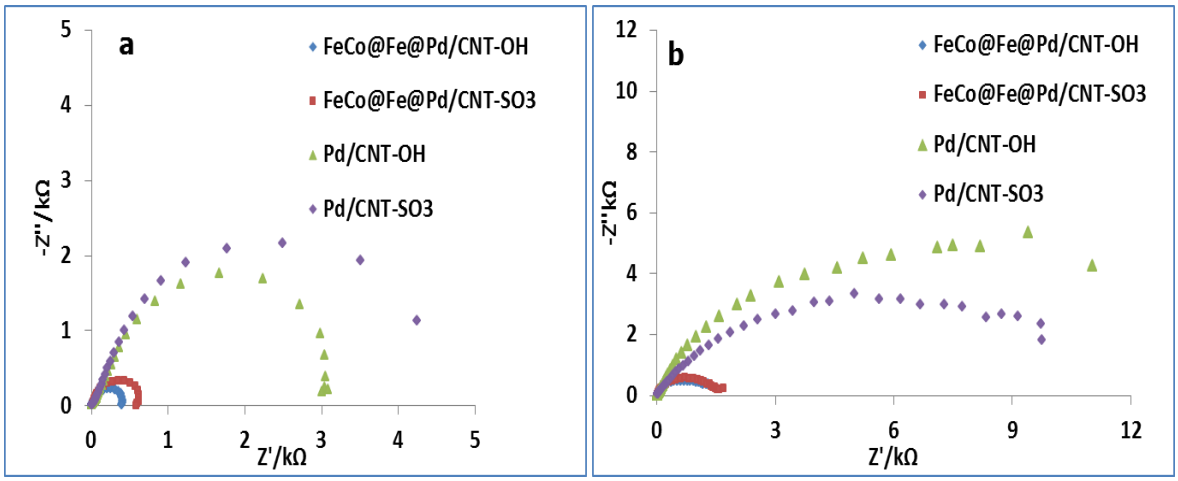

Figure 8.3: Nyquist plots at active negative potentials -0.29V in 0.5M MeOH/1.0 M KOH (a) and at -0.30 V in 0.5M EtOH/1.0 M KOH (b)

It should be noted that the R_{ct} values give the interpretation of the rate of electron transfer at the electrode solution interface. It is the only element that has a physical meaning, describing how fast the rate of charge transfer changes with changing electrode potential during a reaction[16]. The large arc observed in Nyquist plots in both alcohols for Pd/CNT-OH and Pd/CNT-SO_3 corresponds to a large charge transfer resistance (R_{CT}) value. This observation - as also explained by other authors[17], - indicates slow kinetics of their hydrogen desorption processes at the start of the reaction which can

be caused by the strongly adsorbed intermediate species on the Palladium sites thereby blocking continuous adsorption of alcohol molecules. On the other hand, smaller arcs are observed for FeCo@Fe@Pd/CNT-OH and FeCo@Fe@Pd/CNT-SO_3 at the high frequency region, indicating a faster kinetics in the oxidation of both alcohols. FeCo@Fe@Pd/CNT-OH gave smaller R_{CT} values.

Table 8.2: EIS parameters obtained from the oxidation of methanol and ethanol at -0.2 V in 0.5 M [alcohol]/1.0 M KOH sat N_2.

	Electrochemical Impedance Parameters							
Catalysts	**Methanol**				**Ethanol**			
	R_s (Ω)	**R_{ct} (kΩ)**	**Q/CPE**		**R_s (Ω)**	**R_{ct} (kΩ)**	**Q/CPE**	
			Y_o(mF)	**n**			**Y_o (mF)**	**n**
FeCo@Fe@Pd/CNT-OH	13.96 (4.43)	0.393 (4.841)	$0.187e^{-3}$ (13.033)	0.833 (2.876)	13.900 (2.592)	1.349 (3.224)	$0.162e^{-3}$ (2.022)	0.789 (1.149)
FeCo@Fe@Pd/CNT-SO_3	15.38 (3.14)	0.593 (3.482)	$0.103e^{-3}$ (8.984)	0.915 (1.822)	12.280 (2.277)	1.776 (2.219)	$0.763e^{-4}$ (3.886)	0.833 (0.802)
Pd/CNT-OH	16.170 (7.574)	3.990 (14.167)	$0.163e^{-3}$ (10.240)	0.728 (2.789)	12.560 (2.181)	14.300 (2.960)	0.534^{-4} (1.867)	0.776 (0.427)
Pd/CNT-SO_3	20.760 (11.936)	3.130 (10.189)	$0.395e^{-4}$ (2.384)	0.800 (3.778)	16.310 (7.814)	11.050 (1.662)	0.298^{-4} (1.823)	0.681 (0.398)

8.4 Chronoamperometry

To determine the long term electrocatalytic performance and stability of the catalysts, chronoamperograms of the four catalysts were recorded with a bias of – 0.2 V vs Ag/AgCl sat'd KCl in 0.5 M MeOH/1 M KOH and in 0.5 M EtOH/1 M KOH respectively at room temperature. Chronoamperograms are shown in Fig 8.4 (a) and (b). An initial rapid current density decay can be observed in the early stage of the reaction, this is probably due to formation of some intermediate species (CO_{ads} and CHO_{ads}) adsorbed on the catalysts' surface during the oxidation of the alcohols. Quasi steady currents are later seen for all the catalysts after 1000 s duration of the reaction in both alcohols. Despite the current decay for all the catalysts, the limiting or steady current of FeCo@Fe@Pd/CNT-OH catalyst had the highest value out of all the catalysts studied under the same experimental conditions in both alcohols.

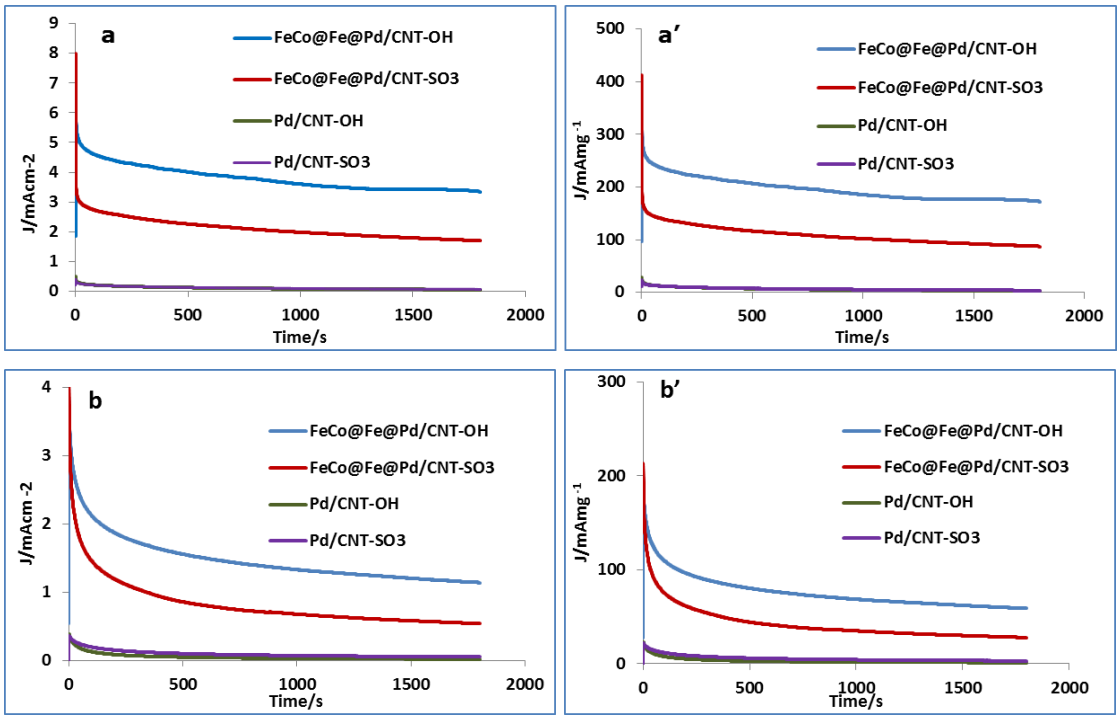

Figure 8.4: Chronoamperograms of FeCo@Fe@Pd/CNT-OH, FeCo@Fe@Pd/CNT-SO_3, Pd/CNT-OH and Pd/CNT-SO_3 in methanol (a and a') and ethanol (b and b').

The percentage of the steady state current at the end of the reaction to original current at the onset of the reaction was found to be 70.48 % and 29.46% in methanol and ethanol oxidation respectively using FeCo@Fe@Pd/CNT-OH as catalysts. These values are higher than those obtained for all the other three catalysts in the oxidation of both methanol and ethanol – FeCo@Fe@Pd/CNT-SO_3 (59.72 %/13.07 %), Pd/CNT-OH (17.15 %/17.70 %) and Pd/CNT-SO_3 (30 %/14.56 %). This further confirms the superior catalytic performance of FeCo@Fe@Pd/CNT-OH for methanol and ethanol oxidation. As noticed earlier with the CV results one also observes the better catalytic reaction in methanol oxidation compared to ethanol.

8.5 Kinetics

The kinetic parameters of methanol and ethanol oxidation on the two best catalysts, FeCo@Fe@Pd/CNT-OH and FeCo@Fe@Pd/CNT-SO_3, were obtained from Tafel plots displayed in Figures 8.5. The conventional Tafel equation for oxidation processes, equations (8.1) and (8.2) were used[18,19].

$$\eta = a + b \log j \qquad (8.1)$$

$$b = \frac{2.303RT}{\alpha nF} \quad \text{and} \quad a = \frac{2.303RT}{\alpha nF} \log j_o \qquad (8.2)$$

where η is the overpotential (difference between the applied potential and open circuit potential), j is the current density , b is the Tafel slope, a is the Tafel constant relating to the exchange current density -j_o, α is the transfer coefficient , n is the number of electrons involved in the rate-determining step, while other symbols retain their usual meaning.

The average values of the Tafel slope, *b,* for FeCo@Fe@Pd/CNT-OH and FeCo@Fe@Pd/CNT-SO_3 are 161.67 and 224.17 $mVdec^{-1}$ respectively in

methanol. This implies a faster kinetics of methanol oxidation on modified FeCo@Fe@Pd/CNT-OH electrode in comparison to FeCo@Fe@Pd/CNT-SO_3. In ethanol oxidation, however, their Tafel values are of the same range, 186.17 $mVdec^{-1}$ and 189.17 $mVdec^{-1}$ for FeCo@Fe@Pd/CNT-OH and FeCo@Fe@Pd/CNT-SO_3, respectively. It is clear that the mechanisms of both catalysts are virtually the same in ethanol oxidation reaction (EOR). These values are in agreement with those observed in literature[21]. They are much lower than those obtained by Maiyalagan and Scott[22] (212-223-$mVdec^{-1}$) using PdNi on carbon nanofibres-PdNi/CNFs and Bambagioni et al. (282-249 $mVdec^{-1}$) using Pd/ MWCNT[17]. One also sees that the mechanisms of MOR and EOR are quite favourable on FeCo@Fe@Pd/CNT-OH nanocatalyst. The electrode surface does not exhibit any form of porosity as this is associated with very large Tafel values.

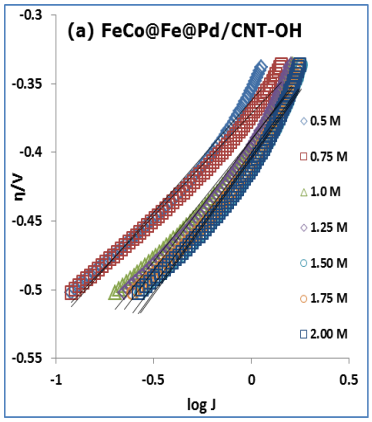

[METHANOL]/M	Tafel slope (2.303RT/anF)	a (-RT/anF) log J_o	J_o	R^2
0.5	163	0.362	0.167	0.9810
0.75	150	0.372	0.306	0.9898
1.00	178	0.390	0.156	0.9791
1.25	190	0.391	0.113	0.9795
1.50	198	0.404	0.111	0.9733
1.75	193	0.400	0.117	0.9735
2.00	193	0.403	0.108	0.9711

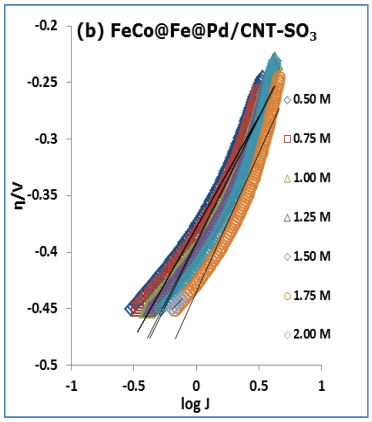

[METHANOL]/M	Tafel slope (2.303RT/anF)	a (-RT/anF) log J_o	J_o	R^2
0.5	196	0.367	0.0748	0.9756
0.75	197	0.378	0.0838	0.9665
1.00	224	0.390	0.0549	0.9632
1.25	231	0.393	0.0507	0.9623
1.50	251	0.412	0.0439	0.9508
1.75	246	0.435	0.0588	0.9527
2.00	248	0.431	0.0545	0.9495

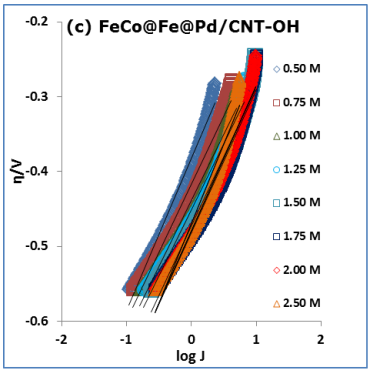

[ETHANOL]/M	Tafel slope (2.303RT/anF)	a (-RT/anF) log Jo	J_o	R^2
0.5	202	0.382	0.077	0.9795
0.75	183	0.417	0.192	0.9732
1.00	177	0.439	0.304	0.9735
1.25	177	0.451	0.358	0.9718
1.50	186	0.473	0.345	0.9611
1.75	192	0.481	0.324	0.9656
2.00	193	0.478	0.302	0.9656
2.50	212	0.470	0.164	0.9575

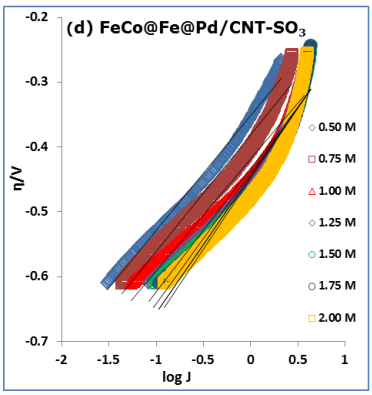

[ETHANOL]/M	Tafel slope (2.303RT/anF)	a (-RT/anF) log Jo	J_o	R^2
0.5	178	0.352	0.0096	0.9857
0.75	180	0.381	0.132	0.9704
1.00	173	0.419	0.265	0.9560
1.25	190	0.433	0.194	0.9510
1.50	203	0.440	0.149	0.9305
1.75	211	0.445	0.127	0.9278
2.00	218	0.448	0.114	0.9333

Figure 8.5: Tafel plots and corresponding kinetics data of FeCo@Fe@Pd/CNT-OH and FeCo@Fe@Pd/CNT-SO_3 catalysts in 0.5 M MeOH /1 M KOH (a, b) and 0.5 M EtOH/1M KOH (c, d).

It should however be noted that for a high current response at low overpotential, an electrochemical reaction must exhibit low Tafel values.[20]

The rate of alcohol oxidation catalysis (K_{cat}) was obtained for both core-shell nanocatalysts in methanol and ethanol oxidation reaction. K_{cat} was obtained using the chronoamperometry data and calculated by employing the conventional equation[23]:

$$\frac{J_{cat}}{J_{buff}} = \pi^{1/2}\left(k_{cat}C_o t\right)^{1/2} \qquad (8.3)$$

Where J_{cat} and J_{buff} are the current densities in the presence and absence of the alcohols, C_o is the bulk concentration (molcm^{-3}) and t is the time (s). A plot of J_{cat}/J_{buff} vs $t^{1/2}$ gives a slope from which K_{cat} is calculated.

Figures 8.6 (a) and (b) display the plots corresponding to methanol and ethanol oxidation with FeCo@Fe@Pd/CNT-OH and FeCo@Fe@Pd/CNT-SO_3. A quick observation of both plots shows a faster rate of catalytic oxidation of methanol by both catalysts. Also one sees a better catalytic oxidation rate performance of FeCo@Fe@Pd/CNT-OH over FeCo@Fe@Pd/CNT-SO_3 in both alcohols.

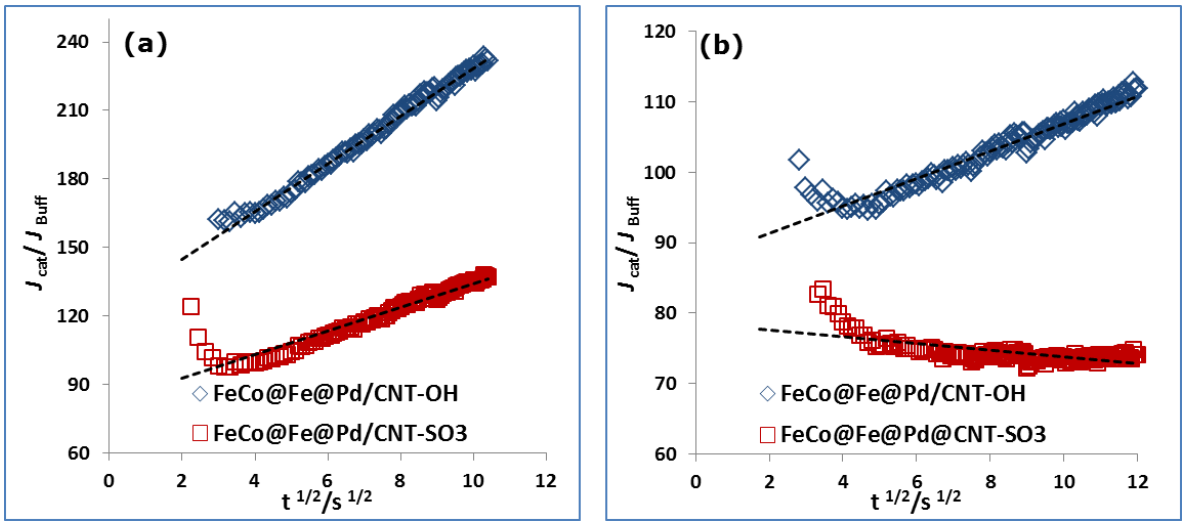

Figure 8.6: Plots of J_{cat}/J_{buff} vs $t^{1/2}$ in methanol (a) ethanol (b) using FeCo@Fe@Pd/CNT-OH and FeCo@Fe@Pd/CNT-SO_3 nanocatalysts

The K_{cat} values of both catalysts in MOR are 6.96 x 10^4 and 1.71 x 10^4 for FeCo@Fe@Pd/CNT-OH and FeCo@Fe@Pd/CNT-SO_3 respectively. While FeCo@Fe@Pd/CNT-OH gave a K_{cat} value of 2.14 x 10^3 in EOR, FeCo@Fe@Pd/CNT-SO_3 had a K_{cat} value of 1.48 x 10^2. These results corroborate all the earlier findings from the other electrochemical analyses carried out.

8.6 Comparison of electrocatalytic activity FeCo@Fe@Pd/CNTs with other Pd based catalysts for MOR in alkaline

A brief comparison of the electrocatalytic behaviour of the better core shell nanocatalysts – FeCo@Fe@Pd/CNT-OH – with other palladium based

catalysts in literature are represented in the two tables (Tables 8.3 and 8.4) below.

Table 8.3: Comparison of electrochemical performance between as prepared FeCo@Fe@Pd/CNT-OH and other Pd based catalysts reported in literature for methanol oxidation

Catalyst	E_{onset} (v)	$-E_{peak}$ (v) / J_{peak}	J_f/J_b	References
Mo@Pd/CNT (pH~9) [a]	-0.550	-0.172/395.61 ($mAmg^{-1}Pd$)	~ 5	11
PdCuSn/CNTs [b]	-0.478	-0.078/395.94 ($mAmg^{-1}Pd$)	~ 1.08	24
PdSn/CNTs [b]	-0.467	-0.033/395.94 ($mAmg^{-1}Pd$)	<1.0	24
PdCu/CNTs [b]	-0.472	-0.088/360.42 ($mAmg^{-1}Pd$)	<1.0	24
Pd-HPN-CNTs [c]	-0.780	-0.160/0.280 ($mA\mu g^{-1}$ Pd)	~3.5	25
Pd-Mn_3O_4/CNTs [d]	-0.690	0.010/715.8 $mAmg^{-1}Pd$	~2.60	26
Ni@Pd/CNTs [d]	-0.640	-0.210/770.7 $mAmg^{-1}Pd$	1.99	27
PdNi/CNTs [d]	-0.550	-0.190/482$mAmg^{1}Pd$	2.16	27
Porous PdNi [e]	~-0.580	-0.190/230$mAmg^{1}Pd$	1.2	28
G-Pd [f]	-0.490	-0.200/0.8 $mAcm^{-2}$	n/a	29
FeCo@Fe@Pd/CNT-OH	0.656/0.653	-0.207/552 $Amg^{1}Pd$ (10.60$mAcm^{-2}$)	3.05	This work

a. **Electrolyte: 1M MeOH/1M KOH, reference electrode: SCE, Scan rate : 50mV s^{-1}**
b. **Electrolyte: 0.5 M MeOH/1M KOH, reference electrode: MMO, Scan rate : 50mV s^{-1}**
c. **Electrolyte: 0.5 M MeOH/0.5M KOH, reference electrode: Ag/AgCl, Scan rate : 50mV s^{-1}**
d. **Electrolyte: 1M MeOH/0.5 M NaOH, reference electrode: SCE, Scan rate : 50mV s^{-1}**
e. **Electrolyte: 0.5 M MeOH/0.5M KOH, reference electrode: MMO, Scan rate : 50mV s^{-1}**
f. **Electrolyte: 1M MeOH/1 M KOH, reference electrode: Ag/AgCl, Scan rate 100mV s^{-1}**
g. **Electrolyte: 0.5 M MeOH/1.0 M KOH, reference electrode: Ag/AgCl, Scan rate : 50mV s^{-1}**

Table 8.4: Comparison of electrochemical performance between as prepared FeCo@Fe@Pd/CNT-OH and other Pd based catalysts reported in literature for ethanol oxidation

Catalyst	E_{onset} (v)	E_{peak} (v) /J_{peak}	I_f/I_b	References
Pt/MgO/CNT) [a]	~ -0.700	-0.360/ 2.370 ($mAcm^{-2}$)	(N/A)	30.
$Pd/SnO_2/CNTs$ [b]	-0.522	-0.100/0.462 ($mAcm^{-2}$)	(N/A)	31
$Pd/TiO_2/CNTs$ [b]	-0.526	-0.01/0.370 ($mAcm^{-2}$)	(N/A)	31
Pd/SnO_2-$TiO_2/CNTs$ [b]	-0.456	-0.01/0.478 ($mAcm^{-2}$)	(N/A)	31
PdNi [1:1] /CNT [c]	~-0.650	0.635/1077 ($mAcm^{-2}mg^{-1}$ Pd)	~3.5	12
PdNi [1:1] /CNT [d]	-0.520	0.307/3.459μA	0.5521	16
PdNi [1:1.5] /CNT [d]	-0.600	-0.307/15.900μA	0.6598	16
PdNi [1:2] /CNT [d]	-0.520	-0.280/7.479 μA	0.5139	16
PdNi [1:1] /CNT [d]	-0.520	-0.293/2.045 μA	0.7428	16
PDDA-RGO-Pd_3Pt_1 [e]	~-0.550	-0.140/2.0 $mAcm^{-2}$	0.77	14
PDDA-RGO-Pd_1Pt_1 [e]	~-0.500	-0.130/5.1 $mAcm^{-2}$	1.04	14
FeCo@Fe@Pd/CNT-OH	-0.692	-0.297/3.98 $mAcm^{-2}$ /3000 $mAcm^{-2}mg^{-1}$ Pd) or (178 μA @ 25mV/280 μA @ 25mV	0.85	This work

a. **Electrolyte: 1M EtOH/1M KOH, reference electrode: SCE, Scan rate : 50mV s^{-1}**
b. **Electrolyte1M EtOH/1M NaOH, reference electrode: SCE , Scan rate : 50mV s^{-1}**
c. **Electrolyte: 1M EtOH/1M KOH, reference electrode: MMO, Scan rate : 50mV s^{-1}**
d. **Electrolyte: 1M EtOH/1M KOH, reference electrode: SCE, Scan rate : 20mV s^{-1}**
e. **Electrolyte : 1M EtOH/1M KOH, reference electrode: SCE,, Scan rate : 50mV s^{-1}**

8.7 Conclusion

FeCo@Fe@Pd core shell nanoparticles have been immobilized on two differently functionalized carbon nanotubes, CNT-OH and CNT-SO_3, respectively. The as-synthesised composites were tested for their electrocatalytic capabilities for the oxidation of methanol and ethanol alongside the single Pd metal incorporated on the same substrates. From the various electrochemical techniques carried out to test their oxidative properties in both alcohols, there was a better ease methanol oxidation on the core shell nanoparticles in comparison to ethanol.

Relative to the mono-metallic Pd/CNT-OH and Pd/CNT-SO_3 modified electrodes, the core shell nanoparticles exhibited a marked improvement in the catalytic activity in oxidation of both alcohols especially towards MOR. Using the d band centre model[32–35], there is an occurrence of an electronic modification effect of the Pd surface as result of the lattice compressive strain or mismatch between the core alloy and Pd shell. Thus the adsorption of poisonous carbonaceous adsorbates as a result of the oxidation of the chemisorbed alcohols is weakened, (leading to their easier removal on the metal surface) and yielding higher oxidation currents in the catalytic oxidation of the two alcohols by the core shell nanocatalysts. In summary, the improved activities of the core shell nanocatalysts are mainly due to a combination of (i) increased ECSA, due to presence of a greater number of active sites, (as a result of the smaller sizes of NPs), and (ii) the electronic effect between the core, FeCo@Fe and the Pd shell resulting in the positive lattice strain on the Pd surface on the core shell nanoparticles.

Core-shell nanocatalysts incorporated on hydroxyl or carboxyl functionalised nanotube (FeCo@Fe@Pd/CNT-OH) exhibited a better catalytic performance than its sulfonate-functionalised carbon nanotube (FeCo@Fe@Pd/CNT-SO_3)counterpart in both alcohols. This can be attributed to the fact that sulfonate groups are known to form adducts

with hydroxyl groups in alkaline medium, thus giving less favourable results[36,37]. Also, the importance of substrate diffusion or product desorption in controlling the electrocatalytic oxidation of alcohols cannot be ignored. The significant amount of surface functional groups attached to the carbon nanotubes may affect both the mass transfer through the catalytic layer and the product desorption rates due to the presence of the adduct forming bonds. The enhanced stability of FeCo@Fe@Pd/CNT-OH during MOR coupled with its high size uniformity, excellent electrocatalytic activity and its low cost shows it can serve as efficient anode catalyst for DMFCs.

8.8 References

(1) Bianchini, C.; Shen, P. K. *Chem. Rev.* **2009**, *109*, 4183–206.

(2) Guo, S.; Dong, S.; Wang, E. *Energy Environ. Sci.* **2010**, *3*, 1307.

(3) Ha, S.; Larsen, R.; Masel, R. I. *J. Power Sources* **2005**, *144*, 28–34.

(4) Roy, P. S.; Bagchi, J.; Bhattacharya, S. K. *Catal. Sci. Technol.* **2012**, *2*, 2302.

(5) Yang, X.; Yang, Q.; Xu, J.; Lee, C.-S. *J. Mater. Chem.* **2012**, *22*, 8057.

(6) Antolini, E. *Energy Environ. Sci.* **2009**, *2*, 915.

(7) Chai, J.; Li, F.; Hu, Y.; Zhang, Q.; Han, D.; Niu, L. *J. Mater. Chem.* **2011**, *21*, 17922.

(8) Qiu, C.; Shang, R.; Xie, Y.; Bu, Y.; Li, C.; Ma, H. *Mater. Chem. Phys.* **2010**, *120*, 323–330.

(9) He, Q.; Chen, W.; Mukerjee, S.; Chen, S.; Laufek, F. *J. Power Sources* **2009**, *187*, 298–304.

(10) Zhao, J.; Sarkar, A.; Manthiram, A. *Electrochim. Acta* **2010**, *55*, 1756–1765.

(11) Kakati, N.; Maiti, J.; Lee, S. H.; Yoon, Y. S. *Int. J. Hydrogen Energy* **2012**, *37*, 19055–19064.

(12) Singh, R. N.; Singh, a. *Carbon N. Y.* **2009**, *47*, 271–278.

(13) Lee, Y.-W.; Ko, A.-R.; Han, S.-B.; Kim, H.-S.; Park, K.-W. *Phys. Chem. Chem. Phys.* **2011**, *13*, 5569–72.

(14) Shi, J.-J.; Yang, G.-H.; Zhu, J.-J. *J. Mater. Chem.* **2011**, *21*, 7343.

(15) Lu, Y.; Jiang, Y.; Wu, H.; Chen, W. *J. Phys. Chem. C* **2013**, 177, 2926-2938.

(16) Ding, K.; Yang, H.; Cao, Y.; Zheng, C.; Rapole, S. B.; Guo, Z. *Mater. Chem. Phys.* **2013**, *142*, 403–411.

(17) Bambagioni, V.; Bianchini, C.; Marchionni, A.; Filippi, J.; Vizza, F.; Teddy, J.; Serp, P.; Zhiani, M. *J. Power Sources* **2009**, *190*, 241–251.

(18) Compton, RG, B. C. *Understanding Voltammetry*; 2007; pp. 249–253.

(19) Wang, .J. *Analytical Electrochemistry* ;3rd Ed.; Wiley VCH,2006; p 272.

(20) Song, C.; Zhang, J. *PEM fuel cell Electrocatal. Catal. layers* **2008**.

(21) Shen, P. K.; Xu, C. *Electrochem. commun.* **2006**, *8*, 184–188.

(22) Maiyalagan, T.; Scott, K. *J. Power Sources* **2010**, *195*, 5246–5251.

(23) Bard, Allen J, Faukner, L. R. *Electrochemical Methods:Fundamentals and Applications*; 2nd ed.; Wiley, New York: New York, 2001; p. 864 Pages.

(24) Zhu, F.; Ma, G.; Bai, Z.; Hang, R.; Tang, B.; Zhang, Z.; Wang, X. *J. Power Sources* **2013**, *242*, 610–620.

(25) Liu, Z.; Zhao, B.; Guo, C.; Sun, Y.; Shi, Y.; Yang, H.; Li, Z. *J. Colloid Interface Sci.* **2010**, *351*, 233–8.

(26) Zhao, Y.; Nie, S.; Wang, H.; Tian, J.; Ning, Z.; Li, X. *J. Power Sources* **2012**, *218*, 320–330.

(27) Zhao, Y.; Yang, X.; Tian, J.; Wang, F.; Zhan, L. *Int. J. Hydrogen Energy* **2010**, *35*, 3249–3257.

(28) Li, R.; Mao, H.; Zhang, J.; Huang, T.; Yu, A. *J. Power Sources* **2013**, *241*, 660–667.

(29) Gao, L.; Yue, W.; Tao, S.; Fan, L. *Langmuir* **2013**, *29*, 957–64.

(30) Liu, B.; Chen, J. H.; Xiao, C. H.; Cui, K. Z.; Yang, L.; Pang, H. L.; Kuang, Y. F. **2007**, 1365–1369.

(31) An, H.; Pan, L.; Cui, H.; Li, B.; Zhou, D.; Zhai, J.; Li, Q. *Electrochim. Acta* **2013**, *102*, 79–87.

(32) Kitchin, J. R.; Nørskov, J. K.; Barteau, M. A.; Chen, J. G. *Phys. Rev. Lett.* **2004**, 4–7.

(33) Xu, Y.; Ruban, A. V; Mavrikakis, M. *J. Am. Chem. Soc.* **2004**, *126*, 4717–25.

(34) Shao, M. H.; Huang, T.; Liu, P.; Zhang, J.; Sasaki, K.; Vukmirovic, M. B.; Adzic, R. R. *Langmuir* **2006**, *22*, 10409–15.

(35) Kibler, L. a; El-Aziz, A. M.; Hoyer, R.; Kolb, D. M. *Angew. Chem. Int. Ed. Engl.* **2005**, *44*, 2080–4.

(36) Baker, R.; Wilkinson, D. P.; Zhang, J. *Electrochim. Acta* **2008**, *53*, 6906–6919.

(37) Shao, Y.; Yin, G.; Zhang, J.; Gao, Y. *Electrochim. Acta* **2006**, *51*, 5853–5857.

Chapter 9*

ELECTROCATALYTIC OXIDATION OF POLYHYDRIC ALCOHOLS (ETHYLENE GLYCOL AND GLYCEROL) ON FeCo@Fe@Pd/MWCNTS

* The following manuscript is in preparation for publication and resulted from part of the research work presented in this chapter.

O.O. Fashedemi Hamish Miller, Andrea Marchionni Francesco Vizza, K.I. Ozoemena "Oxidation of Polyhydric alcohols on Palladium decorated core shell nanocatalysts (FeCo@Fe@Pd) supported on carbon nanotubes in Alkaline Medium".

9.1 Introduction

Polyhydric alcohols such as ethylene glycol (EG) and glycerol (GLY) are being seen as complementary alcohols or replacement of monohydric alcohols in fuel cells. As recent research works have shown[1–3], EG is a fairly new type of liquid feed in the development of fuel cells, and its electro-oxidation in direct ethylene glycol fuel cells (DEGFCs) has attracted considerable interest for mobile, stationary, and portable applications owing to its high theoretical energy capacity (4.8 A h ml^{-1}), high boiling point, and high efficiency of electric power conversion[4–6]. Additionally, recent studies have revealed that EG can be directly produced from catalytic conversion of bio mass- related cellulose with high yields. This also provides new opportunities for sustainable widespread applications of DEGFCs[7,8]. GLY has been considered a promising fuel for direct alcohol fuel cells (DAFC), due to its relatively low price, simple purification and storage, and non-volatile and environment-friendly properties. It has attracted great research interests as it is also a non-toxic, bio renewable alcohol fuel.

Generally, biomethanol and bioethanol, are obtained from the microorganism fermentation process of biomass, on the other hand, biomass derived glycerol is mainly obtained as a waste by product in the production of biodiesel via a trans esterification reaction[9]. In addition, with the highly active triol structure, glycerol demonstrates a high volumetric energy density of 6.4 $KWhL^{-1}$ [10,11]. The attraction of Pd-based electrocatalysts in the oxidation of alcohols in alkaline electrolytes has been well discussed[12–14]. In this work, the FeCo@Fe@Pd was supported on carboxylate (CNT-OH) and sulfonate (CNT-SO_3) multi walled carbon nanotubes. This work has been motivated by previous studies using MWCNTs as support for Pd catalysts for EG or GLY oxidation[15–17]. The present work is the first of its kind wherein a Pd-based core-shell nanocatalysts have been investigated in details for the electrocatalytic oxidation of both polyhydric alcohols (EG and GLY). Outstanding

performances were observed in terms of the current responses and the onset over potential in comparison to their Pd single metal counterparts on the same substrates.

9.2 Comparative Cyclic Voltammetric Experiments

The electrocatalytic performances of the catalysts were initially investigated using cyclic voltammetry (CV). Figure 9.1 shows the polarization curves of the four palladium based catalysts, normalized by the electrode surface area (a and b) in 0.5 M EG/GLY in 1 M KOH solution (saturated with N_2) at room temperature. As shown in Fig 9.1 (a) and (b), the CV curves exhibit typical EG and GLY electro-oxidation features in alkaline medium[15,17–19]

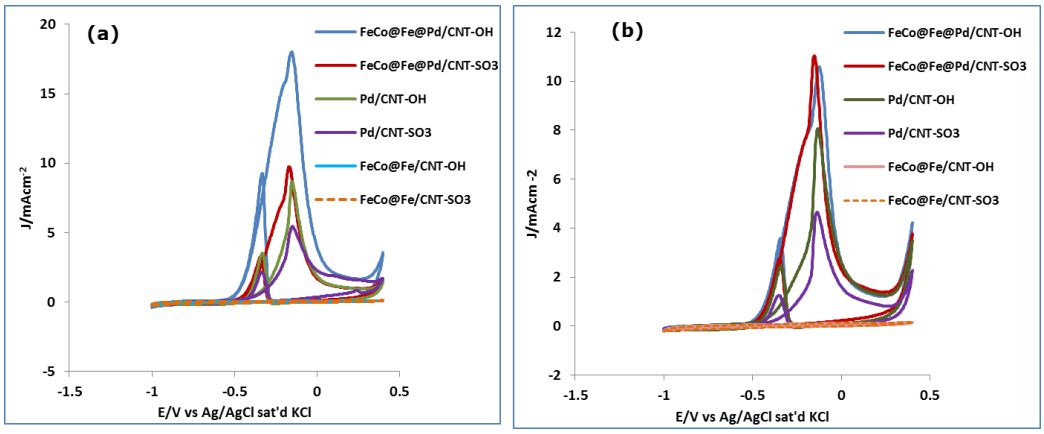

Figure 9. 1: Comparative cyclic voltammograms of catalysts in the 0.5 M EG/1 M KOH (a) and 0.5 M GLY/1 M KOH (b)

Two oxidation (anodic) peaks can be clearly observed, the forward anodic peak from the forward scan (J_f) is attributed to the oxidation of the alcohol while the peak from the backward or reverse scan (J_b) is primarily associated with the removal of carbonaceous species which were not completely oxidized in the forward scan. Thus, a ratio of the J_f/J_b indicates a tolerance of the catalysts to poisonous carbonaceous species[20–22]. The forward anodic peak current density (J_f) and the onset oxidation potential (E_{onset}) are two critical parameters to evaluate the activity of catalysts during the electro-oxidation process[23].

In EG oxidation, FeCo@Fe@Pd/CNT-OH had an E_{onset} of -0.580 V which is lower than that of FeCo@Fe@CNT/SO_3 at 0.521 V. This value is ≈ 140 mV earlier than the E_{onset} value of Pd/CNT-OH (– 0.441 V) and ≈ 150mV earlier than that of Pd/CNT-SO_3 (– 0.431 V) in the same electrolyte solution. FeCo@Fe@Pd/CNT-OH also exhibited the highest current response which was 17.80 $mAcm^{-2}$ density to EG oxidation, which is ≈ 2 times higher than that of both FeCo@Fe@Pd/CNT-SO_3 (9.67 $mAcm^{-2}$) and Pd/CNT-OH (8.53 $mAcm^{-2}$). It is also 3.3 times higher than that of Pd/CNT-SO_3 with 5.37 $mAcm^{-2}$. This result is somewhat surprising considering that Sun et al.[17] obtained the opposite result, i.e. Pd/CNT-SO3 > Pd/CNT-OH. The reasons may be related to the type of MWCNT-support originally used in fabricating the CNT-SO_3. The authors utilised a brand of MWCNT produced by CVD[24], which will certainly have different properties from those used in the present study. The E_{onset} of GLY oxidation is situated at -0.566 V for FeCo@Fe@Pd/CNT-OH which is earlier than -0.536 V of FeCo@Fe@CNT-SO_3, -0.512 V of Pd/CNT-OH and -0.468 V of Pd/CNT SO_3. Both FeCo@Fe@Pd/CNT-OH and FeCo@Fe@Pd/CNT-SO_3 exhibited high oxidation peak current density of about 11.00 $mAcm^{-2}$ which is 1.3 times higher than Pd-OH (8.03 $mAcm^{-2}$) and 2.7 times higher than Pd/CNT-SO_3.

Based on the J_f and E_{onset} criteria for electrocatalytic ranking, both core shell nano catalysts outperformed their mono metallic counterparts. FeCo@Fe@Pd/CNT-OH appears to give a better catalytic response in EG compared to FeCo@Fe@Pd/CNT-SO_3. In GLY oxidation however, both catalysts seem to have the same ease of oxidising the alcohols. A summary of the relevant CV parameters can be seen in Table 9.1. It is obvious (from this summary) that both core shell nanocatalysts exhibit better oxidative electrocatalytic properties in both alcohols compared to the single palladium catalysts.

Table 9.1: Summary of CV parameters of Pd based catalysts in 0.5M [GLY/EG]/1.0 M KOH

	0.5M EG/1.0 M KOH					0.5 M GLY/ 1.0 M KOH				
Catalysts	E_s (V)	E_p (V)	J_f ($mAcm^{-2}$)	J_b ($mAcm^{-2}$)	J_f/J_b	E_s(V)	E_p(V)	J_f ($mAcm^{-}$)	J_b ($mAcm^{-}$)	J_f/J_b
FeCo@Fe@Pd/CNT-OH	-0.580	-0.163	17.80	8.89	2.00	-0.566	-0.131	10.50	3.44	3.05
FeCo@Fe@Pd/CNT-SO_3	-0.522	-0.172	9.67	3.12	3.01	-0.536	-0.155	11.00	2.69	4.09
Pd-CNT-OH	-0.441	-0.155	8.53	3.41	2.50	-0.512	-0.136	8.03	2.39	3.36
Pd-CNT-SO_3	-0.431	-0.155	5.37	2.10	2.60	-0.468	-0.141	4.63	1.170	3.96

As seen in Table 9.1 the J_f/J_b ratio values of the four catalysts in EG oxidation is above 2 and that of GLY oxidation is above 3. Considering the polyhydric nature of both alcohols in this study these values indicate excellent tolerance of the catalysts to the presence of the carbonaceous products from the chemisorbed alcohols on the catalysts' surface during the oxidation process.

9.3 Scan Rate Studies

The presence of the highly conductive carbon nanotube substrates is expected to add to the catalytic improvement of all the catalysts, but the ease of diffusion of adsorbed molecules and product desorption on the modified electrodes using these substrates should also be taken into account as they could also harbour the process of alcohol oxidation. This could be significant especially in polyhydric alcohol oxidation. Both FeCo@Fe@Pd/CNT-OH and FeCo@Fe@Pd/CNT-SO_3 studied in this work have been quite remarkable for their ease of adsorbate diffusion and product desorption during EG and GLY oxidation. This was proved in the scan rate studies performed during EG and GLY oxidation using electrodes modified by these catalysts. Bambagioni et al.[16] recorded CO poisoning and an extremely low stability of their modified electrode during GLY oxidation using Pd on functionalised nanotubes –Pd/MWCNT. They reported an independence of the peak current density from their scan rate studies already at an early scan rate of 50 mVs^{-1} , according to them, this observation "confirms a strong adsorption of substrates and/ products at the modified electrode surface".

The same experiments performed for both EG and GLY oxidation using the two core shell catalysts showed a perfect diffusion controlled kinetics at the surface of the modified electrodes (with no observation or indication of the hindrance of adsorbed oxidation residues) with increasing scan rates. Figure 9.2 shows both the polarisation curves and the plots of the square root of scan ($\nu^{1/2}$) rate vs anodic peak density (j_a) (as insets) for the oxidation of EG and GLY on FeCo@Fe@Pd/CNT-OH (a, a') and FeCo@Fe@Pd/CNT-SO_3 (b, b'). A linear relationship, typical of an electrochemical reaction under diffusion control was still found at a scan rate as high as 800 mVs^{-1}. The correlation factors were found to be near unity for all the plots.

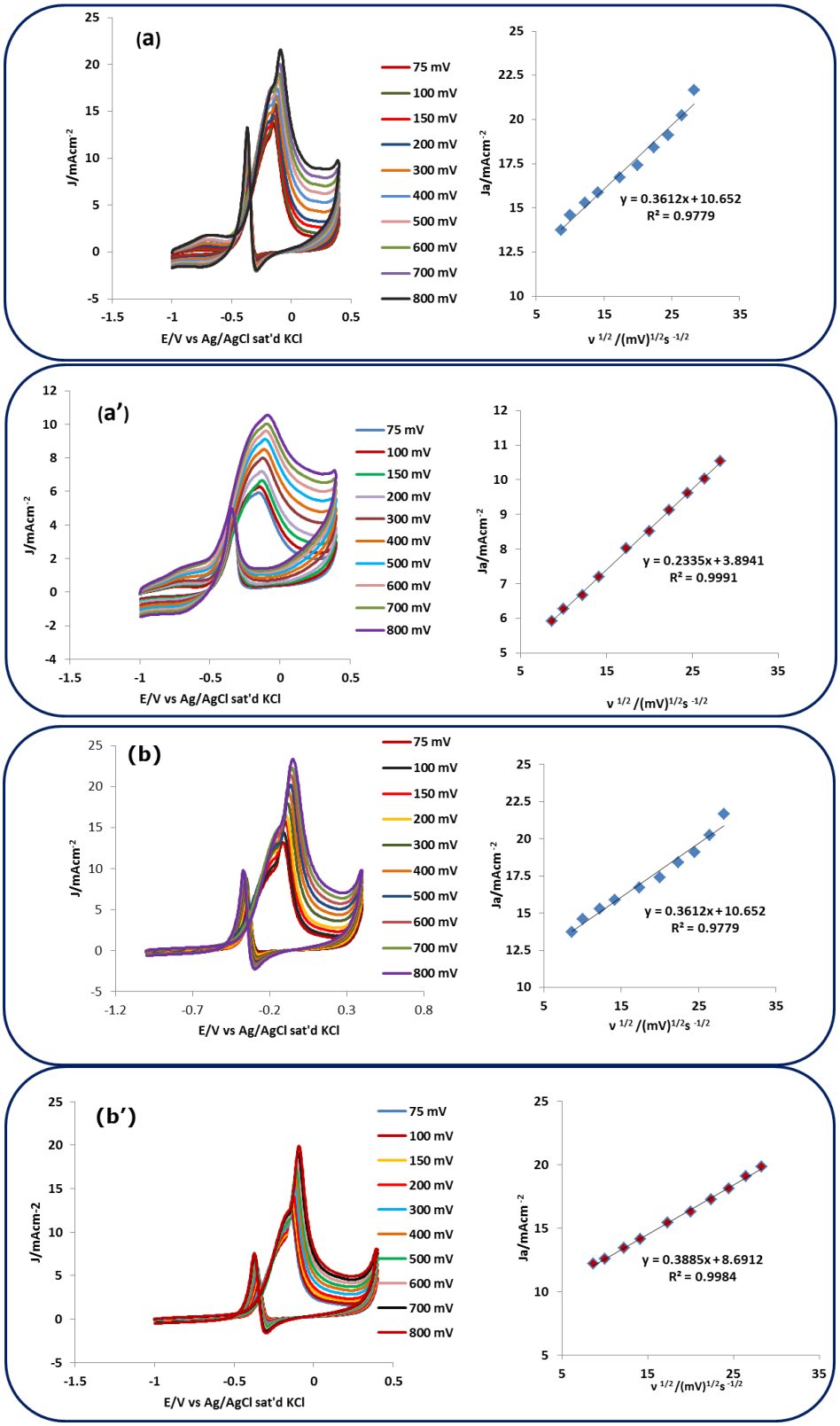

Figure 9.2: Polarisation curves and the plots of the square root of scan rate vs anodic peak density (insets) for the oxidation of EG and GLY on FeCo@Fe@Pd/CNT-OH (a, a') and FeCo@Fe@Pd/CNT-SO_3 (b, b')

9.4 Electrochemical Impedance Spectroscopy

EIS has always been known as a powerful tool that can be used to investigate the interfacial processes and kinetics of electrode reactions and evaluate the electrochemical properties of as-prepared catalysts, it is often used as a complementary technique together with CV[25]. In the electrochemical impedance spectroscopy, semi-circular Nyquist plots were obtained for the modified electrodes at -0.17 V and -0.16 V potentials in both EG and GLY alcohols respectively. Figure 9.3 (a) shows the Nyquist plots of EG electro oxidation and Figure 9.3 (b) displays that of GLY oxidation on FeCo@Fe@Pd/CNT-OH, FeCo@Fe@Pd/CNT-SO_3, Pd/CNT-OH and Pd/CNT-SO_3 in 0.5 M [alcohol]/1.0 M KOH at -0.17 V for EG and –0.16 V for GLY.

Generally, the smaller diameter of the impedance arc (DIA) corresponds to smaller charge-transfer resistance (R_{ct}) and higher electro catalytic activity[26]. As seen in the comparative profiles for all the modified electrodes at -0.17 V (EG)-Fig 9.3a and at -0.16 V (Gly)-Fig 9.3b; FeCo@Fe@Pd/CNT-OH gave the smallest semi circles which indicate very fast kinetics in the oxidation of both alcohols. The chosen voltage values also indicate the optimum potentials for obtaining the best electro catalytic activity at the modified electrodes. These values usually lie between E_s and E_p potential values as obtained from the corresponding cyclic voltammetry studies in both alcohols.

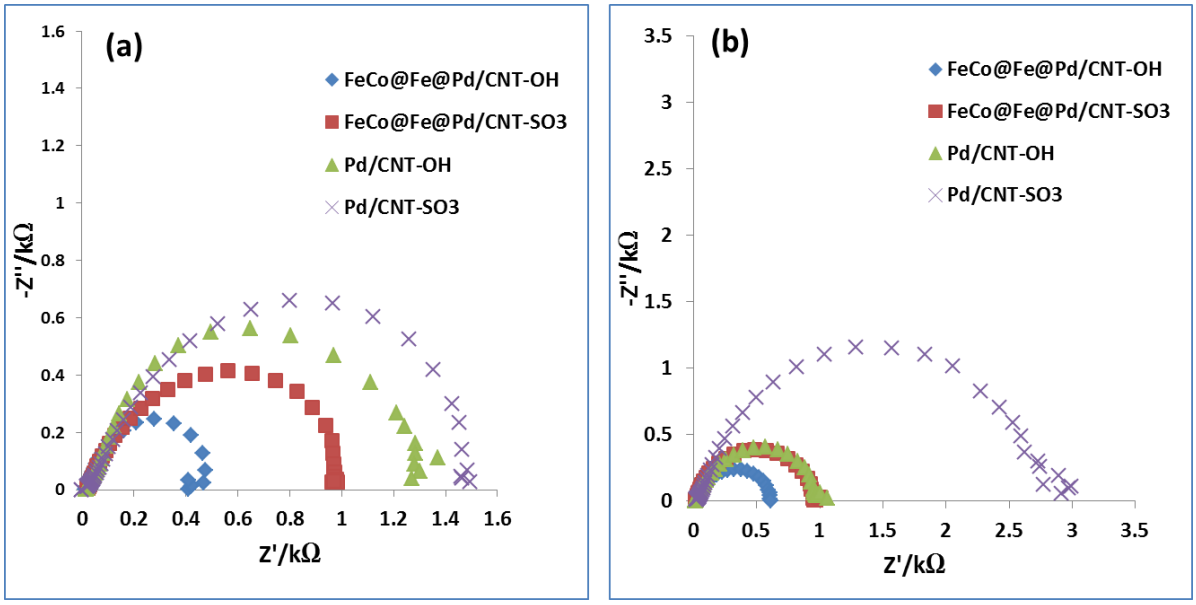

Figure 9.3: Nyquists plots of EG and GLY oxidation on FeCo@Fe@Pd/CNT-OH, FeCo@Fe@Pd/CNT-SO_3, Pd/CNT-OH and Pd/CNT-SO_3 in 0.5 M [alcohol]/1.0 M KOH at -0.17 V for EG and –0.16 V for GLY

Table 9.2: Electrochemical impedance data obtained from the Nyquist plots from Figure 9.3.

	Electrochemical Impedance Parameters							
Catalysts	**Ethylene glycol**				**Glycerol**			
			Q/CPE				**Q/CPE**	
	R_s /(Ω)	**R_{ct} /(kΩ)**	**Y_o(mF)**	**n**	**R_s /(Ω)**	**R_{ct}/(kΩ)**	**Y_o (mF)**	**n**
FeCo@Fe@Pd/CNT-OH	16.17 (4.13)	0.420 (4.186)	$0.921e^{-4}$ (13.033)	0.897 (2.599)	33.60 (2.25)	0.593 (2.252)	$0.660e^{-4}$ (7.711)	0.846 (1.52)
FeCo@Fe@Pd/CNT-SO_3	20.78 (2.90)	1.036 (2.730)	$0.908e^{-4}$ (6.366)	0.786 (1.398)	16.70 (2.88)	0.976 (2.030)	$0.337e^{-4}$ (6.296)	0.854 (1.117)
Pd/CNT-OH	14.85 (4.58)	1.302 (6.223)	$0.201e^{-3}$ (8.604)	0.765 (2.187)	15.79 (1.98)	1.017 (2.008)	0.100^{-4} (4.216)	0.816 (0.908)
Pd/CNT-SO_3	19.92 (7.64)	1.606 (5.106)	$0.583e^{-4}$ (11.934	0.740 (2.545)	23.60 (6.52)	3.103 (5.574)	0.498^{-4} (9.694)	0.763 (2.123)

The Nyquist plots were fitted with the same circuit, the arrangement of the circuit components being $[R_1(R_2Q)]$ where R_1 is the resistance of the electrolyte solution-R_s; R_2 is the charge transfer resistance-R_{CT} and Q is the constant phase element. A similar circuit was used for EG oxidation by Ramulifho et al.[15]. The values of each one of the circuit components are shown in Table 9.2. The R_{CT} values of the electrodes in EG oxidation was found to be (0.42, 1.03, 1.30, 1.60) kΩ for FeCo@Fe@Pd/CNT-OH, FeCo@Fe@Pd/CNT-SO_3, Pd/CNT-OH, and Pd/CNT-SO_3 respectively. The R_{CT} values in GLY oxidation were (0.59, 0.98, 1.02, 3.10) kΩ for FeCo@Fe@Pd/CNT-OH, FeCo@Fe@Pd/CNT-SO_3, Pd/CNT-OH, and Pd/CNT-SO_3 respectively. These values follow the same trend seen in the CV experiments and thus are in agreement with the results obtained in cyclic voltammetry, which all point to the fact that there is a better ease of catalytic oxidation in EG than in GLY at all the catalyst modified electrodes.

9.5 Chronoamperometry

The long term stability or durability of the catalysts during the alcohol oxidation process was investigated under a constant voltage of -0.16 V, using chronoamperometry. As shown in Figure 9.4 (a) and (b), the current densities of all electrodes decreased gradually at the initial stage. This might be ascribed to the deactivation of the Pd catalytic sites as a result of chemisorbed carbonaceous species during alcohol oxidation[27]. After some time of operation, the hyperbolic decay gradually attained a pseudo steady state.

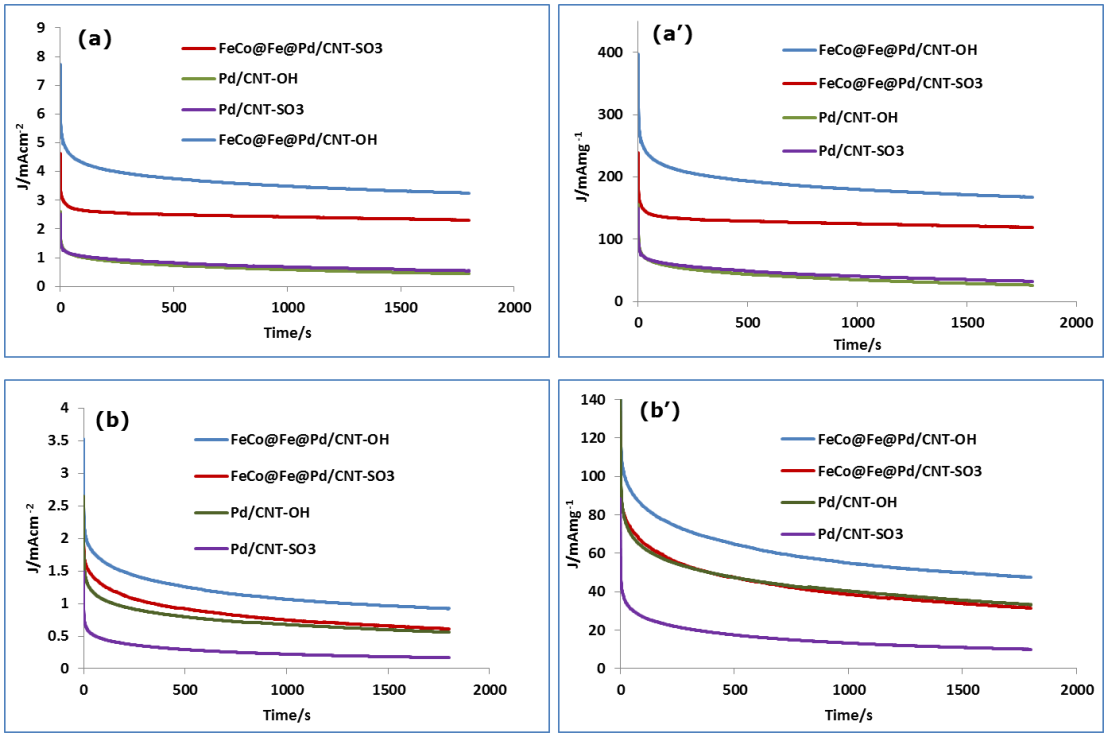

Figure 9.4: Chronoamperometric curves of the four catalysts in 0.5 M EG/1.0 M KOH (a and a') and 0.5 M GLY/1 M KOH (b and b')

As seen in the current peak intensities, FeCo@Fe@Pd/CNT-OH exhibited the highest initial current and the slowest decay rate among all the catalysts in both alcohols. It also maintained the highest oxidation current density at the pseudo steady state, thus giving the best electro catalytic activity and stability. Its pseudo-steady state current (3.25 $mAcm^{-2}$ / 167.30 $mAmg^{-1}_{Pd}$) was higher in the electrocatalytic oxidation of ethylene glycol compared to that in glycerol (0.965mA cm^{-2} / 47.49 $mAmg^{-1}$ (Pd)). The same trend was observed for the other three catalysts regarding both alcohols. This trend is portrayed in the bar charts in Figure 9.5 below:

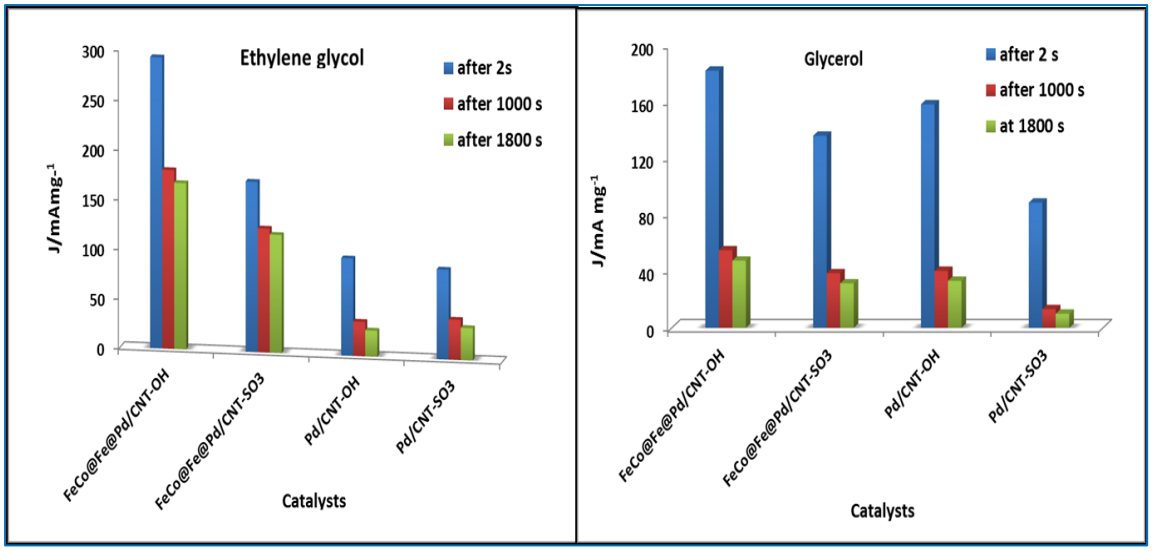

Figure 9.5: Representation of pseudo steady currents at the start of reaction (2 s), after 1000 s into the reaction and at the end of the reaction (after 1800 s).during the oxidation of 0.5 M (EG/GLY)/1 M KOH

9.6 Kinetics

9.6.1 Tafel Analysis

Further scrutiny of the kinetics at the surface of the core shell catalysts led to the investigation of the kinetic parameters in terms of the Tafel values and exchange current densities. The average Tafel plots were obtained from 1 mVs^{-1} scans at different concentrations of the alcohols, the Tafel values were calculated from these scans using the conventional equations. The exchange current densities j_o were obtained from extrapolating the Tafel lines. Figures 9.6 a, b, c, and d show the sets of Tafel plot at each of the concentration of electrolyte studied and the kinetic parameters derived from each of the concentrations for FeCo@Fe@Pd/CNT-OH and FeCo@Fe@Pd/CNT-SO_3 in EG (a and b) and both catalysts in GLY (c and d). A summary of these parameters (average values) is seen in Table 9.3.

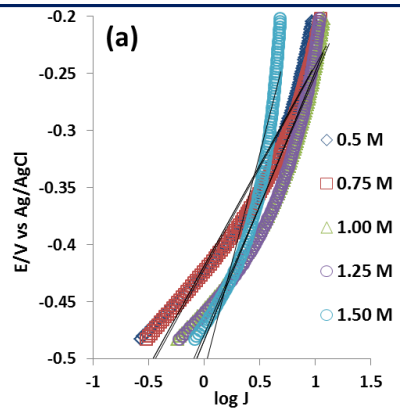

[EG]/M	Tafel slope (2.303RT/ anF)	a (-RT/anF) log Jo	J_o (x 10^1)	R^2
0.5	176	0.418	2.37	0.9415
0.75	178	0.421	2.30	0.9508
1.00	226	0.478	1.29	0.9255
1.25	236	0.484	1.13	0.9149
1.50	378	0.510	0.223	0.8880

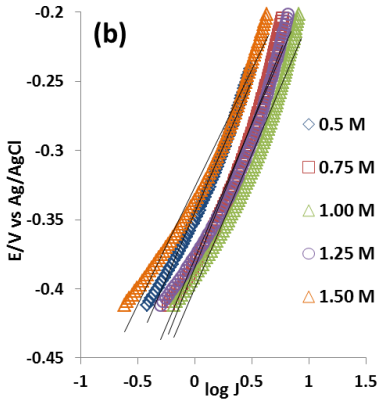

[EG]/M	Tafel slope (2.303RT/ anF)	a (-RT/anF) log Jo	J_o (x 10^2)	R^2
0.5	190	0.350	6.48	0.9874
0.75	209	0.380	6.98	0.9749
1.00	194	0.400	1.15	0.9676
1.25	195	0.380	8.80	0.9670
1.50	170	0.330	8.36	0.9751

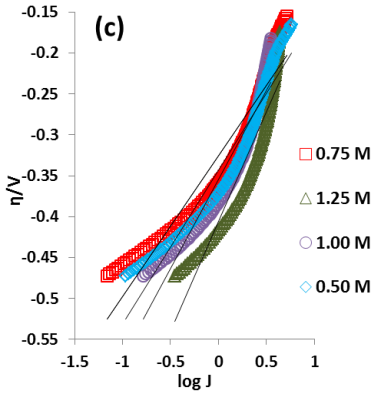

[GLY]/M	Tafel slope (2.303RT /anF)	a (-RT/anF) log J_o	J_o (x 10^2)	R^2
0.5	188	0.34	6.70	0.9256
0.75	172	0.33	7.70	0.9083
1.00	217	0.36	4.29	0.8939
1.25	268	0.41	3.30	0.9019

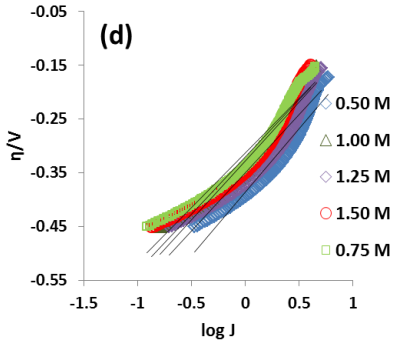

[GLY]/M	Tafel slope (2.303RT /anF)	a (-RT/anF) log J_o	J_o (x 10^2)	R^2
0.5	236	0.39	4.32	0.9392
0.75	202	0.31	3.52	0.9428
1.00	219	0.33	3.14	0.9392
1.25	217	0.35	4.10	0.9170
1.50	213	0.32	3.19	0.9188

Figure 9.6: Tafel plots of FeCo@Fe@Pd/CNT-OH and FeCo@Fe@Pd/CNT-SO_3 in EG (a and b) and in GLY (c and d), the equivalent values are set as insets.

Table 9.3: Kinetic Parameters of core shell catalysts during oxidation of EG and GLY (0.5 M [alcohol]/ 1 M KOH]

Catalysts	Ethylene glycol		Glycerol	
	Tafel slope/ mV dec^{-1}	**J_o/mAcm^{-2}**	**Tafel slope/ mVdec^{-1}**	**J_o/mAcm^{-2}**
FeCo@Fe@Pd/CNT-OH	204	1.17×10^{-1}	209	5.52×10^{-2}
FeCo@Fe@Pd/CNT-SO_3	191	8.40×10^{-2}	217	2.95×10^{-2}

The Tafel slope values (*b*) obtained are quite high, which is an indication of the porosity of the substrates. Their values also fall within the same range which indicates identical reaction mechanisms for the oxidation of both alcohols at the modified electrodes. Although the Tafel values are similar, j_o value for FeCo@Fe@Pd/CNT-OH is still one order higher than that of FeCo@Fe@Pd/CNT-SO_3 in EG oxidation. As the ion exchange density parameter determines how rapid the electrochemical reaction occurs, this further shows the faster rate of EG oxidation on FeCo@Fe@Pd/CNT-OH catalyst.

9.6.2 Catalytic Rate Constant (k_{cat})

The catalytic rate for alcohol oxidation K_{cat} was obtained from the chronoamperometry data. A plot of J_{cat}/J_{buff} vs $t^{1/2}$ gives a slope from which K_{cat} can be calculated. The plots obtained are shown in Figs 9.5 (a) and (b). Table 9.4 gives a summary of the K_{cat} values obtained from the oxidation of both alcohols. As shown below, K_{cat} values for the oxidation of EG are generally higher than those for GLY oxidation in all the catalysts.

The core shell catalysts also outperform the Pd single metal catalysts in oxidation of both alcohols, especially EG with increase of an order higher than the other catalysts. This confirms the results obtained from the EIS and CA studies. FeCo@Fe@Pd/CNT-OH gave the best K_{cat} values in both EG and GLY oxidation compared to the other three catalysts.

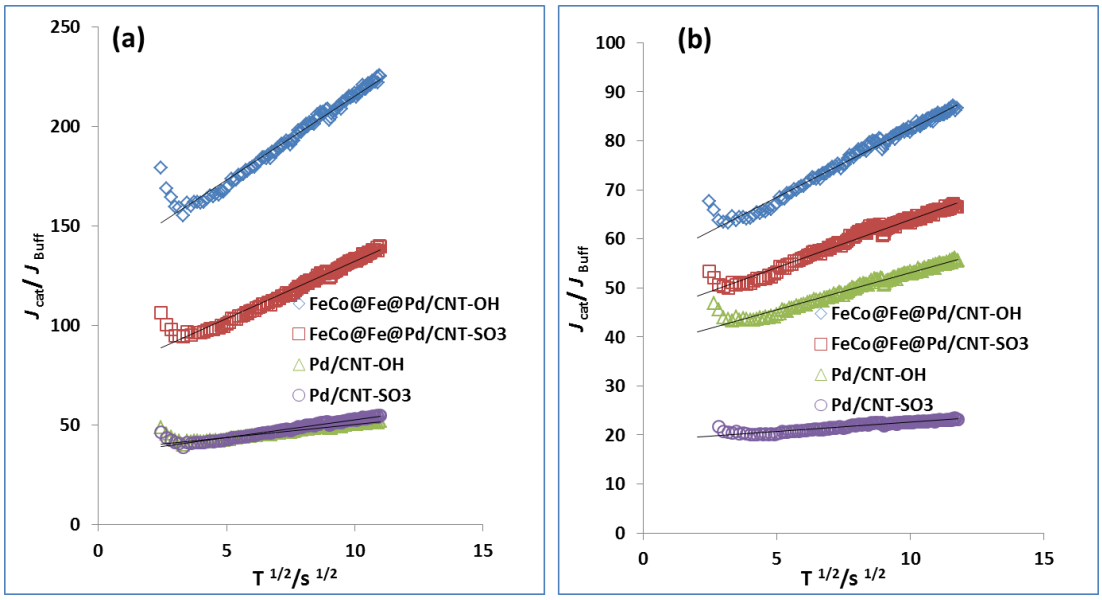

Figure 9.7: A plot of J_{cat}/J_{buff} vs $t^{1/2}$ for the four catalysts in 0.5 EG/ 1 M KOH (a) and 0.5 EG/ 1 M KOH.

Table 9.4: K_{cat} values for EG and GLY oxidation in 0.5M [alcohol] / 1.0 M KOH

Catalyst	K_{cat} /cm^{3}mol^{-1}s^{-1}	
	Ethylene glycol	**Glycerol**
FeCo@Fe@Pd/CNT-OH	4.53 x 10^4	4.93 x 10^3
FeCo@Fe@Pd/CNT-SO_3	2.11 x 10^4	2.40 x 10^3
Pd/CNT-OH	2.07 x 10^3	1.45 x 10^3
Pd/CNT-SO_3	1.09 x 10^3	9.15 x 10^1

9.7 Table of Comparison

As done in previous studies using the core shell catalyst as anodes in monohydric alcohols, a comparison of the electrocatalytic performances of the nano core shell catalysts studied and other Pd based catalysts was carried out. The findings have been summarised in the tables 9.5 and 9.6

Table 9.5: Comparison of electro catalytic activity of FeCo@Fe@Pd/CNT-OH with some Pd based catalysts for EG oxidation

Catalysts	E_{onset} /V	E_{peak}/ V	J_f/J_b
Pd@WC-MO_2/C[28][a]	-0.60	≈1.0	≈2.8
Pd/MO_2C[28][a]	-0.33	-0.08	≈2.0
Pd/SF-MWCNT[15] [b]	-0.24	0.15	1.82
PdNi/SF-MWCNT[15][b]	-0.39	0.25	1.57
PdSn/SF-MWCNT[15][b]	-0.44	0.23	2.10
PdHC8[29][c]	0.46	0.85	≈1.8
FeCo@Fe@Pd/CNT-OH [current study] [d]	-0.58	-0.16	2.05

a. **Scan rate : 50 mVs^{-1}; Ref Electrode: Hg/HgO; Electrolyte : 0.5 M EG/0.5M KOH C: carbon aerogel**
b. **Scan rate: 50 mVs^{-1}, Ref electrode: Ag/AgCl Electrolyte: 0.5 M EG/0.5M KOH,SF-sulfonate**
c. **. Scan rate: 50 mVs^{-1}, Ref electrode: RHE Electrolyte: 0.1M EG/0.1M KOH,PdHC8-One –octyne Pd nanoparticles**
d. **. Scan rate : 50 mVs^{-1}; Ref Electrode: Ag/AgCl; Electrolyte : 0.5 M GLY/1.0M KOH**

Table 9.6: Comparison of electro catalytic activity of FeCo@Fe@Pd/CNT-OH with some Pd based catalysts for GLY oxidation.

Catalysts	E_{onset} /V	E_{peak}/ V	J_f/J_b
PdRh/C[30][a]	≈-0.45	0.90	N/A (> 20)
Pd(DBA)$_2$[31] [b]	-0.33	0.08	≈ 0.5
Pd@WC-MO$_2$/C[32][c]	≈-0.45	-0.08	≈ 3.5
Pd/MO$_2$C[32][d]	≈-0.45	-0.08	≈ 2.5
Pd/MWCNT[16][e]	-0.60	-0.08	≈0.8
Pd/C[33][f]	-0.19	0.19	n/a
FeCo@Fe@Pd/CNT-OH [current study] g	-0.57	-0.13	3.05

a. **Scan rate: 20 mVs^{-1}, Ref electrode: RHE; Electrolyte : 0.1 M GLY / 0.1 M KOH**
b. **Scan rate: 50 mVs^{-1}, Ref electrode: NHE; Electrlyte: 1M Gly/ 2M KOH ,DBA : Bis(dibenzylidene acetone)**
c. **Scan rate : 50 mVs^{-1}; Ref Electrode: Hg/HgO; Electrolyte : 0.5 M GLY/0.5M KOH C: carbon aerogel.**
d. **Scan rate : 50 mVs^{-1}; Ref Electrode: Hg/HgO; Electrolyte : 0.5 M GLY/0.5M KOH C: carbon aerogel**
e. **Scan rate : 50 mVs^{-1}; Ref Electrode: Ag/AgCl Electrolyte : 5 wt% GLY/ 2M KOH**
f. **Scan rate : 50 mVs^{-1}; Ref Electrode: Hg/HgO; Electrolyte : 1.0 M GLY/1.0 M KOH**
g. **Scan rate : 50 mVs^{-1}; Ref Electrode: Ag/AgCl; Electrolyte : 0.5 M GLY/1.0M KOH**

9.8 Conclusion

Observing the resulting data from the electrochemical tests carried out in this work, a superior catalytic activity of the core shell catalysts over the Pd nanocatalysts alone can be seen. The catalytic trend follows the order FeCo@FeCo@Pd/CNT-OH > FeCo@Fe@Pd/CNT-SO_3 > Pd/CNT-OH > Pd/CNT-SO_3 in both EG and GLY oxidation. Some factors contributing to improvement of the core shell catalysts are worth mentioning, a major factor is the one contributed by the lattice strain effect. This is caused by

the lattice contraction of the Pd-rich surface of the core shell catalysts. The lattice strain effect causes a downshift in the metal d-band centre (ε_d) and weakens the interaction between the substrate and the adsorbates[34].

Taking another look at the studies carried out by Norskov and co-workers[35–37], the authors explained that the interaction between the adsorbate states and the metal d states is an important part of the interaction energy. This is because while sp bands of the metal are broad and structure less, the d bands are narrow, and thus small changes in the environment can change the d states and their interaction with adsorbate significantly. Following this d-band theory, when metals with small lattice constants are overlaid on metals with large lattice constants, a lattice strain is induced on the surface of the overlaid metal. The d-band centre (ε_d) shifts up leading to a stronger adsorption ability of the adsorbate on the surface metals. The opposite effect occurs when metals with large lattice constants are laid over those with smaller lattice constants[35–37].

The lattice value of Fe is 2.8664 Å and that of the Pd in the two core shell catalysts are 3.8948 and 3.8973 Å respectively. A contraction of their Pd surface has already been confirmed with the XRD results. A down shift of their d- band centres is expected, leading to a weakening of the residual adsorbed species or adsorbates on the Pd surface and as a result a faster alcohol oxidation process. Thus, the core shell catalysts yielded more negative shift of peak potential and higher oxidation current for the alcohol oxidation compared to the single Pd catalysts.

Another factor is the larger electrochemically active surface area, which also gave a big boost to the catalytic activity of the core shell catalysts. This is specially observed in FeCo@FeCo@Pd/CNT-OH, its larger ECSA can be attributed to its smaller particle size and its excellent dispersion on the carbon nanotubes, (unlike its sulfonate counterpart having lots of

aggregates) thus exhibiting an even coverage over the nanotubes as seen in Figures 3.17 (Chapter 3).

Comparing the catalytic activity of the FeCo@Fe@Pd/CNT-OH and FeCo@Fe@Pd/CNT-SO_3 in both alcohols, one sees an overall better performance in oxidation of EG. There was no adverse effect of both functionalised carbon nanotubes (i.e. CNT-SO_3 and CNT-OH) on the activity of the nanocatalysts as experienced in the oxidation of monohydric alcohols where the core shell nanocatalysts incorporated on CNT-SO_3 gave a lower oxidation performance in all the tests carried out.

9.9 References

(1) Morales-Acosta, D.; Arriaga, L. G.; Alvarez-Contreras, L.; Luna, S. F.; Varela, F. J. R. *Electrochem. commun.* **2009**, *11*, 1414–1417.

(2) Chetty, R.; Scott, K. *J. Appl. Electrochem.* **2007**, *37*, 1077–1084.

(3) Livshits, V.; Philosoph, M.; Peled, E. *J. Power Sources* **2008**, *178*, 687–691.

(4) Kaplan, D.; Burstein, L.; Rosenberg, Y.; Peled, E. *J. Power Sources* **2011**, *196*, 8286–8292.

(5) Kaplan, D.; Alon, M.; Burstein, L.; Rosenberg, Y.; Peled, E. *J. Power Sources* **2011**, *196*, 1078–1083.

(6) Serov, A.; Kwak, C. *Appl. Catal. B Environ.* **2010**, *97*, 1–12.

(7) Ji, N.; Zhang, T.; Zheng, M.; Wang, A.; Wang, H.; Wang, X.; Chen, J. G. *Angew. Chem. Int. Ed. Engl.* **2008**, *47*, 8510–3.

(8) Zheng, M.-Y.; Wang, A.-Q.; Ji, N.; Pang, J.-F.; Wang, X.-D.; Zhang, T. *ChemSusChem* **2010**, *3*, 63–6.

(9) Gerpen, J. Van. *Fuel Process. Technol.* **2005**, *86*, 1097–1107.

(10) Xin, L.; Zhang, Z.; Wang, Z.; Li, W. *ChemCatChem* **2012**, *4*, 1105–1114.

(11) Zhang, Z.; Xin, L.; Li, W. *Appl. Catal. B Environ.* **2012**, *119-120*, 40–48.

(12) Antolini, E. *Energy Environ. Sci.* **2009**, *2*, 915.

(13) Antolini, E.; Gonzalez, E. R. *J. Power Sources* **2010**, *195*, 3431–3450.

(14) Bianchini, C.; Shen, P. K. *Chem. Rev.* **2009**, *109*, 4183–206.

(15) Ramulifho, T.; Ozoemena, K. I.; Modibedi, R. M.; Jafta, C. J.; Mathe, M. K. *J. Electroanal. Chem.* **2013**, *692*, 26–30.

(16) Bambagioni, V.; Bianchini, C.; Marchionni, A.; Filippi, J.; Vizza, F.; Teddy, J.; Serp, P.; Zhiani, M. *J. Power Sources* **2009**, *190*, 241–251.

(17) Sun, Z.-P.; Zhang, X.-G.; Liang, Y.-Y.; Li, H.-L. *J. Power Sources* **2009**, *191*, 366–370.

(18) Zhang, J.; Liang, Y.; Li, N.; Li, Z.; Xu, C.; Jiang, S. P. *Electrochim. Acta* **2012**, *59*, 156–159.

(19) Zhang, Z.; Xin, L.; Li, W. *Int. J. Hydrogen Energy* **2012**, *37*, 9393–9401.

(20) Wu, B.; Wang, B.; Deng, C.; Gao, Y. *Appl. Catal. B Environ.* **2011**, *103*, 163–168.

(21) Yang, X.; Yang, Q.; Xu, J.; Lee, C.-S. *J. Mater. Chem.* **2012**, *22*, 8057.

(22) Lee, Y.-W.; Ko, A.-R.; Han, S.-B.; Kim, H.-S.; Park, K.-W. *Phys. Chem. Chem. Phys.* **2011**, *13*, 5569–72.

(23) Lin, Y.; Cui, X.; Yen, C. H.; Wai, C. M. *Langmuir* **2005**, *21*, 11474–9.

(24) Wang, Y.; Wei, F.; Luo, G.; Yu, H.; Gu, G. *Chem. Phys. Lett.* **2002**, *364*, 568–572.

(25) Xiang, D.; Yin, L. *J. Mater. Chem.* **2012**, *22*, 9584.

(26) Kristian, N.; Yu, Y.; Gunawan, P.; Xu, R.; Deng, W.; Liu, X.; Wang, X. *Electrochim. Acta* **2009**, *54*, 4916–4924.

(27) Jiang, Y.; Lu, Y.; Li, F.; Wu, T.; Niu, L.; Chen, W. *Electrochem. commun.* **2012**, *19*, 21–24.

(28) Zhang, X.; Tian, Z.; Shen, P. K. *Electrochem. commun.* **2013**, *28*, 9–12.

(29) He, G.; Song, Y.; Kang, X.; Chen, S. *Electrochim. Acta* **2013**, *94*, 98–103.

(30) Ferreira Jr., R. S.; Janete Giz, M.; Camara, G. a. *J. Electroanal. Chem.* **2013**, *697*, 15–20.

(31) Zhiani, M.; Rostami, H.; Majidi, S.; Karami, K. *Int. J. Hydrogen Energy* **2013**, *38*, 5435–5441.

(32) Zhang, X.; Shen, P. K. *Int. J. Hydrogen Energy* **2013**, *38*, 2257–2262.

(33) Xu, C.; Tian, Z.; Shen, P.; Jiang, S. P. *Electrochim. Acta* **2008**, *53*, 2610–2618.

(34) Suo, Y.; Zhuang, L.; Lu, J. *Angew. Chem. Int. Ed. Engl.* **2007**, *46*, 2862–4.

(35) Mavrikakis, M.; Hammer, B.; Nørskov, J. K. *Phys. Rev. Lett.* **1998**, *81*, 2819–2822.

(36) Hammer, B and Norskov, J. *Surf. Sci.* **1995**, *343*, 211–220.

(37) Greeley, J.; Nørskov, J. K. *Surf. Sci.* **2005**, *592*, 104–111.

Chapter 10

FUEL CELL STUDIES: FeCo@Fe@Pd/CNT-OH AS EFFICIENT NANOCATALYST FOR DMFC AND DEFC

10.1 Introduction

Compared with hydrogen, non-fossil liquid fuels like methanol (MeOH) and ethanol (EtOH) have many advantages. These small organic molecules have been widely studied for their utilization in energy conversion systems. The main reason is related to their rich abundance, facility of storage/ handling, and primarily their energy density. Moreover, due to their simple molecular structures they should exhibit and reveal excellent conversion efficiency in the fuels' potential utilization as fuel[1–3]. In recent years, great attention has been paid to direct alcohol fuel cells (DAFCs) for portable applications due to some superior advantages over analogous devises fed with hydrogen[4]. Both MeOH and EtOH have high densities [6100 WH kg^{-1} for MeOH and 8000 WH kg^{-1} for EtOH], are easy to store, rich in abundance ,and are readily obtained from renewable sources such as biomass[5–8].

A lot of attention has been focussed on acid-type Direct methanol Fuel cells (DMFCs) and Direct ethanol Fuel cells (DEFCs) and significant progress has been made in their development[9–13]. One of the most critical issues with this type of fuel cell is that a considerable amount of Pt is needed to achieve decent performance. As Pt is scarce and expensive, the high loading of Pt in electrodes is a critical obstacle limiting the wide commercialization of acid-type DEFCs[4,14–17]. However, in the alkaline-type DEFCs, Pd-based catalysts can be an alternative to the Pt-based catalysts for the alcohol oxidation reaction[18–21].

Takamura et al.[22,23] found that Pd catalysts exhibited high electrocatalytic activity to methanol oxidation reaction (MOR) in the alkaline electrolyte. They further studied the kinetics of the MOR and suggested that the dehydrogenation of the methanol occurred quickly and the rate-determining step was the oxidative removal of the methoxi radicals by the hydroxide ions. Shen et al.[19,20] on the other hand, prepared a series of Pd-based catalysts and found that Pd catalysts exhibited higher activity

and stability than did Pt catalysts in ethanol oxidation reaction (EOR) in alkaline solutions. They also demonstrated that the incorporation of a metal oxide, such as NiO and Ce_2O_3, as the support of the Pd catalyst was favourable to EOR. The improvement in the activity was attributed to the enhanced anti-poisoning ability of the catalyst resulting from the introduction of the oxides.

Passive DMFCs do not operate with fuel pumps and oxidant suppliers, thus they have a simpler structure than the conventional active DMFCs. As a result of this, the parasitic power loss from ancillary devices is non-existent during their operation. A number of investigations have been carried out on passive DMFCs[24–28] and many prototypes such as toy cars[29], mobile phones[30] and other portable devices powered by passive DMFCs have been demonstrated. Based on the excellent results of the Pd-based core-shell-shell nanocatalysts (see chapters 4 – 9), it was deemed necessary to conduct a preliminary study of the catalyst in real fuel cell devices and conditions. This chapter reports a preliminary study on the performances of the core shells nanocatalysts (FeCo@Fe@Pd/CNT-OH and FeCo@Fe@Pd/C) and their monometallic Pd nanocatalysts (Pd/CNT-OH and Pd/C) on both Vulcan and carboxylate nanotubes in Passive DMFCs and DEFCs. The core shell nanocatalysts exhibited outstanding performances compared to the single metal nanocatalyst. The positive impact of the presence of the carbon nanotubes on the performances of the catalysts was better noticed in the active DMFC and DEFC.

10.2 Passive DMFC and DEFC in Alkaline Medium

Figures 10.1 a and b show the performance of passive DMFC and DEFC operated at 15°C – 18°C using the four catalysts studied. It can be seen that both the limiting current density and the peak power density exhibited a high increase using the two core shell catalysts (FeCo@Fe@Pd/CNT-OH and FeCo@Fe@Pd/C) in both air-breathing

passive DMFC and DEFC. Their enhanced performances were outstanding compared to their single metal (Pd) counterparts.

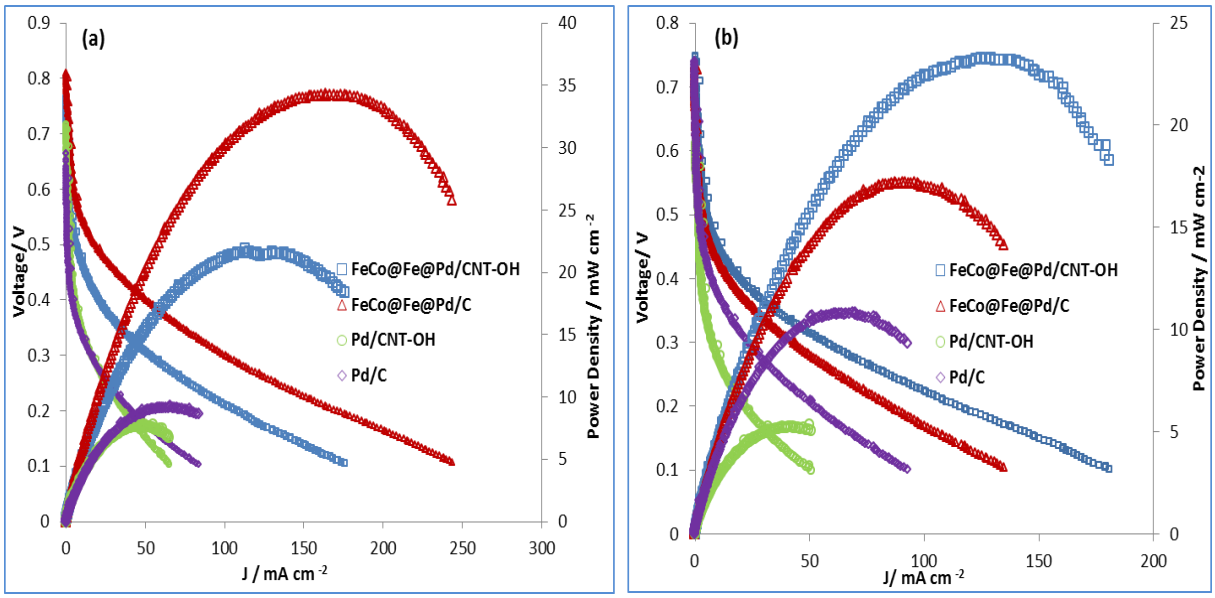

Figure 10.1: Performance of FeCo@Fe@Pd/CNT-OH, FeCo@Fe@Pd/C , Pd/CNT-OH and Pd/C in passive DMFC (a) and DEFC (b) fuelled with 10% alcohol/2 M KOH and operated at ≈ 18°C.

The overall performance of the core shell on Vulcan carbon (FeCo@Fe@Pd/C) was found to be better than that of the same catalyst on carbon nanotubes (FeCo@Fe@Pd/CNT-OH) in DMFC. The opposite was observed for both of their performances in DEFC where FeCo@Fe@Pd/ CNT-OH gave better performance, exhibiting both higher power density and limiting current values. Between the two single metal Pd catalysts, Pd/C gave better performances than Pd/CNT-OH in both DMFC and DEFC. More detailed performance parameters measured using the four catalysts in DMFC and DEFC are listed in Table 10.1 and 10.2. The Tables display the OCV (Open circuit potential), *J* (current densities at a high (0.4 V) and lower (0.2 V) voltages, *P* (maximum power densities exhibited by the catalysts) and *R* (internal resistance of the passive fuel cells using each catalysts).

Table 10.1: Detailed DMFC performance using the four Pd based catalysts

Performance of Passive DMFC at operating temperatures of 15-18°C					
Catalysts	**OCV (V)**	***J*/mAcm^{-2} at 0.4 V**	***J*/mAcm^{-2} at 0.2 V**	***P*/mWcm^{-2}**	***R*/Ω**
FeCo@Fe@Pd/CNT-OH	0.763	20.96	108.18	21.63	0.60
FeCo@Fe@Pd/C	0.810	50.88	171.01	32.27	0.72
Pd/CNT-OH	0.716	6.26	36.74	7.69	0.80
Pd/C	0.664	5.29	41.38	9.15	0.57

Table 10.2: Detailed DEFC performance using the four Pd based catalysts

Performance of Passive DEFC at operating temperatures of 15-18°C					
Catalysts	**OCV (V)**	***J*/mAcm^{-2} at 0.4 V**	***J*/mAcm^{-2} at 0.2 V**	***P*/mWcm^{-2}**	***R*/Ω**
FeCo@Fe@Pd/CNT-OH	0.741	19.69	115.53	23.26	0.55
FeCo@Fe@Pd/C	0.734	15.09	86.11	17.18	0.74
Pd/CNT-OH	0.611	3.04	21.69	5.12	0.58
Pd/C	0.740	7.55	52.20	10.77	0.62

The two core shell catalysts (FeCo@Fe@Pd/CNT-OH and FeCo@Fe@Pd/C) displayed appreciable current density values at high voltages (0.4 V) especially in DMFC. This resulted in their higher power outputs which were 32.27 mWcm^{-2} and 21.63 mWcm^{-2} for FeCo@Fe@Pd/CNT-OH and FeCo@Fe@Pd/C, respectively.

For the passive DEFC the current density values of both catalysts are both lower than that in DMFC at high voltage and almost in the same range. The power output values were 23.26 $mWcm^{-2}$ and 17.18 $mWcm^{-2}$ for FeCo@Fe@Pd/CNT-OH and FeCo@Fe@Pd/C respectively. The presence of nanotubes does not seem to have a remarkable influence on the cell performances of the catalysts embedded on the substrates. This can be readily observed with the values obtained with Pd/CNT-OH in both DMFC and DEFC.

10.3 Columbic and Energy Efficiencies

The high conversion efficiency in Fuel cells is one of its advantages. Thus, this section investigates two of the efficiency types using the studied catalysts in a practical fuel cell system.

The Columbic or Faradaic efficiency ε_f has been earlier defined in section 1.2.6 as the ratio of experimental current to the maximum current converted by the fuel. Thus:

$\boldsymbol{\varepsilon_f} = \frac{I_{exp}}{I_{max}}$ *where* I_{exp} is the actual or experimental current drawn from the cell and I_{max} is the maximum possible current that can be converted by the fuel.

Generally, the electrical behaviour of a fuel cell in a galvanostatic experiment shows a decline in voltage (over time) upon discharge in proportion to the charge removed through its external load. This behaviour is also observed in electrical storage devices. A typical galvanostatic curve obtained from the results of the galvanostatic experimental set up used in these studies is shown in Fig 10.2.

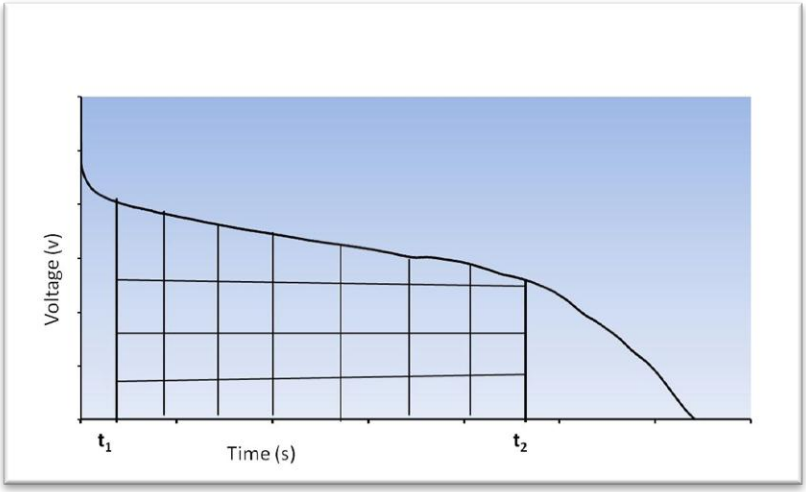

Figure 10.2: A typical plot from the Galvanostatic experiments.

Considering the shaded portion between t_1 and t_2 (ohmic loss region where fuel cells are typically operated); the voltage can be defined as[31]:

$$V = \frac{Q}{C} \qquad (10.1)$$

Where V is the voltage (v), Q is the discharge capacity (Ah) and C is the capacitance (Farad) C can also be evaluated using equation 10.2 below:

$$C = \frac{it}{v} \qquad (10.2)$$

Where i is the current (A); t is the time (s) and v is the voltage (v).

Thus considering the region between t_1 and t_2 (as the slope is negative, absolute values are obtained), the experimental current can be calculated as:

$$\left|I_{exp}\right| = c\left|\frac{dv}{dt}\right| \qquad (10.3)$$

The maximum current that can be converted by the fuel, I_{max} will be:

$$I_{max} = \frac{6C_M V_M F}{t}\ (\text{MeOH})\ \text{and} \quad I_{max} = \frac{12C_M V_M F}{t}\ (\text{EtOH}) \qquad (10.4)$$

where C_M is the alcohol concentration (moldm^{-3}), V_M is the volume of fuel (dm^3), F, Faraday constant (96485 Cmol^{-1}), t is the time (s) of the

discharging process, Factors '6' and '12' are the total number of moles of electrons released in the complete oxidation of MeOH and EtOH respectively. The values of Q (Q_2-Q_1), and V (V_2-V_1) were obtained within the same ranges as t_1 and t_2. These and all other parameters used for the calculations were extracted from the resulting data produced by the instrument after each galvanostatic experiment. Curves obtained from the galvanostatic experiments performed in a passive DMFC and DEFC respectively at 102 mA, using the four catalysts are shown in Figures 10.3 and 10.4. As observed in previous tests, the galvanostatic curves also showed that the potential of the core shell catalysts are higher than both the single monometallic Pd catalysts with longer life spans in both DMFC and DEFC. FeCo@Fe@Pd/C shows a superior performance in DMFC, exhibiting a high cell potential till the last two hours of the experiment. On the other hand the same core shell catalyst on nanotubes-FeCo@Fe@Pd/CNT-OH showed a steady decrease in voltage at each hour till the end of the fuel cell running time. Interestingly, the cell operated for the same period of time using both catalysts. However, in the passive DEFC, the voltage of FeCo@Fe@Pd/CNT-OH is slightly higher than that of FeCo@Fe@Pd/C in the galvanostatic test. Both catalysts experienced a major decline in their potential values after 10 hours of running of the cell.

Slotting in all the corresponding values for obtaining ε_f, the Faradaic efficiency of the four catalysts was calculated. A summary of the results in both DMFC and DEFC is shown in Table 10.3. The Faradaic efficiency becomes less than one if fuel is converted in other side reactions e.g. by the cross-over to the cathode compartment and subsequent direct oxidation of the fuel. All the values obtained are higher than one or can be approximated to the value of one except that of Pd/C in DMFC. In summary, there is a minimal occurrence of fuel cross over during the fuel cell operations using the catalysts. It also gives an indication of the effectiveness of the anion exchange membrane used.

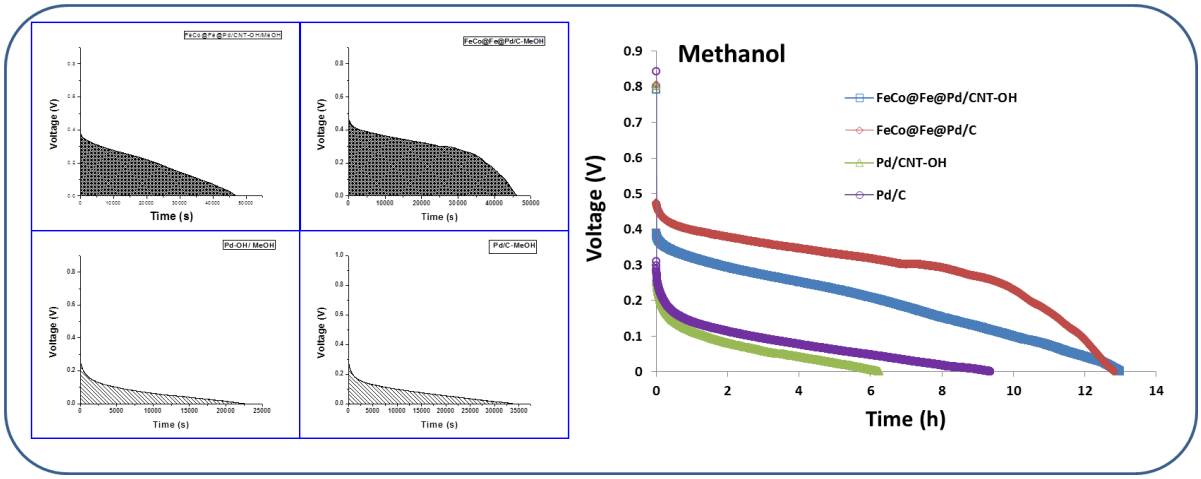

Figure 10.3: Galvanostatic curves for passive DMFCs fuelled with 2 M KOH and 10 wt % MeOH

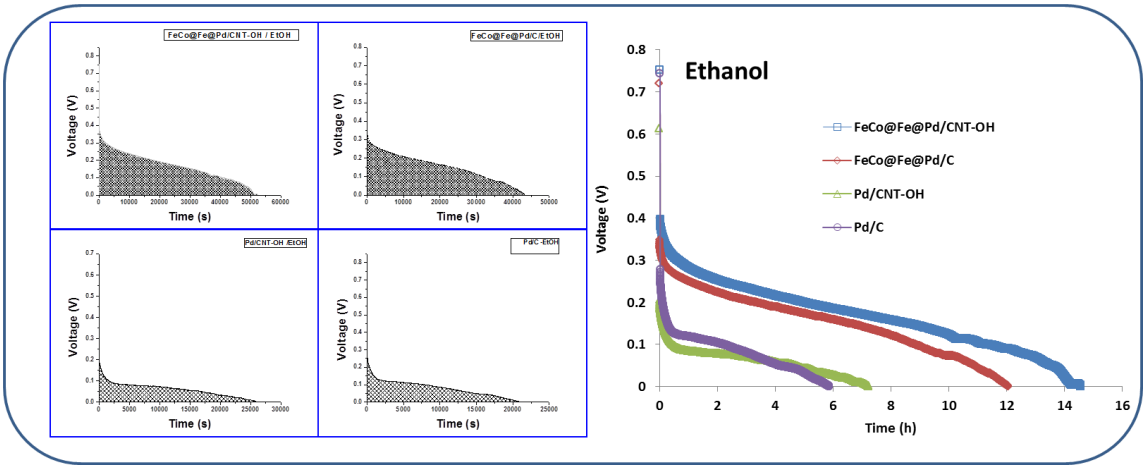

Figure 10.4: Galvanostatic curves for passive DEFCs fuelled with 2 M KOH and 10 wt. % EtOH.

Table 10. 3: Evaluated Faradaic Efficiency of the catalysts in passive DMFC and DEFC

Catalysts	Faradaic (Columbic) Efficiency	
	DMFC	**DEFC**
FeCo@Fe@Pd/CNT-OH	1.63	1.01
FeCo@Fe@Pd/C	1.69	1.00
Pd/CNT-OH	0.97	0.98
Pd/C	0.65	1.00

In addition, the efficiency of a passive DMFC can also be assessed on the basis of the discharge energy (watt–hour) by taking both the voltage and current into account. Thus it follows that the energy efficiency (ξ) can be calculated as shown in equation 10.5[32]:

$$\xi = \frac{I\int_{t=0}^{t-t} v(t)dt}{6C_M V_M\ FE}\ (MeOH) \quad \text{or} \quad \xi = \frac{I\int_{t=0}^{t-t} v(t)dt}{4C_M V_M\ FE}\ (EtOH) \qquad (10.5)$$

where I is the current of the galvanostatic experiment, the theoretical voltage *E* = 1.18 V at 25 °C of a passive DMFC while for a passive DEFC the theoretical voltage *E* = 1.14 V at the same temperature [33,34].

In practical alcohol oxidation, while methanol is completely oxidized to carbonates in DMFCs (Eqn 10.6), Palladium based electrodes have been known for their capacity to oxidize ethanol selectively to acetate ions in strongly alkaline media (Eqn 10.7)[4,35]. Thus, each ethanol molecule can release a maximum of four electrons, instead of the twelve electrons theoretically obtainable from its complete oxidation to carbonates (Eqn 10.8), hence the use of the '4' factor in the efficiency evaluation of DEFCs.

$$CH_3OH + 8\ OH^- \longrightarrow CO_3^{2-} + 6\ H_2O + 6\ e^- \qquad (10.6)$$

$$C_2H_5OH + 5\ OH^- \longrightarrow CH_3COO^- + 4\ H_2O + 4\ e^- \qquad (10.7)$$

$$C_2H_5OH + 16\ OH^- \longrightarrow 2CO_3^{2-} + 11\ H_2O + 12\ e^- \qquad (10.8)$$

The evaluated energy efficiency percentages of the catalysts in DMFC and DEFC determined by equation 10.5 are displayed in Table 10.4. While FeCo@Fe@Pd/C gave the highest value in DMFC (5.3 %) its value (5.89%) is second best to FeCo@Fe@Pd/CNT-OH in DEFC (7.76%)

Table 10.4: Evaluated Energy Efficiency percentages of the catalysts in passive DMFC and DEFC (values for complete oxidation of ethanol are in brackets)

Catalysts	Energy Efficiency/%	
	DMFC	**DEFC**
FeCo@Fe@Pd/CNT-OH	3.50	7.76 (*2.59*)
FeCo@Fe@Pd/C	5.30	5.88 (*1.96*)
Pd/CNT-OH	0.60	1.40 (*0.47*)
Pd/C	1.0	1.50 (*0.50*)

Although one observes low energy efficiency percentages in the operation of the catalysts in both fuel cells; their actual specific energy (Wh) (calculated based on the theoretical specific energies of methanol – 6100 Wh kg^{-1} and Ethanol - 8000 Wh kg^{-1}) in both fuel cells are comparable to the theoretical specific energy of some Li- ion Battery systems. An illustration of this can be seen in Fig 10.5 a and b below. These results further illustrate the advantages of passive DMFCs and DEFCs over some Li ion based batteries in portable appliance applications.

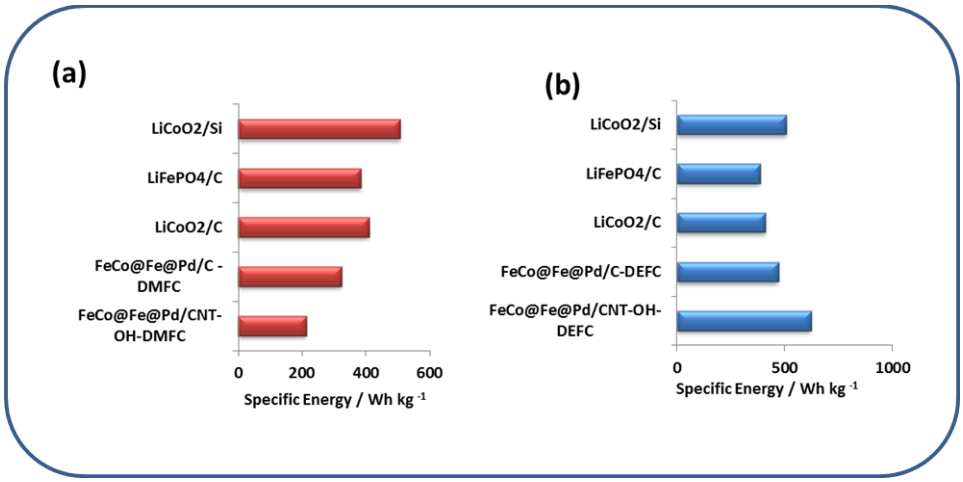

Figure 10.5: Comparison of specific Energies ($Whkg^{-1}$) of FeCo@Fe@Pd/CNT-OH and FeCo@Fe@Pd/C in DAAFCs with other catalysts used in Li-Battery systems.

10.4 Active DMFC and DEFC in Alkaline Medium

The performances of the active DMFCs and DEFCs with the catalysts as anodes were carried out by varying the temperatures at fixed oxygen and fuel flows. This was done to ascertain the influence of the presence of carbon nanotubes as adequate substrates for the catalysts in Fuel cell operations. Figures 10.6 and 10.7 display a series of potentiodynamic and power output scans of each catalyst run in DMFC and DEFC respectively at varying temperatures. The temperature range was from 25°C to 80°C. The conditions of the cell at each temperature were uniform in all the tests. Temperatures of Fuel/Cell/oxygen were 25/25/25; 40/40/40; 60/60/50; 80/80/50.

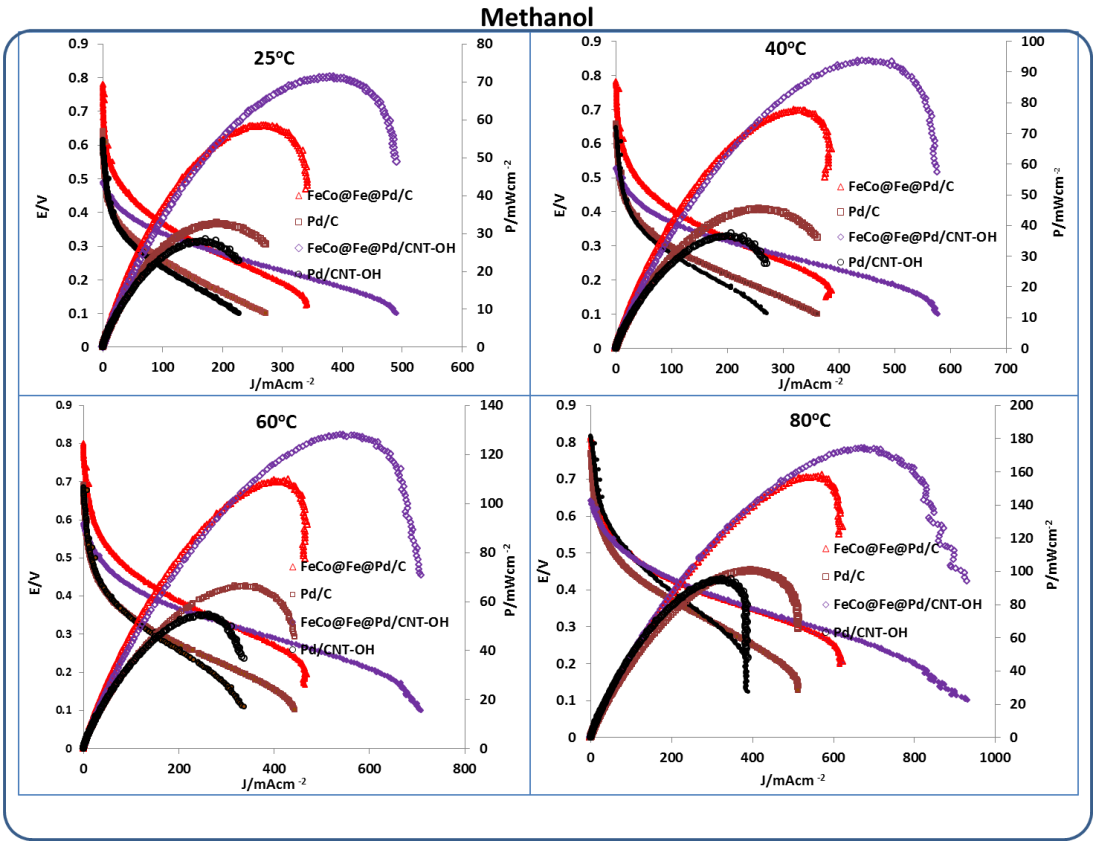

Figure 10.6: Potentiodynamic (filled symbols) and power density (empty symbols) curves for active DMFCs containing FeCo@Fe@Pd/CNT-OH, FeCo@Fe@Pd/C, Pd/CNT-OH and Pd/C anodes and fuelled with 2 M KOH and 10 wt. % MeOH solution at different temperatures

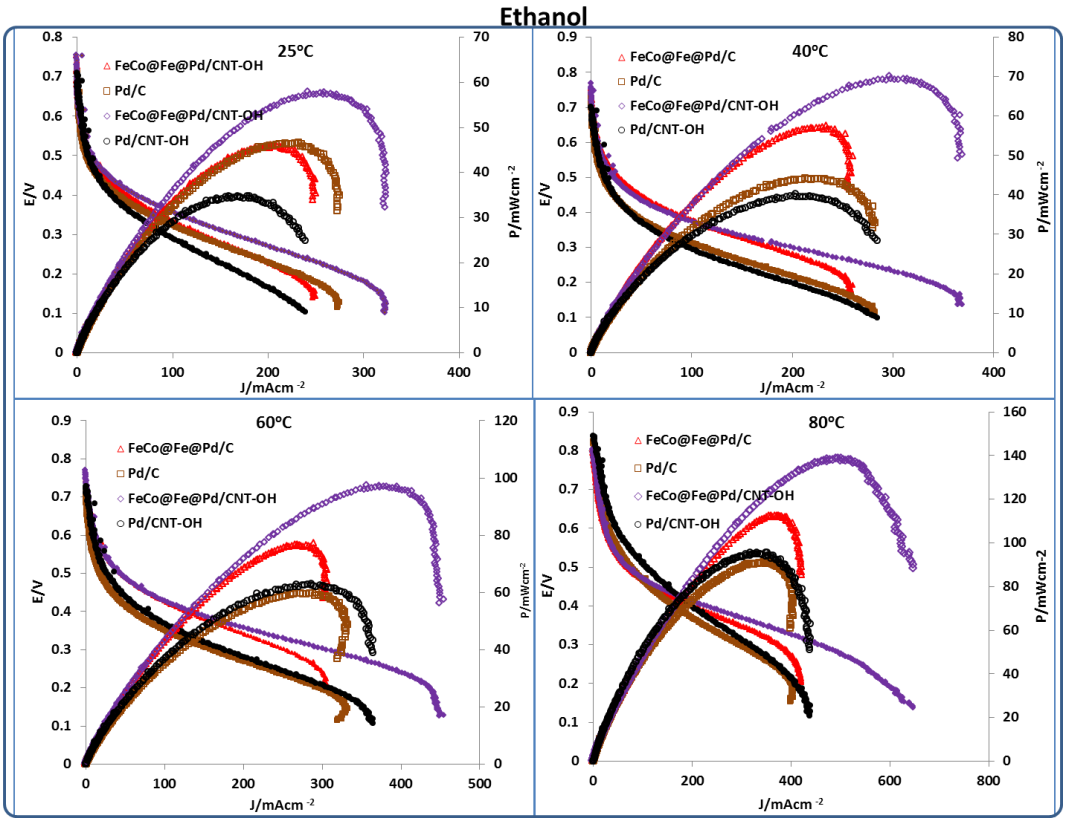

Figure 10.7: Potentiodynamic (filled symbols) and power density (empty symbols) curves for active DEFCs containing FeCo@Fe@Pd/CNT-OH, FeCo@Fe@Pd/C, Pd/CNT-OH and Pd/C anode electrocatalysts and fuelled with 2 M KOH and 10 wt. % EtOH solution at different temperatures

A quick perusal of the figures already shows the positive influence of the presence of the carbon nanotubes in the enhancement of both the power output and the limiting current in both active fuel cells, especially at high temperatures. It should be noted that these temperatures fall within the range of the operating temperatures of active fuel cells in real application conditions. The enhancing influence of the presence of nanotubes in the active fuel cells is also not surprising as carbon nanotubes are materials with enhanced stability and conductivity at high temperatures.

The Power densities of all the catalysts gave a steady increment as temperature increases in both active DMFCs and DEFCs. A 2.5 fold increment of the power density value was found for FeCo@Fe@Pd/CNT-

OH catalysts in both fuel cells with an increase in temperature from 25^{o}C to 80^{o}C. Pd/ CNT-OH which did not show any appreciable power output and current density values when used as anode catalysts in passive DMFC and DEFC gave 3.5 and 2.8 increment in power density in the active DMFC and DEFC respectively with an increase in temperature from 25^{o}C and 80^{o}C. As expected the core shell catalysts still gave better results irrespective of the type of substrate used.

The science of core-shell nano materials is well-known, and the reasons for their higher activity over their bulk monometallic catalysts are also well discussed in the literature. The reasons have been attributed, amongst others, to the modification of the electronic structure of the surface element due to the so-called strain and ligand effects of the core substrate. Thus, the electronic structure of Pd deposited on the surface of the FeCo@Fe/C surfaces is different from that of bulk Pd because of the strain and ligand effects of the core substrate[36–41]

A simple screening using CV was conducted to gain more insights into the electrochemistry of the catalysts with respect to the mechanism of alcohol oxidation on the Pd surfaces of the four Pd based catalysts used in this study.This was to further confirm the reality of the catalytically improved Pd surface of the core shell catalysts due to the incorporation of the cores with respect to the mono metallic Pd catalysts.

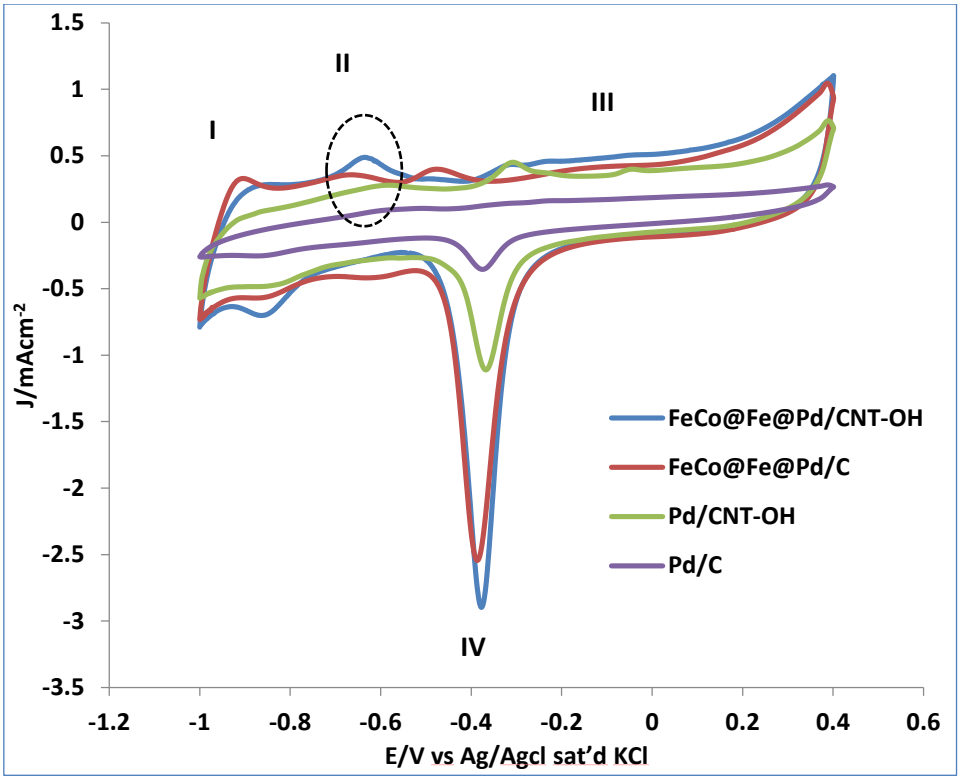

Figure 10.8: Comparative cyclic voltammograms of FeCo@Fe@Pd/CNT-OH, FeCo@Fe@Pd/C, Pd/CNT-OH and Pd/C in 2 M KOH saturated N_2 solution at 50mVs^{-1}

The peaks shown in the voltammograms are typical of Pd in alkaline solution. As also explained by other authors[20,42], peaks I in the potential range of between -0.9 and -0.7 V is due to the oxidation (desorption) of the absorbed and adsorbed hydrogen. The adsorption of OH^- starts at about -0.7 V in which the formation of the surface adsorbed Pd hydroxides species (Pd-OH) are formed, this is shown as peak II. At times this peak can be superimposed with the larger signal of hydrogen desorption as seen in the scans of Pd/CNT-OH and Pd/C (the previously chemisorbed OH- ions can be transformed into higher valence oxides at higher potentials). Peak III which appears at the far negative potential at about -0.2 V can be attributed to the formation of Pd (II) oxide layer. This peak can also be attributed to the oxidation of quinolic groups present especially in the functionalised carbon nanotubes systems. The latter is likely to be the case in the present studies. In the backward scan, the

cathodic peak at -0.4 V can be assigned to the reduction of Pd-O while the broad peaks at -0.8V can be attributed to the hydrogen uptake by Pd.

Using ethanol as a common example of monohydric alcohol, the processes involved in the mechanism of ethanol oxidation on Pd/C in alkaline medium was proposed and explained by Liang et al.[43] as follows:

$$Pd + OH^- \longleftrightarrow Pd\text{-}OH_{ads} + e^- \quad (10.6)$$

$$Pd + CH_3CH_2OH \longleftrightarrow Pd\text{-}(CH_3CH_2OH)_{ads} \quad (10.7)$$

$$Pd\text{-}(CH_3CH_2OH)_{ads} + 3OH^- \longrightarrow Pd\text{-}(CH_3CO)_{ads} + 3H_2O + 3e^- \quad (10.8)$$

$$Pd\text{-}(CH_3CO)_{ads} + Pd\text{-}OH_{ads} \longrightarrow Pd\text{-}CH_3COOH + Pd : \text{slow} \quad (10.9)$$

$$Pd\text{-}CH_3COOH + OH^- \longrightarrow Pd + CH_3COO^- + H_2O: \text{fast} \quad (10.10)$$

The adsorption of OH^- and the further oxidation processes are rather important for EtOH oxidation reaction. Thus the rate-determining step is proposed to be step 4 (Eq. 10.9), in which the adsorbed ethoxy intermediate is removed by adsorbed hydroxyl ions to form acetate as the main product and release free active catalytic sites. As shown in Fig. 10.8, CVs of the Pd core shell and Pd mono metallic catalysts in N_2-saturated 2 M KOH solutions all show a peak around -0.70 to -0.6 V in forward scan, which is assigned to OH adsorption[43]. The OH adsorption peak potentials appeared at -0.67 V, -0.69 V, -0.62 V, and -0.57 V for FeCo@Fe@Pd/CNT-OH, FeCo@Fe@Pd/C, Pd/CNT-OH and Pd/C respectively. The peaks also appear more prominent in the Pd based core shell catalyst than the single Pd catalyst with FeCo@Fe@Pd/CNT-OH having the highest peak intensity, which is also indicative of a larger Pd surface area (28.86 μC). The earlier potential values of OH adsorption peaks indicate that OH^- ions are more easily adsorbed onto the surface of the Pd based core shell catalysts FeCo@Fe@Pd/CNT-OH, and FeCo@Fe@Pd/C. And according to the reaction in step 4 (Eq. 10.9), this facilitates the removal of more intermediates and the availability of more active sites on the surface of the catalysts. It is also interesting to note

that the values of onset potential for the electrocatalytic oxidation of EtOH (10% EtOH/2 M KOH) by the catalysts (as seen in Fig 10.9) not only falls in the same range as that of the OH adsorption peaks on the Pd surface (Fig 10.8) but also follows the same trend. Thus, EOR is seen to proceed continuously with an increase in current till a maximum value is attained and then a decline begins. As stated by the authors in earlier citation[43], the decline in current has been related to the formation of Pd (II) oxide layer on the surface of the electrode at higher potentials which can consequently block the adsorption of the reactive species on the Pd surface. In this system however, this can also include the blocking of the surface as a result of the oxidation of the carbonyl and quinolic groups present on the functionalised carbon nanotubes. The potentials for this decline is around -0.2 V (Fig 10.9) which coincides with the potential of Pd-O formation (Peak III) in Fig 10.8. The fresh Pd surface can be recovered during the cathodic backward sweep.

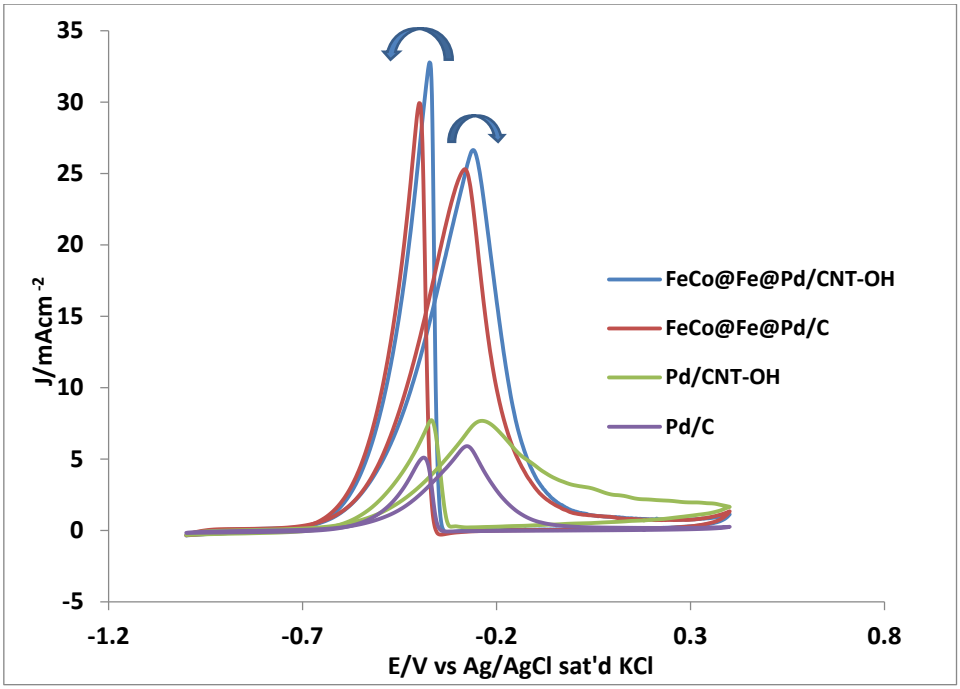

Figure 10.9: Comparative cyclic voltammograms of FeCo@Fe@Pd/CNT-OH, FeCo@Fe@Pd/C, Pd/CNT-OH and Pd/C in 10% EtOH/2 M KOH saturated N_2 solution at 25 mVs^{-1}

10.5 Conclusion

The columbic and energy efficiencies of novel Pd based core shell catalysts have been reported. To the best of my knowledge, this is the first time studies on this type have been done on catalysts with core shell architecture. The core shell catalysts showed better performances compared to their mono metallic counterparts. They even exhibited better energy efficiency as anode catalysts in DEFCs for portable applications compared to some other Li-ion batteries used for the same purpose. The enhanced performances of the core shell catalysts was a result of the electronic effect leading to the modification of the Pd surface as a result of the presence of the core alloy. This resulted in an improved catalytic Pd surface and was also proved by some half-cell studies. More studies are needed for the optimisation of the two core shell catalysts, and to reduce their loading on the devices.

10.6 References

(1) Rice, C.; Ha, S.; Masel, R. I.; Waszczuk, P.; Wieckowski, a.; Barnard, T. *J. Power Sources* **2002**, *111*, 83–89.

(2) Antolini, E.; Gonzalez, E. R. *J. Power Sources* **2010**, *195*, 3431–3450.

(3) Song, S.; Tsiakaras, P. *Appl. Catal. B Environ.* **2006**, *63*, 187–193.

(4) Bianchini, C.; Shen, P. K. *Chem. Rev.* **2009**, *109*, 4183–4206.

(5) Koenigsmann, C.; Wong, S. S. *Energy Environ. Sci.* **2011**, *4*, 1161.

(6) Rousseau, S.; Coutanceau, C.; Lamy, C. *J. Power Sources* **2006**, *158*, 18–24.

(7) Li, Y. S.; Zhao, T. S.; Liang, Z. X. *J. Power Sources* **2009**, *187*, 387–392.

(8) Li, H.; Sun, G.; Jiang, Q.; Zhu, M.; Sun, S.; Xin, Q. *Electrochem. commun.* **2007**, *9*, 1410–1415.

(9) Fang, Y.; Yang, X.; Wang, L.; Liu, Y. *Electrochim. Acta* **2013**, *90*, 421–425.

(10) An, L.; Zhao, T. S.; Shen, S. Y.; Wu, Q. X.; Chen, R. *J. Power Sources* **2011**, *196*, 186–190.

(11) Li, Y. S.; Zhao, T. S. *Int. J. Hydrogen Energy* **2012**, *37*, 15334–15338.

(12) Zhou, W. J.; Song, S. Q.; Li, W. Z.; Zhou, Z. H.; Sun, G. Q.; Xin, Q.; Douvartzides, S.; Tsiakaras, P. *J. Power Sources* **2005**, *140*, 50–58.

(13) Lamy, C.; Devadas, A.; Simoes, M.; Coutanceau, C. *Electrochim. Acta* **2012**, *60*, 112–120.

(14) Wang, C.; Hou, Y.; Kim, J.; Sun, S. *Angew. Chem. Int. Ed. Engl.* **2007**, *46*, 6333–6335.

(15) Song, S.; Zhou, W.; Liang, Z.; Cai, R.; Sun, G.; Xin, Q.; Stergiopoulos, V.; Tsiakaras, P. *Appl. Catal. B Environ.* **2005**, *55*, 65–72.

(16) Wang, X.; Wang, W.; Qi, Z.; Zhao, C.; Ji, H.; Zhang, Z. *J. Power Sources* **2010**, *195*, 6740–6747.

(17) Wang, Y.-L.; Zhao, Y.-Q.; Xu, C.-L.; Zhao, D.-D.; Xu, M.-W.; Su, Z.-X.; Li, H.-L. *J. Power Sources* **2010**, *195*, 6496–6499.

(18) Hu, F.; Chen, C.; Wang, Z.; Wei, G.; Shen, P. K. *Electrochim. Acta* **2006**, *52*, 1087–1091.

(19) Shen, P. K.; Xu, C. *Electrochem. commun.* **2006**, *8*, 184–188.

(20) Xu, C.; Shen, P. K.; Liu, Y. *J. Power Sources* **2007**, *164*, 527–531.

(21) Bagchi, J.; Bhattacharya, S. K. *Transit. Met. Chem.* **2007**, *32*, 47–55.

(22) Takamura, T.; Mochimaru, F. **1969**, *14*, 111–119.

(23) Takamura, T.; Sato, Y. **1974**, *19*, 63–68.

(24) Bae, B.; Kho, B. K.; Lim, T.-H.; Oh, I.-H.; Hong, S.-A.; Ha, H. Y. *J. Power Sources* **2006**, *158*, 1256–1261.

(25) Kho, B. B.; Oh, I.; Hong, S.; Yong, H.;*Electrochimica Acta*. **2004**, *50*, 781-785.

(26) Kim, D.; Cho, E. A.; Hong, S.-A.; Oh, I.-H.; Ha, H. Y. *J. Power Sources* **2004**, *130*, 172–177.

(27) Pan, Y. H. *J. Power Sources* **2006**, *161*, 282–289.

(28) Shimizu, T. *J. Power Sources* **2004**, *137*, 277–283.

(29) Chang, H.; Kim, J. R.; Cho, J. H.; Kim, H. K.; Choi, K. H. *Solid State Ionics* **2002**, *148*, 601–606.

(30) Chen, C. .; Yang, P. *J. Power Sources* **2003**, *123*, 37–42.

(31) Conway, B. E. *Electrochemical supercapacitors. Scientific fundamentals and technology applications.*; Springer Science. New York 199, Ed.; 1999; Vol. 9, p. 698.

(32) Liu, J.; Zhao, T.; Chen, R.; Wong, C. W. *Fuel Cells Bull.* **2005**, 12–17.

(33) An, L.; Zhao, T. S. *Int. J. Hydrogen Energy* **2011**, *36*, 9994–9999.

(34) Liu, J. G.; Zhao, T. S.; Chen, R.; Wong, C. W. *Electrochem. commun.* **2005**, *7*, 288–294.

(35) Bambagioni, V.; Bianchini, C.; Marchionni, A.; Filippi, J.; Vizza, F.; Teddy, J.; Serp, P.; Zhiani, M. *J. Power Sources* **2009**, *190*, 241–251.

(36) Lim, B.; Wang, J.; Camargo, P. H. C.; Jiang, M.; Kim, M. J.; Xia, Y. *Nano Lett.* **2008**, *8*, 2535–2540.

(37) Huang, Y.; Zhou, X.; Yin, M.; Liu, C.; Xing, W. *Chem. Mater.* **2010**, *22*, 5122–5128.

(38) Sasaki, K.; Naohara, H.; Cai, Y.; Choi, Y. M.; Liu, P.; Vukmirovic, M. B.; Wang, J. X.; Adzic, R. R. *Angew. Chem. Int. Ed. Engl.* **2010**, *49*, 8602–8607.

(39) Wang, D.; Xin, H. L.; Yu, Y.; Wang, H.; Rus, E.; Muller, D. a; Abruña, H. D. *J. Am. Chem. Soc.* **2010**, *132*, 17664–17666.

(40) Zhou, W.-P.; Yang, X.; Vukmirovic, M. B.; Koel, B. E.; Jiao, J.; Peng, G.; Mavrikakis, M.; Adzic, R. R. *J. Am. Chem. Soc.* **2009**, *131*, 12755–12762.

(41) Xu, Y.; Ruban, A. V; Mavrikakis, M. *J. Am. Chem. Soc.* **2004**, *126*, 4717–4725.

(42) Grdeń, M.; Czerwiński, a. *J. Solid State Electrochem.* **2007**, *12*, 375–385.

(43) Liang, Z. X.; Zhao, T. S.; Xu, J. B.; Zhu, L. D. *Electrochim. Acta* **2009**, *54*, 2203–2208.

Chapter 11*

FUEL CELL STUDIES: FeCo@Fe@Pd/CNT-OH AS ANODE CATALYSTS IN DIRECT ETHYLENE GLYCOL FUEL CELL (DEGFC) AND DIRECT GLYCEROL FUEL CELL (DGFC)

* The following manuscript is in preparation and resulted from part of the research work presented in this chapter.

Omobosede O. Fashedemi, Hamish Miller, Andrea Marchionni Francesco Vizza, Kenneth I. Ozoemena. "Selectivity towards complete oxidation of Ethylene glycol (EG) and Glycerol (GLY) on Palladium decorated FeCo@Fe core-shell –FeCo@Fe@Pd/C and - FeCo@Fe@Pd/CNT-OH in Alkaline Medium".

11.1 Introduction

The electro oxidation of ethylene glycol (EG) has attracted considerable interest both for practical reasons and fundamental point of view. The interest in EG stems from its higher energy density, lower toxicity, low flammability, and lower permeation through polymer electrolyte membrane compared to methanol[1–3]. In principle, complete oxidation of ethylene glycol to CO_2 produces 10 electrons per glycol[4].

$$(CH_2OH)_2 + 14OH^- \text{-------}\rightarrow 2CO_3^{2-} + 10H_2O + 10e^- \qquad (11.1)$$

Glycerol (GLY) is a non-toxic, non-volatile and non-flammable, highly functionalised molecule. As a main by-product of biodiesel production, glycerol is supplied in large quantities at low price (0.3 US$ kg^{-1}, crude glycerol). The complete oxidation of glycerol to CO_2 in form of carbonates in alkaline media produces 14 electrons per glycol molecule[4].

$$CH_2OH\text{-}CHOH\text{-}CH_2OH + 20\ OH^- \text{-}\rightarrow 3\ CO_3^{2-} + 14\ H_2O + 14\ e \qquad (11.2).$$

A suitable fuel for fuel cell application must be non-toxic, safe to handle, and have high energy density. Moreover, it should be oxidized completely to CO_2 with little or no accumulation of oxidation by-products, should have a high boiling point (for use at temperatures (T) > 100°C at near-ambient pressure) and should be commercially available and inexpensive[1]. Both EG and GLY meet these criteria but a current challenging task for DEGFCs is the incomplete oxidation of EG[4]. Ethylene glycol is a C_2 molecule having a C–C bond in its structure. C–C bond is comparatively strong and cannot be easily cleaved[5].

Platinum-based catalysts are the major group used as anodes for DEGFCs and DGFCs in electrochemical oxidation of EG and GLY. An increase in the amount of platinum supported on carbon materials has been seen to enhance the binding of intermediates, thus leading to improved complete

oxidation[4,6]. But using Pt anodes would result in low efficiencies of fuel utilization and massive emission of undesired incomplete oxidation as Pt catalysts cannot achieve the complete oxidation of ethylene glycol (Eq. 11.3) as seen below:

$$CH_2OH\text{-}CH_2OH + 10\ OH^- \rightarrow COO^- - COO^- + 8H_2O + 8e^- \quad (11.3)$$

Therefore, in order to increase the efficiency of fuel utilization, active catalysts, having sufficient ability to break C–C bond in ethylene glycol, are strongly required.

GLY is also not completely oxidized to CO_2 around room temperature in both acidic or basic media because of slow electro- oxidation kinetics and the high energy barrier for C-C bond dissociation. A raise in reaction temperature has been proposed as an effective means of achieving total oxidation of GLY to CO_2 and accelerate the rate of electro-oxidation to achieve total oxidation of glycerol in DGFCs[7]. Now, it is generally accepted that the oxidation of glycerol suffers partial oxidation[8–10] generating glyceraldehyde, glycerate, mesoxalate, dihydroxyacetone and hydroxypyruvate, among other substances, which causes loss of energetic efficiency. A general equation of this partial oxidation reaction is seen below (Eq. 11.4):

$$CH_2OH\text{-}CHOH\text{-}CH_2OH + 12OH^- \rightarrow COO^-\text{-}CO\text{-}COO^- + 10H_2O + 10e^- \quad (11.4)$$

A strategy for enhancing electro catalytic performance is the substitution of platinum with palladium-based anodes for DEGFCs and DGFCs. In addition, palladium is more abundant in nature and less expensive than Pt[11–17]. Palladium has been known to disfavour the breaking of the C–C bond[18] but the combination of Pd with other metals has been studied over the past years in order to increase activity and stability of Pd based catalysts and also to act as co-catalyst in order to promote the scission of

C-C bonds during the electro oxidation of polyhydric molecules. In view of this, Pd has been diluted with other base metals, as seen with the reaction on nanostructured Pd-(Ni–Zn)/ C and Pd-(Ni–Zn–P)/C, which were found more reactive than Pd/C catalysts[19]. Traces of carbonates have also been detected as products of glycerol electro oxidation on PdRh/C at high concentration of KOH[20].

The attraction of Pd-based electro catalysts originates in the fact that they are more active than Pt-based electro catalysts in alkaline media for the oxidation of a variety of substrates[18,19,21]. Hence, some tests of FeCo@Fe@Pd incorporated on carboxylate nanotubes (CNT-OH) were carried out on both the performance and selectivity for complete oxidation of the two polyhydric alcohols –EG and GLY- using FeCo@Fe@Pd/CNT-OH as anode catalysts in anion exchange membrane (AEM) -DEGFCs and DGFCs. It should be noted that this catalyst was chosen for the study as it had exhibited a consistent improved catalytic performance compared to the other core shell catalysts in the half cell studies in alcohol oxidation previously carried out. Monometallic Pd on CNT-OH was also studied for comparison.

11.2 Passive DEGFC and DGFC Studies in Alkaline Medium

DEGFC and DGFC oxidation was investigated using Passive oxygen –breathing DAAFCs as described in the experimental section (Chapter 2). For a reliable evaluation of the oxidation products, the anode compartment was sealed under a nitrogen atmosphere, while the cathode was exposed to air or oxygen. Galvanostatic experiments were carried out at room temperature on the passive cells where the anode compartment was filled with 8.47 mmol of EG. After a conditioning time of 1 h at the OCV, the circuit of the DEGFC was closed and a constant current of 102 mA was allowed to flow until the cell voltage reached zero. The solution was not refuelled during the experiment.

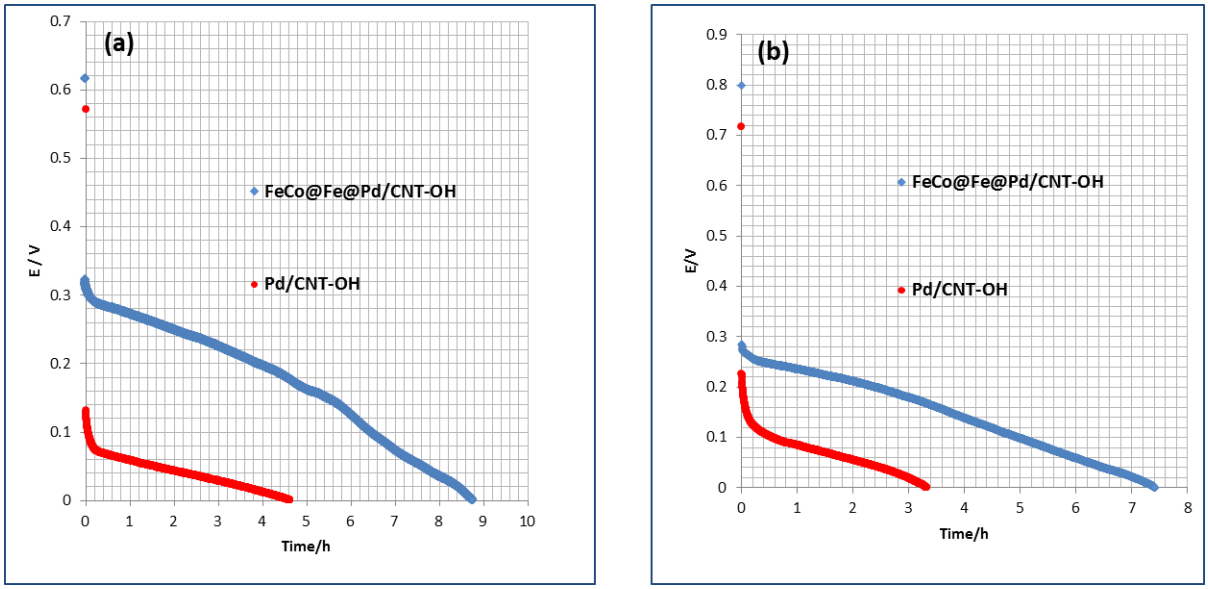

Figure 11.1: Galvanostatic curves for passive DEGFC (a) and DGFC (b) with FeCo@Fe@Pd/CNT-OH and Pd/CNT-OH anodes and fuelled with 2 M KOH and 5 wt. % EG/GLY

The Galvanostatic curves for both catalysts in passive DEGFC and DGFC can be seen in Fig 11.1 (a) and (b), respectively. Their performances in both passive fuel cells operated at 15°C -18°C are shown in Fig 11.2 (a) and (b).

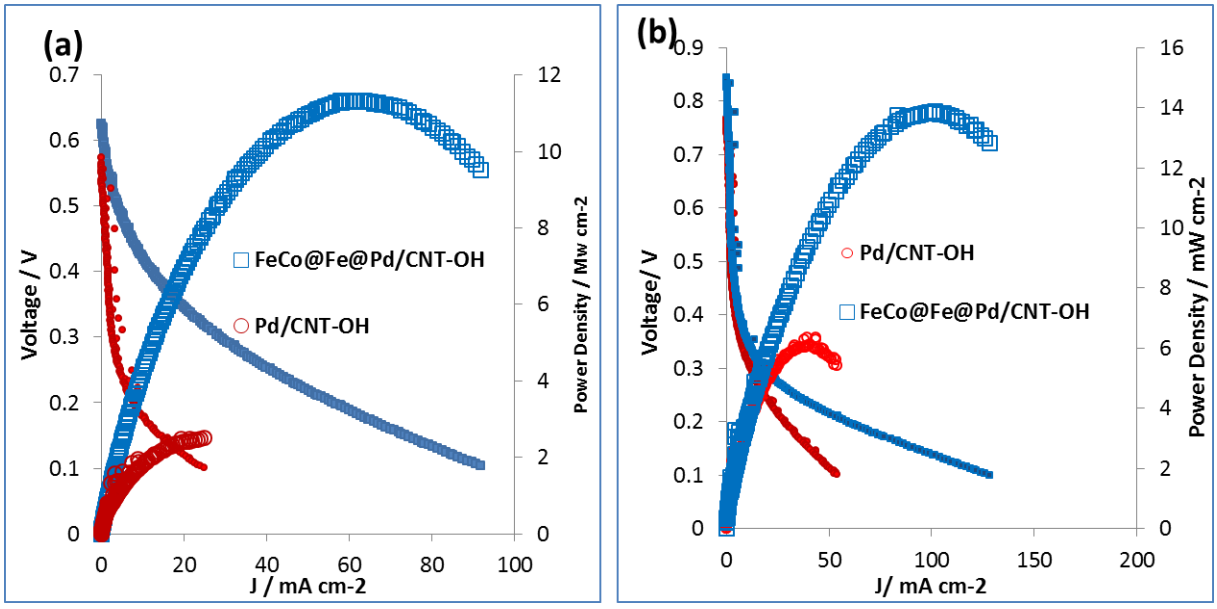

Figure 11.2: Performances of passive DEGFC (a) and DGFC (b) operated at 15°C – 18°C using FeCo@Fe@Pd/CNT-OH and Pd/CNT-OH anodes

While DEGFC containing core shell FeCo@Fe@Pd/CNT-OH anode delivered a constant 102 mA current for 8.8 h (Fig 11.1 a), releasing an energy of 551 J during the reaction, Pd/CNT-OH as anode in the same fuel cell delivered the same amount of current for 4.62 h releasing an energy value of 67 J

The DGFC with FeCo@Fe@Pd/CNT-OH ran for 4.40 h (Fig 11.1 b) and releasing an energy value of 265 J while Pd/CNT-OH delivered only 82 J with the DGFC running for 3.27 h. The core shell nanocatalyst also showed an enhanced performance in terms of the peak power density and limiting current density when used as anode catalysts in both AEM-DEGFC and AEM-DGFC as seen in Figures 11.2 a and b. Other parameters measured using both FeCo@Fe@Pd/CNT-OH and Pd/CNT-OH as anodes in DGFC and DEGFC are shown in Tables 11.1 and 11.2.

Table 11.1: Performance of catalysts in Passive DEGFC at operating temperatures of 15-18^{o}C

Catalysts	**OCV/V**	***J*/mAcm^{-2} (limiting current)**	***P*/mWcm^{-2}**	***R*/Ω**
FeCo@Fe@Pd/CNT-OH	**0.623**	**90.68**	**11.30**	**0.168**
Pd/CNT-OH	**0.571**	**25**	**2.50**	**0.049**

Table 11.2: Performance of catalysts in Passive DGFC at operating temperatures of 15-18^{o}C

Catalysts	**OCV/V**	**J/mAcm^{-2} (limiting current)**	***P*/mWcm^{-2}**	***R*/Ω**
FeCo@Fe@Pd/CNT-OH	**0.861**	**126.0**	**13.76**	**0.149**
Pd/CNT-OH	**0.719**	**0.053**	**6.29**	**0.059**

11.3 Selectivity of FeCo@Fe@Pd for Complete Oxidation of EG and GLY in AEM EGFC and AEM-DGFC: NMR Studies

DEGFC containing core shell FeCo@Fe@Pd/CNT-OH anode delivered a constant 102 mA current for 8.7 h yielding carbonate (67%), formate (2%), oxalate (4%) and glycolate (28%) with a fuel conversion of 65 %. The energy released during the reaction was 551 J. On the other hand, the DEGFC with Pd/CNT-OH as anode delivered the same amount of current for 4.62 h yielding carbonate (26%), formate (4%), oxalate (5%), and glycolate (65%) with a conversion of 29 %. The energy released by the cell was 67 J. The results are summarised in a bar chart Figure 11.3 with a corresponding table (Table 11.3). As seen from the results, the products of the oxidation of EG were the same using both FeCo@Fe@Pd/CNT-OH and Pd/CNT-OH catalysts as anodes. However, the ratios of the percentages of the products were different. One of them was more favourable and selective towards the complete oxidation of EG than the other.

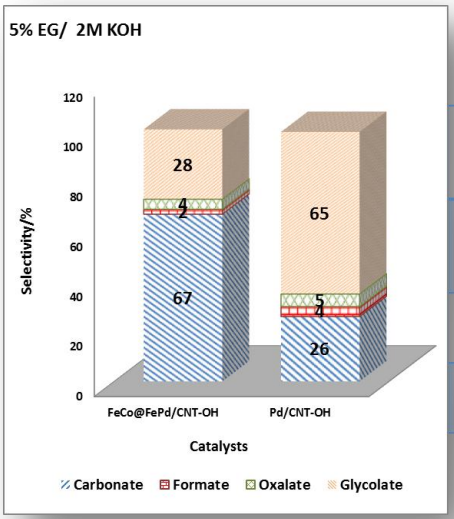

Table 11.3: Products of electro oxidation of EG on catalysts

Catalysts	Conversion (%)	Selectivity (%) (5% EG/ 2M KOH)				
		Formate	Oxalate	Glycolate	Carbonate	Energy (J)
FeCo@Fe@Pd/CNT-OH	65	2	4	28	67	551
Pd/CNT-OH	29	4	5	65	26	67

Figure 11. 3: Percentage selectivity of the products of electro oxidation of 5% EG/2MKOH at FeCo@Fe@Pd/CNT-OH and Pd/CNT-OH

Electrocatalytic oxidation of Glycerol on the other hand gave a plethora of oxidation products. DGFC containing core shell FeCo@Fe@Pd/CNT-OH anode delivered a constant 102 mA current for 8.7 h yielding carbonate

(73%), formate (3%), oxalate (7%), glycolate (7%), tartonate (7%),and glycerate (3%) with a fuel conversion of 16 %. The energy released during the reaction was 265 J. On the other hand, the DGFC with Pd/CNT-OH as anode delivered the same amount of current for 4.62 h yielding carbonate (47%), oxalate (9%), and glycolate (14%), tartonate (15%), and glycerate (15%) with a fuel conversion of 15 %. The energy released during the reaction was 82 J. A summary of these results can be seen in Figure 11.4 with its corresponding table (Table 11.4).

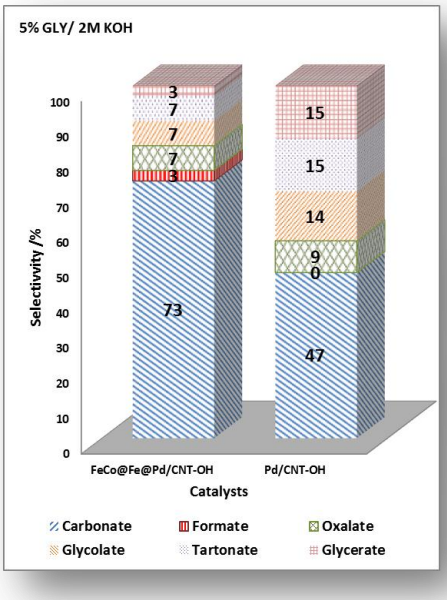

Table 11.4: Products of electro oxidation of GLY on catalysts

Catalysts/Fuel	Conversion (%)	Selectivity (%) (5% GLY/ 2M KOH)						
		FOR	OXA	GLY	TART	GLYC	CO_3^{2-}	Energy (J)
FeCo@Fe@Pd/CNT-OH	16	3	7	7	7	3	73	265
Pd/CNT-OH	15	0	9	14	15	15	47	82

FOR: Formate, OXA: Oxalate, GLY-Glycolate, TART : Tartonate. GLYC: Glycerate, CO_3^{2-} : Carbonate

Figure 11. 4: Percentage selectivity of products of electro oxidation of 5% GLY/ 2M KOH at FeCo@Fe@Pd/CNT-OH and Pd/CNT-OH

All the products of the electro oxidation of both EG and GLY outlined above were obtained from the NMR analyses of the exhausts of both DEGFC and DGFC after the completion of the reaction. From the NMR spectra shown in Figure 11.5 and its detailed segments seen in Figures 11.6, one observes that the main product after EG oxidation in the DEGFC with the FeCo@Fe@Pd/CNT-OH anode is CO_2 (in form of CO_3^{2-} in alkaline medium) which indicates the degree of complete oxidation of EG. Only one main intermediate product, glycolate, was detected. This can be seen

in Figure 11.3 which shows the percentage selectivity of the products of EG oxidation on both catalysts. Glycolate is an intermediate product via a 4e oxidation, without a C-C scission. Other 'minor intermediates' detected in negligible ratios were oxalate and formate.

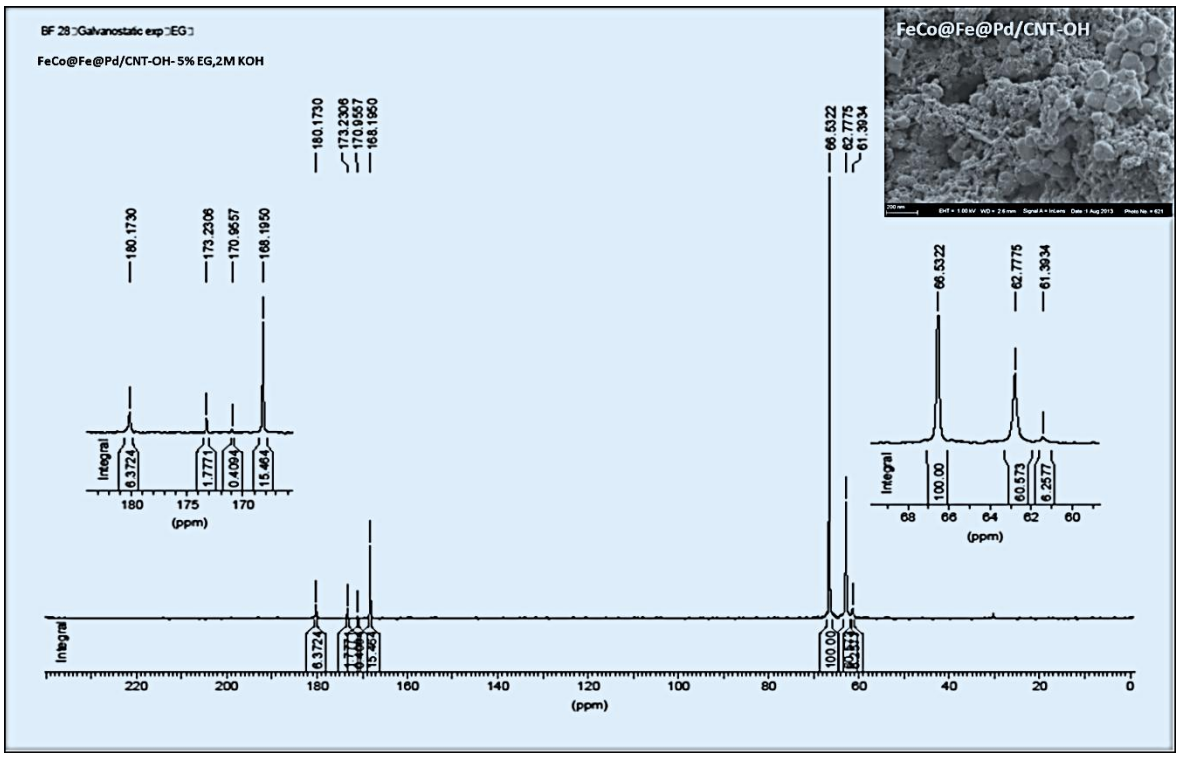

Figure 11. 5: NMR spectra of DEGFC exhausts using FeCo@Fe@Pd/CNT-OH as anodes

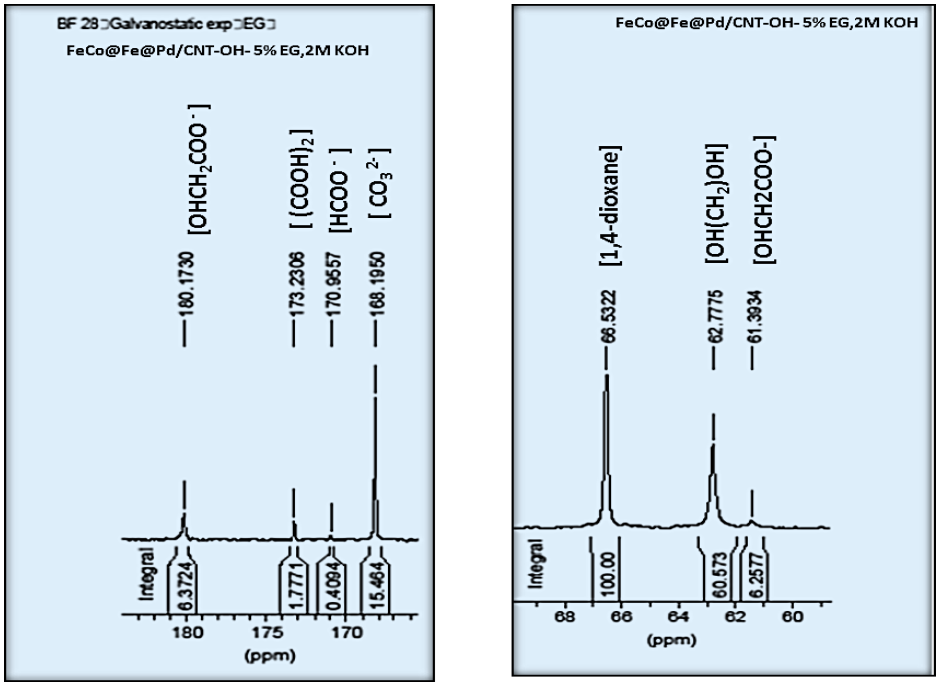

Figure 11. 6: Detailed NMR spectra of main selective products peaks in Figure 11.5

The NMR analysis of the DEGFC exhaust after oxidation reaction of EG using the Pd/CNT-OH anode, yielded glycolate as the main produced product of the reaction as seen from the NMR spectra shown in Figure 11.7 and the detailed segments of the spectra in Figures 11.8. Carbonates was the next major product but with a lower percentage (Fig 11.3). The other minor intermediates produced were oxalate and formate.

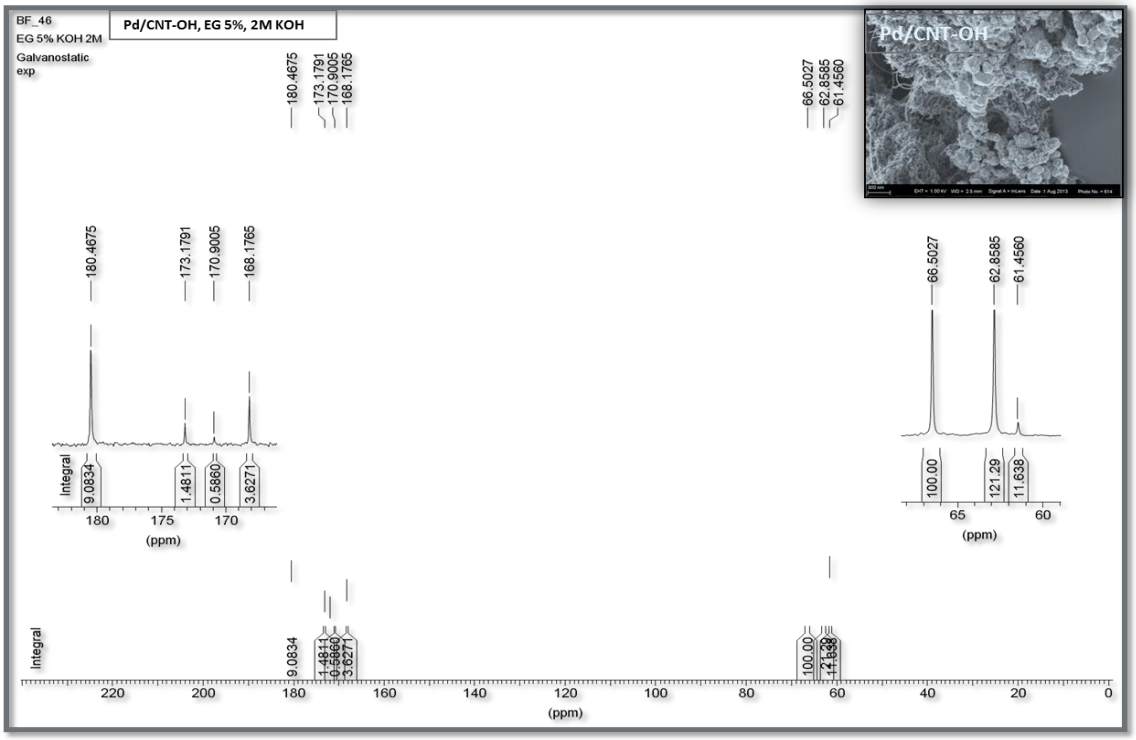

Figure 11.7: NMR spectra of DEGFC exhausts using Pd/CNT-OH as anodes

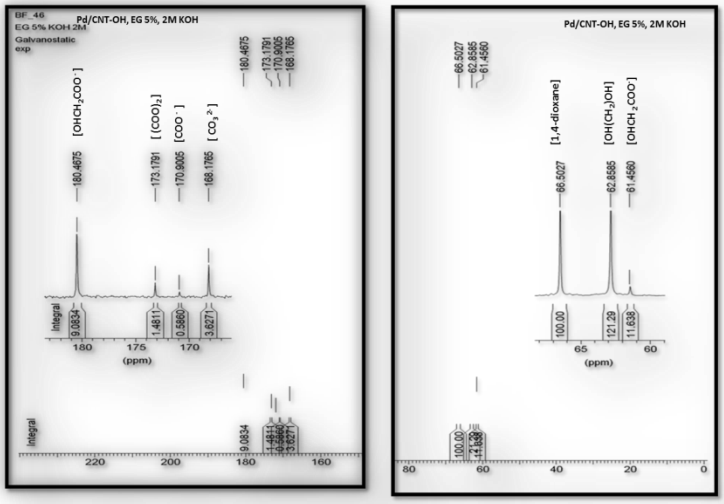

Figure 11.8: Detailed NMR spectra of main selective products peaks in Figure 11.7.

These reaction products have also been observed by other authors for the oxidation of EG in alkaline media[22–24]. Miyazaki et al postulated a reason for the observation of differing percentages of glycolate and formate

products of EG oxidation on Pt/Ru and Pt-Ni alloys on Vulcan carbon. Their observations on both catalysts were explained based on (i) the tolerance for poisoning and (ii) the ability of the C-C bond cleavage. Pt/Ru had a better tolerance for formate but a poor catalytic activity for C-C bond cleavage thus yielding higher amount of C_2 product in form of glycolate, while Pt/Ni alloy had a lesser tolerance for poisoning and thus yielded higher amounts of C_1 product in the form of formate, with reduced glycolate being produced[24]. Xin et al. hypothesized the cleavage of C-C bond to yield formate on Pt and Au catalysts as a common process occurring on vicinal diol compounds like EG, GLY, and 1,2-propanediol in relatively high potentials (above 0.6 V)[25]. The same observation was made by Chang et al. in the study of the electro oxidation of EG on Pt, Au and Ni anode catalysts. They observed the cleavage of the C-C linkage to yield formate only at the vicinal diol functionality and not from the partially oxidized species containing aldehydes and/ carboxylate functional groups. This was observed at low potentials on Pt anode[26].

The two catalysts used in AEM - DEGFC in this study both have a high tolerance for presence of poisonous carbonaceous products like formate as seen in the half cell studies. Thus one can deduce from this that the cleavage of the C-C bond to yield exhaustive electro oxidation of EG to carbonates (in a high percentage) observed on FeCo@Fe@Pd/CNT-OH anode is as a result of the enhanced electronic properties of the Pd surface layer due to the lattice strain caused by the incorporation of the alloy core. As a result of this, the Pd surface layer of the core shell has a highly improved electrocatalytic capability. On the other hand, Pd/CNT-OH catalyst was not as selective in the complete oxidation of EG. Its electrocatalytic reaction for EG oxidation did result in a high production of glycolate under mild conditions. Recalling that the catalyst was also synthesized using the green microwave technique with non-toxic solvents like ethylene glycol as reductant, its use can contribute to a more efficient

and eco – benign way to produce glycolic acid which has a wide range of applications in the pharmaceutical industry.

A two-way pathway for EG electrocatalytic oxidation is proposed at FeCo@Fe@Pd/CNT-OH core shell catalyst. As the C-C bond cleavage mainly occurs on EG and less on glycolate as observed and verified by other authors[25,27], a direct and predominant cleavage of the C-C linkage of EG to yield carbonates is suggested. This will go through the formation of formates which is readily converted to carbonates with trace amount of formate been detected. The second and less favourable pathway is that of glycolate production. As formaldehyde was not detected in any of the exhaust samples, one can assume a fast conversion of glycoaldehyde to glycolate. This can also be slowly converted to oxalate as it was detected in trace amount in the exhaust. The reverse of both suggested pathways will be the case for the electrocatalytic oxidation of EG on Pd/CNT-OH.

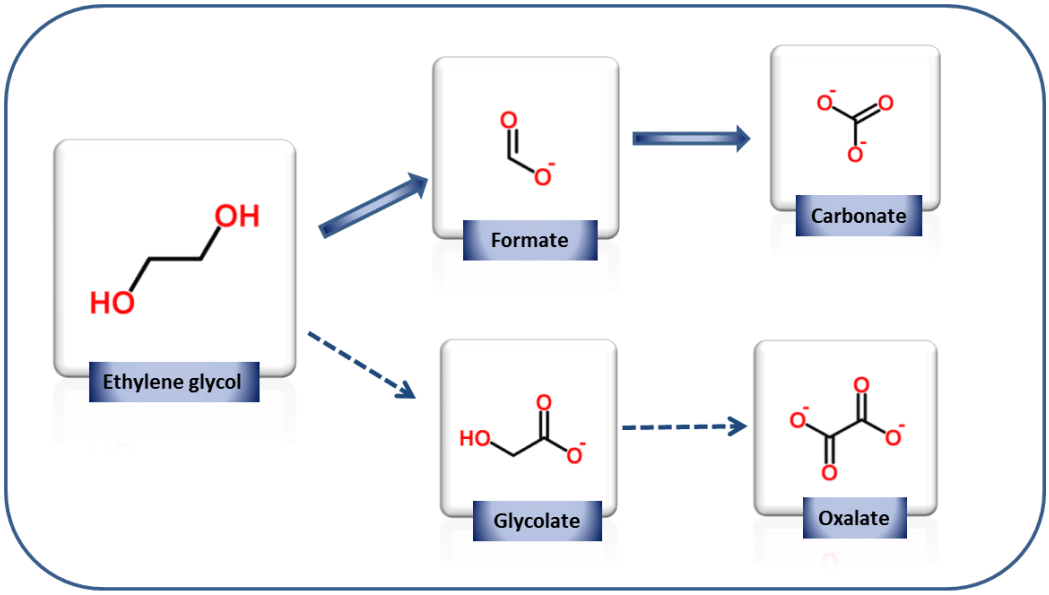

Scheme 11.1: Suggested pathway for the electro oxidation of EG on FeCo@Fe@Pd/CNT-OH. Complete arrows: Favourable and main oxidation pathway, Broken arrows: Less favourable and minor oxidation pathway.

The electrocatalytic oxidation of Glycerol on the other hand gave a greater number of products as outlined earlier. This further illustrates the complex reaction kinetics involved in GLY catalytic oxidation. The NMR spectra of the exhaust from GLY oxidation on both FeCo@Fe@Pd/CNT-OH and Pd/CNT-OH are shown below. Fig 11.9 and 11.10 (FeCo@Fe@Pd/CNT-OH) and Fig 11.11 and Fig 11.12 (Pd/CNT-OH)

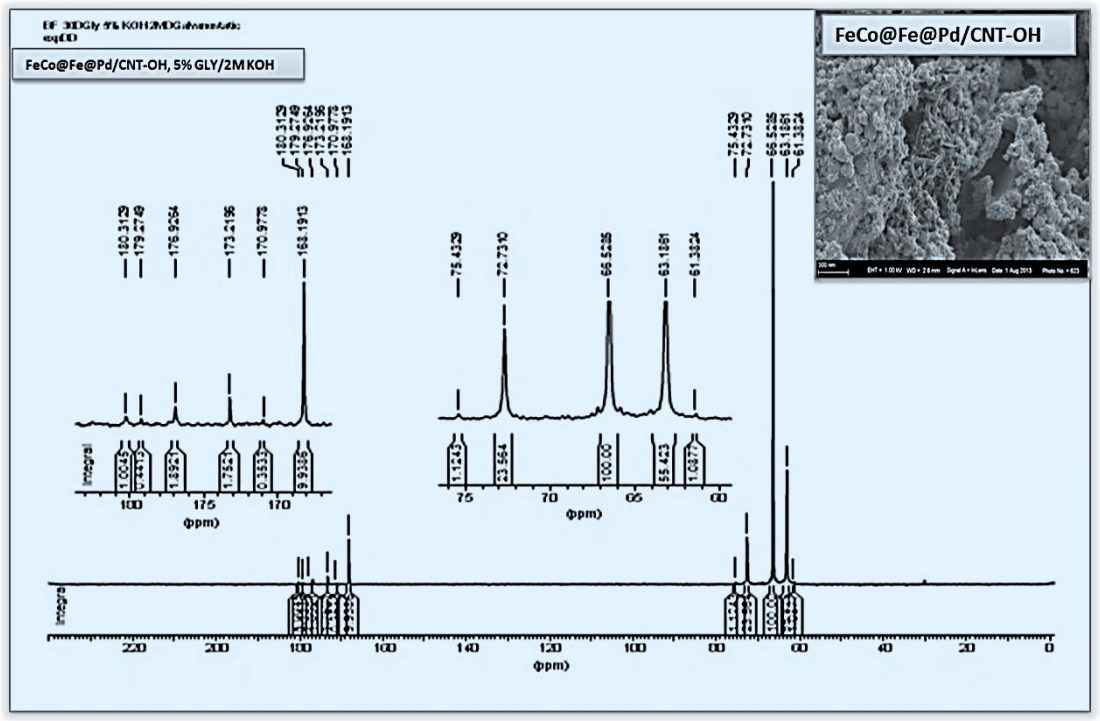

Figure 11. 9: NMR spectra of DGFC exhausts using FeCo@Fe@Pd/CNT-OH as anodes.

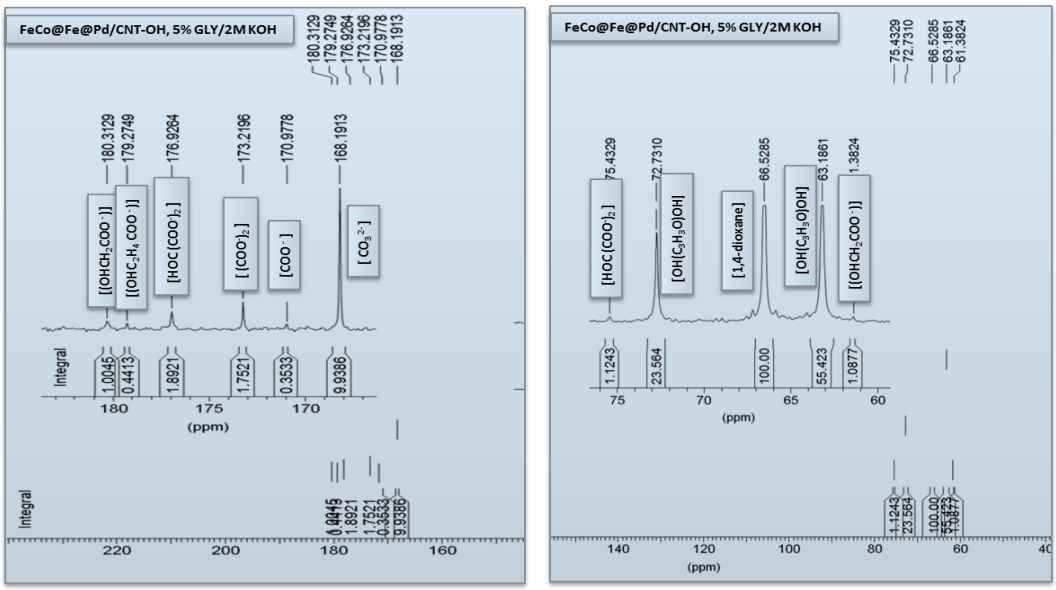

Figure 11.10: Detailed NMR spectra of main selective products peaks in Figure 11.9.

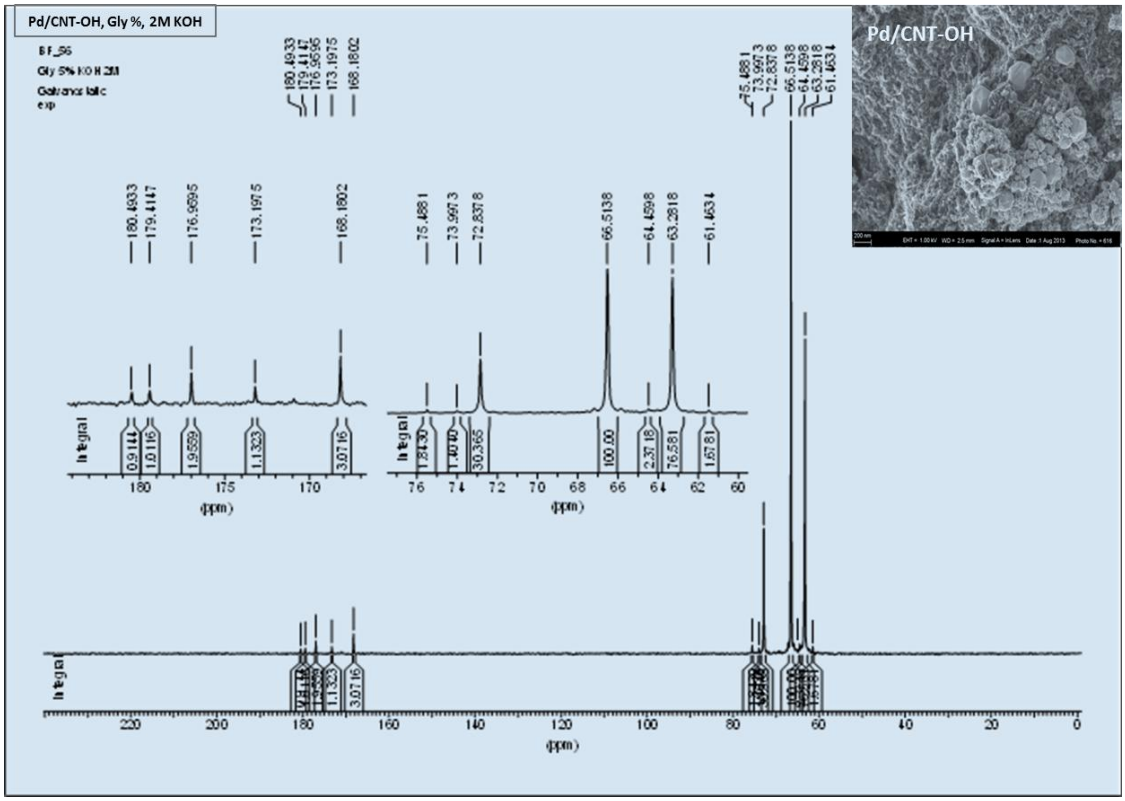

Figure 11.11: NMR spectra of DGFC exhausts using Pd/CNT-OH as anodes.

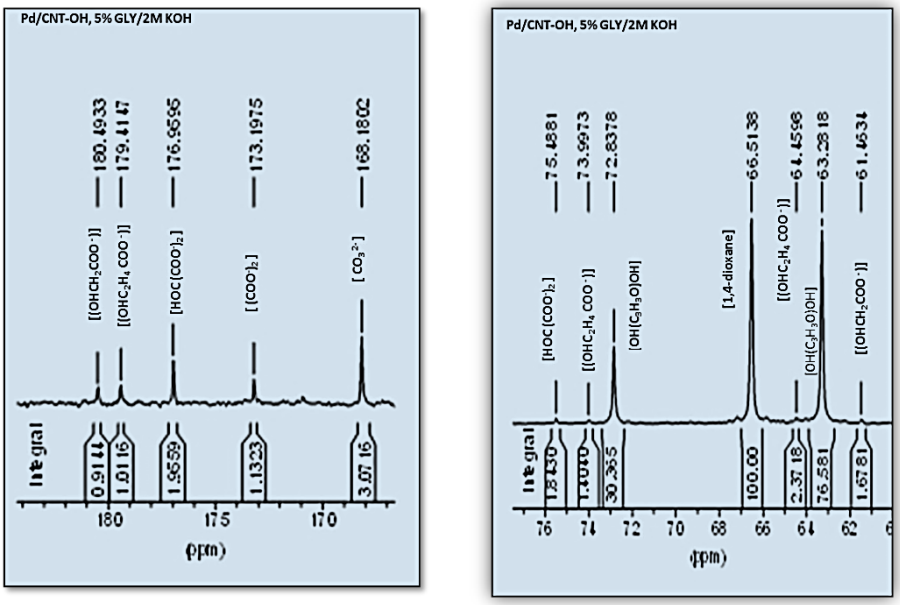

Figure 11.12: Detailed NMR spectra of main selective products peaks in Figure 11.11.

The results from the NMR exhaust analyses however show that both catalysts (but mainly FeCo@Fe@Pd/CNT-OH) were able to dissociate glycerol into fragments containing a single carbon at a high percentage under mild experimental conditions. This is evident by the production of carbonate, thus confirming the capability of the catalysts for complete electro oxidation of glycerol. This is worth noting as quite a number of Pd based catalysts reported recently for the catalytic oxidation of glycerol have not shown any selectivity towards the complete oxidation of GLY. Examples include Pd/CNT[28], PdRh/C[20], PdAu/C and PdNi[29] and PdPtBi/C[30]. According to Ferreira et al.[20], the production of carbonate as a result of GLY oxidation in alkaline medium proceeds via pathways involving H_2O instead of OH^-. This was also explained by Simoes et al[29] stating that for a complete oxidation of a primary alcohol to CO_3^{2-} in alkaline medium , water activation is needed to complete the oxidation reaction. With the involvement of water the production of CO_2 may proceed via a direct and complete glycerol oxidation as shown in the reaction below[31]:

$$CH_2OH\text{-}CHOH\text{-}CH_2OH + 3H_2O \rightarrow 3\ CO_2 + 14\ H^+ + 14e^- \qquad (11.5)$$

This proposal can also be used to explain the oxidation reaction on FeCo@Fe@Pd/ CNT-OH surface but as a result of the other side products detected in the analyses an alternative catalytic pathway is proposed for GLY oxidation on FeCo@Fe@Pd/ CNT-OH.

A major pathway involving the oxidation of glycerol to glycerate, which is further oxidised to glycolate and glycolate generates carbonates through production of formates. On the other hand, there is also evidence of another less favoured pathway (which will be a very minor one considering the high percentage of Carbonate produced). This involves the conversion of some glycerate to tartonate and then to oxalate. Oxalate has been known as a fairly stable oxidation product in alkaline medium[31].

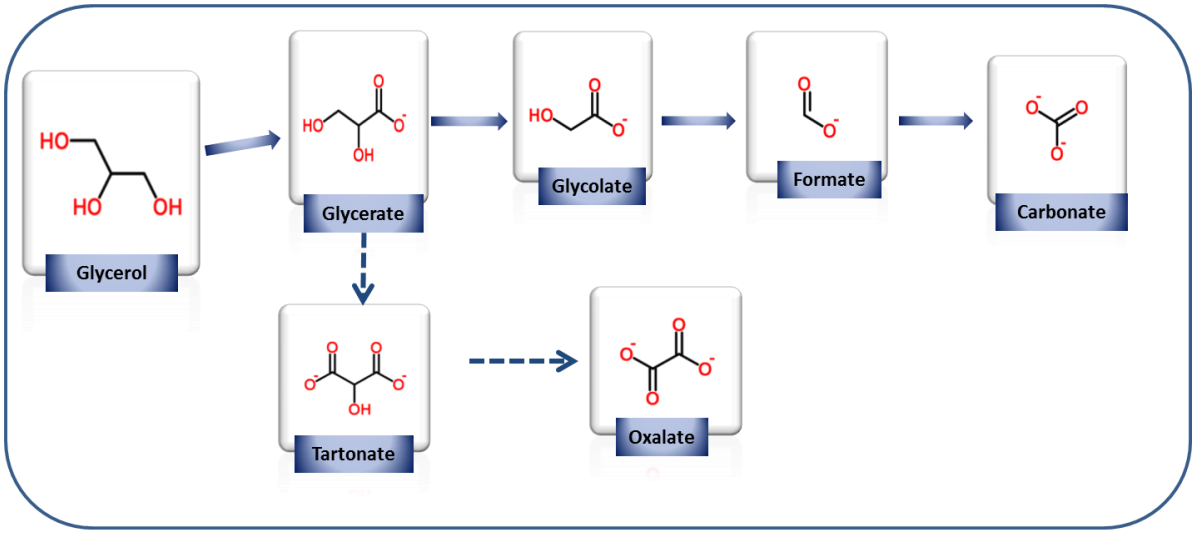

Scheme 11.2: Suggested pathway for the electro oxidation of GLY on FeCo@Fe@Pd/CNT-OH. *Complete arrows*: Favourable and main oxidation pathway, *Broken arrows*: Less favourable and minor oxidation pathway

11.4 Active DEGFC and DGFC Studies in Alkaline Medium

Performances of the active DEGFCs and DGFCs with both FeCo@Fe@Pd/CNT-OH and Pd/CNT-OH as anodes were carried out by varying the temperatures of the fuel cells at fixed oxygen and fuel flows. The tests were performed to get a preliminary insight into the power generating properties of the catalysts Fuel cell operating conditions. Figures 11.13 and 11.14 display a series of potentiodynamic and power output scans of each catalyst run in DEGFC and DGFC respectively at varying temperatures. The temperature range was from 25°C to 80°C. The conditions of the cell at each temperature were uniform in all the tests. Temperatures of Fuel / Cell / oxygen were 25/25/25; 40/40/40; 60/60/50; 80/80/50.

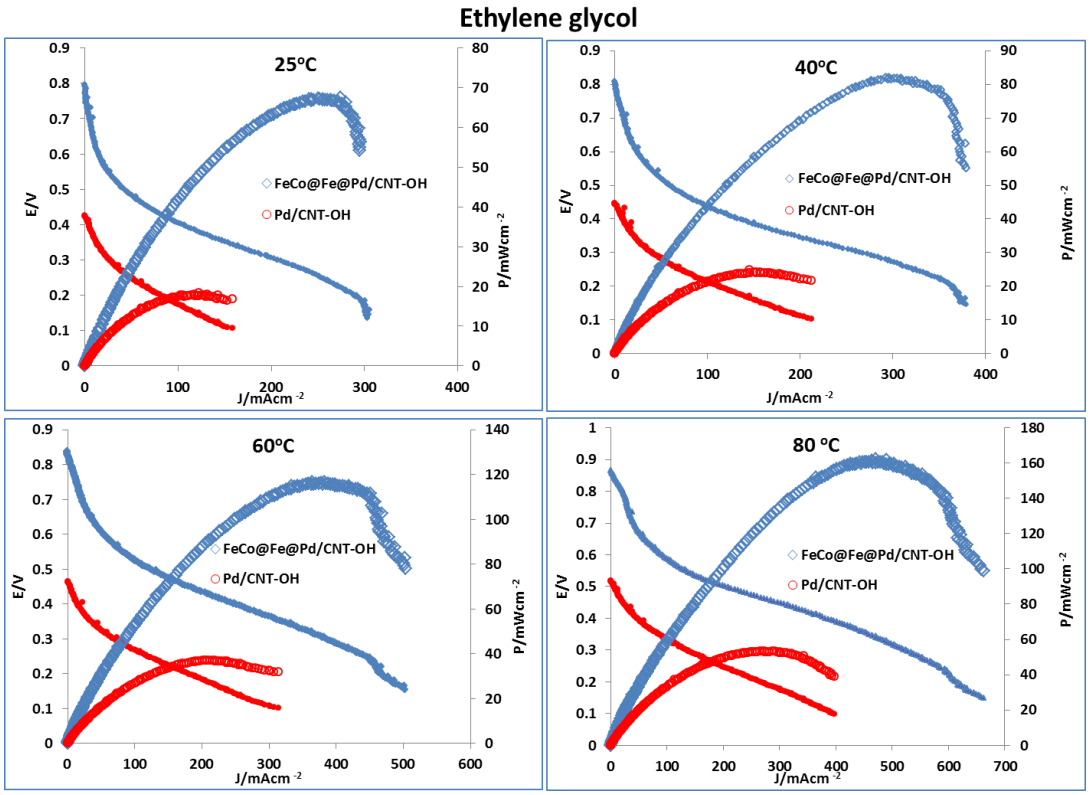

Figure 11.13: Potentiodynamic (filled symbols) and power density (empty symbols) curves for active DEGFCs with FeCo@Fe@Pd/CNT-OH, and Pd/CNT-OH anodes, fuelled with 2 M KOH and 5 wt. % EG solution at different temperatures

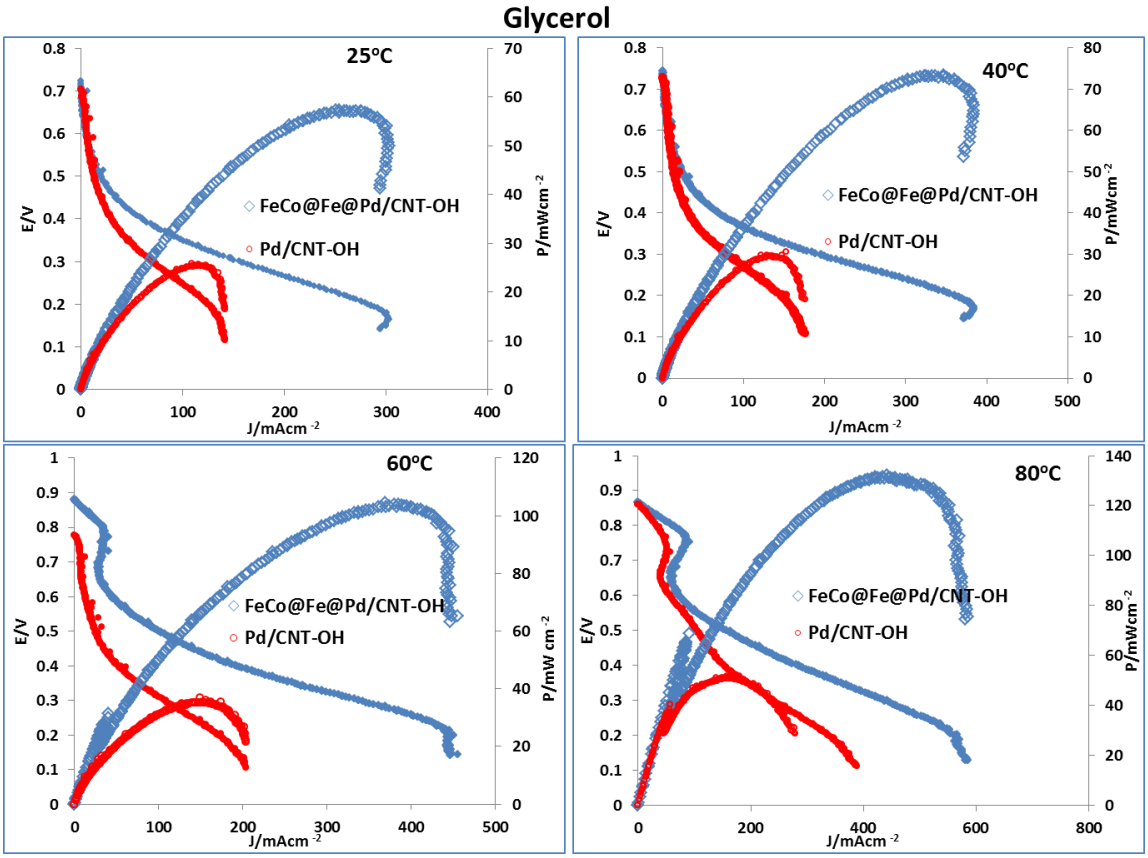

Figure 11.14: Potentiodynamic (filled symbols) and power density (empty symbols) curves for active DGFCs with FeCo@Fe@Pd/CNT-OH, and Pd/CNT-OH anodes, fuelled with 2 M KOH and 5 wt. % GLY solution at different temperatures

A 2.3 fold increment in the power density value was found for FeCo@Fe@Pd/CNT-OH catalysts in DEGFC and a 2 fold increase was obtained in DGFC with an increase in temperature from 25°C to 80°C.

Pd/ CNT-OH did not show any appreciable power density increase in both fuel cells through the temperature range studied. On the other hand Pd/CNT-OH had exhibited significant power density values in the operating parameters of DMFCs and DEFCs (discussed in previous chapter). These sets of results confirm its unsuitability as anode catalysts in polyhydric fuel cells.

11.5 Application of FeCo@Fe@Pd/CNT-OH as Anode in AEM-DAAFC- (Hexagonal-Stack DEGFC)

This section deals with a practical proof of the concepts described in the last two chapters. Already used Gas diffusion layers (Nickel foam) with FeCo@Fe@Pd/CNT-OH core shell nanocatalysts were assembled in a hexagonal DEFC or DEGFC stack to charge a cellular phone. An OCV of 3,600 mV with a resistance of 761 mΩ was obtained when fuelled with 10 % wt. EtOH/ 2M KOH while and OCV of 3,200 mV with a resistance of 636 mΩ was obtained with DEGFC 5 % wt. EG/ 2M KOH. The pictorial representation is seen in Scheme 11.3.

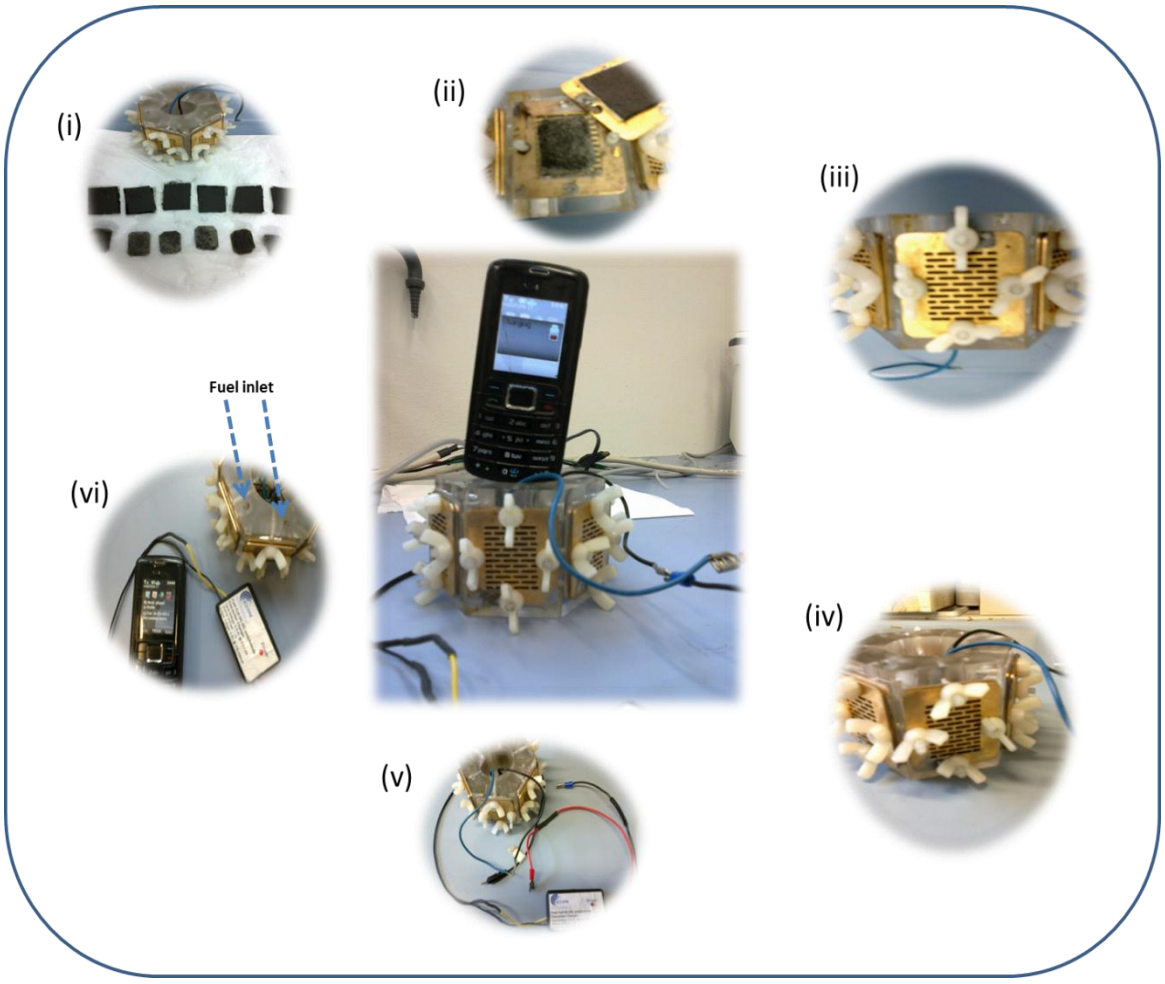

Scheme 11.3: Application of FeCo@Fe@Pd/CNT-OH as anode catalysts in a 6 AEM-DEGFC stack: (i) GDLs containing anode and cathode catalysts (ii) MEA assembly (iii) tightening up each cell in the fuel cell stack (iv)

arranging wires of fuel cell stack for connection (v) connecting wires to DC-DC converter and to the cellular phone (vi) filling each cell in the stack with 5 % wt. EG/ 2M KOH fuel. The central image depicts the charging of cellular phone using an hexagonal AEM-DEGFC stack.

11.6 Conclusion

This work looked at a study carried out using FeCo@Fe@Pd/CNT-OH and Pd/CNT-OH as anode catalysts in DEGFC and DGFC. From the NMR analysis of the exhaust products of the working passive AEM-DEGFC and AEM-DGFC operated at low temperatures used in these preliminary tests; FeCo@Fe@Pd/CNT-OH as anode catalyst revealed a high selectivity towards the complete and exhaustive oxidation of both polyhydric fuels under benign experimental conditions. Its high catalytic response can be explained as a result of the improved electronic properties of its Pd - surface (due to the incorporation of the core alloy). More work is underway in our laboratories to optimise the power generating properties of this catalyst.

11.7 References

(1) Livshits, V.; Philosoph, M.; Peled, E. *J. Power Sources* **2008**, *178*, 687–691.

(2) Chojak Halseid, M.; Jusys, Z.; Behm, R. J. *J. Electroanal. Chem.* **2010**, *644*, 103–109.

(3) Wang, L.; Meng, H.; Shen, P. K.; Bianchini, C.; Vizza, F.; Wei, Z. *Phys. Chem. Chem. Phys.* **2011**, *13*, 2667–73.

(4) Serov, A.; Kwak, C. *Appl. Catal. B Environ.* **2010**, *97*, 1–12.

(5) Miyazaki, K.; Matsumiya, T.; Abe, T.; Kurata, H.; Fukutsuka, T.; Kojima, K.; Ogumi, Z. *Electrochim. Acta* **2011**, *56*, 7610–7614.

(6) Schmidt, T. J.; Gasteiger, H. A.; Behm, R. J. *J. Electrochem. Soc.* **1999**, *146*, 1296–1304.

(7) Ishiyama, K.; Kosaka, F.; Shimada, I.; Oshima, Y.; Otomo, J. *J. Power Sources* **2013**, *225*, 141–149.

(8) Fernández, P. S.; Martins, M. E.; Camara, G. a. *Electrochim. Acta* **2012**, *66*, 180–187.

(9) Gomes, J. F.; de Paula, F. B. C.; Gasparotto, L. H. S.; Tremiliosi-Filho, G. *Electrochim. Acta* **2012**, *76*, 88–93.

(10) Jeffery, D. Z.; Camara, G. a. *Electrochem. commun.* **2010**, *12*, 1129–1132.

(11) Rousseau, S.; Coutanceau, C.; Lamy, C. *J. Power Sources* **2006**, *158*, 18–24.

(12) Sun, Z.-P.; Zhang, X.-G.; Liu, R.-L.; Liang, Y.-Y.; Li, H.-L. *J. Power Sources* **2008**, *185*, 801–806.

(13) Shen, P. K.; Xu, C. *Electrochem. commun.* **2006**, *8*, 184–188.

(14) Wang, Y.; Nguyen, T. S.; Liu, X.; Wang, X. *J. Power Sources* **2010**, *195*, 2619–2622.

(15) Pandey, R. K.; Lakshminarayanan, V. *J. Phys. Chem. C* **2009**, *113*, 21596–21603.

(16) Cherevko, S.; Xing, X.; Chung, C.-H. *Electrochim. Acta* **2011**, *56*, 5771–5775.

(17) Ksar, F.; Ramos, L.; Keita, B.; Nadjo, L.; Beaunier, P.; Remita, H. *Chem. Mater.* **2009**, *21*, 3677–3683.

(18) Bianchini, C.; Shen, P. K. *Chem. Rev.* **2009**, *109*, 4183–206.

(19) Bambagioni, V.; Bevilacqua, M.; Bianchini, C.; Filippi, J.; Marchionni, a.; Vizza, F.; Wang, L. Q.; Shen, P. K. *Fuel Cells* **2010**, *10*, 582–590.

(20) Ferreira Jr., R. S.; Janete Giz, M.; Camara, G. a. *J. Electroanal. Chem.* **2013**, *697*, 15–20.

(21) An, L.; Zhao, T. S.; Shen, S. Y.; Wu, Q. X.; Chen, R. *Int. J. Hydrogen Energy* **2010**, *35*, 4329–4335.

(22) De Lima, R. B.; Paganin, V.; Iwasita, T.; Vielstich, W. *Electrochim. Acta* **2003**, *49*, 85–91.

(23) Wang, L.; Meng, H.; Shen, P. K.; Bianchini, C.; Vizza, F.; Wei, Z. *Phys. Chem. Chem. Phys.* **2011**, *13*, 2667–73.

(24) Miyazaki, K.; Matsumiya, T.; Abe, T.; Kurata, H.; Fukutsuka, T.; Kojima, K.; Ogumi, Z. *Electrochim. Acta* **2011**, *56*, 7610–7614.

(25) Xin, L.; Zhang, Z.; Qi, J.; Chadderdon, D.; Li, W. *Appl. Catal. B Environ.* **2012**, *125*, 85–94.

(26) Chang, S. C.; Ho, Y.; Weaver, M. J. *J. Am. Chem. Soc.* **1991**, *113*, 9506–9513.

(27) Marchionni, A.; Bevilacqua, M.; Bianchini, C.; Chen, Y.-X.; Filippi, J.; Fornasiero, P.; Lavacchi, A.; Miller, H.; Wang, L.; Vizza, F. *ChemSusChem* **2013**, *6*, 518–28.

(28) Villa, a.; Plebani, M.; Schiavoni, M.; Milone, C.; Piperopoulos, E.; Galvagno, S.; Prati, L. *Catal. Today* **2012**, *186*, 76–82.

(29) Simões, M.; Baranton, S.; Coutanceau, C. *Appl. Catal. B Environ.* **2010**, *93*, 354–362.

(30) Simões, M.; Baranton, S.; Coutanceau, C. *Appl. Catal. B Environ.* **2011**, *110*, 40–49.

(31) Zhang, Z.; Xin, L.; Li, W. *Appl. Catal. B Environ.* **2012**, *119-120*, 40–48.

Chapter 12*

NANOSTRUCTURED PHTHALOCYANINES AS ELECTROCATALYSTS FOR OXYGEN REDUCTION REACTION

* The following publications resulted from part of the research work presented in this chapter and they are not referenced further.

1. O.O. Fashedemi and K.I. Ozoemena, "A facile approach to the synthesis of hydrophobic iron tetrasulfophthalocyanine (FeTSPc) nano-aggregates on multi-walled carbon nanotubes: A potential electrocatalyst for the detection of dopamine" *Sens. Actuators: B. Chem.* **2011**, 160, 7-14.

2. O.O. Fashedemi and K.I. Ozoemena "Non noble Iron (II) tetrasulfophthalocyanine on multi walled carbon nanotubes: potential cathode catlaysts in direct alcohol alkaline fuel cell" (yet to be published manuscript).

12.1 Introduction

In the emerging fuel cell technology, the research toward non noble metal-based catalysts for hydrogen oxidation and oxygen reduction is a field of intense research[1,2]. Oxygen reduction reaction which takes place in the cathode provides maximum energy when the oxygen molecule is completely reduced to water via four electrons. Though the reaction appears simple, it is in fact rather complex (as explained in previous chapters) proceeding via high - energy intermediates which slow down the overall reaction. On most electrode materials, it stops after the transfer of two electrons to give hydrogen peroxide. If the reaction proceeds via two electrons, it provides nearly half of the energy given by four electron reduction[3,4]. Thus, the research in this domain is still on-going. Platinum which is currently the most effective electrocatalyst for the ORR is obtained at high cost and its scarcity prevents its wide application in fuel cells in day to day application.

Transition metal macrocycles and their various transition metal (TS)derivatives have been used as electrocatalysts for oxygen reduction[5]. Some of these TS derivatives include iron phthalocyanines (FePc) species. Iron (II) tetrasulfophthalocyanine (FeTSPc, Figure 12.1) belongs to the N4-macrocyclic metal compounds related to the metalloporphyrins. Like every other sulfonate metallophthalocyanine (MTSPc) complex, FeTSPc is a highly water-soluble molecule and very well recognized for its unique physico-chemical properties and wide range of applications ranging from catalysis[6,7] to sensing[8,9] and photo catalysis[10–12]. The major handicap to the use of FeTSPc film in heterogeneous electrocatalysis is its high water-solubility[9,13,14]. The ease with which MTSPc complexes are washed away from electrodes during electrochemical studies has long been a major setback and has limited their fundamental studies and potential applications to heterogeneous electrocatalysis in aqueous environment. For example, the main problems usually associated with physical

anchorage (such as drop-casting method) of FeTSPc films onto an electrode are poor stability as well as the difficulty in controlling the amount of film deposited. To curb the solubility problems, researchers have resorted to several techniques. For example the layer-by-layer self-assembly electrode modification strategy involving the use of polycationic and/or highly branched polymeric complexes such as polyamidoamine[15] dendrimers[16], chitosan, and dimethylaminoethanethiol/carbon nanotubes[17]. These techniques are often laborious, make use of expensive and/or toxic reagents, and sometimes give semi-stable films. There is need therefore to explore means of making MTSPc complexes hydrophobic without compromising on their electrocatalytic activity towards the detection of analytes in aqueous conditions. Importantly, an ideal synthetic technique for such hydrophobic MTSPc should be easy to perform, produce large-surface area FeTSPc (nanostructures) for enhanced catalytic activity, and offer the possibility of mass production.

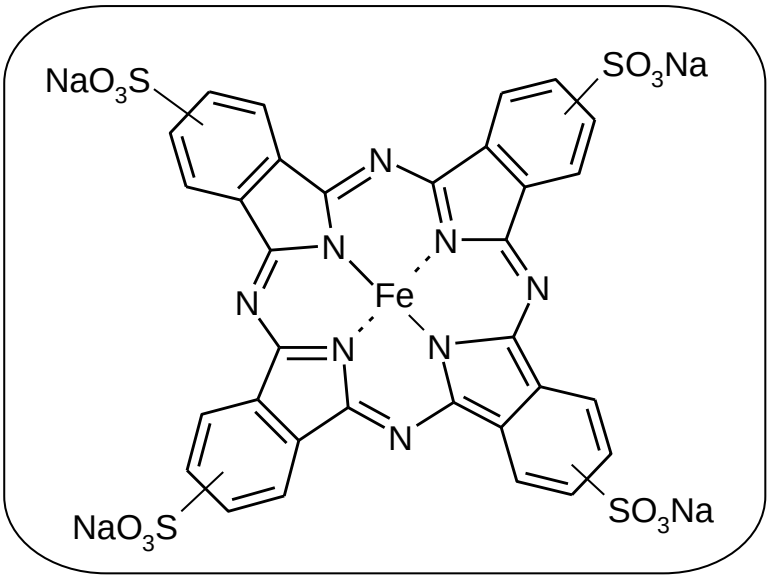

Figure 12.1: Molecular structures of sodium salt of iron (II) tetrasulphophthalocyanine (FeTSPc)

The synthesis of hydrophobic MTSPc complexes is hugely limited[18] and neither their structural morphology nor their electrochemical properties

have been reported. FePc species have been actively researched as promising alternatives to Pt. But the poor electron conductivity of FePc does not facilitate electron transfer in ORR process. Several authors have fixed FePc on various carbon materials to solve these problems[19–22]. Carbon nanotubes are one of the target carbon materials. The crystalline nature of carbon nanotubes (CNTs) makes them act as a good conductive substrate and hence their high performance when used as supports. They enlarge the surface area, raise the strength and increase the conductivity of composites[23,24]. Functionalising CNTS with hydrophilic groups like carboxylic (COOH)[25,26], and sulfonic groups (SO_3H)[27–29] enhances their dispersibility in aqueous media mainly because of the easy access and interaction with protons.

In this work, a study of the first synthesis of hydrophobic nanostructured FeTSPc complex assisted by hexadecyltrimethylammonium bromide (CTAB) was done. The nanostructured FeTSPc (nanoFeTSPc) were also integrated on both sulfonic and hydroxyl functionalised MWCNTs (s-MWCNT and o-MWCNT) respectively. We report for the first time a study on the ORR activity in alkaline medium and the anti –crossover effect, namely, the selectivity for ORR of the nanoFeTSPc composites. Some very interesting results were obtained as it was discovered that the ORR onset potential of *o*MWCNT-nanoFeTSPC with a 10 % active material loading was almost the same as that on commercial Pt/C (80 wt% Pt on Vulcan XC-72, Alfar Aesar) while the ORR current response was higher. *o*MWCNT-nanoFeTSPC also exhibited excellent tolerance to the cross over effect with practically no difference in its ORR current with the coexistence of methanol and oxygen in alkaline solution. The results obtained were definitely better than using Pt/C as cathode catalyst under the same experimental conditions.

12.2 Physical Characterisation of nanoFeTSPc

All synthesised materials were characterised to ascertain their true structures after modification. For example, unlike the highly hydrophilic FeTSPc, the nanoFeTSPc complex is hydrophobic, soluble in organic solvents such as the DMF, DMSO and ethanol. Thus, the preparation protocol adopted in this work led to changes in the physico-chemical properties of the nanoFeTSPc complex

12.2.1 EDX

EDX spot analysis (Fig 12.2) provided semi quantitative information on elemental concentrations of the FeTSPc and nano FeTSPc at different locations in the film. For example, a typical atomic percent gave the following result for nanoFeTSPc: S 24.95±0.23%, Fe 5.85±0.22%, Br 6.78±0.11%, giving the expected atomic ratio of Fe:4S. The result also suggests a trace amount of Br; that at least 3 of the 4 sulfonate groups of the FeTSPc molecule are associated with the ammonium head groups of the CTAB via coordinate covalency.

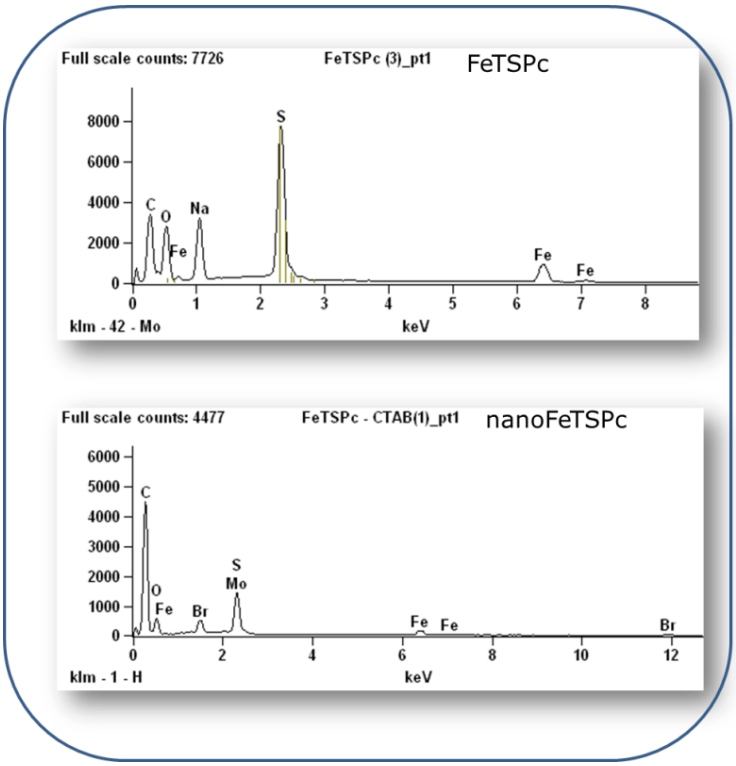

Figure 12. 2: EDX images of FeTSPc and nano FeTSPc.

12.2.2 UV Spectroscopy

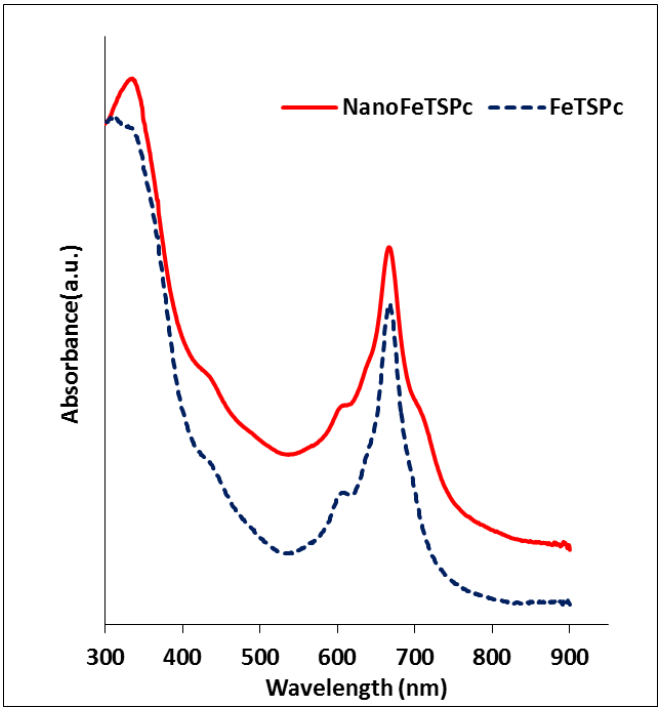

Figure 12. 3: UV spectra of FeTSPc and nanoFeTSPc in DMF solution.

Fig. 12.3 shows the comparative UV–visible spectra for the FeTSPc, nanoFeTSPc, in DMF. The observed spectra exhibited the characteristic Q-band typical of monomeric species of metallophthalocyanine complexes. There is no detectable difference between the spectra of the FeTSPc and nanoFeTSPc, which is an indication that the synthetic protocol adopted here did not impact on the structural properties of the pristine FeTSPc. The FeTSPc and nanoFeTSPc show the characteristic absorption bands at 350 nm (B-band) and 685 nm (Q-band). This corresponds to the electronic absorption of FeTSPc monomeric species. The shoulder at about 616 nm and 618 nm correspond to the electronic absorption of dimeric species of FeTSPc[30,31] bridged by O_2 molecules. The weak band at about 430 nm is typical of a low-spin six-coordinate Fe(II)Pc species and are usually associated with metal-to-ligand charge transfers (MLCT) for FeTSPc and nanoFeTSPc respectively[32,33]. Hence its presence is a good indication that the central metal ion remains in the +2 oxidation state.

12.2.3 IR Spectroscopy

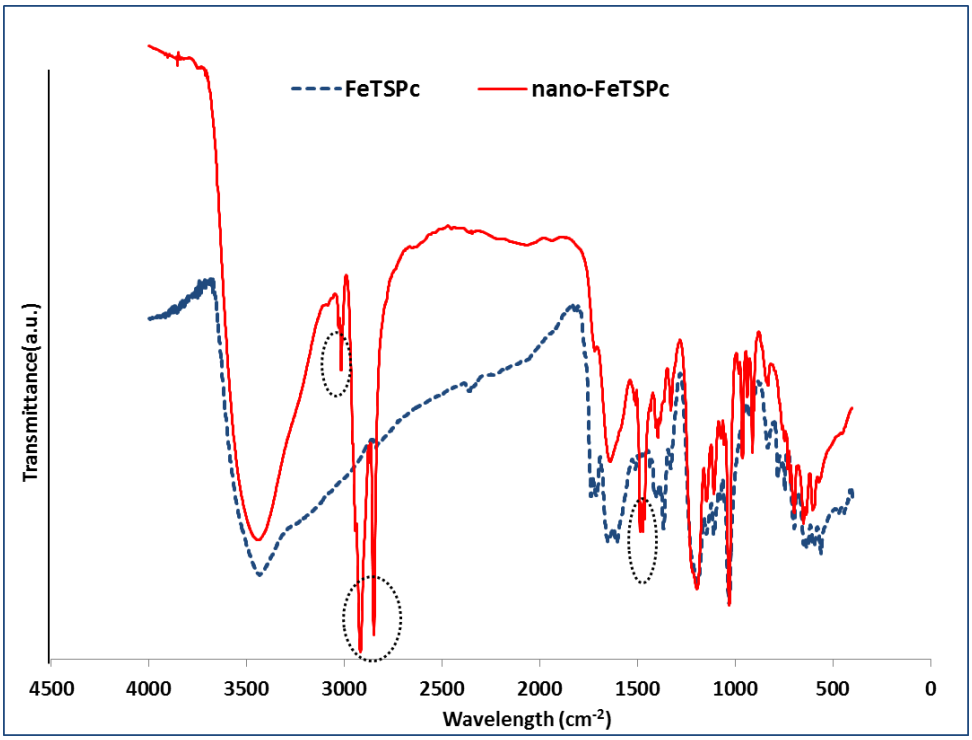

Figure 12.4: IR spectra of FeTSPc and nanoFeTSPc

The IR spectra (Fig 12.4) show the typical bands corresponding to FeTSPc. Both FeTSPc and nanoFeTSPc KBR pellets displayed the main absorption bands for Fe-Pc at about 1000 cm^{-1}, this is normally seen at about 994 cm^{-1}. The strong absorption peak at 1107 cm^{-1} is characteristic of the symmetric and anti-symmetric stretching motions assigned to the O=S=O group coupled with the absorption band at 1190 cm^{-1}. The peaks observed at 701 cm^{-1},843, cm^{-1} 1171 cm^{-1}, are attributed to the in plane, out plane and stretching motions of the aromatic C-H groups. The typical stretching bands of aromatic C=C groups can be seen at 1637 cm^{-1} [18,34,35]. All of these also confirm that the intrinsic property of FeTSPc has not been destroyed as a result of the modification made in the synthesis of nanoFeTSPc, thus corroborating the observations from the UV spectra. However, nanoFeTSPc also displays some other additional bands (encircled in broken lines). The intense peak of the C-H group of alkyl ammonium chains can be seen at 2919 cm^{-1} [18]; this further confirms that

the ionic exchange took place. One also observes the presence of intense peaks around 3100 cm^{-1} and 995 cm^{-1} which corresponds to the presence of olefin groups, peaks of methyl and methylene groups are also seen at 2980-2850 cm^{-1} and 1480 cm^{-1} [35].

12.2.4 FESEM and TEM

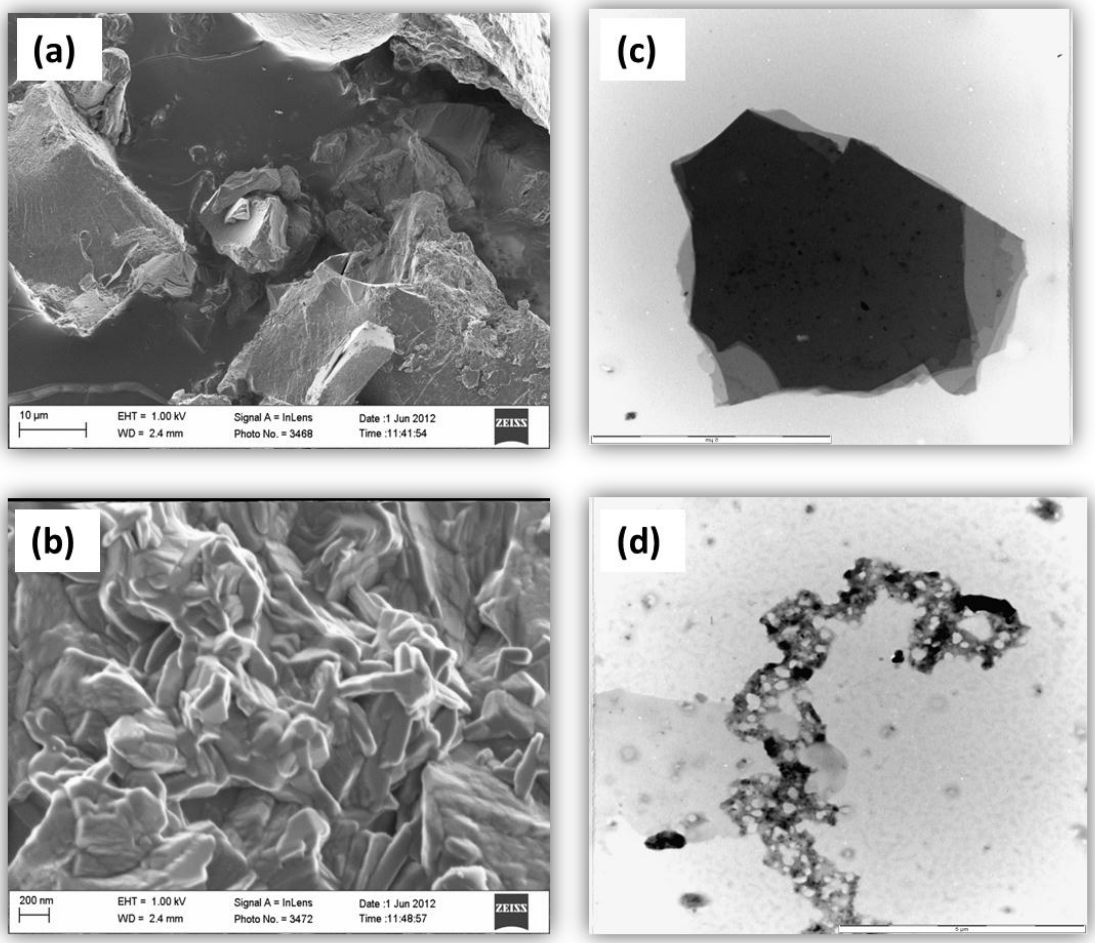

Figure 12.5: FESEM images of (a) FeTSPc, (b) nanoFeTSPc, and their corresponding TEM images (c) and (d)

The amorphous structure of nanoFeTSPc can be clearly seen against the crystalline morphology of FeTSPc crystals in Figures 12.5 (a) and (b). The reduced particle size of nanoFeTSPc in comparison to FeTSPc is also obvious. The magnification of the FESEM images for FeTSPc crystals are in the 'micron range' while Nano FeTSPc can already be obtained in the

'nano' range, which befits its structure and name. The TEM images Figures 12.5 (c) and (d) confirm the observations made in the FESEM images.

12.3 Physical Characterisation of MWCNT-nanoFeTSPc

12.3.1 FESEM and TEM

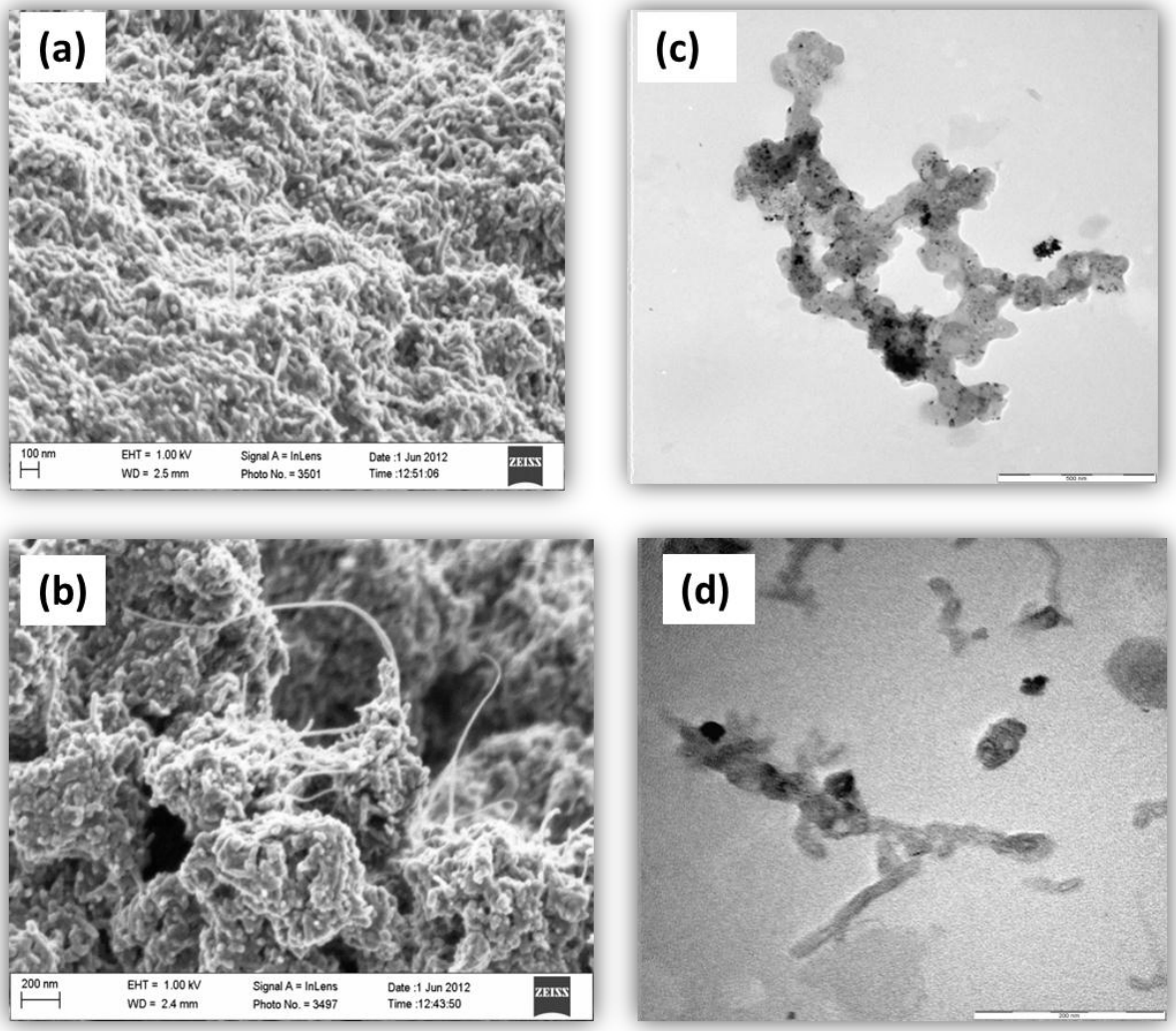

Figure 12.6: FESEM images of (a) *o*MWCNT-nanoFeTSPc and (b) *s*MWCNT-nanoFeTSPc, and their corresponding TEM images (c) and (d)

The FESEM images (Fig 12.6) do not reveal much about the components incorporated on the functionalised nanotubes in both composites. This may be due to the type of carbon nanotubes used. However the

aggregate nature of *s*MWCNT-nanoFeTSPc can be clearly observed as the components are in form of clumps. TEM images further show the evenly spread nanoFeTsPc composites on the o-MWCNTs as opposed to the uneven formation of the composites on s-MWCNTs.

12.3.2 Raman Spectroscopy

Raman scattering has been used as a probe of disorder in the carbon skeleton of sp^2 and sp^3 carbon materials[36]. It can also provide in situ surface information for investigating the structure and interaction between carbon nanotubes and the loaded materials[37]. Figure 12.7 shows the Raman spectra of pristine MWCNT, o-MWCNT, s-MWCNT, nanoFeTSPc-*o*MWCNT and nanoFeTSPc-*s*MWCNT.

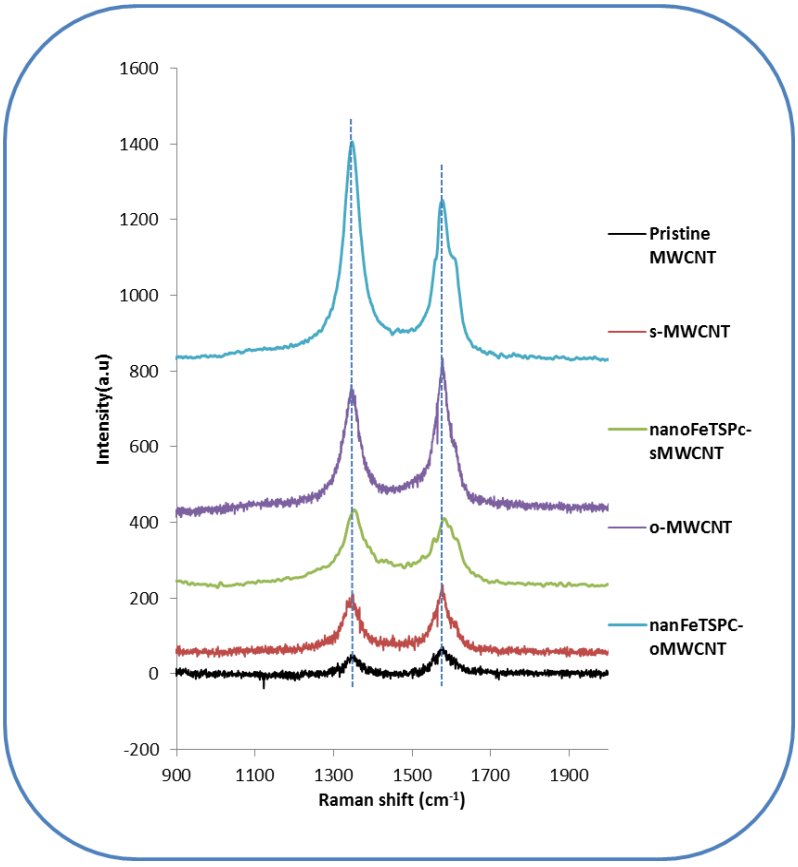

Figure 12.7: Raman spectra of pristine MWCNT, o-MWCNT, s-MWCNT, nanoFeTSPc-*o*MWCNT and nanoFeTSPc-*s*MWCNT

The tangential G- band and D- band of carbon nanotubes were observed in both the functionalised MWCNTs and the MWCNT composites. The D-band reflects the disorder in the carbon nanotubes, thus increase in the intensity of the D-band is an indication of the rise in the defect density (amount of defects) in the CNTs or a decrease in the structural order of the carbon nanotubes bundles[38]. These defects can be brought about as a result of added functional groups, missing carbon atoms in the walls of the carbon nanotubes or the inhomogeneous decoration of the tube wall by functional groups[36].

From the spectra above, the D bands appear at ≈ 1344 cm^{-1} for all of the groups studied (except that of nanoFeTSPc-*s*MWCNT, which appears at ≈ 1360 cm^{-1}). There is an increase in the intensities of the two functionalized MWCNT bands compared with the raw pristine MWCNT, though the D-band intensity of the o-MWCNT is more intense than that of s-MWCNT. Thus we can rightly deduce that there are more anionic surface groups anchored on the walls of the o-MWCNT than s-MWCNTs. The same trend is observed in the composites .The intensities of the D-band peaks can be attributed to the presence of more surface groups, thus, causing more defects on the walls of the MWCNTs. The D-band with the highest intensity among the groups studied is that of nanoFeTSPc-*o*MWCNT. This may imply a higher degree of attachment of nanoFeTSPc to o-MWCNT causing a further increase of the defects on the o-MWCNTs. The opposite can be implied for the nanoFeTSPc-*s*MWCNT.

G-band is the graphite band and appears at ≈ 1577 cm^{-1} in all the spectra except that of nanoFeTSPc-*s*MWCNT, which appears at ≈ 1578 cm^{-1}. There is an up shift of 1cm^{-1} in the G-band of nanoFeTSPc-*s*MWCNT compared to its parent s-MWCNT. An up shift in the G-band after functionalising is the result of electron transfer from the carbon nanotubes bundle to the acceptor molecules bonded to it[39,40],.which in

this case are nanoFeTSPc aggregates. This charge transfer may be the cause of the formation of adduct generally observed between sulfonate groups of Phthalocyanines in the presence of hydroxyl groups and the carbonyls on functionalised carbon nanotubes. This tends to affect their reactivity in a less favourable way. On the other hand, there is no noticeable change in positions of the G-bands of both nanoFeTSPc-*o*MWCNT and o-MWCNT which means the electronic characteristics of both compounds are almost intact after doping.

The degree of functionalization of the MWCNT walls can also be quantified using the D to G band intensity ratio [I_D/I_G]. An increase in the [I_D/I_G].indicates an increase in number of defects[41]. NanoFeTSPc-*o*MWCNT has the highest ratio of 1.37, while nanoFeTSPc-sMWCNT has a value of 1.12. o-MWCNT and s-MWCNT have 0.84 and 0.83 values of [I_D/I_G].ratios respectively. Both functionalized MWCNTs appear to have the same degree of functionalization but the attachment of nanoFeTSPc has somewhat resulted in a lesser alteration to s-MWCNTs. As one should expect a further increase of roughness of s-MWCNTs as a result of doping with nanoFeTSPc, the lower value obtained may confirm the supposition of other reactions of nanoFeTSPc with s-MWCNTs other than anchorage.

12.4 Comparative Cyclic Voltammetry Experiments

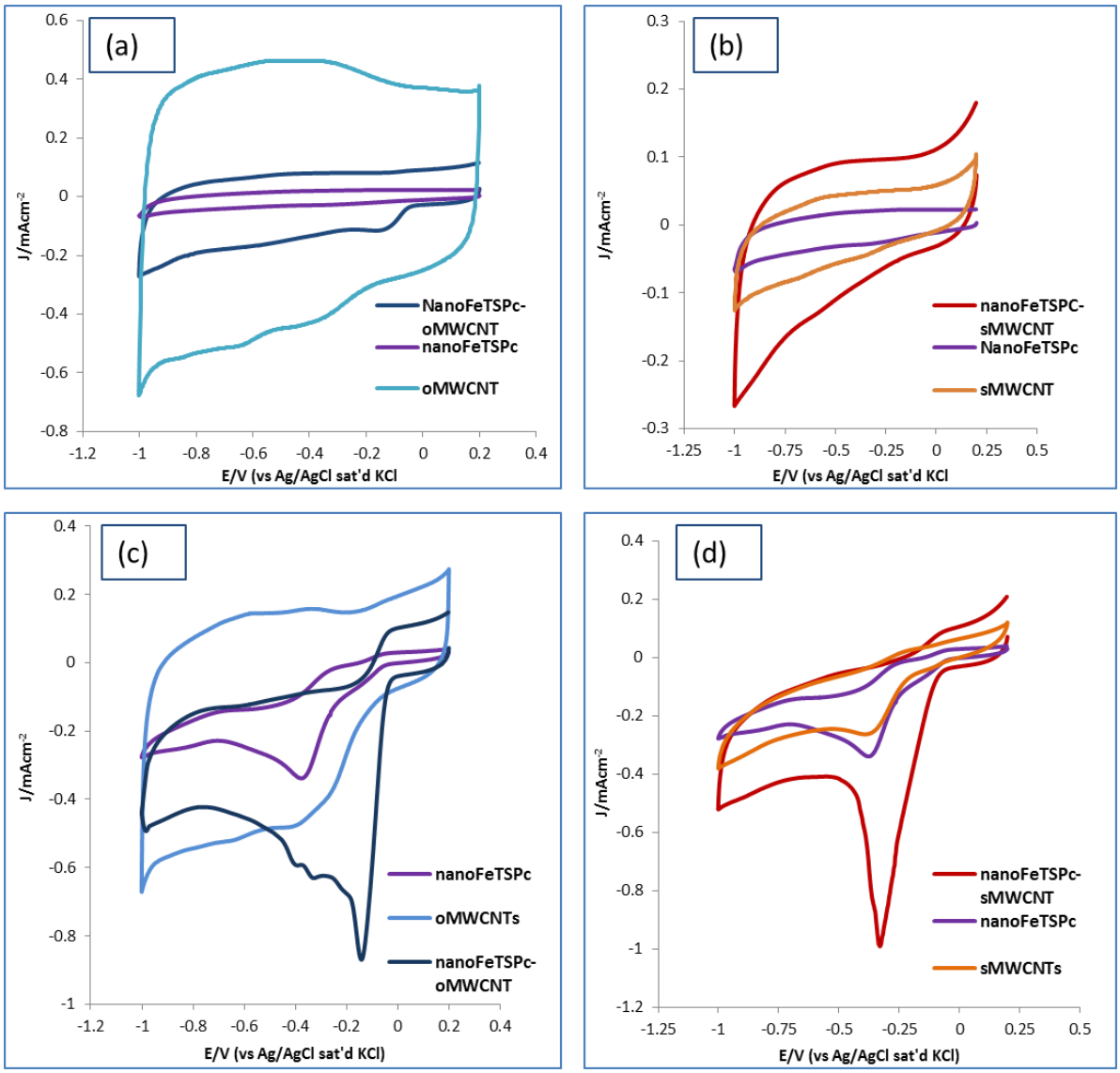

Figure 12. 8: Comparative CVs of *o*MWCNTs, nanoFeTSPc, nanoFeTSPc-*o*MWCNTs (a) and *s*MWCNTs, nanoFeTSPc, nanoFeTSPc-*s*MWCNTs (b) at a scan rate of 25 mV^{-1} in 0.1 M KOH solution saturated N_2. Figures (c) and (d) display the CVs of the same sets of catalysts in saturated O_2, 0.1 M KOH solution.

Figures 12.8 (a) and (b) show the CV voltammograms of the catalysts studied in N_2 saturated 0.1 M KOH at a speed of 25 mVs^{-1}. The peaks exhibited are attributed to the intrinsic redox peaks of, nanoFeTSPc, *o*MWCNT, nanoFeTSPc-oMWCNT, *s*MWCNT and nanoFeTSPc-*s*MWCNT.

After the solution was saturated with O_2 (Figs 12.8 c and d) the ORR peaks appeared on the electrodes modified with nanoFeTSPc, *s*MWCNT, nanoFeTSPc-*o*MWCNT, and nanoFeTSPc-*s*MWCNT with the exception of *o*MWCNT which still retained its broad capacitive peak. These pair of broad redox peaks have been observed by other authors[42,43]. They are attributed to the presence of oxygenated species at the ends of the MWCNTs and oxygen–containing surface functional groups such as quinolic groups and carbonyls[44–46]. These electro active groups are usually formed during the acid purification of MWCNTs.

The ORR performances of the composites are obviously better than those of their corresponding substrates alone. Though ORR reduction begins at an earlier potential in *o*MWCNT, it also exhibits a higher reducing current compared to its sulfonate counterpart *s*MWCNT. NanoFeTSPc-*o*MWCNT displays an intense reduction peak at -0.14 V and two other less prominent peaks at -0.29 V and -0.36 V. Several authors[3,4,47] have proved that the onset potential for the catalytic reduction of O_2 is very close to the Fe(III)/Fe(II) transition for Iron phthalocyanines complexes. In other words the reduction peak at 0.14 V can be attributed to the Fe (III)/Fe (II) redox couple. The other two peaks at -0.29 V and -0.36 V are due to the Hydroquinone-quinone (HQ-Q) redox reaction and reduction of the other surface oxygenated species found on the *o*MWCNT surface[44]. The ORR onset potential (E_{onset}) is more positive at nanoFeTSPc-*o*MWCNT > nanoFeTSPc > nanoFeTSPc-sMWCNT as seen in Figures 12.8 (c) and (d). Though nanoFeTSPc-*s*MWCNT displays the highest reduction current response (J_{ORR}) out of the three active composites, (1.00 $mAcm^{-2}$, 0.85 $mAcm^{-2}$, 0.33 $mAcm^{-2}$ for nanoFeTSPc-*s*MWCNT nanoFeTSPc-*o*MWCNT and nanoFeTSPc respectively), the potential value at which reduction occurs (E_{ORR}) is quite high, which indicates a sluggishness in its ORR process. For oxygen reduction on active catalysts surface reduction potential voltages as close as possible to the onset reduction potential is most desirable.

Based on these observations a comparison of the ORR activities of nanoFeTSPc-*o*MWCNT and nanoFeTSPc-*s*MWCNT was made with Pt/C. This is displayed in Fig 12.9.

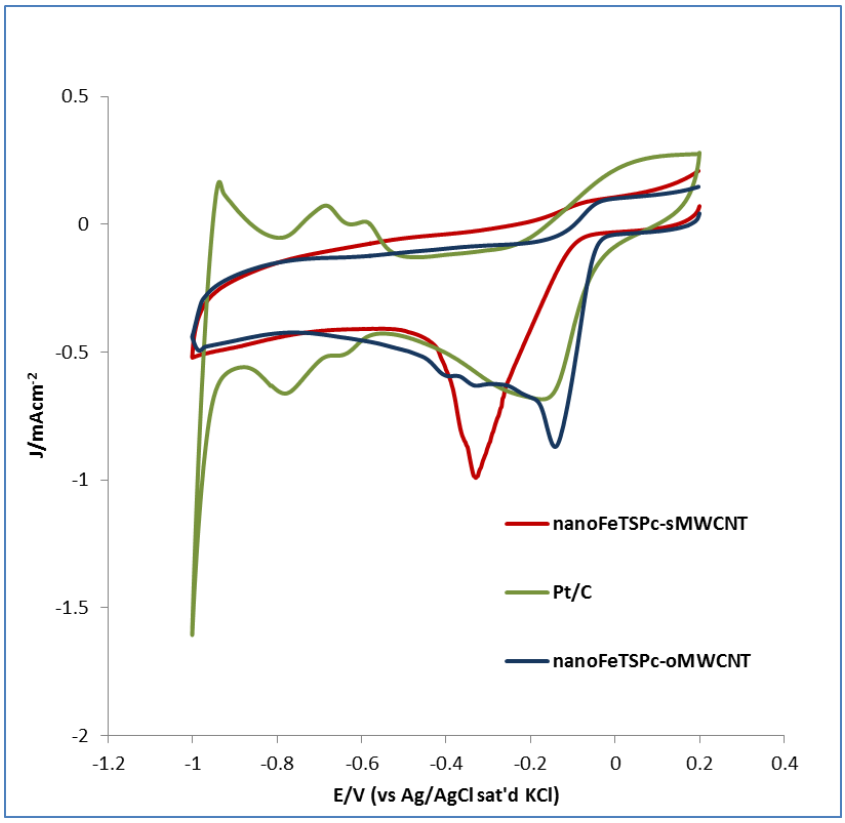

Figure 12.9: Comparative CVs of *o*MWCNTs, nanoFeTSPc, nanoFeTSPc-*s*MWCNTs and Pt/C at a scan rate of 25 mVs^{-1} in 0.1 M KOH solution saturated with O_2

Although the ORR onset potential on Pt/C is about at 40 mV earlier than that on nanoFeTSPc-*o*MWCNT, the MWCNT composites both produced higher oxygen reduction current responses than Pt/C. Table 12.1 gives a summary of the activities of the catalysts.

Table 12.1: Summary of the ORR activities of all the catalysts studied at a scan rate of 25mV^{-1} in 0.1 M KOH solution saturated with O_2

Catalysts	E_{onset}/ V	E_{ORR}/ V	J_{ORR} /mAcm^{-2}
nanoFeTSPc-*o*MWCNT	0.002	-0.141	0.85
nanoFeTSPc-*s*MWCNT	-0.047	-0.327	1.00
Pt/C	0.043	-0.161	0.72
NanoFeTSPc	-0.049	-0.376	0.34
***o*MWCNT**	-0.047	-0.410	0.48
***s*MWCNT**	-0.098	-0.362	0.26

12.5 ORR

In order to gain better insight into the ORR electrochemical procedure of nanoFeTSPc-*o*MWCNT and nanoFeTSPc-*s*MWCNT, the RDE -Hydrodynamic voltammograms -for ORR was performed at different rotation rates. Pt/C was also used for comparative studies. Figs 12.10 show the RDE plots for nanoFeTSPc-*o*MWCNT (a), nanoFeTSPc-*s*MWCNT (b), and Pt/C (c) at various rotation rates. These polarization curves display a steady increase in limiting current as the rotation speed increases and there is a clear pre-wave present at low over potentials for nanoFeTSPc-*o*MWCNT and Pt/C. The second reduction wave potential for both catalysts starts at about -0.2 V. This has been observed with FePc on MWCNT[48]. Also, while the polarization curves for nanoFeTSPc-*o*MWCNT gave very steady plateaux in the high potential range for all the rotation speeds studied, nanoFeTSPc-

*s*MWCNT and Pt/C did not display such features; instead one observes a more inclined plateau as rotation speed increases.

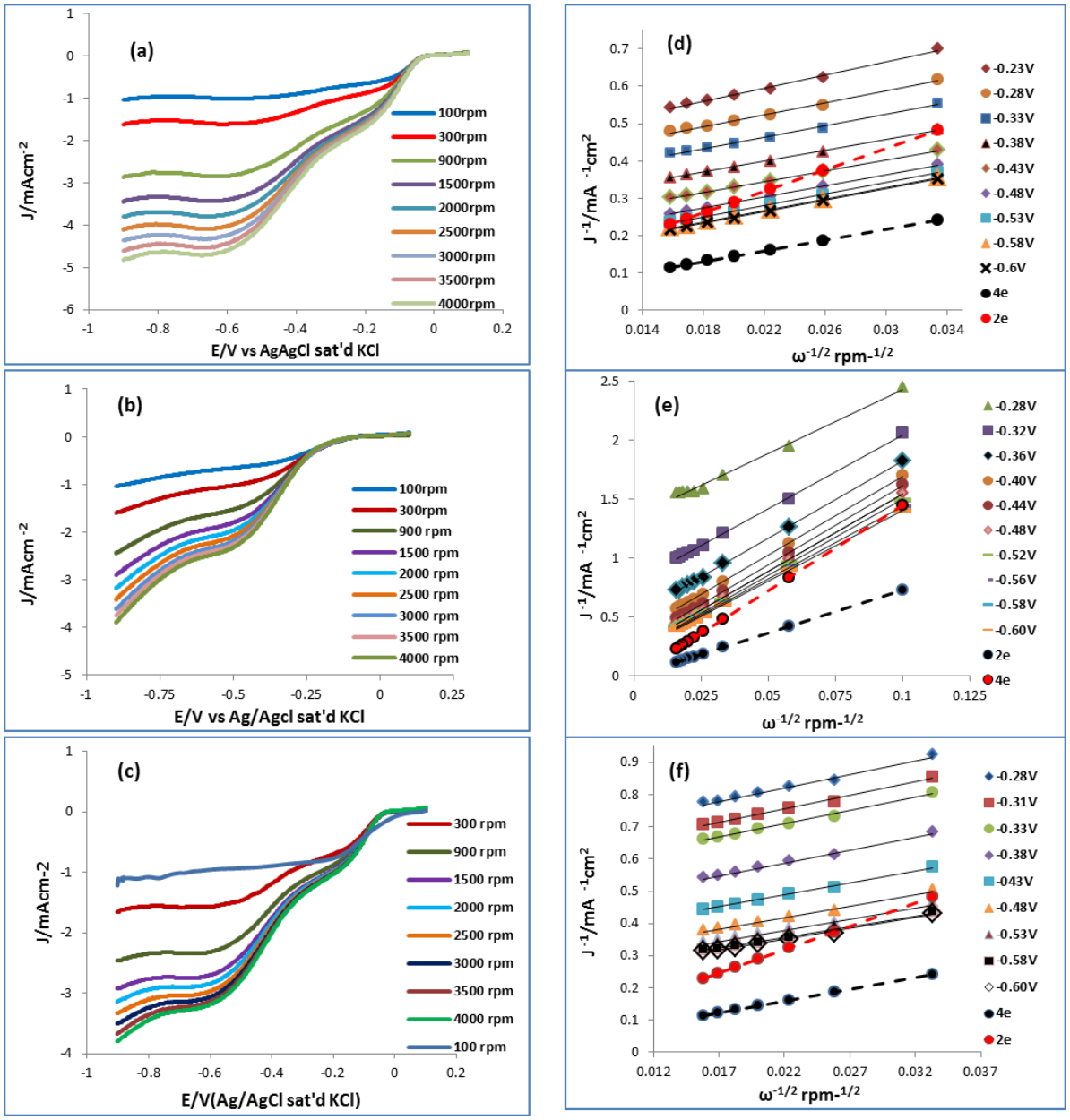

Figure 12.10: RDE plots of nanoFeTSPc-*o*MWCNT (a), nanoFeTSPc-*s*MWCNT (b), and Pt/C (c) and their equivalent Koutecky –Levich plots in (d) nanoFeTSPc-*o*MWCNT, (e) nanoFeTSPc-*s*MWCNT and (f) Pt/C

Looking at the RDE plots in Figs 12.10 a, b, and c , the onset ORR potential for nanoFeTSPc-*o*MWCNT started at about -0.02 V while that of nanoFeTSPc-*s*MWCNT began at about -0.07 V, Pt/C displays the same ORR onset voltage as that of nanoFeTSPc-*o*MWCNT. But the limiting current densities for nanoFeTSPc-*o*MWCNT were higher than the other two under the same rotation rates. It was found to be ≈1.2 times as that of Pt/C. The limiting current densities of nanoFeTSPc-*s*MWCNT are about the same as that of Pt/C.

The number of electron transferred per oxygen molecule involved in the ORR process was evaluated using the Koutecky-Levich equation (K-L) (eqn 12.1)[49,50].

$$\frac{1}{j} = \frac{1}{jk} + \frac{1}{jl} \qquad (12.1)$$

The kinetic contribution to the current is given by $J_k = nFK_f C_o$ and the Levich equation is expressed as $J_l = 0.21\ nFAC_{O_2}D^{2/3}v^{-1/6}\omega^{1/2}$ where n is number of electrons transferred per O_2 molecule, F is the Faraday constant (96840 $Cmol^{-1}$), A is the area of the electrode (0.196 cm^{-2}), K_f is the heterogeneous rate constant, D is the diffusion coefficient of O_2 in the solution(1.95 x 10^{-5} cm^2s^{-1}), C is the concentration of O_2 in the solution (1.15 x 10^{-3} $moldm^{-3}$), v is the kinematic viscosity of the solution (8.98 x 10^{-3} cm^2s^{-1}), ω is the rotation rate (rpm). The constant 0.21 is adopted when the rotation rate is expressed in rpm. Inserting these parameters into the K-L equation gives:

$$\frac{1}{j} = \frac{1}{nFKCo\,\Gamma} + \frac{1}{0.21n\,FACoD^{\frac{2}{3}}\nu^{-\frac{1}{6}}\omega^{\frac{1}{2}}} \qquad (12.2)$$

The plot of $\frac{1}{j}$ vs $\frac{1}{\omega^{\frac{1}{2}}}$ at fixed over potentials will generate straight lines having slopes proportional to $\frac{1}{n}$ and intercept proportional to $\frac{1}{K}$.

The K-L plots of nanoFeTSPc-*o*MWCNT, nanoFeTSPc-*s*MWCNT, and Pt/C at different electrode potentials are shown in Figs 12.10 (d), (e), and (f). Fig

12.10 (d) indicates that the plots of nanoFeTSPc-*o*MWCNT exhibit an excellent linear relationship between $1/j$ and $1/\omega^{1/2}$ over the potential range studied. The transferred electron number (n) was calculated to be 3.7.(≈4) This is in good agreement with results observed by other authors as FePc and FeTSPc are known to undergo ORR with production of water through the 4 electron reduction pathway in alkaline media[1,51].

For K-L plots of nanoFeTSPc-sMWCNT, seen in Fig 12.10 (e), the n value was calculated to be 2.14. This result indicates a 2 electron pathway reduction of O_2. This is an unexpected result and could be due to the effect of the sulfonate functionalised MWCNT support on the nanoFeTSPc substituents. Some Fe-based N_4 catalysts have been known to undergo reduction O_2 pathways different from the usual $4e^-$ path due to the effect of substituents or ligands attached to the macrocycle[52–54]. Baker et al.[53] performed a detailed study on the effects of various electron withdrawing and electron donating substituents on FePc derivatives. The same performance was observed for $FePc(SO_3H)_4$ and $FeNpPc(tBu)_4$; the electron transfer number calculated for ORR for FePc $(SO_3H)_4$ was also found to be 2 in most of the temperatures studied. Considering the difference in the electron withdrawing and donating substituents a better performance was expected at the $FePc(SO_3H)_4$ modified electrodes. Thus they deduced that as $FePc(SO_3H)_4$ is known to form adducts with O_2, (nucleophilic $[SO_3H]^-$ groups form adducts with carbonyls [C=O] of aldehydes, methyl ketones and cyclohexanones) the increase in ORR onset potential could be the result of the reduction of the adduct before the catalyst can participate in the ORR. This can also be the reasoning behind the activity of nanoFeTSPc-sMWCNT. Being a sulfonate derivative of FePc and also incorporated on sulfonate MWCNTs; there is an excessive presence of surface (SO_3H) groups bound to the catalysts which can readily lead to the formation of adduct once it is in contact with O_2 or hydroxide anions or other free carbonyls on the functionalised carbon nanotubes. The $[I_D/I_G]$ value of NanoFeTSPc-sMWCNT from results of its

Raman spectra further confirms the supposition of the adduct formation of nanoFeTSPc with s-MWCNTs. This value is opposed to the envisaged expected one which was meant to be higher due to further increase of roughness of the s-MWCNTs as a result of nanoFeTSPc doping.

Fig 12.10 (f) depicts the K-L plots of Pt/C at various potentials. The transferred electron number (n) was calculated to be 3.5 (≈4). Thus the ORR process for Pt/C was also a four electron pathway, agreeing well with reports from other authors [49,55,56].

The kinetic rate constant (k) was calculated from J_{kin} values from the K-L plots. The values were estimated as 1.57 x 10 cms^{-1}; 1.38 x 10 cms^{-1} and 1.48 x 10 cms^{-1} for nanoFeTSPc-*o*MWCNT, nanoFeTSPc-*s*MWCNT and Pt/C respectively. These values are better and comparable to those reported for other substituted FePc including some with incorporation of noble metals like Pt[51,57]. NanoFeTSPc-*o*MWCNT gave the best k value. The Tafel values were obtained from diffusion corrected plots. Correcting the polarization curve for mass diffusion for the first order reaction, one obtains: [58]

$$j_k = \left(\frac{j}{j_L - j}\right) \qquad (12.3)$$

The j_k is related to the Tafel equation as follows:

$E_{app} = E_{eq} - b \log j_k$ where b is the Tafel slope. (12.4)

where E_{app} is the applied potential, E_{eq} is the equilibrium potential, j_k is the kinetic current density, j_L is the limiting current density at a given potential. The plot of E_{app} vs log j_k yielded Tafel slope values of 216 $mVdec^{-1}$, 371 $mVdec^{-1}$ and 53 $mVdec^{-1}$ were obtained respectively for nanoFeTSPc-*o*MWCNT, nanoFeTSPc-*s*MWCNT and Pt/C. The composites with carbon nanotubes had higher Tafel values which is an indication of porosity of the modified electrode. This can be due to the presence of the MWCNTs.

Table 12.2 below gives a summary of the kinetic parameters obtained from the ORR studies using RDE. A comparison of the catalysts is also made with two other Iron phthalocyanine based catalysts in literature.

Table 12.2: Kinetic parameters, *b* (Tafel value) and *k* (kinetic rate constant) and (*n*) the number of electrons transferred in the ORR process for nanoFeTSPc *o*MWCNTs, nanoFeTSPc-*s*MWCNTs and Pt/C and a few other phthalocyanine-based catalysts

Catalysts	**Catalyst loading**	**J_{kin} /mAcm^{-2} (at -0.60 V vs Ag/AgCl)**	**(*n*)**	***k*/cms^{-1}**	***b*/mVdec^{-1}**	**Reference**
nanoFeTSPc-*o*MWCNT	≈ 10 %	10.59	3.7	1.57 x10^{-2}	216	This work
nanoFeTSPc-*s*MWCNT	≈ 10 %	4.94	2.1	1.38 x10^{-2}	371	This work
Pt/Vulcan C	80 %	6.28	3.5	1.48 x10^{-2}	153	This work
FePc/SWCNT	20 %	-	3.9	n/a	n/a	37
PtFeOCPc-MWCNT	50 %	n/a	3.9	2.78 x10^{-2}	180	57
FePc(CP)$_4$/Gr	n/a	n/a	3.8	n/a	387	59
PtFeOcPc: Iron (II) tetrakis (diaquaplatinum) octacarboxy phthalocyanine **FePc(CP)$_4$/Gr : Iron (III) tetracumylphenoxy phthalocyanine / Graphene**						

12.6 Methanol Tolerance

The methanol cross over effect on nanoFeTSPc-*o*MWCNT and Pt/C was evaluated in an O_2 saturated 0.1 M KOH solution with sequential additions of 0.1 ml, 1 M methanol; the last and final CV carried out under this experiment was run with an addition of 1ml methanol to the O_2 saturated 0.1 M KOH solution The results obtained can be seen in Fig 12.11.

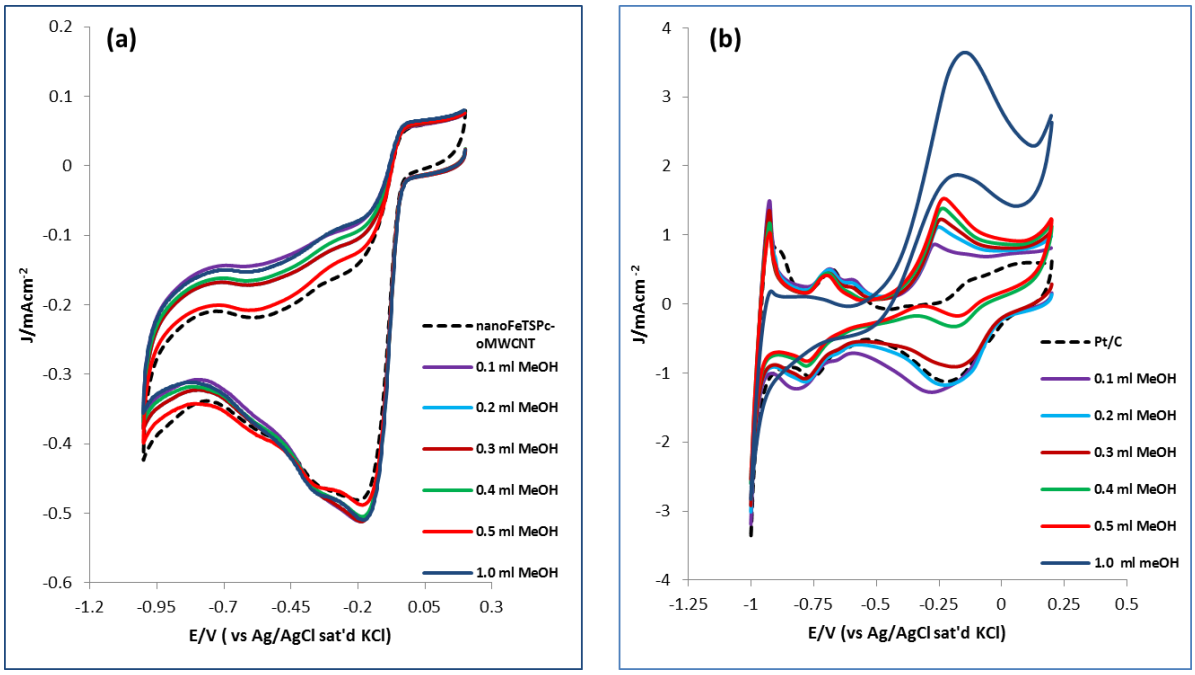

Figure 12.11: CVs of ORR on nanoFeTSPc-*o*MWCNT and Pt/C without (broken lines) and with (straight lines) additions of volumes of 1 M methanol to 0.1 M KOH saturated with O_2. (Scan rate = 25 mVs^{-1})

Fig 12.11 (a) shows the CV scans for the ORR at electrode modified nanoFeTSPc-*o*MWCNT in O_2 saturated 0.1 M KOH solution contaminated with methanol. The CV scan before the addition of methanol is denoted with broken lines. There was no noticeable change in the CV curves in the presence and absence of 1 M methanol in the O_2 saturated 0.1 M KOH solution. This implies that nanoFeTSPc-*o*MWCNT has a very high selectivity for ORR in the presence of methanol.

However, the performances of Pt/ C under the same conditions leave much to be desired. For Pt/C shown in Fig 12.11 (b) the ORR peak at -0.198 V begins to diminish steadily, and an immediate appearance of a

methanol oxidation anodic peak -0.24 V is seen. This anodic peak is seen to increase steadily with fresh additions of methanol to the O_2 saturated 0.1 M KOH solution. The ORR peak is almost non-existence after the addition of 0.4 ml, 1 M methanol and with the subsequent addition of 1 ml methanol a complete methanol oxidation reaction takes place as seen in the CV scan. All of these observations indicate a strong cross over effect of methanol on the Pt/C during ORR

12.7 Conclusion

A novel non-noble, metal electrocatalyst – nanoFeTSPc was synthesised and incorporated on both OH functionalised MWCNTs (nanoFeTSPC-*o*MWCNT) and SO_3H functionalised MWCNTs (nanoFeTSPc-*s*MWCNT.through a microwave mediated process. The composites were investigated for their ORR properties. The electrochemical investigation of ORR shows that nanoFeTSPc on -*s*MWCNT (nanoFeTSPc-*s*MWCNT) gave a poorer electrocatalytic performance compared to its hydroxyl functionalised based counterpart (nanoFeTSPc-*s*MWCNT). It also gave an unprecedented result of a 2 electron process, whereby O_2 is reduced primarily to peroxide for ORR mechanism for a FeTSPc based catalysts whose ORR process is predominantly that of a 4 electron transfer. This change in O_2 reduction mechanism has been the result of the change in substituent groups on the MWCNT substrate. On the other hand, nanoFeTSPc-*o*MWCNT has proved to be an excellent ORR catalyst with high activity and perfect selectivity. Its performance in terms of ORR onset potential, reduction current density response and favourable oxygen reduction pathway is comparable and better than some other 'FePc-MWCNT' composites in literature [1,48,60]. In comparison to Pt/C which has a noble metal loading, nanoFeTSPc-*o*MWCNT exhibited a better ORR current density response. Its high selectivity for oxygen reduction in the presence of methanol rates it a comparable and even better catalyst than commercial Pt/C., this makes it a promising catalyst for alkaline fuel cells.

12.8 References

(1) Morozan, A.; Campidelli, S.; Filoramo, A.; Jousselme, B.; Palacin, S. *Carbon N. Y.* **2011**, *49*, 4839–4847.

(2) Bezerra, C. W. B.; Zhang, L.; Lee, K.; Liu, H.; Marques, A. L. B.; Marques, E. P.; Wang, H.; Zhang, J. *Electrochim. Acta* **2008**, *53*, 4937–4951.

(3) Zagal, J. H.; Griveau, S.; Silva, J. F.; Nyokong, T.; Bedioui, F. *Coord. Chem. Rev.* **2010**, *254*, 2755–2791.

(4) Zagal, J. H. *Coord. Chem. Rev.* **1992**, *119*, 89–136.

(5) Viswanathan, B.; Varadaraju, U. V; Rao, C. V. *On the search for non-noble based electrodes for oxygen reduction reaction*; 2006; Vol. 661, pp. 1–59.

(6) Ji, D.; Lu, X.; He, R. *Appl. Catal. A Gen.* **2000**, *203*, 329–333.

(7) Ozoemena, K.; Nyokong, T. *J. Chem. Soc. Dalt. Trans.* **2002**, 1806–1811.

(8) Griveau, S. Gulppi, M. Pavez, J. Zagal, H. Bedioui, F. *Electroanalysis* **2003**, *15*, 779–785.

(9) Li, N.; Zhu, M.; Qu, M.; Gao, X.; Li, X.; Zhang, W.; Zhang, J.; Ye, J. *J. Electroanal. Chem.* **2011**, *651*, 12–18.

(10) Ozoemena, K.; Kuznetsova, N.; Nyokong, T. *J. Mol. Catal. A Chem.* **2001**, *176*, 29–40.

(11) Flora, W. H.; Hall, H. K.; Armstrong, N. R. *J. Phys. Chem. B* **2003**, *107*, 1142–1150.

(12) Agboola, B.; Ozoemena, K. I.; Nyokong, T. *J. Mol. Catal. A Chem.* **2006**, *248*, 84–92.

(13) Pirouzmand, M.; Amini, M. M.; Safari, N. *J. Colloid Interface Sci.* **2008**, *319*, 199–205.

(14) Oni, J.; Nyokong, T. *Polyhedron* **2000**, *19*, 1355–1361.

(15) Siqueira, J. R.; Crespilho, F. N.; Zucolotto, V.; Oliveira, O. N. *Electrochem. commun.* **2007**, *9*, 2676–2680.

(16) Siqueira, Jr., J. R.; Gasparotto, L. H. S.; Oliveira, Jr., O. N.; Zucolotto, V. *J. Phys. Chem. C* **2008**, *112*, 9050–9055.

(17) Francisco Silva, J.; Griveau, S.; Richard, C.; Zagal, J. H.; Bedioui, F. *Electrochem. commun.* **2007**, *9*, 1629–1634.

(18) Sanchez, M.; Fache, E.; Bonnet, D.; Meunier, B. *J. Porphyr. Phthalocyanines* **2001**, *05*, 867–872.

(19) Adebayo Akinbulu, I.; Nyokong, T. *New J. Chem.* **2010**, *34*, 2875.

(20) Zagal, J.; Paez, M.; Tanaka, A. *J. Electroanal. Chem.* **1992**, *339*, 13–30.

(21) Zhang, Y.; Mo, G.; Li, X.; Ye, J. *J. Power Sources* **2012**, *197*, 93–96.

(22) Chen, R.; Li, H.; Chu, D.; Wang, G. *J. Phys. Chem. C* **2009**, *113*, 20689–20697.

(23) Antolini, E. *Appl. Catal. B Environ.* **2009**, *88*, 1–24.

(24) Eletskii, A. V. *Physics-Uspekhi* **2009**, *52*, 209–224.

(25) Majedi, F.; Zavareh, S.; Sharif, M. S.; Golestani-Fard, F. *Int. J. Nanosci.* **2010**, *09*, 175–180.

(26) Siswana, M. P.; Ozoemena, K. I.; Nyokong, T. *Electrochim. Acta* **2006**, *52*, 114–122.

(27) Du, C. Y.; Zhao, T. S.; Liang, Z. X. *J. Power Sources* **2008**, *176*, 9–15.

(28) Sun, Z.-P.; Zhang, X.-G.; Liu, R.-L.; Liang, Y.-Y.; Li, H.-L. *J. Power Sources* **2008**, *185*, 801–806.

(29) Gao, B.; Yuan, C.; Su, L.; Chen, S.; Zhang, X. *Electrochim. Acta* **2009**, *54*, 3561–3567.

(30) Nevin, W.A, Liu, W., Melnik, M and Lever. *J.Electroanal. Chem.,* **1986**, 217–234.

(31) Grootboom, N.; Nyokong, T. *J. Mol. Catal. A Chem.* **2002**, *179*, 113–123.

(32) Lever, A. B. P.; Pickens, S. R.; Minor, P. C.; Licoccia, S.; Ramaswamy, B. S.; Magnell, K. *J. Am. Chem. Soc.* **1981**, *103*, 6800–6806.

(33) Zucolotto, V.; Ferreira, M.; Cordeiro, M. R.; Constantino, C. J. L.; Balogh, D. T.; Zanatta, A. R.; Moreira, W. C.; Oliveira, O. N. *J. Phys. Chem. B* **2003**, *107*, 3733–3737.

(34) Zucolotto, V.; Ferreira, M.; Cordeiro, R.; Constantino, C. J. L. *J. Phys. Chem. B* **2003**, *107*, 3733–3737.

(35) Günzler, H.; Gremlich, H.-U. *IR spectroscopy: an introduction*; Wiley-vch, 2002.

(36) Kim, U. J.; Furtado, C. a; Liu, X.; Chen, G.; Eklund, P. C. *J. Am. Chem. Soc.* **2005**, *127*, 15437–15445.

(37) Dong, G.; Huang, M.; Guan, L. *Phys. Chem. Chem. Phys.* **2012**, *14*, 2557–2559.

(38) Zhang, R.; Wang, X. *Chem.MaterMater* **2007**, *19*, 976–978.

(39) Filho, A. G. S.; Meunier, V.; Terrones, M.; Sumpter, B. G.; Barros, E. B.; Villalpando-Páez, F.; Filho, J. M.; Kim, Y. A.; Muramatsu, H.; Hayashi, T.; Endo, M.; Dresselhaus, M. S. *Nano Lett.* **2007**, *7*, 2383–2388.

(40) Furtado, C. a; Kim, U. J.; Gutierrez, H. R.; Pan, L.; Dickey, E. C.; Eklund, P. C. *J. Am. Chem. Soc.* **2004**, *126*, 6095–6105.

(41) Jeong, Y.; Kim, J.; Lee, G., *Colloids. Polym. Sci* **,2010,** *288*, 1–6.

(42) Jürmann, G.; Tammeveski, K. *J. Electroanal. Chem.* **2006**, *597*, 119–126.

(43) Shanmugam, S.; Gedanken, A. *J. Phys. Chem. B* **2006**, *110*, 2037–2044.

(44) Shao, Y.; Yin, G.; Zhang, J.; Gao, Y. *Electrochim. Acta* **2006**, *51*, 5853–5857.

(45) Gooding, J. J. *Electrochim. Acta* **2005**, *50*, 3049–3060.

(46) Moore, R. R.; Banks, C. E.; Compton, R. G. *Anal. Chem.* **2004**, *76*, 2677–2682.

(47) Stefan, I. C.; Mo, Y.; Ha, S. Y.; Kim, S.; Scherson, D. a. *Inorg. Chem.* **2003**, *42*, 4316–4321.

(48) Kruusenberg, I.; Matisen, L.; Shah, Q.; Kannan, a. M.; Tammeveski, K. *Int. J. Hydrogen Energy* **2012**, *37*, 4406–4412.

(49) Wang, S.; Yu, D.; Dai, L. *J. Am. Chem. Soc.* **2011**, *133*, 5182–5185.

(50) U.A. Paulus, A. Wokaun, G. G. S.; T. J. Schmidt, V. Stamenkovic, V. Radmilovic, N. M. Markovic, and P. N. R. *J. Phys. Chem. B* **2002**, *106*, 4181–4191.

(51) Lili Cui, Guojun Lv, Zhiyu Dou, X. H. *Electrochim. Acta* **2013,** *106*,272-278.

(52) Cardenas-Jiron, G. I. *J. Phys. Chem. A* **2002**, *106*, 3202–3206.

(53) Baker, R.; Wilkinson, D. P.; Zhang, J. *Electrochim. Acta* **2008**, *53*, 6906–6919.

(54) Baker, R.; Wilkinson, D. P.; Zhang, J. *Electrochim. Acta* **2009**, *54*, 3098–3102.

(55) Demarconnay, L.; Coutanceau, C.; Léger, J.-M. *Electrochim. Acta* **2004**, *49*, 4513–4521.

(56) Bambagioni, V.; Bianchini, C.; Filippi, J.; Lavacchi, A.; Oberhauser, W.; Marchionni, A.; Moneti, S.; Vizza, F.; Psaro, R.; Dal Santo, V.; Gallo, A.; Recchia, S.; Sordelli, L. *J. Power Sources* **2011**, *196*, 2519–2529.

(57) Mamuru, S. A.; Ozoemena, K. I. *Electrochem. commun.* **2010**, *12*, 1539–1542.

(58) Koç, İ.; Çamur, M.; Bulut, M.; Özkaya, a. R. *Catal. Letters* **2009**, *131*, 370–380.

(59) Cui, L.; Lv, G.; Dou, Z.; He, X. *Electrochim. Acta* **2013**, *106*, 272–278.

(60) Mamuru, S. A.; Ozoemena, K. I. *Electroanalysis* **2010**, *22*, 985–994.

Chapter 13

CONCLUSIONS AND FUTURE PERSPECTIVES

13.1 Conclusions and Future Perspectives

A novel FeCo@Fe@Pd/ core shell nano catalyst has been successfully synthesized and incorporated on Vulcan carbon, carboxyl carbon nanotube (CNT-OH) and sulfonate carbon nanotube (CNT-SO_3). These catalyst have been tested for their elctrocatlaytic performances as both cathode and anode catalysts in four different alkaline alcohol fuel cells – DMFC, DEFC, DEGFC and DGFC, using both the half cell studies and the real MEA fuel test.

Looking at the half cell studies done in all four fuels, FeCo@Fe@Pd/CNT-OH gave an overall best catalytic activity in all tests carried out. Its catalytic capabilities as anodes in the four fuel cells have been outstanding among other Pd based catalysts in terms of its ealier onset potentials, high current responses, high electrocatlaytic rate constant values, and quick charge transport capabilities by giving very low resistance to electron transport during the fuel oxidation process. Coupled to all of these is also its high stability in alkaline fuel cell medium during alcohol oxidation reaction.

MEA experiments in the real DAAFCs showed its best fuel cell efficiency performance when used as anode in DEFC where it exhibited a good faradaic and energy efficiency, and running for a longer period of time during the fuel cell operation. Its better catalytic performance was also the initial half-cell studies using the same fuel compared to methanol.

It also exhibited a spectacular selectivity for the complete oxidation of polyhydric fuels through conversion of the fuels to mostly carbonate during the operations of DEGFCs and DGFCs. This was especially seen in DGFCs where it gave a 73% carbonates as its fuel cell exhaust product after using it as an anode in a working passive DGFC.

Its obvious potency as a leading anodic catalyst in fuel cell operations is very obvious but the following suggestions may further enhance its electro-oxidative performance:

(i) Optimising the amount of noble metal in the shell to further reduce the amount of Pd used.

(ii) Optimising the mass loading of the catalyst in Fuel cell applications.

(iii) Incorporating the core-shell nanocatalysts on other high-conducting carbon materials like graphene.

(iv) Taking advantage of the icosahedral morphology obtained as a result of the synthetic procedure and stabiliser used, to fabricate special high index facet (HIF) core shell nanocatalysts (with no substrates) to improve the catalytic surface of Pd.

(v) Incorporating the as-prepared HIF Pd nanocore shell in (iv) on graphene to enhance its conductivity.

The second aspect of the thesis deals with the synthesis of a novel nano size and hydrophobic form of soluble Fe (II) sulfonatephthalocyanine – nanoFeTSPc. It was successfully used as a cathodic catalyst in alkaline fuel cells. The half studies done revealed its very high resistance to the presence of alcohol (methanol) during its ORR catalysis.

Some suggestions for further investigation using the catalysts include:

(i) Performing some MEA studies in alkaline medium using nanoFeTSPc as cathodes.

(ii) Incorporating the catalysts on graphene so as to enhance its conductivity.

Appendix 1

List of Publications arising from the thesis

1. O.O. Fashedemi and K.I. Ozoemena, "A facile approach to the synthesis of hydrophobic iron tetrasulfophthalocyanine (FeTSPc) nano-aggregates on multi-walled carbon nanotubes: A potential electrocatalyst for the detection of dopamine", *Sens. Actuators: B. Chem.* **2011**, 160, 7-14.

2. O.O. Fashedemi, Basil Julies and K.I. Ozoemena, "Synthesis of Pd-coated FeCo@Fe/C core-shell nanoparticles: microwave-induced 'top-down' nanostructuring and decoration", *Chem. Commun,* **2013**, 49, 2034-2036.

3. Omobosede O. Fashedemi and Kenneth I. Ozoemena. "Enhanced methanol oxidation and oxygen reduction reactions on palladium-decorated FeCo@Fe/C core–shell nanocatalysts in alkaline medium", *Phys. Chem. Chem. Phys.*, **2013**,**15**, 20982-20991.

4. Omobosede O. Fashedemi and Kenneth I. Ozoemena**. "**Comparative electrocatalytic oxidation of ethanol, ethylene glycol and glycerol in alkaline medium at Pd-decorated FeCo@Fe/C core-shell nanocatalysts'', *Electrochimica Acta*, 128, **2014**, 279-286.

5. O.O. Fashedemi and K.I. Ozoemena, "Palladium decorated FeCo@Fe core-shell (FeCo@Fe@Pd) supported on carbon nanotubes for Methanol and Ethanol oxidation in Alkaline Medium" (Manuscript in preparation).

6. O.O. Fashedemi Hamish Miller, Andrea Marchionni Francesco Vizza, K.I. Ozoemena, "Oxidation of Polyhydric alcohols in Alkaline Medium on Palladium decorated core shell nanocatalysts (FeCo@Fe@Pd) supported on carbon nanotubes" (Manuscript in preparation).

7. Omobosede O. Fashedemi, Hamish Miller, Andrea Marchionni Francesco Vizza, Kenneth I. Ozoemena, "Selectivity towards complete oxidation of Ethylene glycol (EG) and Glycerol (GLY) on Palladium decorated FeCo@Fe core-shell FeCo@Fe@Pd/C and FeCo@Fe@Pd/CNT-OH in Alkaline Medium"(Manuscript in preparation).

8. O.O. Fashedemi and K.I. Ozoemena, "The Effects of Carbon Supports on the Oxygen Reduction Reactions at Palladium Nanocatalysts in Alkaline Medium", (Manuscript in preparation).

9. O.O. Fashedemi and K.I. Ozoemena, "Non noble Iron (II) tetrasulfophthalocyanine on multi walled carbon nanotubes: potential cathode catlaysts in direct alcohol alkaline fuel cell" (Manuscript in preparation).

Appendix 2

List of Some Conference Presentations arising from the thesis

1. *"Alcohol Oxidation and Oxygen Reduction Reactions in Alkaline media at Palladium Core-Shell Nanocatalysts".* Kenneth I. Ozoemena, **Omobosede O. Fashedemi**, 65th Annual Meeting of ISE Lausanne, Switzerland, 31st August – 5th September 2014 (Poster Presentation).

2. *"Microwave-Assisted Synthesis of Palladium-Decorated FeCo@Fe Core-Shell Nanocatalysts: Applications in Direct Alcohol Alkaline Fuel Cells"*, Kenneth I. Ozoemena, **Omobosede O. Fashedemi**, 224th ECS Meeting San Francisco, California, USA, 27 October – 1st November 2013 (Oral Presentation).

3. *"Novel palladium core-shell nanocatalyst for efficient oxygen reduction reaction and alcohol-tolerance",* Kenneth I. Ozoemena, **Omobosede O. Fashedemi**, 24th Annual CATSA Conference, Wild Coast Sun, Port Edward, 17 – 20 November 2013 (Oral Presentation).

4. *"Direct ethanol Fuel Cell performance and energy efficiency enhancement of core shell, FeCo@Fe@Pd/C in active and passive fuel cells"*. **Fashedemi O**, Miller H, Marchionni A, Vizza F, Ozoemena K., 12th International Chemistry Conference Africa – Chemistry for Sustainable Growth, 7th -12th July 2013, Pretoria, South Africa (Oral Presentation).

5. *"Non –noble Iron Tetrasufophthalocyanine on Multi-walled Carbon nanotubes: Potential Cathode Catalyst in Direct Alcohol Alkaline fuel Cells".* **Omobosede Fashedemi**, Kenneth Ozoemena, 13th Tropical Meeting of the International Society of Electrochemistry (ISE), 7th – 10th April, 2013, Pretoria, South Africa (Oral Presentation).

6. *"Palladium-based Nanoelectrocatalysts for Direct Alcohol Oxidation and Oxygen Reduction Reaction in Alkaline Media"*. Kenneth I. Ozoemena, Remegia M. Modibedi, **Omobosede O. Fashedemi**, 23rd Annual Conference of Catalysis society of South Africa, 2012. Langebaan, Capetown, South Africa, 11th -14th November (Oral Presentation)

7. *"Active and stable FeCo@Pd nanoalloy in alkaline fuel cells."* **Omobosede O. Fashedemi** and Kenneth I. Ozoemena, 23rd Annual Conference of Catalysis society of South Africa, 2012, Langeban, Capetown, 11th -14th November (Poster Presentation).

8. *"Palladium–rich nanoalloy as cathode material for hydrogen evolution reaction in alkaline medium."* **Omobosede O. Fashedemi** and Kenneth I. Ozoemena, South Africa -Korea H_2 Fuel cell workshop, Bela Bela, South Africa, 11-12 July, 2012 (Poster Presentation)

9. *"FeCo@Pd core-shell nanocatalysts for direct alcohol alkaline fuel cell applications",* **Omobosede O. Fashedemi** and Kenneth I. Ozoemena, 6th International Conference of the Africa Materials research Society, Victoria Falls,Zimbabwe, 11 – 16 December , 2011 (Oral Presentation)

10. *Physico-electrochemical Properties of disordered* $LiMn_{1.5}Ni_{0.5}O_4$ *obtained in the presence of Carbon Nanotubes using the modified Pechini Method."* Kenneth I. Ozoemena, **Omobosede O. Fashedemi**, Charl J. Jafta1, Mkhulu K. Mathe, 220th ECS Conference, The Electrochemical society, Boston, U.S.A. October 2011 (Poster Presentation)

11. *"Microwave –assisted modified Pechini method for the preparation of nanosized, aluminium doped, carbon nanotube coated Li* $[Li_{0.2}Mn_{0.54}Ni_{0.13}Co_{0.13}]O_2$ *cathode material for lithium ion battery".* Kenneth I. Ozoemena, **Omobosede O. Fashedemi**, Charl J. Jafta, Mkhulu K. Mathe, 220th ECS Conference, The Electrochemical society Boston, U.S.A. October 2011 (Poster Presentation).

12. *"Microwave –assisted syntheses of FeCo@Pd core shell nanocatalysts for oxygen reduction in fuel cells".* **Omobosede O. Fashedemi** and Kenneth I. Ozoemena, 2nd Annual South African Young Scientists' conference (ASSAF-DST-NRF), Pretoria, South Africa, 26th -18th September, 2011 (Oral Presentation).

13. *"Formation of Hydrophobic Iron (II) tetrasulfophthalocyanine nanoaggregates on multiwalled carbon nanotubes and their electrocatalytic properties as sensors".* **Omobosede O. Fashedemi** and Kenneth I. Ozoemena, 11th International Conference on Frontiers of Polymers and advanced Materials (ICPFAM), Pretoria, South Africa (22nd – 27th May, 2011) (Oral Presentation).